E-735

A MEASUREMENT OF THE BOSE-EINSTEIN CORRELATION FOR TWO PIONS IN PROTON-ANTIPROTON COLLISIONS AT CENTER OF MASS ENERGY 1.8 TEV

by

THEODOROS ALEXOPOULOS

A thesis submitted in partial fulfillment of the

requirements for the degree of

Doctor of Philosophy

(Physics)

at the

UNIVERSITY OF WISCONSIN–MADISON

1991

AAB2559

Abstract

A MEASUREMENT OF THE BOSE-EINSTEIN CORRELATION FOR TWO PIONS IN PROTON-ANTIPROTON COLLISIONS AT CENTER OF MASS ENERGY 1.8 TEV

Theodoros Alexopoulos

Under the supervision of Professor Albert R. Erwin, U.W.-Madison

The intensity interferometry or the Bose-Einstein correlation between two like charged pions produced in high energy $p\bar{p}$ collisions at $\sqrt{s} = 1.8$ TeV was measured using data collected with the E735 detector at the TEV collider complex at Fermilab. The method used for this measurement was that of the Hanbury-Brown and Twiss (HBT) phenomenon. Spatial and lifetime sizes of pion source are measured as a function of the charged particle multiplicity, n_{ch}, and as a function of the total momentum of pion pair. The results from this thesis are compared with the results from the CDF and UA1 experiments.

In addition, a new method for identifying particle resonances is presented using a Neural Network (NN) pattern recognition technique. This method uses a feed-forward NN in order to construct an efficient mapping between certain observed kinematical variables of a resonance and a background event. This NN method was applied to a series of different types of resonances, like K^0, ρ^0, K^{*0}, and Λ^0.

αφιερωνεται

στην μνημη του πατερα μου

ACKNOWLEDGMENTS

This thesis would not have been possible made without the contribution of many people. I would like to thank my thesis adviser Professor Albert R. Erwin for providing the research opportunity which led to this thesis as well as for his encouragement and guidance over the past six years. I would also like to thank Frank Turkot and Carlos Hojvat for giving me their help, knowledge, and insight during the E735 run and analysis period.

Special thanks go to Ken S. Nelson and Charles Findeisen for their time and effort spent in teaching me so much about research here at the University of Wisconsin-Madison.

Also, I am grateful to John Jennings for hundreds of worthwhile discussions during the long hours in the lab. Working and talking with Kavoos Deilamian, John Matthews, and Mark Lomperski has been a memorable experience and they have become truly good friends. In addition, my fellow E735 members at the University of Wisconsin-Madison deserve thanks for their effort to help me. They are Jordan Bevic, and Stephen Tufte. Also I thank Casey Durandet for help with reading and corrections in this thesis. I am very grateful to Antonis Sofocleous for preparing 90% of the figures, thus saving me at least 1 month of work.

In addition I would like to thank all the members of the collaboration for their warmth, friendship and for making my working time at Fermilab both interesting and enjoyable.

I would like to thank Professor Richard Prepost and Professor Loyal Durand for their reading of this thesis and their helpful comments and suggestions.

I'd also like to thank all my Greek compatriots here in Madison, Wisconsin; we have spent so many hours together. Special thanks go to all of the "*αφασιες*" of Doksa Madison soccer team: Thanassis Diplas, Kostas Sedikides, Sid Sarinopoulos, Mike Papadimitrakis, Antreas Katsiotis, Yiannis Ioannidis, Dimitris Tsagaris, Nikos Galatsanos, Pantelis Sinos, Vasilis and George Borovas, and Thanos Tzavaras. Also to Roulis Kazantzis, Haris Kiafoulis and Alexios Zavras. I would also thank the beautiful Greek ladies here in Madison: Maria Spyropoulou, Marianna Hajidimitriou, Natalia Ioannidou and Tasoula Sedikides.

I am thankful to my early adviser at the Nuclear Research Center in Greece, "Demokritos", Manolis Dris for providing me with the initial training in experimental high energy physics and for helping me continue my Physics education at the University of Wisconsin-Madison. Also thanks goes to my good friends Dimitri Loukas and Nikos Papadakis.

None of my education would have been possible without the continual support of my parents, Marigw and Elias Alexopoulos my sister Eugenia and my brother in law Takis. During my years back home in Eagaleo they provided love and strength at all times. Unfortunately my father can not see that his efforts did not go away, after working behind the "steering wheel" for so many years! Many thanks to all the people back in my neighborhood (Eagaleo) where I grew up.

Finally, I thank my wife and *καψουρα μου* Vasso for her support, love, and all the things she has done for me during our relationship for these past ten

years. Without her I would have been a "big zero".

Contents

Abstract i

Acknowledgments iii

List of Tables xi

List of Figures xii

Introduction 2

1 **Bose-Einstein Correlation Review** 6

1.1 Hanbury-Brown and Twiss Effect 6

1.2 Review of Two-Pion B.E. Correlations 10

1.2.1 Gaussian Parameterization 12

1.2.2 Uniform Sphere 13

1.2.3 Ellipsoid Source Shape 14

1.2.4 Spherical Uniform Shell 14

1.2.5 Gaussian Source in the Rest Frame of 2 π's 14

1.2.6 Uniform Disk of Radius R 15

1.2.7 Weiner Parameterization 16

1.3 Review of N-Particle B.E. Correlations 18

2 The Experimental Apparatus **22**

2.1 Tevatron 22

2.2 The C0 Coordinate System 25

2.3 An Overview of the E735 Detector 26

2.3.1 Z-Chamber 28

2.3.2 Central Tracking Chamber 44

2.3.3 Hodoscope 46

2.3.4 Pre- and Post-Magnet Chambers 47

2.3.5 Magnet 52

2.3.6 Straw Drift Chambers 53

2.3.7 TOF System 54

2.3.8 Endcap Chamber 58

3 Data Acquisition and Triggers **103**

3.1 Data Acquisition 103

3.2 Triggers 104

3.2.1 $T0$ Trigger 105

3.2.2 PT Trigger 105

3.2.3 TOF_1 Trigger 106

3.2.4 Spectrometer Trigger 107

3.2.5 dE/dx Trigger 108

4 Event Reconstruction **121**

4.1 Event Vertex 123

4.1.1 Global Method A 123

4.1.2 Global Method B 124

4.2 Track Reconstruction 127

4.3 Event and Track Selection 130

4.3.1 Event Selection 131

4.3.2 Track Selection 132

4.4 Multiplicity Calculation 134

4.5 Particle ID and Mass 135

4.6 Single Track Momentum Resolution 136

4.6.1 Pion, Kaon, and Proton Mass Widths 137

4.6.2 K^0 Mass Width 141

4.6.3 Λ^0 Mass Width 143

4.6.4 Magnet-Off Data 146

5 Resonance Search Using Neural Network Method 194

5.1 Neural Network Method 195

5.2 $K^0 \rightarrow \pi^+\pi^-$ Signal 199

5.2.1 Training the Neural Network 199

5.2.2 Test of K^0 Decays Using the Neural Network 201

5.3 $\rho^0 \rightarrow \pi^+\pi^-$ Signal 201

5.3.1 Training the Neural Network 201

5.3.2 Test of ρ^0 Decays Using the Neural Network 203

5.4 $K^{*0} \rightarrow \pi K$ Signal 204

5.4.1 Training the Neural Network 204

5.4.2 Test of K^{*0} Decays Using the Neural Network 205

5.5 $\Lambda^0 \to \pi p$ Signal 205

5.5.1 Training the Neural Network 205

5.5.2 Test of Λ^0 Decays Using the Neural Network 206

6 HBT Data Analysis **226**

6.1 Measurement of the BE Correlation 226

6.1.1 Pairs from Different Events 228

6.1.2 Pairs from the Same Events 229

6.2 Systematic Biases 230

6.2.1 E735 Aperture Problem 231

6.2.2 Fake Background Correlations 232

6.2.3 Gamow Corrections 234

6.2.4 Momentum Error 236

6.2.5 Opening Angle Problem 238

6.2.6 Vertex Problem 240

6.3 Control Experiment 241

6.3.1 Unlike-sign $+-$, $K\pi$, etc., Correlations 242

6.4 Radius and Lifetime Measurement 243

6.4.1 Correlation C_2 versus q_t 243

6.4.2 Correlation C_2 versus q_0 246

6.4.3 Directional Dependence of the Radius R 248

6.5 Tables 250

7 Conclusion: Summary of Observations **325**

Computer Simulations **328**

A.1 Monte Carlo Program 328

A.1.1 Monte Carlo Description 328

A.1.2 Comparisons with the Data 333

A.1.3 Bending Algorithm 334

Useful Relations **341**

B.1 $\vec{q_t}$, $\vec{q_l}$ 341

B.2 Invariant Mass M_2 and M_3 342

B.3 Invariant Momentum Difference Q_2 and Q_3 343

B.4 Mean Velocity of the Pair of the π's 344

Bose-Einstein Correlation and Metropolis Monte Carlo **346**

C.1 Metropolis's Algorithm 347

C.2 Application of Metropolis Algorithm to B.E. Correlation 349

Electric and Potential Field of the Z-Chamber **350**

E735 Collaboration **353**

Bibliography **355**

List of Tables

6.1 R and λ vs multiplicity in Gaussian parametrization 250

6.2 R and λ vs multiplicity in Weiner parametrization 251

6.3 R and λ vs multiplicity in Podgoretsky parametrization 251

6.4 R and λ vs multiplicity in Gaussian parametrization 252

6.5 R and λ vs momentum in Gaussian parametrization 252

6.6 R and τ vs multiplicity in Gaussian parametrization 253

6.7 R and τ vs multiplicity in Gaussian parametrization 253

6.8 R and τ vs momentum in Gaussian parametrization 254

A.1 Coefficients used for modeling magnetic field $B_y(x)$ 331

List of Figures

1.1 Two pions emitted from a pion source. 21

2.1 Fermilab accelerator layout 64

2.2 Top view of the E735 detector at C0. 65

2.3 Side view of the E735 detector at C0. 66

2.4 C0 coordinate system. 67

2.5 Z-chamber drift cell 68

2.6 Equipotential, electric field , and isochrones map. 69

2.7 Z-chamber frame type 1. 70

2.8 Z-chamber frame type 2. 71

2.9 Mechanical cross section of the z-chamber. 72

2.10 Cross section of the transmission line. 73

2.11 Preamplifier schematic of z-chamber. 74

2.12 Discriminator schematic of z-chamber. 75

2.13 Z-chamber resolution vs H.V. 76

2.14 Z-chamber resolution vs track slope. 77

2.15 CTC drift cell. 78

2.16 Pre-magnet drift cells. 79

2.17 Pre-magnet equipotential field map. 80

2.18 Pre-magnet electric field map and isochrones lines. 81

2.19 Pre-magnet time to distance conversion. 82

2.20 Pre-magnet time to distance conversion vs track slope. 83

2.21 Measured pre-magnet residuals for normal tracks. 84

2.22 Measured post-magnet residuals for normal tracks. 85

2.23 Pre- and post-magnet chamber resolution as a function of the track slope. 86

2.24 Pre-magnet plane efficiency. 87

2.25 Post-magnet plane efficiency. 88

2.26 $B_y(x, z)$ at the center of the magnet. 89

2.27 Straw chamber efficiency. 90

2.28 Layout of the trigger counters TOF_p and $TOF_{\bar{p}}$. 91

2.29 ADC and TDC configuration of the TOF_1 system. 92

2.30 ADC and TDC configuration of the TOF_2 system. 93

2.31 Attenuation length of TOF_1. 94

2.32 Cross section through C0 along the beam line. 95

2.33 Top view of an endcap segment. 96

2.34 Equipotential lines of an endcap drift segment. 97

2.35 Drift and isochrones lines of an endcap drift segment. 98

2.36 Delay line endcap amplifier. 99

2.37 Delay line endcap discriminator. 100

2.38 A typical track through an endcap segment. 101

2.39 Endcap resolution. 102

3.1 Spectrometer one-track trigger logic. 113

3.2 Spectrometer two-track trigger logic. 114

3.3 Spectrometer trigger outline. 115

3.4 Current summing unit. 116

3.5 Gating unit for the spectrometer trigger. 117

3.6 Discriminator spectrometer trigger. 118

3.7 Description of variables used in the dE/dx trigger. 119

3.8 Integrator circuit used in the dE/dx trigger. 120

4.1 Example of the vertex reconstruction. 154

4.2 $z_{vertex} - z_{interc.}$ at the beam line. 155

4.3 Example of two-vertex reconstruction. 156

4.4 Two hits in the z-chamber. 157

4.5 Vertex reconstruction using method B. 158

4.6 Vertex reconstruction using method B. 159

4.7 Vertex reconstruction using method B. 160

4.8 $z_{gen} - z_{rec}$ using M.C. data. 161

4.9 $z_{gen} - z_{rec}$ using M.C. data. 162

4.10 Drift cirles in z-chamber. 163

4.11 Z_{TOF_1} for spectrometer tracks. 164

4.12 A typical high multiplicity reconstructed event. 165

4.13 A typical high multiplicity reconstructed event. 166

4.14 A typical high multiplicity reconstructed event. 167

4.15 Hodoscope asymmetry plot. 168

4.16 $z_1 - z_2$ intercepts for two reconstructed tracks. 169

4.17 $Y_{trk} - Y_{TOF1}$ of reconstructed tracks. 170

4.18 $Z_{trk} - Z_{TOF1}$ of reconstructed tracks. 171

4.19 m^2 distribution using TOF_1. 172

4.20 m^2 distribution using TOF_1. 173

4.21 Pion, kaon, and proton m^2 widths computed with TOF_1 system. 174

4.22 Pion, kaon, and proton m^2 widths computed with TOF_2 system. 175

4.23 Invariant mass distribution of $\pi^+\pi^-$ pairs. 176

4.24 Invariant mass distribution of $\pi^+\pi^+$ and $\pi^-\pi^-$ pairs. 177

4.25 Invariant mass distribution of $\pi^+\pi^-$ pairs. 178

4.26 Invariant mass distribution of pion pairs. 179

4.27 Invariant mass distribution of K^0 M.C. decays into E735 detector. 180

4.28 Proper decay-length ($L_0 = L/\beta\gamma$) distribution of K^0. 181

4.29 Invariant mass distribution of $p\pi^- + \bar{p}\pi^+$ pairs. 182

4.30 Invariant mass distribution of Λ. 183

4.31 Invariant mass of $\Lambda^0 + \bar{\Lambda}^0$ M.C. decays. 184

4.32 Proper decay-length ($L_0 = L/\beta\gamma$) distribution of $\Lambda^0 + \bar{\Lambda}^0$. 185

4.33 P_t acceptance curve of lambdas in the spectrometer. 186

4.34 Momentum distribution dn/dp_t^2 for $\Lambda^0 + \bar{\Lambda}^0$. 187

4.35 p_t spectrum using tracked Magnet-off data. 188

4.36 Field-free track which is bent due to multiple scattering. 189

4.37 Monte Carlo p_t spectrum compared to a transverse momentum, P_T, spectrum from magnet-off data. 190

4.38 Monte Carlo p_t spectrum using 0.030 radiation lengths. 191

4.39 Monte Carlo no-field momentum spectrum using only multiple scattering from 0.030 radiation lengths. 192

4.40 Monte Carlo no-field momentum spectrum using only a 500 micron measuring error. 193

5.1 Invariant mass distribution of $\pi^+\pi^-$ pairs accepted by the E735 spectrometer. 208

5.2 Architecture of a three layer feed-forward neural network. 209

5.3 Fraction of correct classifications versus training epochs for the first 100 epochs in the K^0 search. 210

5.4 Fraction of correct classifications versus training epochs for the first 500 epochs in the K^0 search. 211

5.5 Invariant mass distribution of $\pi^+\pi^-$ pairs superimposed with the invariant mass distribution of $\pi^+\pi^+$, $\pi^-\pi^-$ pairs. 212

5.6 Invariant mass distribution of $\pi^+\pi^-$ pairs superimposed with the invariant mass distribution of $\pi^+\pi^+$, $\pi^-\pi^-$ pairs. 213

5.7 Invariant mass distribution of K^0 with the neuron output value greater than 0.7. 214

5.8 Invariant mass distribution of K^0 with the neuron output value greater than 0.8. 215

5.9 Fraction of correct classifications versus training epochs for the first 100 epochs in the ρ^0 search. 216

5.10 Invariant mass distribution of $\pi^+\pi^-$ pairs for ρ^0 search. 217

5.11 Invariant mass distribution of $\pi^+\pi^-$ pairs for ρ^0 search. 218

5.12 Invariant mass distribution of ρ^0 with output neuron value greater than 0.6. 219

5.13 Invariant mass distribution of ρ^0 with output neuron value greater than 0.7. 220

5.14 Output response of the neural net Trial 1. 221

5.15 Output response of the neural net Trial 2. 222

5.16 Invariant mass distribution of ρ^0 with the Trial 2 neuron output value greater than 0.7. 223

5.17 Invariant mass distribution of K^{*0} with the neuron output value greater than 0.7. 224

5.18 Invariant mass distribution of $\Lambda^0 + \bar{\Lambda}^0$. 225

6.1 Total momentum $\vec{p}$, $\vec{q_t}$ and $\vec{q_l}$ vector definitions of a $\pi\pi$ pair . . . 255

6.2 Momentum distribution, dn/dq_μ, as a function of $(|\vec{q}|, q_0)$ over the spectrometer acceptance used in this experiment. 256

6.3 Relation of q_0 versus q_l for our data. 257

6.4 Relation of Q versus q_t for our data. 258

6.5 Vertex distribution of events accepted by E735 Monte Carlo analysis for $\pi^+\pi^+$, $\pi^-\pi^-$, and $\pi^+\pi^-$. 259

6.6 q_t distribution of events accepted by E735 Monte Carlo analysis for $\pi^+\pi^+, \pi^-\pi^-$, and $\pi^+\pi^-$ pairs. 260

6.7 Correlation function, $C_2 = (\pi^+\pi^+)_S/(\pi^+\pi^-)_S$, versus q_t. 261

6.8 Correlation function, $C_2 = (\pi^-\pi^-)_S/(\pi^+\pi^-)_S$, versus q_t. 262

6.9 Correlation function $C_2 = (\pi^+\pi^+ + \pi^-\pi^-)_S/(\pi^+\pi^-)_S$ versus q_t. . 263

6.10 G_u, G_l, G_u/G_l Gamow correction factors as a function of Q^2. . . 264

6.11 Monte Carlo correlation function, C_2, as a function of q_t after momentum error. The fitted curve is of the form $C_2 = P_1(1 + P_2 \exp(-P_3 q_t^2))$. 265

6.12 Relative radius error ($\delta R/R$) due to momentum single track error. 266

6.13 Radius with momentum error versus radius without momentum error. 267

6.14 Input opening angle (θ_{xz}) distribution using tracking data taken in the magnet-off configuration. 268

6.15 Input opening angle (θ_{xz} at the beam line) distribution using $\pi^+\pi^+ + \pi^-\pi^-$ tracking data taken in the magnet-on configuration. 269

6.16 Input opening angle (θ_{xz} at the beam line) distribution using $\pi^+\pi^-$ tracking data taken in the magnet-on configuration. 270

6.17 Input opening angle (θ_{xz} at the beam line) distribution using $\pi^+\pi^+ + \pi^-\pi^-$ tracking data taken in the magnet-on configuration, but the two tracks in the pair are taken from different events. . . 271

6.18 Input opening angle (θ_{xz} at the beam line) distribution using $\pi^+\pi^-$ tracking data taken in the magnet-on configuration, but the two tracks in the pair are taken from different events. 272

6.19 Correlation function, C_2, vs q_t using Monte Carlo $\pi^+\pi^+ + \pi^-\pi^-$ data without Bose-Einstein correlations. 273

6.20 Correlation function, C_2, vs Q using Monte Carlo $\pi^+\pi^+ + \pi^-\pi^-$ data without Bose-Einstein correlations. 274

6.21 Vertex distribution for tracks coming from the same and different Monte Carlo $(\pi^+\pi^+ + \pi^-\pi^-)$ events. 275

6.22 Vertex distribution for tracks coming from the same and different Monte Carlo $(\pi^+\pi^+ + \pi^-\pi^-)$ events. 276

6.23 Correlation function, C_2, vs q_t using Monte Carlo $\pi^+\pi^+ + \pi^-\pi^-$ data without Bose-Einstein correlations. 277

6.24 Correlation function, C_2, vs Q using Monte Carlo $\pi^+\pi^+ + \pi^-\pi^-$ data without Bose-Einstein correlations. 278

6.25 Correlation function, $C_2 = (\pi^\pm K^\pm + p^\pm K^\pm + \pi^\pm p^\pm)_S/(\pi^\pm K^\pm + p^\pm K^\pm + \pi^\pm p^\pm)_D$, as a function of q_t. 279

6.26 Correlation function, $C_2 = (\pi^\pm K^\pm + p^\pm K^\pm + \pi^\pm p^\pm)_S/(\pi^\pm K^\pm + p^\pm K^\pm + \pi^\pm p^\pm)_D$, as a function of q_t for $q_0 < 0.200$ GeV. 280

6.27 Correlation function C_2 as a function of q_t for charged multiplicity $0 < n_{ch} < 60$ and $q_0 < 0.200$ GeV. 281

6.28 Correlation function C_2 as a function of q_t for charged multiplicity $60 < n_{ch} < 100$ and $q_0 < 0.200$ GeV. 282

6.29 Correlation function C_2 as a function of q_t for charged multiplicity $100 < n_{ch}$ and $q_0 < 0.200$ GeV. 283

6.30 Correlation function, C_2, as a function of q_t for charged multiplicity $0 < n_{ch} < 60$, $\theta_{xz} > 20^0$ and $q_0 < 0.200$ GeV. 284

6.31 Correlation function, C_2, as a function of q_t for charged multiplicity $60 < n_{ch} < 100$, $\theta_{xz} > 20^0$ and $q_0 < 0.200$ GeV. 285

6.32 Correlation function, C_2, as a function of q_t for charged multiplicity $100 < n_{ch}$, $\theta_{xz} > 20^0$ and $q_0 < 0.200$ GeV. 286

6.33 Correlation function, C_2, as a function of q_t for $\theta_{xz} > 10^0$ and $q_0 < 0.200$ GeV. 287

6.34 Correlation function, C_2, as a function of q_t for $\theta_{xz} > 15^0$ and $q_0 < 0.200$ GeV. 288

6.35 Correlation function, C_2, as a function of q_t for $\theta_{xz} > 20^0$ and $q_0 < 0.200$ GeV. 289

6.36 Radius of the source as a function of opening angle θ_{xz} cut. . . . 290

6.37 Correlation function, $C_2 = (\pi^+\pi^+)_S/(\pi^+\pi^+)_D$, as a function of q_t, $q_0 < 0.200$ GeV, and for all multiplicities. 291

6.38 Correlation function, $C_2 = (\pi^-\pi^-)_S/(\pi^-\pi^-)_D$, as a function of q_t, $q_0 < 0.200$ GeV, and for all multiplicities. 292

6.39 Correlation function, C_2, as a function of q_t for $0 < n_{ch} < 60$ and $q_0 < 0.200$ GeV. 293

6.40 Correlation function, C_2, as a function of q_t for $60 < n_{ch} < 100$ and $q_0 < 0.200$ GeV 294

6.41 Correlation function, C_2, as a function of q_t for $100 < n_{ch}$ and $q_0 < 0.200$ GeV. 295

6.42 Correlation function, C_2, as a function of q_t for $0 < n_{ch} < 80$ and $q_0 < 0.200$ GeV. 296

6.43 Correlation function, C_2, as a function of q_t for $80 < n_{ch} < 120$ and $q_0 < 0.200$ GeV. 297

6.44 Correlation function, C_2, as a function of q_t for $120 < n_{ch}$ and $q_0 < 0.200$ GeV. 298

6.45 Radius of the source as a function of multiplicity in the Gaussian representation compared with the UA1 and CDF data points. . . 299

6.46 Momentum distribution, dn/dq_μ, as a function of $(|\vec{q_0}|, q_t)$ over the spectrometer acceptance used in this experiment. 300

6.47 Chaoticity parameter, λ, versus mean charged multiplicity $< n_{ch} >$.301

6.48 Radius of the source as a function of multiplicity in the Podgoretsky representation. 302

6.49 Radius of the source (R_g) extrapolated from a Gaussian parameterization of the correlation function $(C_2 = 1 + \lambda \exp(-R^2 q_t^2))$ vs radius of the source (R_p) extrapolated from a Podgoretsky parameterization of the correlation function $(C_2 = 1 + \lambda(2J_1(Rq_t)/Rq_t)^2)$.303

6.50 Radius of the source as a function of multiplicity in the Weiner representation. 304

6.51 Correlation function, C_2, as a function of q_t for $q_0 < 0.200$ GeV and total momentum of the pair $P_{tot} < 0.9$ GeV/c. 305

6.52 Correlation function, C_2, as a function of q_t for $q_0 < 0.200$ GeV and total momentum of the pair $P_{tot} > 0.9$ GeV/c. 306

6.53 Correlation function, C_2, as a function of q_0 for $0 < n_{ch} < 60$ and $q_t < 0.200$ GeV/c. 307

6.54 Correlation function, C_2, as a function of q_0 for $60 < n_{ch} < 100$ and $q_t < 0.200$ GeV/c. 308

6.55 Correlation function, C_2, as a function of q_0 for $100 < n_{ch}$ and $q_t < 0.200$ GeV/c. 309

6.56 Correlation function, C_2, as a function of q_0 for $0 < n_{ch} < 80$ and $q_t < 0.200$ GeV/c. 310

6.57 Correlation function, C_2, as a function of q_0 for $80 < n_{ch} < 120$ and $q_t < 0.200$ GeV/c. 311

6.58 Correlation function, C_2, as a function of q_0 for $120 < n_{ch}$ and $q_t < 0.200$ GeV/c. 312

6.59 Lifetime of the source as a function of multiplicity. 313

6.60 Correlation function, C_2, as a function of q_0 for $0 < n_{ch} < 60$ and $q_t < 0.200$ GeV/c. 314

6.61 Correlation function, C_2, as a function of q_0 for $60 < n_{ch} < 100$ and $q_t < 0.200$ GeV/c. 315

6.62 Correlation function, C_2, as a function of q_0 for $100 < n_{ch}$ and $q_t < 0.200$ GeV/c. 316

6.63 Correlation function, C_2, as a function of q_0 for $q_t < 0.200$ GeV/c and total momentum of the pair $P_{tot} < 0.9$ GeV/c. 317

6.64 Correlation function, C_2, as a function of q_0 for $q_t < 0.200$ GeV/c and total momentum of the pair $P_{tot} > 0.9$ GeV/c. 318

6.65 Definition of angle, α, between the beam z-axis and the momentum difference of the pion pair. 319

6.66 Correlation function, $C_2 = (\pi^+\pi^+ + \pi^-\pi^-)_S/(\pi^+\pi^+ + \pi^-\pi^-)_D$, as a function of q_t, $q_0 < 0.200$ GeV and $\cos\alpha > 0.8$. 320

6.67 Definition of angle ϕ illustrates the orientation of the pion pair plane. 321

6.68 Correlation function, $C_2 = (\pi^+\pi^+ + \pi^-\pi^-)_S/(\pi^+\pi^+ + \pi^-\pi^-)_D$, as a function of q_t, $q_0 < 0.200$ GeV and $\phi < 6^0$. 322

6.69 Correlation function, $C_2 = (\pi^+\pi^+ + \pi^-\pi^-)_S/(\pi^+\pi^+ + \pi^-\pi^-)_D$, as a function of q_t, $q_0 < 0.200$ GeV, and $\phi > 6^0$. 323

6.70 Correlation function, $C_2 = (\pi^+\pi^+ + \pi^-\pi^-)_S/(\pi^+\pi^+ + \pi^-\pi^-)_D$, as a function of (q_{xy}, q_z) for $q_0 < 0.200$ GeV. 324

A.1 Diagram of spectrometer model with dimensions used in the Monte Carlo simulation. 335

A.2 Diagram of steps used in the calculation of spectrometer acceptance of stable pions. 336

A.3 Graph showing B-field ($B_y(x)$) measurements and fit to superposition of two Gaussian functions. 337

A.4 Diagram used for calculating effects of magnetic focusing. 338

A.5 Difference in calculated position of *positive* particle track at the TOF_1 plane and position obtained from the RCT data tracking algorithms. 339

A.6 Difference in calculated position of *negative* particle track at TOF-1 plane and position obtained from the RCT data tracking algorithms. 340

INTRODUCTION

The measurement of the size and lifetime of the interaction region using pion Bose-Einstein correlations has been a fruitful and interesting pursuit for the last 10 years. It is well known that Hanbury-Brown and Twiss showed that the detection of two-photon correlations makes it possible to measure the angular diameters of stars [1]. At a fundamental level the pion source is analogous to a star emitting photons, and there must exist some analog of the Hanbury-Brown and Twiss method, which makes it possible to measure the diameter of the region of pion generation. It was shown [1] that such a method does exist. It is called the Bose-Einstein correlation or HBT (Hanbury-Brown and Twiss correlation). Use of the Bose-Einstein correlation makes possible the measurement not only of the size R but also of the shape of the interaction region from which identical particles are emitted and, in addition, the lifetime of the generation process τ.

This Bose-Einstein correlation method is the basis of a new and rapidly developing direction in elementary-particle physics. Many detailed theoretical studies have appeared, and a very large number of investigations have confirmed the actual existence of the correlations and provided information about the space-time parameters of the interaction region. This thesis reports on a study of the Bose-Einstein interference effect of two charged pions produced in $p\bar{p}$ collisions at $\sqrt{s} = 1.8$ TeV using the E735 detector at the C0 intersection region of the Fermi National Laboratory's Tevatron.

E735 was designed to measure soft p_t (transverse momentum) physics in

order to search for the deconfined QGP state (Quark-Gluon Plasma) [2]. The list of E735 Collaboration members is given in Appendix E. The goals of E735 were complementary to CDF (Collider Detector at Fermilab) which is primarily interested in high p_t processes [3].

A first order phase transition between the hadron and the QGP phase of nuclear matter is expected as the temperature increases. Lattice Monte Carlo QCD calculations [4] are used since perturbative QCD methods cannot be applied due to the fact that the involved momentum transfers are small [5]. The equation of space-time (EOS) evolution of a QGP state can be described by using phenomenological models.

An example is the hydrodynamic model by Bjorken [6]. It assumes that the processes involved are invariant with rapidity, y [7], and the system is in local thermal equilibrium. This model relates the energy density, ϵ_0, at the time of the collision to the charged particle density, dN/dy, and the average hadronic transverse energy in the final state:

$$\epsilon_0 = \frac{3}{2}\frac{dN}{dy}\frac{\sqrt{< p_t^2 > + m_\pi^2}}{\tau_0 A}, \tag{0.1}$$

where m_π is the pion mass, $A = \pi r^2$ is the overlapping area between the two colliding beam particles, and the initial proper time $\tau_0 = 1$ fm. Applying Bjorken's formula to $p\bar{p}$ collisions at $\sqrt{s} = 1.8$ TeV yields an energy density of the order of ϵ_0=4 GeV/fm^3. This is in the region of the expected phase transition ($2 - 3$ GeV/fm^3) [5].

There is no convincing observational evidence for QGP formation yet. It is believed [5] that information on the possible QGP can be gained by study-

ing ultra-relativistic nuclear collisions or very high multiplicity fluctuations in hadron-hadron collisions. Potential experimental probes are [5,8,9]:

1. Correlation between $< p_t >$ and dN/dy, where $< p_t >$ is related to the temperature of the interaction, and dN/dy is related to the energy density ϵ_0.

2. Strangeness enhancement for K/π, Λ/π as a function of dN/dy.

3. Di-lepton production like $q + \bar{q} \rightarrow l^+ + l^-$.

4. Direct gamma production.

5. Resonance melting, studied by measuring the J/Ψ production rate.

6. Enhancement of the production of ϕ mesons.

7. Pion correlations using the Hanbury-Brown Twiss effect. Using the HBT phenomenon, the space-time evolution of matter produced can be estimated.

The basic analysis of the Bose-Einstein correlations using quantum mechanics is reviewed in the first chapter. Chapter Two gives a description of the E735 detector, which is used to perform this measurement. The TEV collider complex is also briefly described. In describing the E735 detector, special attention is given to the z-chamber vertex detector, a subcomponent of the E735 detector which has been particularly useful in the analysis and was built by the University of Wisconsin-Madison. Chapter Three gives a review of the different trigger configurations used to enhance multiple track events in the spectrometer of the

E735 detector. Chapter Four describes the single charged particle reconstruction event finding algorithms using the z-chamber vertex and the data reduction chain of the E735 detector. The experimental single track momentum resolution is discussed using three different methods. In chapter Five, a new technique based on the Neural Network (NN) method is presented in order to search for resonances. Chapter Six describes the analysis procedure used in forming the two-pion correlation function, C_2, and the different systematic biases that affect this correlation function. Finally the space-time parameters of the interaction source are studied as functions of the charged particle multiplicity, n_{ch} and total momentum, P_{tot}, of the pion pair.

Some of the more technical subjects such as the Monte Carlo studies, relations between the various variables used in the Bose-Einstein analysis, Bose-Einstein Monte Carlo studies and z-chamber electrostatic potential studies are included in appendices.

Chapter 1

Bose-Einstein Correlation Review

In this thesis a new type of experimental approach, essentially different from the "barometers", "speedometers", and "thermometers" that measure quantities which are well-defined only for the macroscopic systems in local equilibrium, will be described. This type of experimental approach, called "interferometric microscopy", or "second-order interference", can also be used for non-equilibrium systems. It provides detailed information about the space-time evolution of the system being studied. The term "second-order interference" describes the intensity correlations between two identical particles emitted by a source [1].

First, a simplified presentation of the "interferometric microscope" will be given. This will be followed by a more detailed description of the two boson intensity correlation.

1.1 Hanbury-Brown and Twiss Effect

The main idea of the "second-order interference", or Bose-Einstein correlation was first suggested in radioastronomy by R. Hanbury-Brown and R. Twiss [1,10] in 1954 as a method of measuring the radii of distant stars. The Bose-Einstein

phenomenon is caused by the ambiguity in the path of two identical boson particles (photons) considered:

- The direct amplitude due to the particle produced by source $S_1(S_2)$ hitting detector $D_1(D_2)$, respectively and,
- The exchange amplitude due to the particle produced by source $S_1(S_2)$ hitting detector $D_2(D_1)$, respectively.

The above two amplitudes overlap, and the probability of detecting a coincidence between the signals in D_1 and D_2 contains an interference term which depends on the dimensions of the source. This can be seen as follows:

Consider two points S_1 and S_2 on a source as shown in Figure 1.1, each of which emits an infinitely long train of monochromatic photons with momenta $|\vec{p_1}| = |\vec{p_2}| = k$, and two detectors, D_1 and D_2, measuring the intensity of the photons at distant points. The total amplitude A of this experiment can be written as a sum of the two above described amplitudes, (direct and exchange amplitude):

$$A \sim e^{ika_1}e^{ikb_1} + e^{ika_2}e^{ikb_2}, \tag{1.1}$$

where k is the momentum of the monochromatic photons, and a_1, a_2, b_1, and b_2 are the lengths of the four possible paths: $a_1 = |\vec{r_1} - \vec{x_1}|$, $a_2 = |\vec{r_2} - \vec{x_1}|$, $b_1 = |\vec{r_2} - \vec{x_2}|$, and $b_2 = |\vec{r_1} - \vec{x_2}|$. After some algebra the probability of observing the two photons is given by:

$$|A|^2 \sim 1 + \cos(kR\theta), \tag{1.2}$$

where R is the separation distance between the two source points $\vec{r_1}$, $\vec{r_2}$, and θ is the angular separation of the two detector points $\vec{x_1}$ and $\vec{x_2}$. A measurement of this probability or correlation function, $|A|^2$, as a function of the angular separation, θ, will be maximum at:

$$\frac{kR\theta}{2\pi} = 0, 1, 2, ..., n. \tag{1.3}$$

Thus, by measuring the the angular separation, θ, of the two detector points $\vec{x_1}$ and $\vec{x_2}$ an estimation can be made of the separation distance between the two source points $\vec{r_1}$, and $\vec{r_2}$, as shown in Figure 1.1.

The extension of the above phenomenon to high energy physics was confirmed by Goldhaber, *et al.* [11]. This first experimental evidence for Bose-Einstein correlation in particle physics goes back to 1960, when an enhancement at small angles in like-sign pion pairs was observed in $p\bar{p}$ annihilation at 1.05 GeV/c in a hydrogen bubble chamber. No similar effect was found in unlike-sign pairs. This enhancement was in contradiction with the statistical model, which could not predict this correlation in the opening angle of a pion pair. The reactions studied were of the form:

$$\bar{p} + p \rightarrow n^+\pi^+ + n^-\pi^- + n^0\pi^0, \tag{1.4}$$

where n^+, n^-, and n^0 are the number of produced positive, negative, and neutral pions, respectively.

In order to explain the above observed result, Goldhaber *et al.* [11] had to symmetrize the wave function that characterized the production of the n-pion state.

In the Fermi statistical model [12], the wave function of an n-pion state can be expressed as:

$$\Psi_n \sim e^{i\sum_{i=1}^{n} \vec{p_i}\cdot\vec{r_i}}, \tag{1.5}$$

where $\vec{p_i}$ is the momentum vector of the i-th particle. The probability of observing the n-pion state created in an interaction region Ω is given by:

$$P_n \sim \int_\Omega |\Psi_n|^2 d\vec{r_1}...d\vec{r_n}. \tag{1.6}$$

By using Equation 1.5, $P_n \sim \Omega^n$.

The only modification required by Goldhaber *et al.* in order to explain the observed angle of the like-sign pion pair was the explicit symmetrization of the wave function:

$$\Psi_n \sim \sum_\sigma e^{i\sum_{i=1}^{n} \vec{p}_{\sigma(i)}\cdot\vec{r}_i}, \tag{1.7}$$

where $\sigma(i)$ is the i-th element of the permutation σ on n objects.

Many people followed Goldhaber *et al.* in studying the correlation of the opening angle of pion pairs [13].

An enhancement in the production of pairs of like charge and similar momentum has been observed in a variety of experiments including hadronic reactions [14,15,16], heavy-ion collisions [17], e^+e^- interactions [18,19,20], and μ-hadron collisions [21]. As the energy of the interaction increased, more complicated dynamics created limitations on the direct application of the Goldhaber *et al.* results. The difficulty was created by the inability to calculate the probability P_n. For the case of the two-pion state, Kopylov and Cocconi [22,23,24] derived probability P_2. They used the fundamental work of R. Hanbury-Brown and R.

Twiss [1,10] as a guide in their work. The derivation of the probability function is given in the next section.

1.2 Review of Two-Pion B.E. Correlations

In this section some of the basic properties of a 2-π state arising from a pion source distributed in space and time will be reviewed. Suppose the density of this source is given by $\rho(r^\mu)$, with $r^\mu = (t, x, y, z)$. Consider two identical pions created in the same event, as shown in Figure 1.1. A pion with 4-momentum p_1^μ is detected at the space-time point x_1^μ in the detector. At the same time a second π with a 4-momentum p_2^μ is detected at the point x_2^μ in the same detector. One π was created at the source position r_1^μ and the other at r_2^μ, however since the particles are identical, it is impossible to determine which π was emitted from r_1^μ and which from r_2^μ.

Suppose that these two pions can be described by a free particle wave function after their last strong interaction, then the wave function Ψ_2 that describes this 2-π state is a symmetric state according to Bose-Einstein statistics and is given by [25]:

$$\Psi_2(x_1, x_2; r_1, r_2) = \frac{1}{\sqrt{2}}(e^{ip_1(x_1-r_1)}e^{ip_2(x_2-r_2)} + e^{ip_1(x_1-r_2)}e^{ip_2(x_2-r_1)}). \tag{1.8}$$

After some modifications this wave function can be written as:

$$\Psi_2(x_1, x_2; r_1, r_2) = \frac{1}{\sqrt{2}}(e^{i\sum_{i=1}^{i=2} p_i x_i} \sum_{\kappa=1}^{2!} e^{-i\sum_{i=1}^{i=2} p_i r_{\sigma_\kappa(i)}}), \tag{1.9}$$

where $\sigma_\kappa(i)$ denotes the i-th element of a permutation κ of the set $\{1, 2\}$ and the sum over σ denotes the sum over all 2! permutations of the set $\{1, 2\}$. For

example the 2! permutations σ_κ for the set $\{1,2\}$ are:

$$\sigma_1(i) = (1,2), \tag{1.10}$$

and

$$\sigma_2(i) = (2,1). \tag{1.11}$$

The probability of observing the two π's at the points x_1^μ and x_2^μ is given by

$$P_2 = \int_V |\Psi_{p_1,p_2}(x_1,x_2;r_1,r_2)|^2 \rho(r_1)\rho(r_2) d^4r_1 d^4r_2. \tag{1.12}$$

After performing the integration over the whole space-time of the pion source, the probability, P_2, can been written as:

$$P_2 = \sum_{\kappa=1}^{2!} F_{1,\sigma_\kappa(1)} F_{2,\sigma_\kappa(2)} = F_{1,1}F_{2,2} + F_{1,2}F_{2,1}, \tag{1.13}$$

where $F_{i,j}$ is the Fourier transform of the source density $\rho(r^\mu)$ in space-time

$$F_{i,j} = \int e^{iq_{i,j}^\mu x_\mu} \rho(x^\mu) d^4x, \tag{1.14}$$

and $q_{i,j} = p_i - p_j$, with indices i and j running over the set $\{1,2\}$.

$F_{1,1} = 1$ and $F_{2,2} = 1$ for a normalized source density, so:

$$P_2(q_{i,j}) = 1 + F_{1,2}F_{2,1}. \tag{1.15}$$

$F_{i,j} = F_{j,i}^*$, where $F_{j,i}^*$ is the complex conjugate of $F_{i,j}$. Under this, the probability of observing the two π's is:

$$P_2(q_{i,j}) = 1 + |F_{1,2}|^2. \tag{1.16}$$

Some examples of the probability P_2 for the different existing parameterizations will be given.

1.2.1 Gaussian Parameterization

Gaussian Time Parameterization

Suppose a Gaussian distribution [26] of the spatial part of the source is considered:

$$\rho(\vec{r}) = e^{-(\frac{x^2}{2x_0^2}+\frac{y^2}{2y_0^2}+\frac{z^2}{2z_0^2})}. \tag{1.17}$$

Then a Gaussian distribution of the time of emission from the source with mean lifetime τ is,

$$\rho(t) = e^{-t^2/2\tau^2}. \tag{1.18}$$

From Equation 1.15, the probability of observing two $\pi's$ is:

$$P_2 = 1 + e^{-q_x^2 x_0^2 - q_y^2 y_0^2 - q_z^2 z_0^2 - q_0^2 \tau^2}. \tag{1.19}$$

In the case in which the source is distributed in a Gaussian characterized by a standard deviation $\sigma = R$, and where $x_0 = y_0 = z_0 = R$, the probability assumes the form:

$$P_2 = 1 + e^{-|q|^2 R^2 - q_0^2 \tau^2}, \tag{1.20}$$

$\vec{q} = \vec{p_1} - \vec{p_2}$ and $q_0 = E_1 - E_2$.

Exponential Time Parameterization

Suppose the same Gaussian distribution of the spatial source part is:

$$\rho(r) = e^{-(\frac{x^2}{2x_0^2}+\frac{y^2}{2y_0^2}+\frac{z^2}{2z_0^2})}, \tag{1.21}$$

but the time distribution of the source must be expressed as an exponential with mean lifetime τ,

$$\rho(t) = e^{-t/\tau}. \tag{1.22}$$

The probability P_2 in this case can be written (assuming $x_0 = y_0 = z_0 = R$) as:

$$P_2 = 1 + \frac{e^{-|q|^2 R^2}}{1 + q_0^2 \tau_0^2}. \tag{1.23}$$

1.2.2 Uniform Sphere

In this model a density $\rho(\vec{r})$ (keeping only the spatial part of the density) as a uniform sphere [11] of radius R was assumed:

$$\rho(\vec{r}) = \frac{3}{4}\pi R^3. \tag{1.24}$$

$F_{1,2}$ then takes the form

$$F_{1,2} = \int_0^R \int_0^\pi \int_0^{2\pi} e^{-iqr\cos\theta} r^2 \rho(\vec{r}) \sin\theta \, dr \, d\theta \, d\phi. \tag{1.25}$$

Carrying out the integration, the probability, P_2, becomes

$$P_2 = 1 + |I(qR)|^2, \tag{1.26}$$

where $I(x) = 3(\sin x - x\cos x)/x^3$.

In the special case where $qR < 1$, $I(x)$ can be expressed as a Gaussian function

$$I(x) = e^{-x^2/5}, \tag{1.27}$$

and the probability function has the form

$$P_2 = 1 + e^{-R^2 q^2/5}, \tag{1.28}$$

which is practically identical to the Gaussian parameterization.

1.2.3 Ellipsoid Source Shape

In this model [27] a source density $\rho(\vec{r})$ (again keeping only the spatial part of the density) as an ellipsoid with semi-axes A, B, and C along the three spatial axes x, y, and z was assumed. This case is a generalization of a uniform spherical source by changing qR to $\sqrt{(q_x^2A^2 + q_y^2B^2 + q_z^2C^2)}$, where q_x, q_y, and q_z are the three cartesian coordinates of $\vec{q}$.

1.2.4 Spherical Uniform Shell

In this model [28] $\pi's$ are emitted from the surface of a uniform spherical shell of radius R. The density $\rho(\vec{r})$ (keeping only the spatial part of the density) is a uniform hollow sphere of radius R:

$$\rho(\vec{r}) = \frac{\delta(r - R)}{4\pi R^2}. \tag{1.29}$$

$F_{1,2}$ can be written as:

$$F_{1,2} = \int_0^{+\infty} \int_0^{\pi} \int_0^{2\pi} e^{-iqr\cos\theta} r^2 \rho(\vec{r}) \sin\theta \, dr \, d\theta \, d\phi. \tag{1.30}$$

Carrying out the integration, the probability P_2 becomes

$$P_2 = 1 + |\frac{\sin(qR)}{qR}|^2. \tag{1.31}$$

1.2.5 Gaussian Source in the Rest Frame of 2 π's

Suppose a Gaussian distribution [11] for the source density in the rest frame of the two π's is considered. P_2 can be expressed as:

$$P_2 = 1 + e^{-R^2Q_2^2}, \tag{1.32}$$

where Q_2^2 is given by Equation B.12.

This parameterization appears very attractive for a couple of reasons:

- It is Lorentz invariant.
- It involves only one kinematic variable, but it is not directional.
- One may treat any correlations of any multiplicity from a common point of view.

For example, the n-particle correlation, P_n, can be written as:

$$P_n = 1 + e^{-R^2 Q_n^2}, \tag{1.33}$$

where Q_n is the invariant momentum difference of the $n\pi$ system (Equation B.28).

Note that relations 1.20 and 1.32 are identical if one chooses the two energies E_1 and E_2 of the two identical particles to be equal, i.e.,

$$E_1 = E_2. \tag{1.34}$$

1.2.6 Uniform Disk of Radius R

In this model [22], assume that the single-particle source uniformly fills a disk of radius R, oriented perpendicular to the total momentum $\vec{u}$ of the two π's. The spatial part of the source density, $\rho(\vec{r})$, can be written in cylindrical coordinates ρ, ϕ and z as:

$$\rho(\vec{r}) = \frac{\delta(z)}{\pi R^2}, \tag{1.35}$$

where $\delta(z)$ is the Dirac delta function and $\vec{u}$ is the total momentum of the two π's (Equation B.10). $F_{1,2}$ can be expressed in cylindrical coordinates as:

$$F_{1,2} = \int_0^R \int_0^{2\pi} \int_0^{+\infty} e^{-i\vec{q}\cdot\vec{r}} \rho(\vec{r}) \rho d\rho \, d\phi \, dz. \tag{1.36}$$

Carrying out the integration, the probability P_2 becomes:

$$P_2 = 1 + |2J_1(q_t R)/q_t R|^2, \tag{1.37}$$

where $J_1(x)$ is the first order Bessel function and q_t is given by Equation B.5. To a sufficiently good approximation of the Bessel function $J_1(x)$ the probability P_2 can be expressed as a Gaussian function:

$$P_2 = 1 + \exp^{-(\frac{q_t^2 R^2}{4})}. \tag{1.38}$$

1.2.7 Weiner Parameterization

Lately another approach to two-particle correlations was suggested by R.M. Weiner [29]. It is based on quantum statistical considerations only. He discusses a possible problem with the previous relation (the one that involves one exponential 1.20) for the two particle Bose-Einstein correlation function, C_2, used in many experimental studies.

Weiner maintains the apparent coherence observed in the data ($\lambda \neq 1$) is probably due to long-lived resonances, hydrodynamical expansion, and other specific strong interaction effects. It seems that this coherence has been ignored in the past. The parameterization of the correlation function, C_2, is incomplete, and under certain circumstances, totally wrong according to quantum statistical

methods. One must take this coherence into account by superimposing a chaotic field with a coherent field,

$$\Psi = \Psi_{co} + \Psi_{ch} \tag{1.39}$$

where Ψ_{co} is the coherent field and Ψ_{ch} is the chaotic field. The intensity is defined as $I = |\Psi|^2$ and is related to the number of particles n by $< n >=< I >$, where the brackets $<>$ define the ensemble average. The correlation function, C_2, for a Gaussian source is expressed as:

$$C_2 = 1 + 2p(1-p)e^{-|q|^2R^2} + p^2e^{-2|q|^2R^2}, \tag{1.40}$$

where p (chaoticity factor) is defined by

$$p = \frac{< n_{ch} >}{< n >}, \tag{1.41}$$

$< n >=< n_{co} > + < n_{ch} >$, and $< n_{co} >= |\Psi_{co}|^2$. $< n_{co} >$ is the mean value of the multiplicity distribution for the coherence part of the source.

It is clear that for $p = 1$ the above equation reduces to Equation 1.20. Therefore, for $p \neq 1$ Equation 1.20 has no quantum statistical meaning. This consideration has a further interest, as the new formulation connects the Bose-Einstein correlation function to the multiplicity distributions. This connection between the correlation function, C_2, and the moments of the multiplicity distribution is displayed in the relation:

$$< n(n-1) >= \int C_2(p_1, p_2)dp_1dp_2. \tag{1.42}$$

In this case the parameters that characterize the correlation function, C_2, (p and R), determine the multiplicity behavior as well.

Note that there are many different models representing quite different physical and geometrical interpretations of the observed correlations. In practice most experimenters make use of the Gaussian (Section 1.2.1), Podgoretsky (Section 1.2.6), and the Weiner (Section 1.2.7) parameterizations, so that for direct comparisons with the other experiments the following analysis has made use of these three models.

1.3 Review of N-Particle B.E. Correlations

Because the produced number of particles increases with energy, it is possible to study identical particle correlations of high n_{ch} multiplicities. The extension to n-particle correlations can be made by generalizing the two-particle wave function (Equation 1.9) to the case of n-particles [25]. Suppose there are n-single particle sources at space-time points r_1^μ,r_2^μ,...,r_n^μ producing identical particles with 4-momenta p_1^μ,p_2^μ,...,p_n^μ, and they are detected at space-time points x_1^μ,x_2^μ,...,x_n^μ. The n-particle state detected with p_i at x_i $\forall i \in \{1,2,3,..,n\}$ is symmetrized under the interchange of n particles:

$$\Psi_n(x_1,x_2,x_3,...,x_n;r_1,r_2,r_3,...,r_n) = \frac{1}{\sqrt{n!}}(e^{i\sum_{i=1}^{i=n} p_i x_i} \sum_{\kappa=1}^{n!} e^{-i\sum_{i=1}^{i=n} p_i r_{\sigma_\kappa(i)}}), \tag{1.43}$$

where $\sigma_\kappa(i)$ denotes the i-th element of a permutation κ of the set S:

$$S = \{1,2,3,..,n\}. \tag{1.44}$$

The sum over σ denotes the sum over all n! permutations of the set S.

The probability P_n of observing these n particles with momenta p_1, p_2, and $p_3, .., p_n$ at the space-time points x_1, x_2, and $x_3, ..., x_n$ is given by:

$$P_n = \int_V |\Psi_n(x_1, x_2, x_3, ..., x_n; r_1, r_2, r_3, ..., r_n)|^2$$
$$\rho(r_1)\rho(r_2)\rho(r_3)...\rho(r_n)d^4r_1d^4r_2d^4r_3...d^4r_n \tag{1.45}$$

or

$$P_n = \sum_{\kappa=1}^{n!} F_{1,\sigma_\kappa(1)}F_{2,\sigma_\kappa(2)}F_{3,\sigma_\kappa(3)}...F_{n,\sigma_\kappa(n)}, \tag{1.46}$$

where $F_{i,j}$ is the Fourier transform of the source $\rho(r^\mu)$ in space-time as given by Equation 1.14.

In the case of equal momenta :

$$p_1^\mu = p_2^\mu =, ..., = p_n^\mu, \tag{1.47}$$

all the $F_{i,j} = 1$ so the probability function $P_{1,2,3,...,n}$ is :

$$P_n = n! \tag{1.48}$$

The probability $P_{p_1,p_2,...,p_n}$ can be written as :

$$P_n = perm\{F_{i,j}\}, \tag{1.49}$$

where $perm\{F_{i,j}\}$ is the permanent of the matrix $F_{i,j}$.

In the case of an n-fermion state (i.e. n identical electrons) the wave function (Equation 1.43) is anti-symmetric and the probability of observing this n-fermion state is :

$$P_n = det\{F_{i,j}\}, \tag{1.50}$$

where $detF_{i,j}$ is the determinant [30] of the matrix $F_{i,j}$.

Nijenhuis and Wilf [31,25] give the $Perm\{F_{i,j}\}$ of an $n \times n$ $F_{i,j}$ matrix as:

$$perm\{F_{i,j}\} = 2(-1)^{n-1} \sum_{S} (-1)^{|S|} \prod_{i=1}^{n} (F_{i,n} - \frac{\sum_{j=1}^{n} F_{i,j}}{2} + \sum_{j \in S} F_{i,j}), \qquad (1.51)$$

where S =subsets of the set $A = \{1, 2, 3, ..., n-1\}$, namely :

$$S = \{\{0\}, \{1\}, \{2\}, ..., \{n\}, \{1,2\}, ..., \{1,2,...,n-1\}\}, \qquad (1.52)$$

and the number of elements of this set S is 2^{n-1}. $|S|$ is the number of elements in a given subset of the set A. The number of computations needed to estimate the $F_{i,j}$ using this algorithm is $n2^{n-1}$ in contrast to the $nn!$ required if one uses Equation 1.46.

Figures for Chapter 1

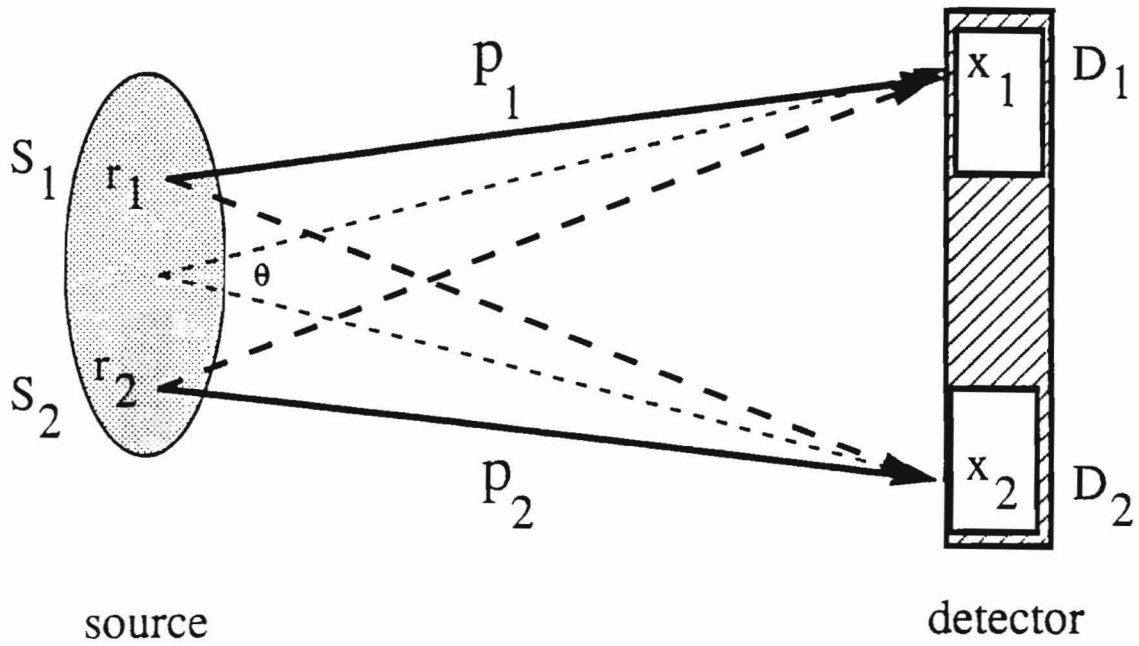

Figure 1.1: Two pions emitted from a pion source.

Chapter 2

The Experimental Apparatus

2.1 Tevatron

The data for the Bose-Einstein correlation studies performed and analyzed in this thesis were collected at the TEVatron collider located at the Ferm National Accelarator Laboratory (FNAL) in Batavia, Illinois, USA between June 1988 and May 1989.

The TEV storage ring [32], shown in Figure 2.1 is six kilometers (3.9 miles) in circumference. It is used to study high energy collisions between protons (p) and antiprotons ($\bar{p}$). The TEV is composed of six straight sections. Four of these six sections have interaction halls (B0, C0, D0, and E0). Figure 2.1 shows the features of the TEV Ring (as well the Main Ring, antiproton Accumulator, etc.). The E735 experiment shown in Figure 2.2 is located at the C0 interaction hall.

Throughout this experiment, each beam of particles had an energy of 900 GeV giving a total center of momentum energy of $\sqrt{s} = 1.8$ TeV. The $\bar{p}$ are produced by bombarding 120 GeV protons from the main ring on a copper target. This interaction produces 8 GeV $\bar{p}$. They are not produced in large quantities and must therefore be accumulated. This is achieved by storing them

in the Accumulator Ring. Once enough $\bar{p}$ were available to constitute a bunch, typically 0.5 to 1.5×10^{10} particles, they were extracted from the Accumulator Ring and injected into the Main Ring which was then ramped to 150 GeV, and there were subsequently dumped into the Tevatron in six bunches. The limitation of the luminosity was the intensity of the antiprotons that can be produced. The limitation of the intensity of the antiproton comes from the antiproton production cross-section, the collection efficiency of antiprotons produced from the target, and the transfer efficiency from the Accumulator Ring to the TEV. Six proton bunches were extracted to the Tevatron from the Main Ring through a similar process. A small frequency offset was introduced into the proton radio-frequency cavities relative to the antiproton radio-frequency cavities, in order to establish collisions at the proper places within the interaction regions around the ring (Figure 2.1). The Tevatron is then ramped to 900 GeV giving a total center of momentum energy of $\sqrt{s}$ = 1.8 TeV. This whole process, that is, to inject antiprotons and protons into the TEV in order to produce collisions is referred to as a "shot". After stabilizing the proton and antiproton beams in the TEV, the Main Ring returns to its production cycle producing antiprotons for the next shot. The average lifetime of a shot was 12 hours. The antiproton stack rate was of the order of 1.2×10^{10}/hour.

A useful measure of the performance of the accelerator is the luminosity L [33]. The connection between physics (σ: cross section for the reaction under consideration) and accelerator technology (L: luminosity) is given by the reaction

rate R (number of events of interest per second):

$$R = L\sigma. \tag{2.1}$$

The luminosity (measured in units of $\mathrm{cm}^{-2}\mathrm{sec}^{-1}$) is given for the case of two oppositely directed beams of N relativistic particles that are circling the storage ring with frequency f. The luminosity L at the intersection point is:

$$L = \frac{N^2 f}{A}, \tag{2.2}$$

where A is the effective cross-sectional area of the beams, assuming them to overlap completely. If two unequal Gaussian beams are bunched with k bunches per revolution in each beam, the luminosity is:

$$L = f\frac{kN_1N_2}{4\pi\sigma_h\sigma_v}, \tag{2.3}$$

where N_1 and N_2 are the number of particles per bunch and σ_h, σ_v are the rms horizontal and vertical dimensions. The horizontal beam dimension σ_h depends on the amplitude of the horizontal beta function (β_h) and the horizontal emittance (ϵ_h) of the beam as:

$$\sigma_h = \sqrt{\epsilon_h\beta_h}. \tag{2.4}$$

Similarly, for the vertical beam dimension, σ_v,

$$\sigma_v = \sqrt{\epsilon_v\beta_v}, \tag{2.5}$$

where ϵ_v is the vertical emittance of the beam and β_v is the amplitude of the vertical beta function (β_v).

During the above mentioned running period, the average number of protons per bunch was $N_1 = 5\times10^{10}$, while the average number of antiprotons per bunch was N_2=0.5-1.5$\times10^{10}$. The number of proton and antiproton bunches was six and their crossing rate was 280 kHz. The average luminosity L at B0 (location of CDF experiment) was 1×10^{30}. The luminosity at C0, which is a high $\beta(= 75$ meters) point in the accelerator complex, is down from the peak luminosity of the TEV (at the B0 interaction hall) by a factor of 1/75.

I should also point out that the C0 experimental area was a high radiation environment due to the presence of the TEV and main ring abort pipes (Figures 2.1 and 2.3). The Main Ring is located 56 cm above the TEV ring. During the 1988-1989 period the radiation monitors at C0 measured total radiation loss equal to 8958 R. The radiation loss rate was of the order of 1 R/hour. Operation of the TEV at the center of mass energy was $\sqrt{s} = 1.8$ TeV.

2.2 The C0 Coordinate System

In this thesis the following coordinate system (Figure 2.4) was used:

- The positive z-axis is along the proton (p) beam and the negative z-axis is along the antiproton ($\bar{p}$) beam.
- The positive y-axis is vertically upward.
- The positive x-axis is horizontally pointing away from the Tevatron Ring into the E735 spectrometer.

- The polar angle θ is defined from the positive z-axis:

$$\theta = \cos^{-1}(p_z/p). \tag{2.6}$$

- The azimuthal angle, ϕ, is defined in the x-y plane perpendicular to the beam. 0^0 is along the positive x-axis.

$$\phi = \tan^{-1}(p_y/p_x). \tag{2.7}$$

The transverse momentum, p_t, of a particle in this coordinate system is defined as the cartesian component of the momentum $\vec{p}$ perpendicular to the z-axis:

$$p_t = \sqrt{p_x^2 + p_y^2}. \tag{2.8}$$

2.3 An Overview of the E735 Detector

In this section the various parts of the E735 detector are described. Essentially, the E735 detector, shown in the top view of Figure 2.2, measured the multiplicity of charged particles and simultaneously measured a sample of time-of-flight identified charged particles with momenta below 3 GeV/c near θ =90 degrees with respect to the beam.

The E735 detector has the following main capabilities:

1. It measures the charged multiplicity.

2. It measures the charged particle momenta over 0.5 ster solid angle.

3. It identifies charged particles up to a momentum of 3 GeV/c.

The measurement of the charged particle multiplicity n_{ch} was carried out by:

- A segmented plastic scintillator hodoscope (HODO) with a pseudo-rapidity range $-3.25 < \eta < 3.25$. ($\eta = pseudorapidity = -\ln(\tan\frac{\theta}{2})$).
- A central tracking chamber (the CTC) covering a pseudo-rapidity range $-1.5 < \eta < +1.5$ to measure multiplicity.
- Two delay line based drift chambers (the END-CAP chambers) covering a pseudo-rapidity range $+1.5 < |\eta| < +3.25$ to measure the forward and backward charged multiplicity.

The measurement of the charged particle momentum $\vec{p}$ was done by using a one side arm magnetic spectrometer over a solid angle of 70^0 ($40^0 < \theta < 110^0$) opening angle in polar and 20^0 ($0^0 < \phi < 20^0$) opening angle in azimuthal angle. The magnetic spectrometer components are:

- A three plane vertex multi-wire proportional chamber (Z-chamber) to provide the determination of the event vertex is 15 cm away from the beam line.
- A four plane drift chamber (the PRE-MAGNET chamber) at the entrance of the magnet to measure the initial direction of the charged particle. The position of the first plane of the pre-magnet chamber is 56.5 cm.
- A dipole magnet (MAGNET) provides the magnetic field necessary for signed momentum measurement at 75 cm from the beam pipe.

- A four plane drift chamber (the POST-MAGNET chamber) at the exit of the magnet measures the final direction of the charged particle. The position of the first plane of the post-magnet chamber is 86 cm.

- A 14 plane straw drift chamber (the STRAW drift chamber) at a distance of 104 cm away from the beam pipe gives an estimation of the final trajectory of the charged particle.

The identification of the charged particles with up to 3 GeV/c momentum was done by using a time-of-flight (TOF) system consisting of:

- Proton (antiproton) trigger counter, TOF_p ($TOF_{\bar{p}}$) to measure the interaction time, t_0, and the vertex of the event.

- A system of seven horizontal scintillator counters (TOF_1) 2 m away from the beam pipe used to identify the mass of the charged particles.

- A system of 32 vertical scintillator counters (TOF_2) 4 m away from the beam pipe to identify the mass of the charged particles and to get a better differentiation of the pion, kaon, and proton masses.

In the next sections the various components of the E735 detector will be reviewed and described.

2.3.1 Z-Chamber

The particles from the interaction region (event vertex) emerged from the 2 mm thick aluminum vacuum pipe (whose inner radius is 10 cm) to enter the E735 detector.

In this experiment the position of the vertex of $\bar{p}p$ interactions was located along the beam line with the aid of a one meter long low-mass mini drift chamber [34] (MDC) comprised of three planes. The goals of the experiment made necessary a low mass for the vertex chamber. This was achieved through the use of plastic materials in the construction. Details of the plastic construction of this chamber and its operation are reported below. In addition, the chamber performance obtained in tests with sources and cosmic rays is compared with related data collected during the 1988-89 $\bar{p}p$ collider run.

The requirements of the vertex chamber were threefold: Firstly, the rms spatial resolution along the z-axis had to be better than 700 μm per wire for tracks accepted by the spectrometer. Secondly, in order to reduce the production of secondary particles the entire vertex chamber had to be built of low-mass materials and had to have its read-out electronics outside the hodoscope detector. Finally, the dimensions of the sensitive gas volume were dictated by the distribution of the $\bar{p}p$ interactions ($\sigma = \pm 30$ cm) along the beam line (z-axis) and the given vertical aperture of the magnetic spectrometer of 20 degrees. The limited space between the beam pipe and the inner radius of the CTC allowed only three planes with sufficiently thick sensitive gas volume per plane.

The average number of charged particles traversing the vertex chamber per $\bar{p}p$ interaction was estimated to be less than one track per cell. This assumed that $dN_c/d\eta < 50$ (maximum value observed was about 30 charged particles/unit pseudorapidity), that the particles were uniformly distributed in η and in ϕ, and that the drift chamber plane was located at $x = 13.1$ cm with a cell width of

1.10 cm. The sensitive portion of the sense wires was 10 cm long in the vertical direction.

Practically, the vertex chamber was not accessible during the one year run period. This demanded a reliable construction. Radiation bursts were expected from Main Ring (MR, see Figure 2.3) activity during $\bar{p}$ production and abort activity at C0 [35]. (C0 was the abort section for both the MR and the Tevatron system.). Thus, the high voltage of the vertex chamber could be expected to trip off frequently. The gas mixture used should not contain hydrocarbon molecules in order to prevent carbon whisker growth during frequent high voltage breakdown. High voltage breakdowns in chambers with hydrocarbon gas mixtures accelerate the deposit of various substances on chamber wires. Carbon whiskers render a chamber inoperative more quickly than some other deposits (see [36] for further discussion). The selected gas mixture $Ar(85\%) - CO_2(15\%)$ at atmospheric pressure was used throughout this report, unless otherwise stated.

Construction

The frames of the vertex chamber were cut out with a diamond saw from 0.50 cm thick kevlar reinforced Rohacell 71 panels [37]. Each plane surface of a panel was clad with two layers of 0.13 mm thick kevlar fabric attached with a two-component epoxy resin. The weaves of one layer were inclined by 45 degrees with respect to the weaves of the other layer to minimize warping of the final composite panels.

Due to the limited mechanical strength of the kevlar reinforced frames, the

number of sense and field wires of the drift cells, as well as the applied wire tensions, were limited.

As indicated in the previous section, the spacing between the sense wires was 1.1 cm, the field wires were located midway between sense wires. The distance between adjacent planes was also 1.1 cm (Figure 2.5). The electrode windows and the field wires were held at the same potential. These conditions give a favorable aspect ratio for reducing charge collection time [38] and [39].

The equipotential and electric field maps are shown in Figure 2.6. An analytic expression for the potential and electric field was derived. The isochrones (Figure 2.6) were derived from the electric field map and from the electron drift velocity in the used gas mixture as a function of the electric field E [40] (c.f. Appendix D).

Pairs of frames (see Figures 2.7 and 2.8) were glued together with a flexible two component epoxy resin [41] resulting in a frame module (Figure 2.9). Because Rohacell is permeable to moisture, all sides not covered with the kevlar reinforcement were sealed with Epolite resin [42] which has a high dielectric strength and is easy to machine. Great care was given to embed all ends of the cut kevlar filaments with Epolite resin. Otherwise these might have been a source of corona during operation of the chamber. After curing, the resin was sanded with sandpaper of various grades resulting in a smooth surface.

The holes for the dowels and the Delrin rods used to fasten frames together were drilled oversized into the kevlar reinforced Rohacell frames. The holes were filled with Epolite resin and redrilled with the desired precision. A template

ensured the proper alignment of the holes for all the frames.

The frame modules were prestressed with the expected amount of wire tension using a set of spring loaded clamps. After about a one week waiting period, waiting for plastic creeping to stabilize, the wires were attached to the frames. On the average, the deflection under load at the center of the long side was 1 mm. The possibility of a long term creep in the frame material had to be taken into account when selecting wire tensions and mounting the cathode planes.

Wire planes were constructed by simultaneously winding sense and field wires onto an oversize aluminum frame with a stepping motor and precision screw. The wire tensions were 0.96 N for the field wires (gold plated coin-silver [43], 125 μm diameter, Young's modulus = 7.72×10^{10} N/m^2) and 0.2 N for the sense wires (gold plated tungsten, 25 μm diameter, Young's modulus = 3.9×10^{11} N/m^2), respectively. The tensions were chosen to produce comparable amounts of elongation in the sense and field wires, about 0.02 cm for a 20 cm long section of wire. Spacing between successive sense wires was controlled to better than 0.007 cm and to better than 0.01 cm over a length of 100 cm. An effort was made to maximize the free length of the wires inside the gas volume so that wire elongation might compensate for any long term mechanical creep of the frames (see Figure 2.8).

While still under stress, each frame module was aligned with the wound sense and field wires. The clearance between the field wires and the surface of the frame module was adjusted to about 0.2 mm. Epolite resin was applied to the wires at the outer flat portion of the frames (Figures 2.8 and 2.9). Plugs of white

RTV [44] prevented the resin from flowing into the mounting holes. A 125 μm thick Mylar sheet with the appropriate holes for the RTV plugs was put over the resin to ensure a flat surface with the wires embedded.

During application of the Mylar sheet onto the Epolite resin, one could not entirely avoid shifting some wires out of position. The maximum displacement of a sense wire was less than that of the field wires because their smaller diameter allowed the sense wires to restore more readily to their original positions. The estimated maximum displacement was less than 0.01 cm for the sense wires and less than 0.05 cm for the field wires.

Curing the Epolite resin at a temperature of 40° C for several days increased the electric strength of the glue substantially. Both the Mylar sheet and the prestressing devices were removed only after the glue was completely cured.

It is worth mentioning that the vapor of the Epolite resin was observed to initiate the growth of alum crystals on goldplated aluminum field wires in a similarly constructed chamber. The crystals, whose size was of the order of the wire diameter, penetrated and damaged the gold plating. The growth of these crystals could be prevented by covering the resin during the curing process. Nevertheless, goldplated coin silver was used in the final vertex chamber construction instead of goldplated aluminum field wires. No such crystal growth was observed in the case of gold plated tungsten wire.

The cathode planes consisted of a composite of 13 μm aluminum on both sides of a 250 μm thick FR4 panel [45]. The sufficiently stiff cathode planes had to accommodate some small deformation (e.g. due to the wire tension) of the

frames without changing the spacing to the two adjacent wire planes. Each panel was attached with silicone sealant at only one point on the upper edge of the type 2 frames on the side opposite to the wires. Kapton feathers, embedded in the Rohacell of the accompanying Type 1 frame (Figures 2.7 and 2.9), held the panel flat and parallel to the wire planes while still permitting movements parallel to the frame surface. The cathode electrodes on both sides of the FR4 panels were attached to a flexible fine wire with a small screw in one of the corners to avoid sparking to the sense wires under high voltage.

The silicone rubber sheets [46] used as gaskets (thickness = 0.794 mm) were cleaned with ethanol and water to remove talcum powder residuals. Baking the cleaned rubber sheets at 50° C for a 24 hour period increased the electric impedance tenfold.

All frames and rubber sheets were stacked and clamped together with threaded delrin rods (0.3 cm diameter) and nylon nuts (Figure 2.9). The torque used was about 0.01 Nm. Delrin was preferred over aluminum due to its electric insulation and low Z composition. This technique provided a sufficient mechanical stability and an adequate gas seal over more than one year of operation.

The cathode panels, while not being completely gas tight, presented a relatively high impedance to gas flow between adjacent gas volumes. The first and the last of the cathode panels were buffered from the outside with one more gas volume which was sealed from the outside atmosphere. The outer windows were not flat but were curved towards the outside to minimize the force on the frames tangential to the wires which would reduce wire tension with increasing

gas pressure (Figure 2.9).

Each of the five gas volumes had its own inlet and outlet consisting of teflon tubing inserted in 0.32 cm diameter through holes in the narrow sides of the frames and sealed with flexible two component epoxy [41]. The five gas tubes were fed in parallel by using sixfold Omnifit connectors [47]. The parallel gas supply was preferred over a serial one to minimize effects due to any leakage into some of the gas volumes from the outside. The total gas flow rate was about 4 cm^3/sec. No corrections were made for fluctuations of gas density due to temperature or atmospheric pressure changes. The gas passed through a two stage micro-fiber filter [48] before entering the vertex chamber. One filtered moisture and the other hydrocarbons out of the gas stream.

The mounting of the chamber in the CTC consisted of two lucite-delrin feet which provided vertical adjustment and two lucite clamps at the top which provided horizontal adjustment with nylon screws. Rohacell pedestals were attached with epoxy to the inside surface of the CTC to support the chamber's feet and clamps.

Readout Electronics

The signals from the 288 sense wires were carried away from the chamber on 18 transmission lines 270 cm long (Z=38 Ω) composed of 16 strips above a ground plane separated by a Mylar dielectric (Figures 2.8 and 2.10). Cu cladding of the Mylar was chosen for simplification during manufacturing and for durability reasons. A minimum strip width of 0.064 cm and 270 cm length were chosen so

that lines could be produced reliably using simple in-house facilities.

In an effort to reduce mass an attempt was made to use aluminum clad Mylar transmission lines. However, it proved to be difficult to control the etch rate for aluminum as well as the quality of the copper plating required on the ends for soldering to external connections. A long time test demonstrated that the aluminum strips developed cracks from bending the lines. During high voltage tests this resulted in sparks and break through of the Mylar insulation.

The transmission lines were terminated outside the detector region in a transition board (Figure 2.8) which capacitively coupled the fast signals to the amplifier and simultaneously provided D.C. high voltage biasing to the sense wires through the signal strips. In this way noisy wires, or shorted sections due to wire breakage, could be selectively disabled from outside of the detector. In practice this proved to be unnecessary.

The transmission lines were glued with a two component flexible epoxy onto the handle of the type 2 frames (Figures 2.8 and 2.9). All sense wires were soldered to the strips and all field wires were soldered to the ground side. The entire length of a transmission line was electrically isolated with one layer of 50 μm thick Mylar film and another layer of 1 mm thick foam sheet.

The strip-over-ground geometry of the transmission line presented a 500 pf capacitance to the amplifier input, resulting in a relatively large input noise charge. This configuration, while not optimal from the point of view of noise considerations, was chosen in order to reduce the possibility of RF pick-up. Nevertheless a small amount of pick-up, characteristic of SCR (Silicon Controlled

Rectifier) firing, was present in the Tevatron tunnel. In addition, pick-up from the scintillation hodoscope was present in very high multiplicity events. Both of these effects necessitated setting the discriminator thresholds a factor of two higher than desired (c.f. Collider Performance). The cross talk amplitude between adjacent channels on the transmission line was of the order of 2%-3%.

A schematic of the amplifier and its interconnection with the transition board are shown in Figure 2.11. The standing current of the input transistor was chosen to match the dynamic emitter impedance to the transmission line impedance in order to have efficient transfer of charge without reflections. The transfer gain of the amplifier was measured to be 3 mV/fC (differential) for an impulse input of 4 nsec FWHM. The rise and fall times (10%-90%) of the preamp output measured at the end of a 10 meter length of twisted pair ribbon cable ($Z = 100\Omega$) were 7 nsec and 40 nsec, respectively. An equivalent input noise charge of $\sim 16,000e$ due to the transmission line capacitance was estimated using the technique of Jarron and Goyot [49].

The amplifier output traveled on 10 meters of twisted pair ribbon cable to a discriminator. The discriminator used for the Tevatron run is shown in the schematic of Figure 2.12. In this circuit the discriminated signals of two sense wires are combined after a relative delay of $\sim$ 400 nsec (more than twice the expected maximum drift time of the first arriving electron) and sent to a single multi-hit TDC channel. This reduced the cost of the readout and was permissible due to the relatively long time between $\bar{p}p$ bunch crossings.

Source Tests

The efficiency of a drift cell along the length of a sense wire was measured with a collimated electron beam (^{106}Ru source, $E_{max} = 3.55$ MeV) 1 mm in diameter. The electrons were recorded with a 1×10 mm^2 scintillator, located on the opposite side of the plane. The 1 mm edge was held parallel to the sense wire. The threshold of the scintillator signal was set above the gamma radiation of 0.51 MeV in order to suppress the background stemming from Compton scattering. This measurement was performed on a test chamber with the same dimensions as the vertex chamber except that it had only 16 sense wires and only one plane covered with two 0.8 mm thick aluminum windows.

The efficiency along a sense wire dropped from 95% at 0.6 cm from the frame edge down to 50% at the frame edge. The efficiency at distances greater than 1 cm from the cell edge is defined as 100%.

The nominal gas filling was an analyzed mixture of $Ar(85\%) + CO_2(15\%)$. A source of ^{55}Fe was used to determine that the gas amplification doubled for every increase of 80 V at a sense wire H.V. of about 1800 V. This gain measurement was repeated with the gas mixture of $Ar(70\%) + CO_2(30\%)$. For the same gas amplification, the high voltage had to be 300 V higher than that for $Ar(85\%) + CO_2(15\%)$.

Cosmic Ray Tests

The trigger counters consisted of two scintillators S1 and S2 covering about 30 drift cells per plane of the vertex chamber with a solid angle of 0.12 steradians.

Only tracks which were at least 2 cm away from the frame edges were sampled. The time jitter of the coincidence S1·S2 was better than 1 nsec(rms). The wire planes of the vertex chamber were horizontal during all the cosmic ray tests.

The sense wire amplifiers were the same as those used in the Tevatron run (Figure 2.11). The discriminators were similar to those used in the Tevatron run, but they did not merge pairs of direct and delayed signals. Their output pulse width was 50 nsec with a dead time of about 10 nsec.

Plateau Measurements

The plateau of the vertex chamber was measured with cosmic ray tracks having an S1·S2 coincidence in the telescope. The plateau begins at a high voltage of about 1650 V using a discriminator threshold of 40 mV. The high voltage started to break down above 1970 V.

Spatial Resolution

A sample of 75K triggers was recorded at a high voltage of 1900 V. The samples at other high voltages consisted of 25K events each. There was no additional external reference for the tracks crossing S1, S2, and the vertex chamber.

A track candidate was considered to consist of hit cells forming a tower structure throughout the three planes (see Figure 2.5) and having times selected in the following way. Since slanted tracks may traverse more than one cell in the same plane and lead to clusters of several adjacent hit drift cells [50], only those times were selected in a cluster which were the minimum times with respect to

their two adjacent cells.

The drift velocity of the electrons was estimated from the distribution of selected times. Under the assumption of uniform illumination, $dN/dt = (dN/dx) \times (dx/dt)$, with $dN/dx = constant$. The time distribution dN/dt of the track candidates was parameterized with a sequence of linear approximations.

For all used tracking algorithms the isochrones in Figure 3b were assumed to be circles around the sense wire and only the projections onto the $x - z$ plane were considered. All four possible tangents to the 'drift circles' with radii r_i in planes $i = 1$ and $i = 3$ were calculated yielding four different slopes m_j.

A minimum was found for the quantity ($d_{123} = z_1 + z_3 - 2z_2$), with $z_i = zcell_i \pm r_i \sqrt{1 + m_j^2}$, $i = 1, 2, 3$. $zcell_i$ is the z position of wire i. This was assumed to determine the track.

The drift time to distance conversion was reevaluated by using tracks with $|m_j| \leq 0.075$. The criterion for a better conversion was that there should be no correlation between the drift distance r_2 and d_{123}. The same correlation also yielded the corrections for the individually displaced sense wires (c.f. section on construction). Note that with this method only the correction of the z location in plane 2 relative to the outer two planes could be obtained.

The intrinsic spatial resolution of a drift cell, σ_{int}, was calculated for normal tracks ($|m_j \leq 0.075|$) as $\sigma_{int} = \Gamma/(2.354\sqrt{6})$, where Γ was the FWHM of the d_{123} distribution. Only tracks with $0.15 < r_2 < 0.4$ cm were accepted in order to avoid boundary effects [39].

This method limited the accuracy of the time to distance conversion which

is dictated by the lack of an external track reference, available statistics, and the influence of unavoidable asymmetry in the drift cell construction. These limitations were less serious for normal tracks than for slanted ones.

For a high voltage of 1900 V and a threshold of 20 mV, the best obtainable spatial resolution is around 140 μm (rms) if all 30 cells are included and 90 μm if one selected cell with presumably well defined geometry is used (Figure 9). The lower the high voltage or the higher the threshold, the worse the spatial resolution.

Collider Performance

During the collider run, the high voltage of the sense wires was set to +1750 V instead of +1900 V and the threshold was set to 50 mV for the following reasons.

- The background radiation stemming from losses in the Main Ring of the proton accelerator and the halo of the p and $\bar{p}$ beams in the Tevatron caused the high voltage to trip off frequently when set above +1750 volts.

- Due to the effect of spurious late pulses the high voltage should be as low as possible and the discriminator threshold as high as possible.

- There was electronic cross talk from other apparatus in E735, especially radiation from the coaxial cables of the scintillator phototubes to the electronics of the vertex chamber. Additional shielding of accessible portions of the cables reduced this cross talk but was not sufficient to eliminate it. This effect was more serious for larger multiplicity. The later times of

most induced signals helped distinguish them from prompt chamber signals. Nevertheless, the threshold of the discriminators had to be set to 50 mV to avoid the effect as discussed under the second point.

- Even at 1750 volts and the higher threshold the obtained spatial resolution was within the required limits.

During the last months of the run period, the loss rates of the Tevatron stores were more than five times higher than in the preceding months. This demanded further reduction in the high voltage, down to 1730 volts.

The injection losses of the Main Ring beam (Figure 2.3) used to produce $\bar{p}$'s dictated gating down the vertex chamber high voltage by 10% every 2.6 seconds for a half second of the acceleration cycle in order to avoid tripping off the high voltage supplies. It was necessary to insert a large resistor (180 kΩ) in series with the power supply to provide critical damping of the chamber recharge in about 150 msec. This gating procedure, together with not running the vertex chamber at all when the collider beam loss rates were high at the C0 intersection, limited the integrated z-chamber wire current. During the 11 month running period when this chamber was used, the collected charge, averaged over all sense wires, was approximately 0.025 Coulombs/cm, almost an order of magnitude below the amount which might be expected to result in some performance degradation for an $Ar - CO_2$ gas mixture [51].

Resolution During The Tevatron Run

The tracks stemming from $p - \bar{p}$ interactions were defined by the spectrometer arm using all drift chamber planes except those of the vertex chamber. The spatial resolution of those tracks was of the order of 1 mm (rms) at the vertex chamber. That was not precise enough to correlate drift-times with drift-distances with the desired accuracy.

Practically, the time to distance conversion was obtained with the same method as with cosmic rays except that the tracks were selected by the spectrometer and that the projections of their slopes into the $x - z$ plane were used instead of m_j (c.f. cosmic ray section). The intrinsic spatial resolution of $\sigma_{int} = 440\,\mu$m was derived for normally incident tracks with 0.15 mm$< r_2 <$ 0.4 mm (Figure 2.13). The nominal locations of the sense wires were used instead of the unknown actual ones. This and the use of tracks with externally defined slopes appeared to have made the resolution almost two times worse at 1750 volts than the resolution obtained with the method used for cosmic ray tests.

Tracks were reconstructed, using the method discussed later, and the residuals were studied as a function of the track slope in the $x - z$ plane with respect to the x-axis. From these residuals, the measured z-chamber resolution is a function of the track slope as shown in Figure 2.14. In this figure the measured z-chamber resolution for 1988 data where the H.V. of the sense wires was at 1750 volts and for 1989 data where the H.V. of the sense wire is at 1730 volts was plotted. It is clear that the z-chamber resolution is worse for the 1989 data (600 μm). Also note that the resolution is better at slopes of the order of 0.4 to 0.5. This is due to the fact that the 0.5 slope tracks are the ones that traveled through a well

defined drift area of the cells from all three planes, as shown in Figure 2.5.

2.3.2 Central Tracking Chamber

Charged particles are tracked in the central tracking chamber [52] (CTC), shown in Figure 2.3. It measures the charged particle multiplicity, n_{ch}, of an event in the pseudorapidity (η) range $-1.7 < \eta < 1.7$.

The primary design considerations were that the chamber have good two-track separation so that high-multiplicity events could be measured accurately, that it consist of as little material as possible in order to minimize the production of secondary particles, and that it be capable of operating for an extended period in the high-radiation environment at the C0 interaction hall.

The CTC was a 2 m long cylinder with an inner radius of 22 cm and outer radius of 42 cm. The chamber was made in two lengthwise halves so that it could be quickly installed around the beam pipe at C0. The CTC consists of 24 15^0 sectors each containing 24 sense wires. The sense wires were 0.5 cm apart with a double row of potential wires as shown in Figure 2.15 (one cell of 24). The whole drift cell was tilted 5^0 with respect to the radial direction in order to resolve left-right ambiguity of tracks. The field wires forming the boundaries of the drift region are also shown in Figure 2.15, too. All wires are horizontally oriented, parallel to the beam pipe, along the z-axis. The potential wires near to the sense wires were run at -1975 Volts, and the field wires, which formed the boundary were held at -4200 volts. The sense wires were at zero potential.

The chamber was filled with a gas mixture of 95% argon 4% methane and

1% CO_2 at atmospheric pressure. The drift velocity in this gas mixture and in the drift field of 480 V/cm was 3.15 cm/μs (a relatively slow velocity which helps in the resolution of multiple hits). This gave a maximum drift time of 1.6 μs which was less than the 3.5 μs bunch crossing time interval when the collider was operating with 6 proton and 6 antiproton bunches.

Charged particles passing the chamber ionize the gas, and the ionized electrons cascade toward the sense wire. Near the sense wire, due to the large electric field gradient, electrons form an avalanche. This produced a pulse, which was read out at each end of the sense wire. This charge from both the left and right side of the sense wire was digitized by 100 MHz FADC (Flash Analog to Digital Converter). These FADC's measured the position along the sense wire (z coordinate of the hit) by this charge division technique. Namely, this z is given by:

$$z = z_0 + gL/2(Q_r - Q_l)/(Q_r + Q_l), \tag{2.9}$$

where z_0 is an offset due to differences in preamplifier input impedances and Q_r and Q_l are the integrated FADC counts correspoding to the charge on the right and left ends of the sense wire. L is the length of the chamber and g is a scale factor depending on the preamp input impedances and the wire resistance.

The CTC provided hit information with hit resolution in the (x,y) plane of 250 μm averaged across the drift cell and provided two-hit separation with 60% efficiency for hits separated by 3 mm.

2.3.3 Hodoscope

The scintillator hodoscope [53] system measures the charged particle multiplicity, n_{ch}. It consists of three parts as shown in Figure 2.2:

- The barrel hodoscope.
- The up-stream endcap hodoscope.
- The down-stream endcap hodoscope.

The barrel hodoscope covers the pseudorapidity range $-1.64 < \eta < 1.64$ and consists of 96 counters arranged in two 48-counter sections up-stream and down-stream of the interaction point. The counters are arranged in slats (5.4 cm wide, 97 cm long and 0.635 cm thick) running parallel to the beam pipe and spanning 7.5^0 in azimuth. There is a window in the barrel hodoscope matching the spectrometer window. This window reduced the total hodoscope solid angle coverage by about 2%. The counters in the barrel are at a radius of 42.4 cm from the beam line and cover the outside surface of the CTC (central tracking chamber).

Each up-stream and down-stream endcap hodoscopes is divided into three rings of 24 counters. Each counter spans about 0.5 units of pseudorapidity and 15^0 in azimuth. The endcap hodoscope extends the pseudorapidity range to $-3.25 < \eta < +3.25$. The total number of counters in the whole hodoscope is 240.

The scintillation material used in the hodoscope was polyvinyltoluene (PVT)-based Bicron BC-408. The PMT used for all counters is the 28.5 mm diameter,

ten-stage Hamamatsu 1398 tube with UV glass window. The anode signal was split into two outputs. One splitter output was used for pulse height analysis while the other went to a discriminator in order to feed the trigger processor, TDC's and scalers.

The hodoscope was used not only for on-line triggering but also in the off-line analysis to determine the true primary charged particle multiplicity, n_{ch}, of the collisions from the number of hodoscope hits, n_h. Monte Carlo studies determined this conversion factor as described in reference [54].

2.3.4 Pre- and Post-Magnet Chambers

The only difference between the pre- and post-magnet chambers is the size, so the general characteristics of one of these two chambers will be described. Each chamber was constructed of a rectagular, aluminum reinforced, window and contained four wire planes. The post-magnet chamber (at the exit of the magnet) was graduated in size so that the active area subtended approximately the same angle with respect to the interaction point as the pre-magnet chamber and the rest of the spectrometer as shown in Figure 2.2.

A magnet chamber cell (Figure 2.16) was defined by a sense wire of 25 μm diameter gold-plated tungsten wire between two field shaping wires of 125 μm gold-plated copper in the z-direction. This sense wire was also guarded by two guard shaping wires of 125 μm gold-plated copper in the x-direction as shown in Figure 2.16. The distance between the sense wire and the field wire is 2.5 cm forming drift cells 5 cm wide in the z-direction. The distance between the sense

wire and guard wire is 0.95 cm forming drift cells 1.9 cm in the x-direction. The magnet chamber delimiters, or windows, in the z-y plane were aluminized 50 μm Mylar foil with 25 μm aluminum and 25 μm Kapton with 13 μm aluminum. All the wires in both the pre- and post-magnet chambers were perpendicular to xz-plane and parallel to the two windows of each chamber (y direction).

Each pre-magnet chamber plane has 25 sense wires and each post-magnet chamber has 30 sense wires spaced 5 cm apart along planes parallel to the z-axis. Planes 1 and 3 are staggered by 1 mm with respect to planes 2 and 4 in order to resolve left-right ambiguities. The first sense wire in the pre-magnet chamber is at -30.3 cm and the 25th sense wire is at 89.7 cm in z-direction. The location of the first plane in the pre-magnet chamber is at 56.45 cm while the location of the first post-magnet plane is at 85.96 cm from the $p\bar{p}$ TEV beam line.

The sense wires were held at ground. The field shaping wires were at -3900 volts, while the guard shaping wires were at -900 volts and the windows were at -1800 volts through a 1.2 $M\Omega/2W$ resistor in order to sensitize outside cellsclose to the windows. The chambers were filled with an $Ar(85\%)+CO_2(15\%)$ gas mixture. The equipotential and electric field maps with the isochrone lines are shown in Figures 2.17 and 2.18, respectively. The equipotential lines are drawn every 150 volts for a range of -3800 Volts to -800 volts, and the isochrone lines are drawn every 50 nsec. This calculation was done using GARFIELD [55] (a drift chamber simulation program developed at CERN by R. Veenhof).

Because of the complexity of the electric field in the pre-magnet chamber, the drift velocity of electrons is different in planes 1 and 4 from the drift velocity

in planes 2 and 3. Using magnet-off calibration data, it was found that the drift velocity also depended on the slope of the track in the $x - z$ plane with respect to the x-axis. For example, the measured drift velocity of electrons, produced by charged particles passing the drift cell, for each of the 4 planes in the pre-magnet chamber is given by Figure 2.19 for a track slope of 0.5 in the $x - z$ plane with respect to the x-axis. Figure 2.20 shows the dependence of the drift velocity as a function of the track slope in the $x - z$ plane with respect to the x-axis.It should be pointed out here that the drift velocity depended on both the slope and which side of the sense wire a track passed.

A study of the pre- and post-magnet chambers resolution was made by reconstructing real tracks in the pre- or post-magnet chamber only. The residuals were calculated as a function of the track slope in the $x - z$ plane with respect to the x-axis. Figures 2.21 and 2.22 show the measured residuals for normal tracks ($-0.1 <$slope$< +0.1$) in the pre- and post-magnet chamber, respectively. Figure 2.23 shows the dependence of the pre- and post-magnet chambers resolution as a function of the track slope.

Each drift chamber sense wire signal was amplified using a homemade amplifier and passed through a discriminator. The resulting logic pulse was passed to a PSL TDC (time to digital converter) (Section 2.3.4) where the time difference between a reference pulse, generated by the TOF_p and $TOF_{\bar{p}}$ (trigger) scintillation counters, and the chamber pulse was digitized. By studying the actual time distribution of the arriving times a t_0 can be defined when a charged particle passed by a sense wire (when a charged particle "hits" the wire). The drift time

was defined as the time taken by the ionization electrons (freed by the passing charged particles) to reach the sense wire:

$$t_d = t_{TDC} - t_0, \tag{2.10}$$

where t_d is the drift time, t_{TDC} is the time digitized by the TDC's and t_0 is the reference time. From this, the drift distance of the charged particle from the sense wire is given by:

$$z_d = v_d t_d, \tag{2.11}$$

where z_d is the drift distance and v_d is the drift velocity of the ionization electrons.

An attempt was made to calculate the average measured efficiency per plane for the pre- and post-magnet chamber as a function of the angle θ of the particle with respect to the x-axis. The measured efficiency, ϵ^{meas}, was defined for each plane of a chamber as the ratio of the number of times a sample of reconstructed tracks had a hit in that plane of the chamber to the number of reconstructed tracks. These tracks were taken from a sample of one track magnet-off events tracked by our tracking program, the same one used in the magnet-on events. The accepted tracks were accepted only if they had a good TOF1 hit and came close (3 cm) to the vertex of the event defined by the z-chamber. Figures 2.24 and 2.25 show the measured efficiency, ϵ^{meas}, for all 4 planes in the pre- and post-magnet chamber, respectively, over a range of $-40^0 < \theta < 60^0$. The efficiency for all four planes in the the pre- and post-magnet chambers was the same, of the order of 90%.

PSL TDC

The PSL TDCs [56] (time to digital converter) used in this experiment for the pre-magnet, post-magnet, and end-cap chambers were built by the Physical Sciences Laboratory of the U.W.-Madison (PSL). Each TDC is a single width FASTBUS board with 8 units of 12 inputs each and can record 96 input wires. The features of this TDC are:

- It is linear so the integer recorded for each pulse is proportional to the elapsed time for some arbitrary early common initial instant.
- It runs continuously and records hits for later readout after a very slow trigger. This permits "slow triggers", for example, slow moving particles.
- It has a resolution of 1 ns.
- It has the ability to record multiple hits on individual wires. A total of 16 pulses can be recorded from each group of 12 inputs.
- It is read out to computers via a FASTBUS system and has a readout speed matching that of FASTBUS.
- It cannot measure signals from wires which are very busy. The difference between two input hits in one of the 8 TDC units must be greater than $\sim$ 15 nsec.
- It cannot handle all types of pulses.The standard input pulse expected is 20 to 50 ns long.

The PSL TDCs are completely digital using counters and RAMs with a clock frequency of 100 MHz. The time for each event hit is derived from two components:

- A binary counter of 12 bits which rolls over each 40.96 μs and which is incremented each 10 ns.
- A vernier which consists of a 15 ns delay line with 16 taps and a 16 input RAM which can be written to each 10 ns.

2.3.5 Magnet

The momentum of a particle in the E735 spectrometer was found from its measured curvature through the E735 magnet. The magnet has a dipole configuration at x=75 cm (center of the magnet) in the C0 coordinate system as shown by the top and side views in Figures 2.2 and 2.4, respectively. The measured $B_y(x,z)$ (y-component of field B as function of x-axis and z-axis) at y=15 is displayed in Figure 2.26. The strength of the magnet in the $x-z$ plane at the middle of the magnet is fairly uniform (3.8 KG) and provides a 50 MeV/c effective momentum kick to charged particles ($\int \vec{B} \cdot \vec{l} = 50$ MeV/c). The magnetic field was measured using the ZIPTRACK [57] and Hall probe measuring devices at Fermilab. The components of the magnetic field (B_x, B_y, B_z) were calculated by linear interpolation between adjacent measured grid points of the field map.

2.3.6 Straw Drift Chambers

The straw chamber [58] was a 14 plane drift chamber located behind the post-magnet chamber 100 cm away from the beam pipe as shown in Figure 2.2. It was a part of the spectrometer used to measure the final direction of a track.

There were seven straw drift chamber boxes with different sizes ranging from 75 cm high $\times$ 220 cm long to 110 cm $\times$ 340 cm. Each straw drift chamber box had 2 planes of staggered wires. Each plane contained 60 to 90 tubes with sense wires. Four of the seven straw boxes had wires vertical to the $x-z$ plane and the remaining three boxes had wires slanted at 4^0 with respect to the vertical axis for stereo reconstruction. Boxes with vertically oriented tubes were alternated with boxes with slanted tubes.

The main features of the straw chamber are:

- Modularity: if a sense wire breaks, it is easy to isolate a straw tube and remove it.
- Crosstalk: because of the electrical isolation, crosstalk is less of a problem.
- The electric field and potential maps are uncomplicated. Tthere is no need to do any slope correction in the time to distance conversion.
- However the straw drift chamber is massive, creating multiple scattering and interactions.

Each straw tube was constructed of a 5 cm diameter aluminized Mylar cylinder. In detail, the wall of the tube includes 0.018 mm of aluminum, 0.075 mm

paper, and 0.075 mm of Mylar. Aluminum plates on the top and bottom of the chamber hold the tubes in place. In the center of each tube is a 50 μm gold plated copper-beryllium wire at a tension of 0.25 Kg. The tubes were filled with a 90% Argon 10% Methane gas mixture. The wall of the straw tube was at zero volts and the centered sense wire was at +200 volts. The output of each sense wire was connected to an amplifier-discriminator mounted on the top of each straw drift chamber box. The signal was read by LeCroy single hit 4299 TDCs.

The resolution of the chamber during the 1988-1989 run period was measured by studying the residual of the fitted tracks. It was found to be 500 μm. The measured chamber efficiency was studied per straw chamber plane for the straw drift chamber. The measured straw plane efficiency is defined the same way as it is defined for the pre and post-magnet chambers in Section 2.3.4 by using tracks reconstructed in the magnet-off mode. Figure 2.27 shows the measured chamber efficiency for the first two normal (tubes are vertical to the $x - z$ plane) and two titled planes as a function of the track angle θ defined as:

$$\theta = \tan^{-1}(p_z/p_x). \tag{2.12}$$

There seems to be an inefficiency at small angles due to the geometric topology of the tubes.

2.3.7 TOF System

Here the four arrays that make up the Time of Flight (TOF) counters will be reviewed. The TOF system includes the two trigger counters TOF_p and $TOF_{\bar{p}}$ and the TOF_1, TOF_2 counters [59]. Two of these are in the TEV tunnel upstream

and downstream of the interaction point (TOF_p, $TOF_{\bar{p}}$ trigger counters) as shown in Figure 2.2, and two are part of the magnetic spectrometer (TOF_1 and TOF_2 counters). The TOF_1 was set at x =1.96 m and TOF_2 was put at x = 4.0 m away from the beam pipe as shown in Figure 2.2.

The purpose of the TOF_1 and TOF_2 system is to provide pion, kaon, and proton identification and to separate pion, kaon, and proton up to momenta of about 3 GeV/c. There were seven TOF_1 and 32 TOF_2 counters. Each of the seven TOF_1 counters was placed horizontally, forming a vertical wall in the $x - y$ plane. Each of these counters was 3 m long, 10 cm high, and 5 cm thick. Each of the 32 TOF_2 counters was 1.5 m long, 15 cm wide, and 5 cm thick, placed vertically in the $x - z$ plane. The purpose of the TOF_p, $TOF_{\bar{p}}$ system was to provide the interaction time and provide a second piece of information on the vertex of the interaction (the first vertex information was given by the z-chamber). There were 15 TOF_p and 15 $TOF_{\bar{p}}$ trigger counters. Each bunch of protons or antiprotons in the TEV had a longitudinal spread of about 40 cm, which introduced an uncertainty of 2 ns in the timing of the beam-beam interaction. Hence Beam pickups could not be used to determine the time of the interaction. The TOF_p was located about 2 m downstream of C0 with respect to the proton bunch, while the $TOF_{\bar{p}}$ was located 2 m upstream. These counters were used to measure the flight times of particles with highest momenta.

The layout of the TOF_p and $TOF_{\bar{p}}$ trigger counters is shown in Figure 2.28. The thickness of each trigger counter was 2.5 cm. They covered a region of $3 < |\eta| < 4.5$. To obtain good time resolution, at least one minimum ionizing hit

was needed in each of the TOF_p and $TOF_{\bar{p}}$ trigger counters. The segmentation of TOF_p, $TOF_{\bar{p}}$ trigger counters was determined by Monte Carlo studies [59].

The scintillator for all counters was Bicron BC-408 with a measured attenuation length $\lambda = 210$ cm (next section). The counters were wrapped with opaque anti-static material. Plastic light fibers were mounted on each counter in order to monitor and calibrate the system during the collider run. The light guides for TOF_p, $TOF_{\bar{p}}$ trigger counters were made out of Bicron nonscintillating PVT plastic to withstand high doses of radiation. The TOF_1, TOF_2 counters were made out of UVT lucite as these were placed further away from the beam pipe. The photomultiplier tubes (PMT's) were Amperex XP-2020. The PMTs were used at each end of each scintillator counter. The PMT's were shielded from magnetic fields with μ-metal and soft iron shields. The anode at each end of the TOF_1 and TOF_2 counters was fed to various types of TDC's (Time to Digital Converter's) in order to measure the hit time and the signals received from two different dynodes (DY-9 and DY-12) were fed to ADC's (Analog to Digital Converter's) in order to measure the charge as shown schematically in Figures 2.29 and 2.30 .

The interaction time and the event vertex were defined through the following relations:

$$t_0 = (t_{\bar{p}} + t_p)/2 - d/2c, \tag{2.13}$$

and

$$z_{ev} = c(t_{\bar{p}} - t_p)/2, \tag{2.14}$$

where d is the separation between $TOF_{\bar{p}}$ and TOF_p counters, $t_{\bar{p}}$ and t_p are the

time walk [59] corrected values from the $TOF_{\bar{p}}$ and TOF_p counters.

The time of flight for TOF_1 and TOF_2 are given by:

$$t_1 = t_{TOF1} - t_0, \tag{2.15}$$

and

$$t_2 = t_{TOF2} - t_0, \tag{2.16}$$

where t_0 is the interaction time (Equation 2.13) and t_{TOF1}, t_{TOF2} are the TOF_1 and TOF_2 times, respectively.

By using the time difference at the two ends of the TOF_1 or TOF_2 the z coordinate of a hit can be determined:

$$z = (t_l - t_r)v_{eff}/2 + z_{offset}, \tag{2.17}$$

where t_l is the left TDC time for a counter, t_r is the right one, v_{eff} is the effective velocity of light in a counter, and z_{offset} is the calculated time offset for the TOF_1 or TOF_2 counters. This time offset was determined by comparing the calculated time of flight of pions using the tracked momentum and the flight path from the time determined by the counter. The experimental time resolution of TOF_1 and TOF_2 was calculated by determining the mass width of the pion, kaon and proton as a function of momentum (Section 4.6).

Attenuation Length λ of TOF_1

The attenuation length of the TOF_1 counters, by using minimum ionizing particles (MIP) hitting the TOF_1 counters, was determined. Namely the MIP was determined as a particle which obeyed the following cuts:

- Momentum of the particle was $0.3 < p < 0.5$ GeV/c.
- Mass of the particle, determined by TOF_1, was $0.10 < M < 0.17$. (The previous two conditions define a MIP particle.)
- $\chi^2_{pdf} < 8$.
- the beam intercept of the particle at the beam line was within 5 cm of the z-chamber vertex.

Figure 2.31 shows the z dependence of the light (I) deposited by the MIP particle, where I is given theoretically by:

$$I_0 = I(z)e^{-z/\lambda}P_x/P, \tag{2.18}$$

where I_0 is the total released light when a charged particle crosses the scintillator, P_x/P is the x direction cosine of the particle, z is the hit position of the track given by the tracking program, and λ is the attenuation length of the counter. By fitting the z dependence of $I(z)P_x/P$ the attenuation length, $\lambda = 212 \pm 30$ cm was calculated, (for counter number 5 in TOF_1 system) which is close to the attenuation length ($\lambda = 210$ cm) value given in the spec sheet of Bicron BC-48.

2.3.8 Endcap Chamber

The endcap chamber is a delay line drift chamber. A delay line drift chamber measures the transit time of signals induced in a delay line that runs parallel to the sense wire. The difference in arrival times of signals at the two delay line ends yields the radial coordinate of the hit ρ (the dimension parallel to the delay

line). The sum of the times yields the usual drift coordinate d. Delay line drift chambers have been used before in an actual experiment [60].

There were two endcap delay line drift chambers deployed upstream and downstream of the interaction point. They measured the charged particle multiplicity in the region $1.5 < |\eta| < 3.25$, as shown in Figures 2.2 and 2.32. An endcap chamber has 32 pie-shaped segments, each divided by a delay line into half-segments. Figure 2.33 shows the top view of an endcap segment. As shown in the figure, the main components of an endcap segment were:

- four delay lines running radially from the beam pipe defining 4 chamber cells.
- eight 1 mil tungsten gold-plated ambiguity sense wires, 2 mm in front of each side of the delay line.
- four 1 mil gold plated tungsten regular sense wires.
- eleven 5 mil aluminum gold-plated field wires.
- two 5 mil copper-Kapton field planes parallel to the delay lines, and
- two 5 mil copper-Kapton field-planes normal to the delay lines.

The delay lines were held in tension by a mechanical construction using a spring. The tension on the delay line was adjusted to 250 g. The delay line consisted of a copper pattern etched on each side of a 4 mil thick Mylar strip 1.05 cm wide and 41.5 cm long. The computer generated pattern was a square wave displaced by a half wavelength on opposite sides. Conductor width and spacing were each 250

μm. The impedance of the delay line was about 120 Ω. Inverse signal velocity of the delay was 1.67 ns/cm. Because the signal was taken directly from both sides of the delay lines, it was convenient to keep these lines at ground potential. The ambiguity wires were held at +1350 volts through a 1 $M\Omega$ resistor by-passed to ground by a 0.001 μF capacitor, and the regular sense and field wires were held at 0 volts. The tension on the ambiguity-sense and regular-sense wires was 60 g, while the tension on the field wires was 120 g. The voltage on the copper Kapton windows was varied across the cell by using a resistor voltage divider held at -5000 volts at the top line of the voltage divider. It was ordered to produce a uniform electric field from the edges of the drift cell to the sense wire. The endcap chambers were filled with an 85% Ar-15% CO_2 gas mixture. The potential and drift fields were studied using GARFIELD [55] (the drift chamber simulation program). Figure 2.34 shows the equipotential lines of a drift cell including a delay line, the two ambiguity-wires, two regular-sense wires to the left and right of the delay line and four field wires. Figure 2.35 shows the drift lines to the ambiguity and regular sense wires. The equipotentials are separated by 244 volts plotted from -4800 to 1300 volts. The indicated isochrones are separated by 100 ns and omitted for $t > 1$ μs.

An electron avalanche on an ambiguity sense wire is recorded independently (by a separate PSL TDC) and the signal it induces on the delay line is recorded by 2 other PSL TDC's at its top and bottom. The delay line amplifier, Figure 2.36, uses standard ECL logic with symmetric DC feedback. Matching the delay line impedance (120 Ω) is accomplished by the use of a pair of grounded base

transistors at the input. Four amplifier channels were built per card. The ECL discriminator, Figure 2.37, was designed to fire on either a positive or negative pulse. Pulses from one side of the delay line are positive and from the other are negative. The delay line signal recorded by the TDC's, for either the top or bottom end of the delay line, consists of three components:

- The drift time of the produced ionization electrons, t_{dr}, produced from the passing charged particle through the endcap drift cell.
- The pulse induced on the delay line which requires a transit time, t_{tr}, to reach the end (top or bottom) of a delay line.
- The time that the signal needs to travel from the amplifier to the TDC.

The radial coordinate, ρ, from the induced delay line signal is given by:

$$\rho = v_l(t_t - t_b)/2, \tag{2.19}$$

where v_l is the signal velocity in the delay line and t_t, and t_b are the TDC times relative to the interaction time recorded at the top and bottom of the delay line, respectively. The coordinate ρ is measured from the center of the delay line.

The drift coordinate d is given by:

$$d = d_w \pm (t_0 - t_l/2 - (t_t + t_b)/2)v_g, \tag{2.20}$$

where t_l is the total transit time for a signal along the delay line, v_g is the gas drift velocity, t_0 is the earliest time a signal can arrive at either end of the delay line, and d_w is the coordinate relative to the delay line of the sense wire responsible

for inducing the signal in the delay line. This d coordinate can have left-right ambiguity, but this can be resolved by using the signal of the ambiguity-sense wires next to the delay line.

Figure 2.38 shows an endcap event resulting from a $p\bar{p}$ collision. A top and side view of the same track are plotted in the figure.

Cosmic Ray Tests

The trigger counters for the cosmic ray tests consisted of two scintillators S1 and S2 covering the two sides of an endcap chamber segment. The wires and the delay lines of the endcap chamber were horizontal during the cosmic ray tests. The ambiguity-sense wire amplifiers and discriminators were the same as those used for the Tevatron running. The signals from delay lines and sense wires were read with the PSL TDC's.

The plateau of the endcap chamber was measured with cosmic ray tracks having an $S1 \cdot S2$ coincidence. The plateau of the delay lines was studied as a function of the ambiguity-sense wire voltage. The voltage divider was held at -5000 volts. The plateau begins at a voltage of about 1300 volts and the chamber begins to break down above 1400 volts. However, as the operating point, 1350 volts for the sense wire high voltage was chosen.

A sample of 1,000 triggers was recorded at an ambiguity sense-wire high voltage of 1350 volts.

A triple coincidence $(top + bottom + sensewire)$ in a half-segment thus over-determines the space coordinates for a hit. Signals from the 4 possible ambiguity-

sense wires in a segment are used to determine which side of the delay line the top and the bottom signals refer to. These 4 points, probably belonging to a track, were fitted using a straight line with ρ as a function of z, where ρ is the radius of a hit on the delay line from the beam line and z is the coordinate of the hit along the z-axis. Plotting the track with the best χ^2 (because sometimes more than one hit on the delay line was recorded) shown in Figure 2.39, the straight line fit of the obtained spatial resolution for ρ was 0.44 ± 0.04 cm. This is close to the theoretical limit of 0.42 cm imposed by the TDC least count. The fit in the above figure is the χ^2 distribution for 2 degrees of freedom

$$dn/d\chi^2 = Ae^{-\chi^2/2\sigma_\rho^2}, \tag{2.21}$$

where A is a normalization factor, and σ_ρ is the delay line resolution. Four data points with a two parameter function (straight line) was fitted. The limit in the ρ spatial resolution is defined by the resolution of the PSL TDC's. In principle the PSL multihit TDC's have a resolution of 1 ns which yields a theoretical spatial resolution for the delay lines of $\sigma_\rho = 0.42$ cm.

An attempt was also made to determine the spatial resolution of the delay lines, σ_ρ, and ambiguity-sense wires, σ_d, using the 1988-1989 Tevatron data [61] for hodoscope charged multiplicity, $n_{ch} < 60$. The obtained spatial resolution was $\sigma_d = 0.065$ cm for sense wires and $\sigma_\rho = 0.6$ cm for the delay lines.

Figures for Chapter 2

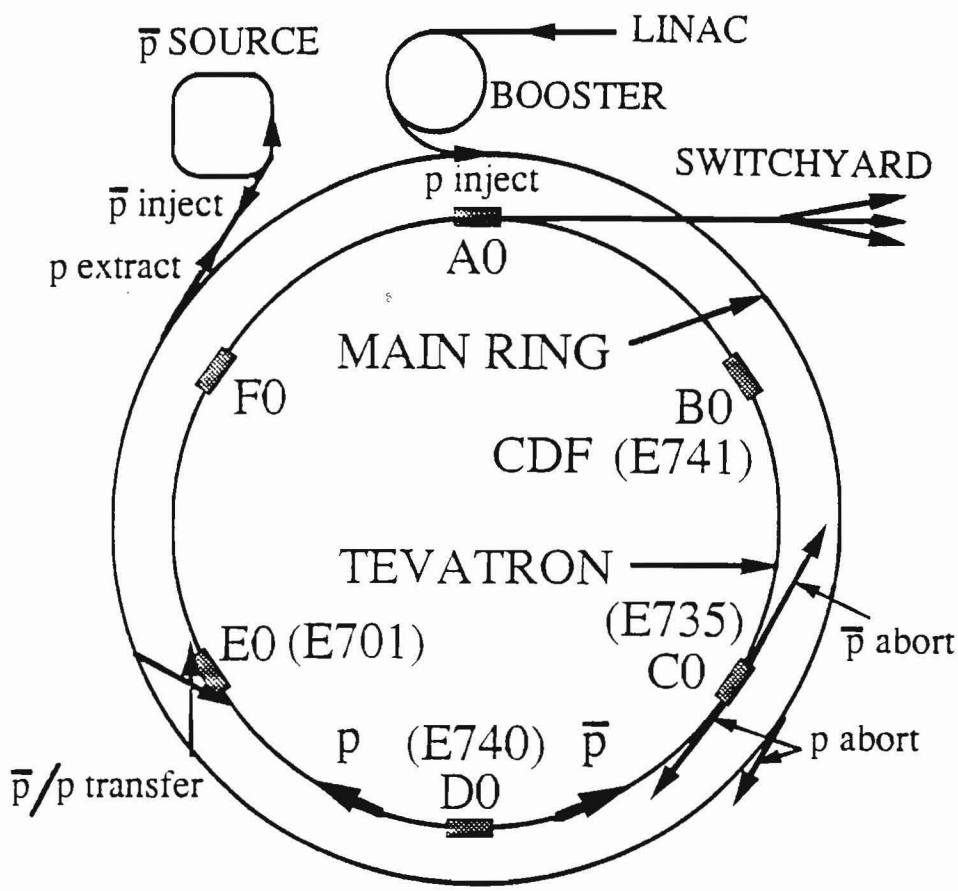

Figure 2.1: Fermilab accelerator layout. The C0 experimental hall is also shown.

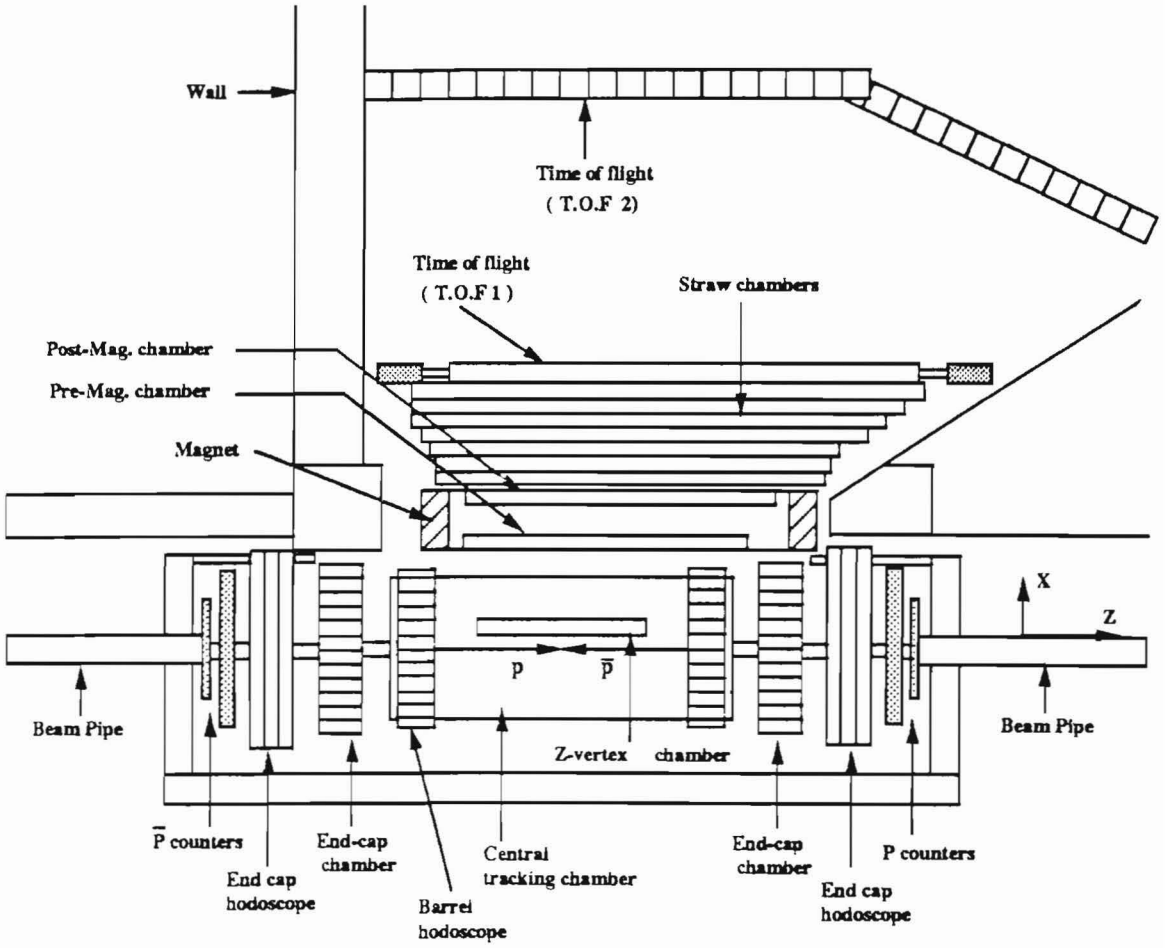

Figure 2.2: Top view of the E735 detector at C0.

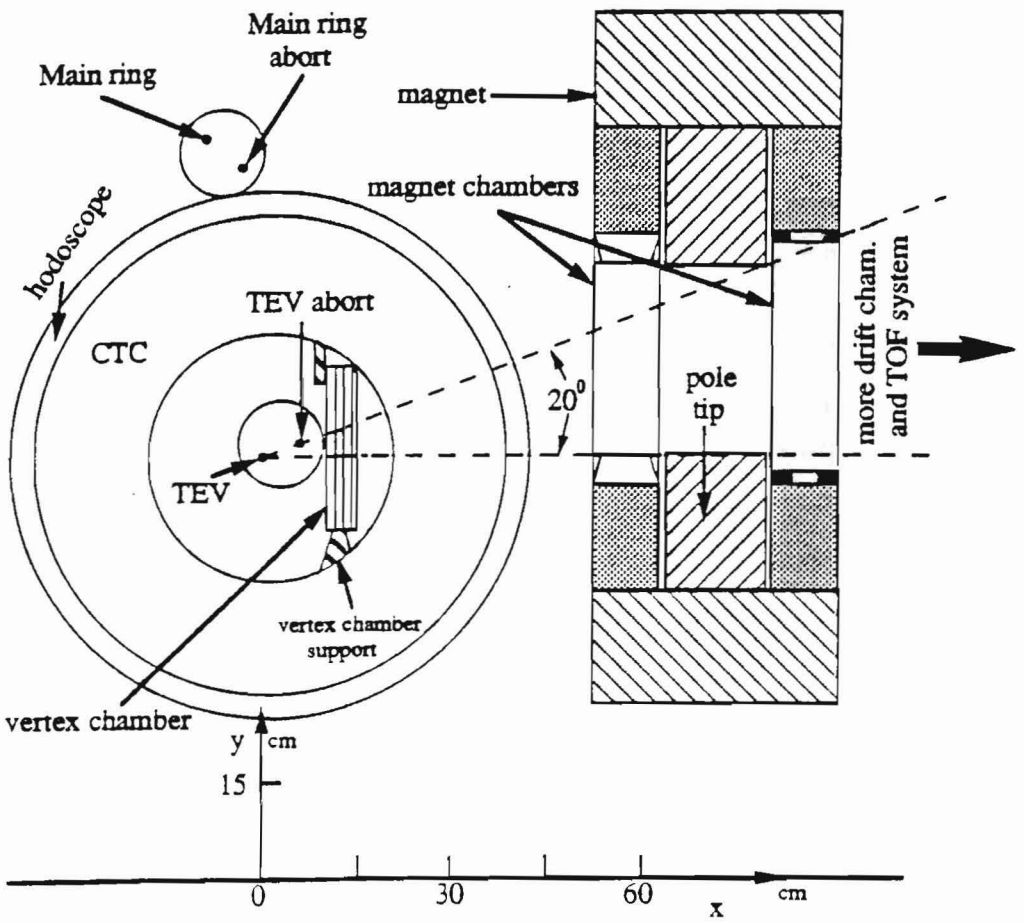

Figure 2.3: Cross section of the E735 detector at C0 showing the position of the vertex chamber and magnet chambers. Each magnet chamber contained four planes of sense wires while the vertex chamber contained three.

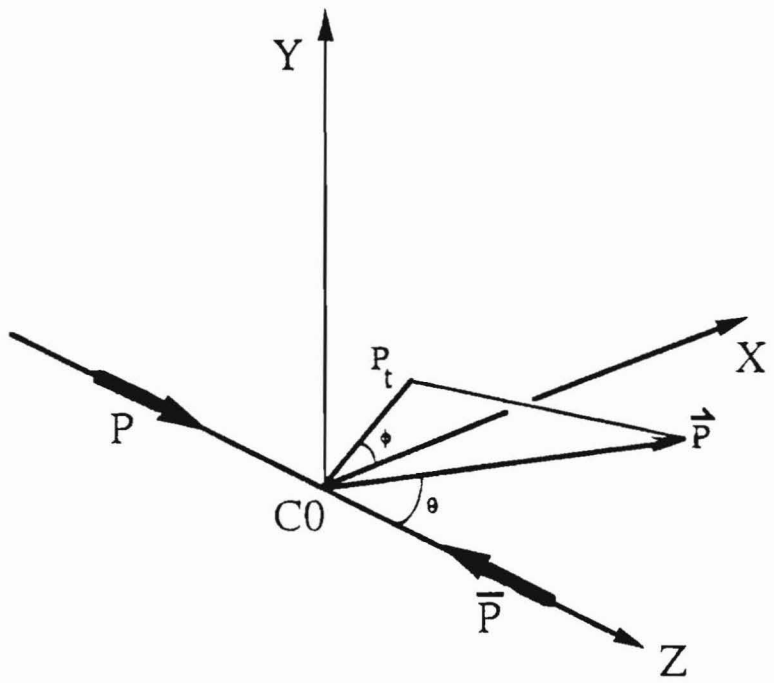

Figure 2.4: C0 coordinate system.

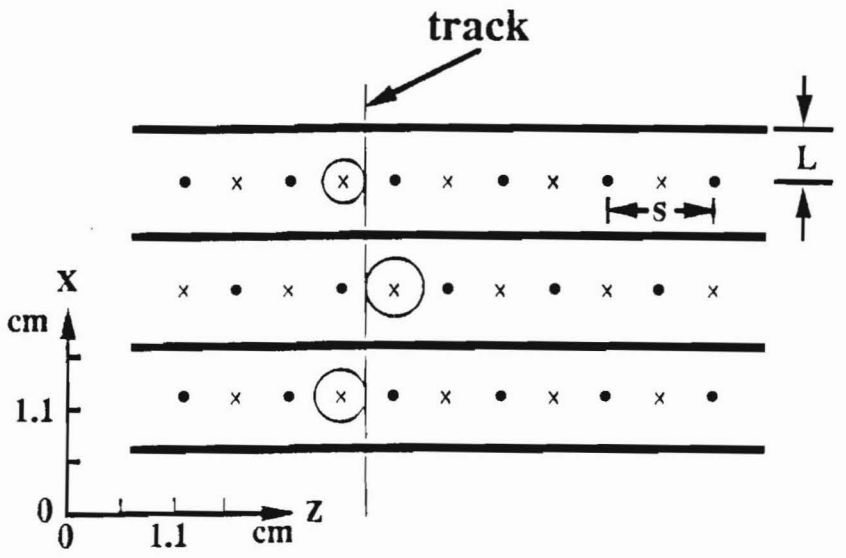

Figure 2.5: The dimensions of the drift cells showing an example of the tower structure produced by track hits. The middle drift plane is displaced by half a drift cell width with respect to the outer two planes. ("×"=sense wires, "•"=field wires, solid lines = cathode planes.) s=1.1 cm. L=0.55 cm.

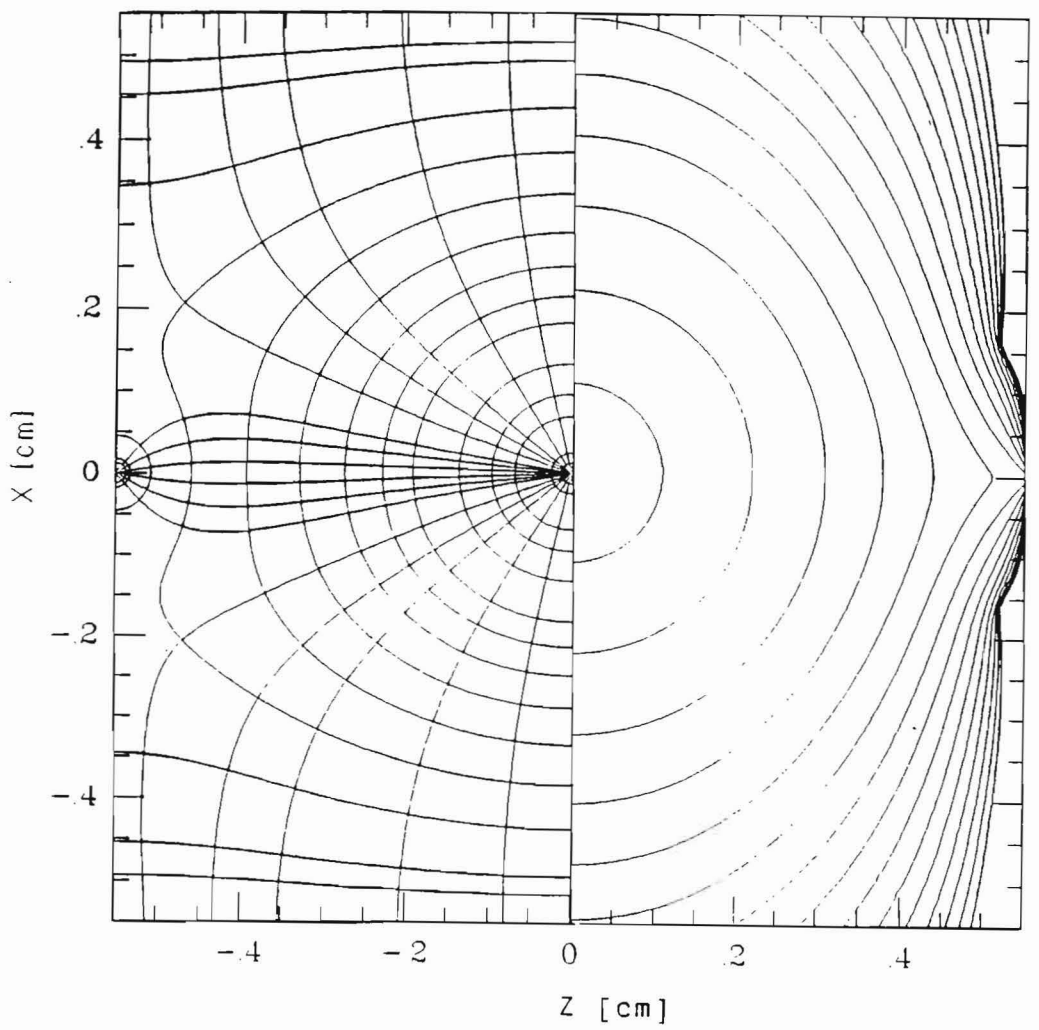

Figure 2.6: Equipotential and electric field map with the field wires and cathode planes at ground potential and the sense wires at a high voltage of U=+1900 volts. The equipotentials are separated by 50 volts and omitted above 750 volts. The sense wire is at z=0, x=0. The two field wires are at $x = 0, z = \pm 0.55$ cm from the sense wire. The cathode planes are parallel to the x-axis at $x = \pm 0.55$. The isochrones are obtained by using the gas mixture of $Ar(85\%)$-$CO_2(15\%)$. The indicated isochrones are separated by 20 nsec and omitted for $t > 300$ nsec.

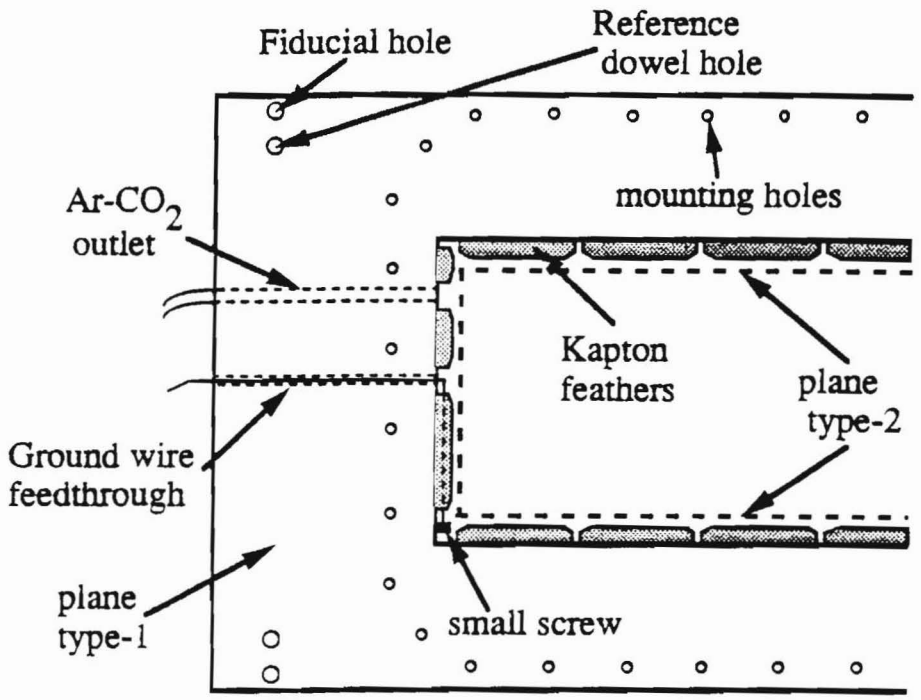

Figure 2.7: Left side of a kevlar reinforced frame of type 1. Shown are the Kapton feathers, holes, and screw for electrode attachment to the window. Dashed lines show the aperture of the adjoining type 2 frame.

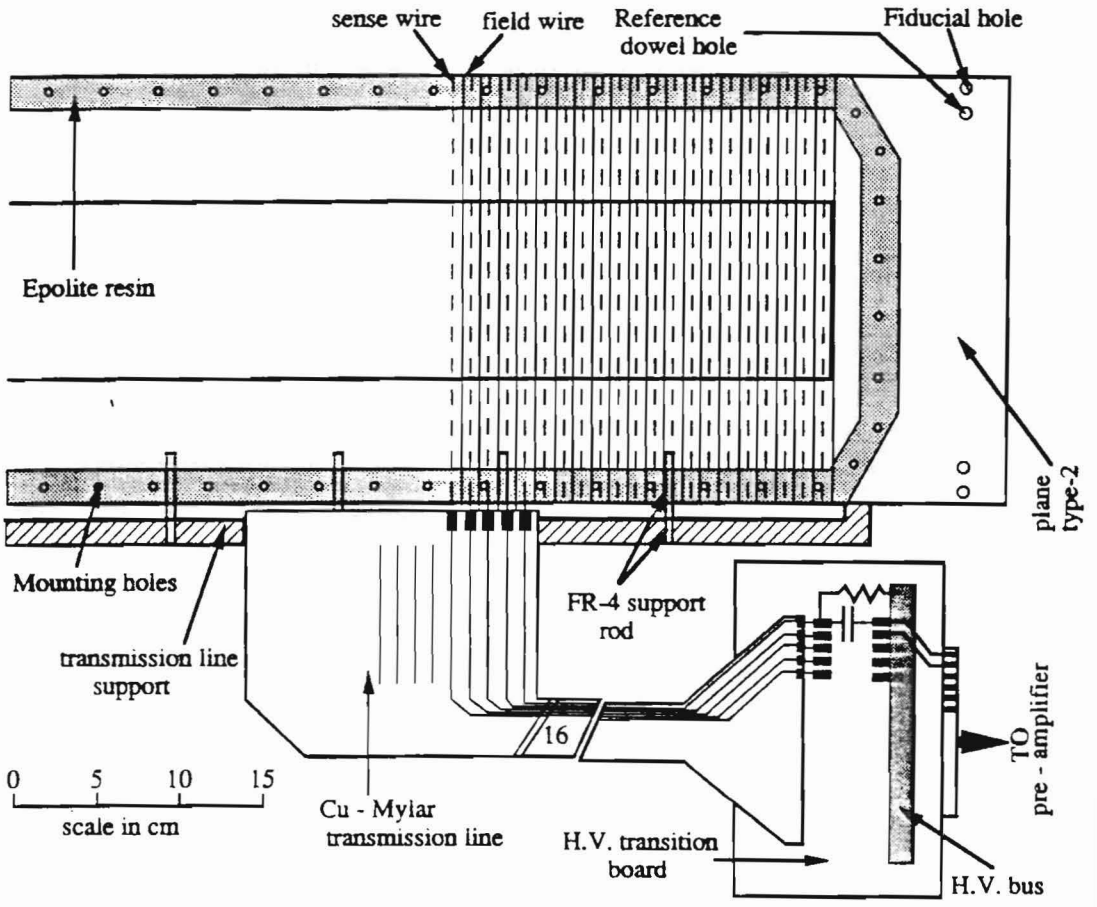

Figure 2.8: Right side of kevlar reinforced type 2 frame carrying the wires, transmission lines and cathode plane. Shown are the handles providing transmission line support and its reinforcement rods, transmission lines, and wires.

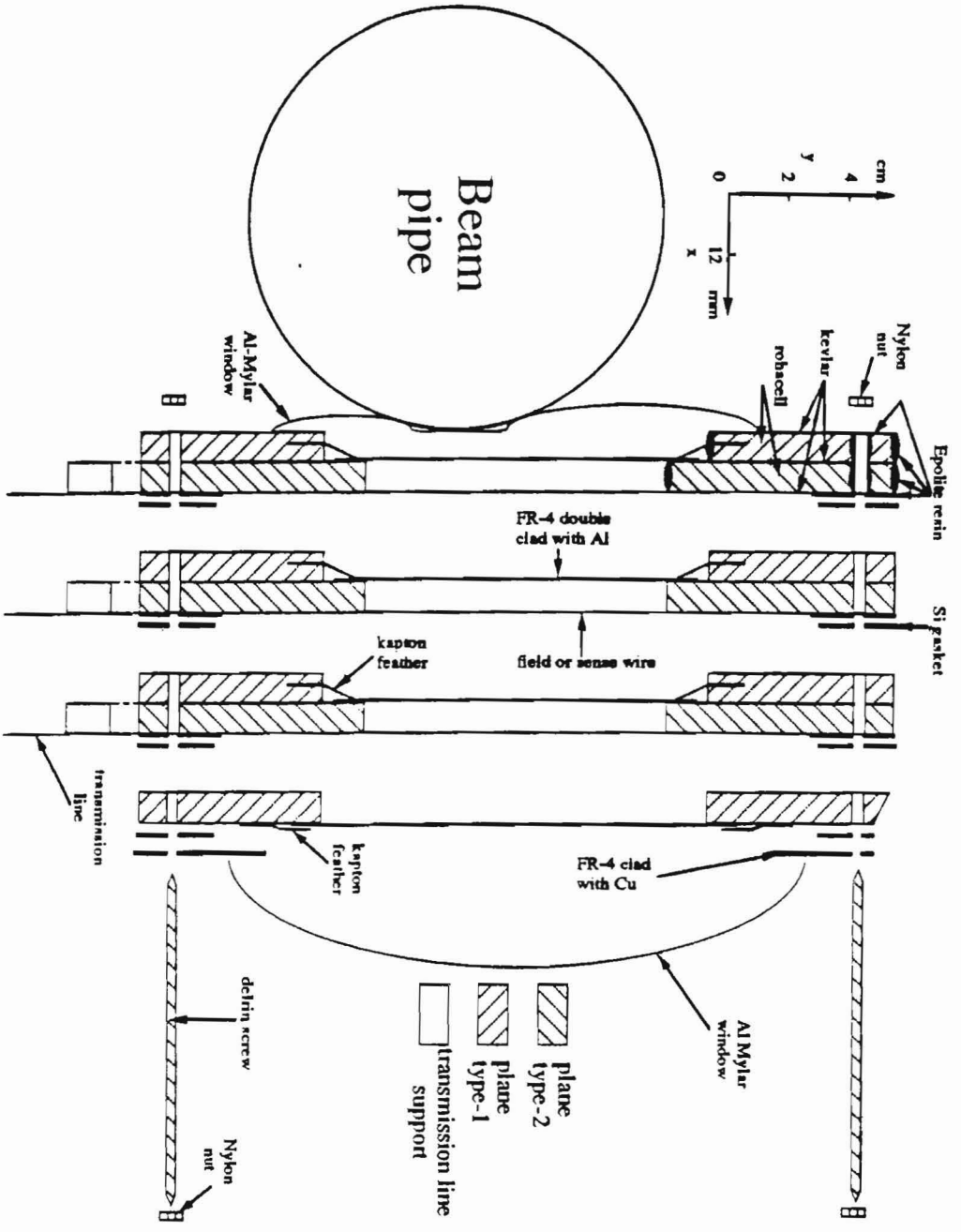

Figure 2.9: Mechanical cross section of the vertex chamber. Shown are the wires, electrode windows, rubber seals, outer windows with FR4 frames, and Kapton feathers. Typical seals with Epolite resin are indicated in the upper side of the left frame module.

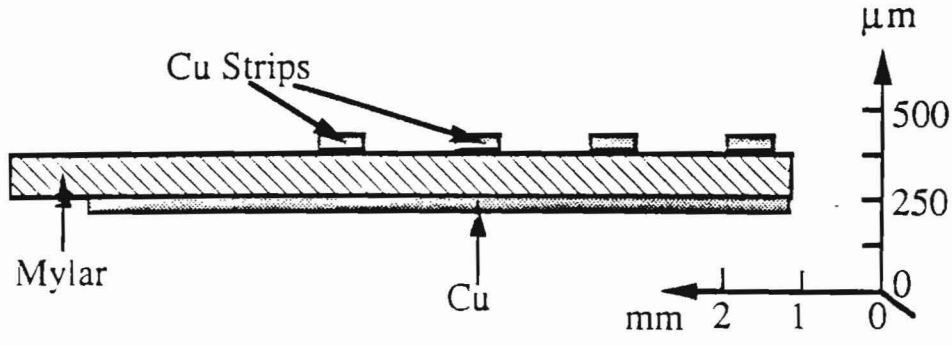

Figure 2.10: Cross section of the transmission line. Only four out of 16 Cu strips are shown.

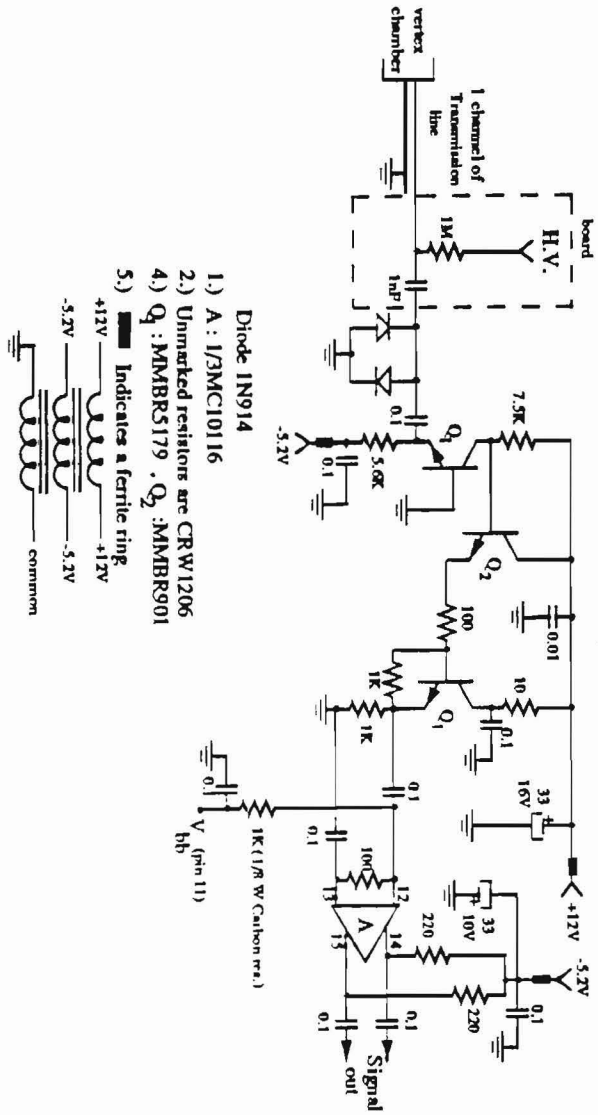

Figure 2.11: Interconnection of transmission line with high voltage transition board and the preamplifier schematic.

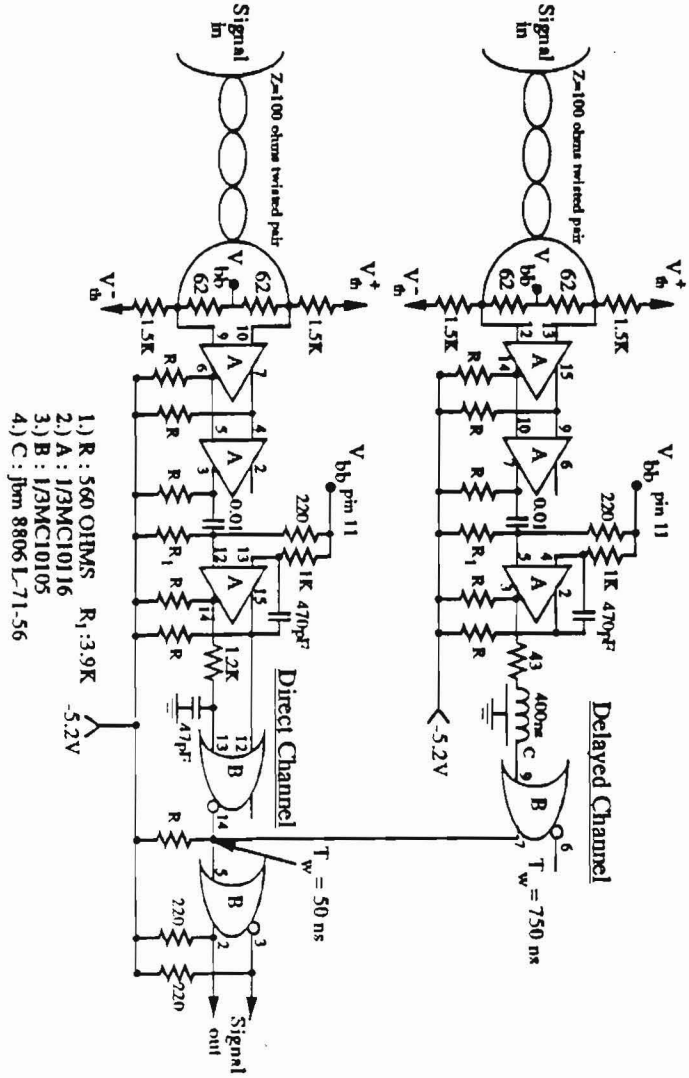

Figure 2.12: A discriminator showing the direct (lower) and the delayed (upper) channel. The thresholds used in this report correspond to $(V_{th}^{+} - V_{th}^{-}) \times 62/1500$.

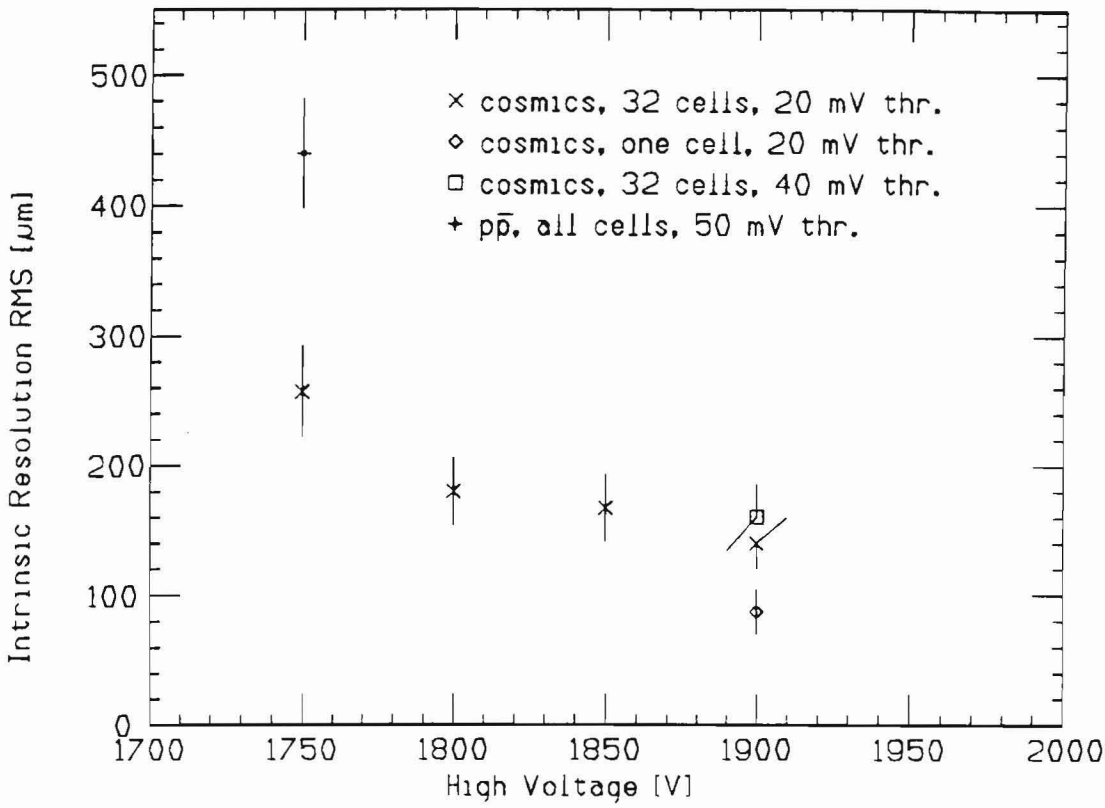

Figure 2.13: The intrinsic spatial resolution as a function of high voltage. Parameters adjusted are threshold and type of data (cosmic ray or $\bar{p}p$ data).

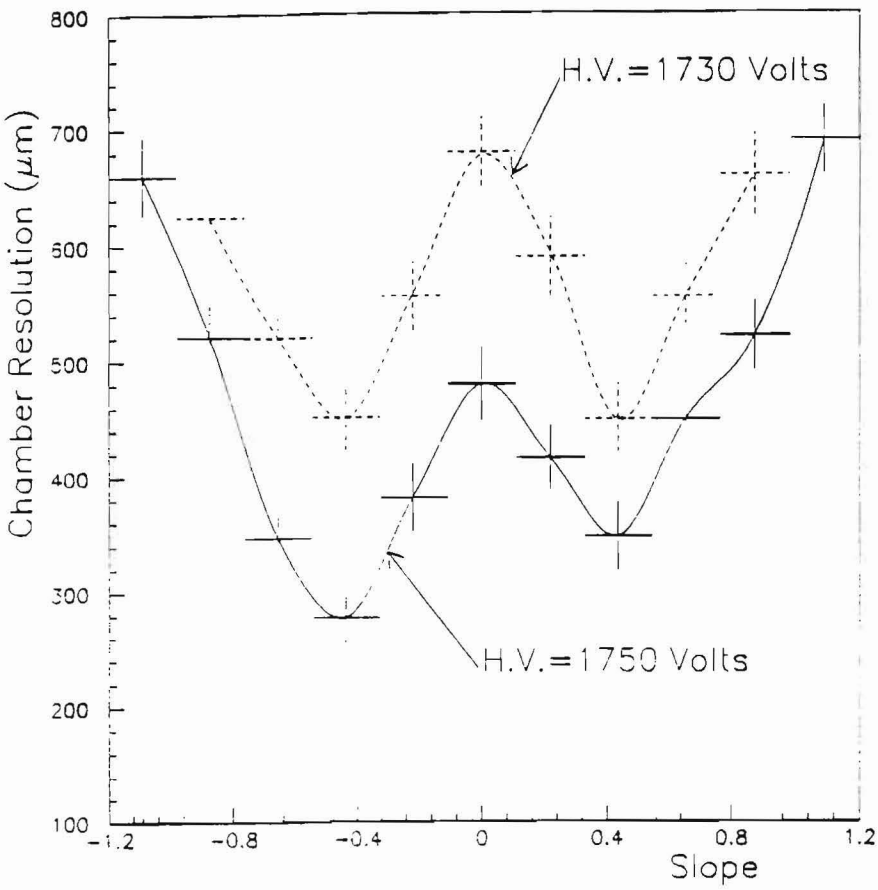

Figure 2.14: Z-chamber track resolution as a function of the track slope with respect to the x-axis for 1988 (H.V. 1750 volts) and 1989 (H.V. 1730 volts) data.

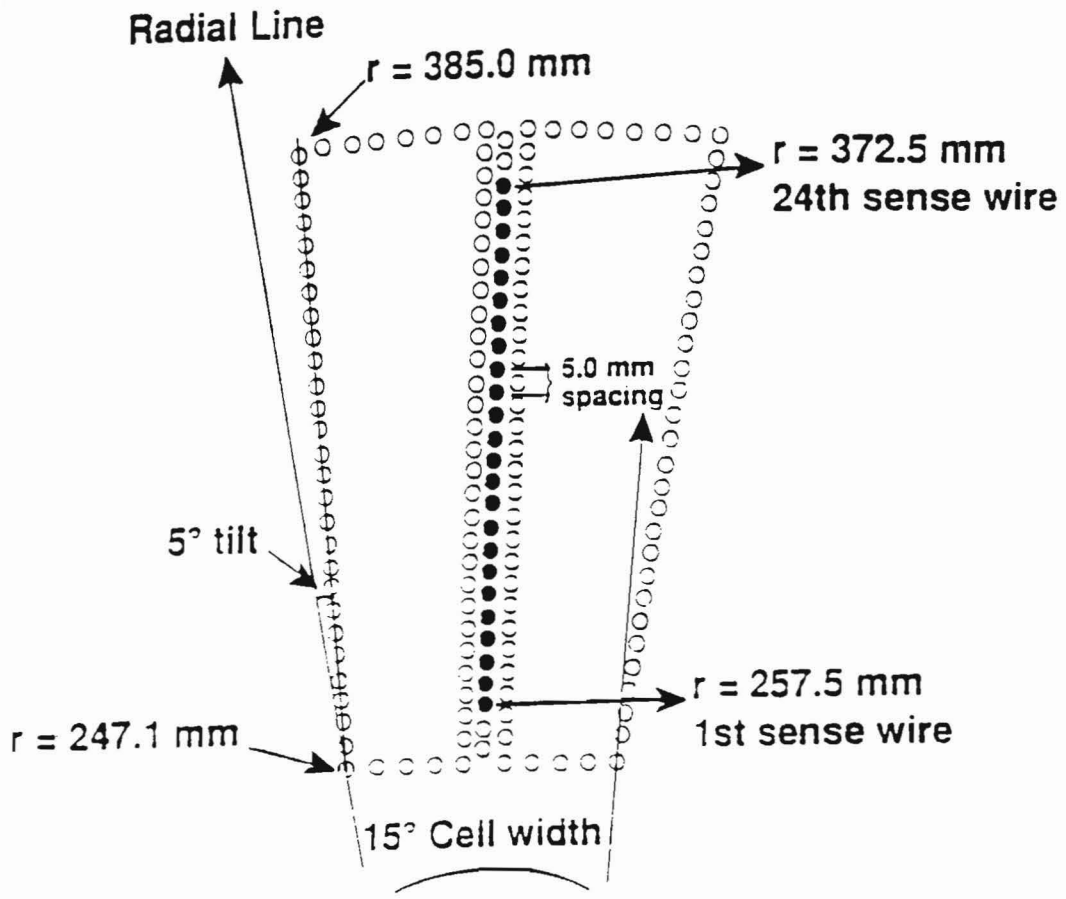

Figure 2.15: Layout for one of the 24 15^0 drift cells.

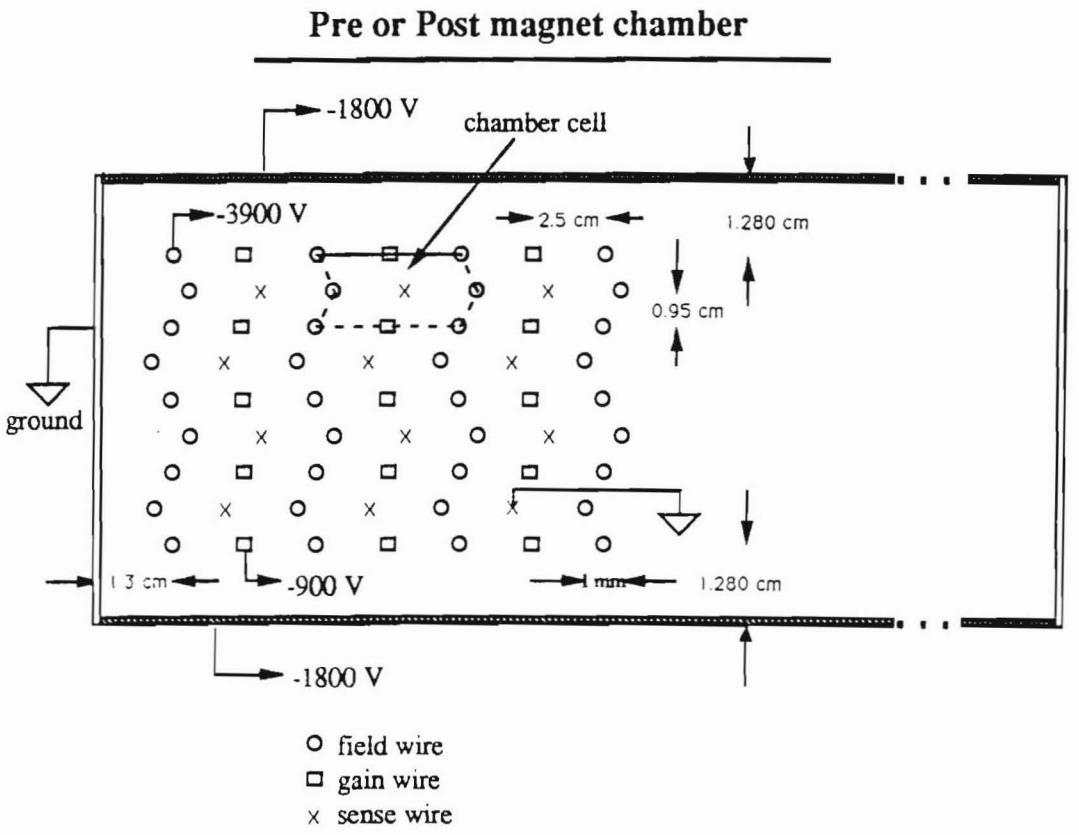

Figure 2.16: Layout of four cells (one cell per plane) in the pre- or post-magnet chamber.

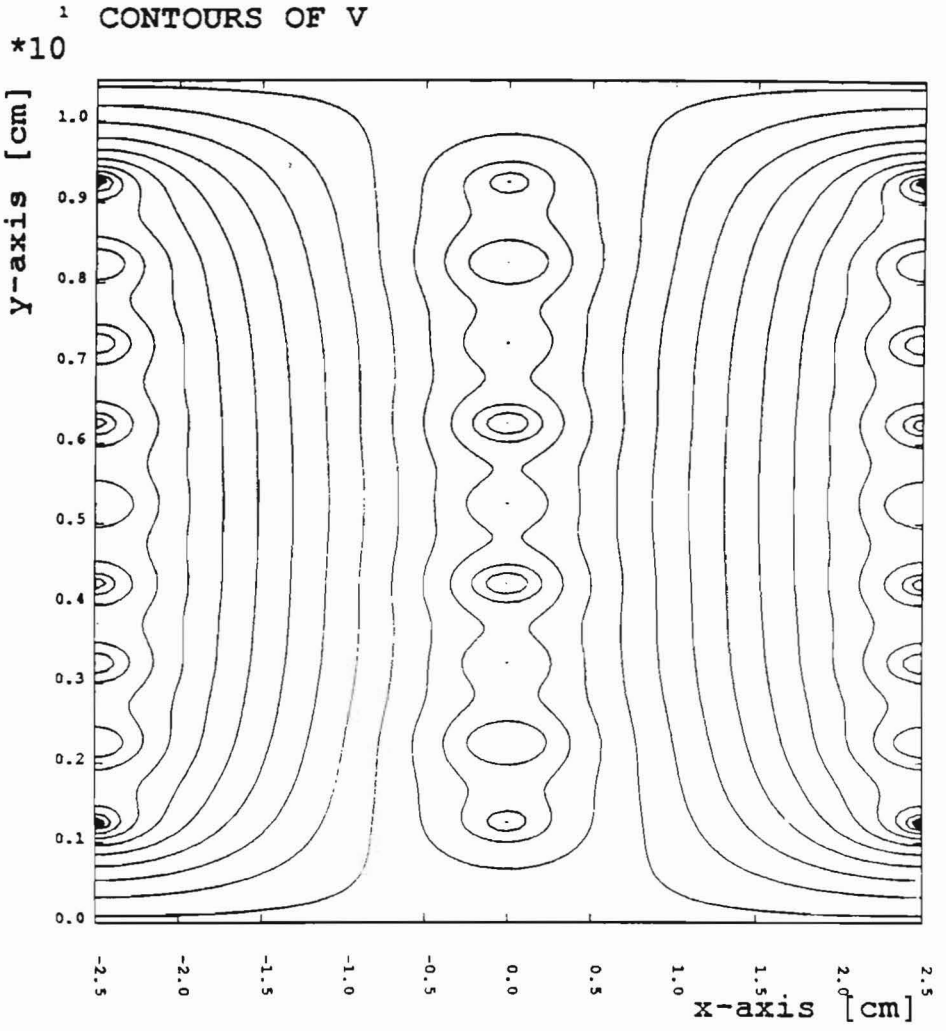

Figure 2.17: Equipotential field map with the sense wires at 0 volts, field wires at -3900 volts, guard wires at -900 volts and window planes at -1800 volts. The equipotentials are separated by 150 volts from -3800 to -800 volts. The four sense wires are at (0,2), (0,4), (0,6), (0,8). The windows are at y=0 cm and y=10 cm.

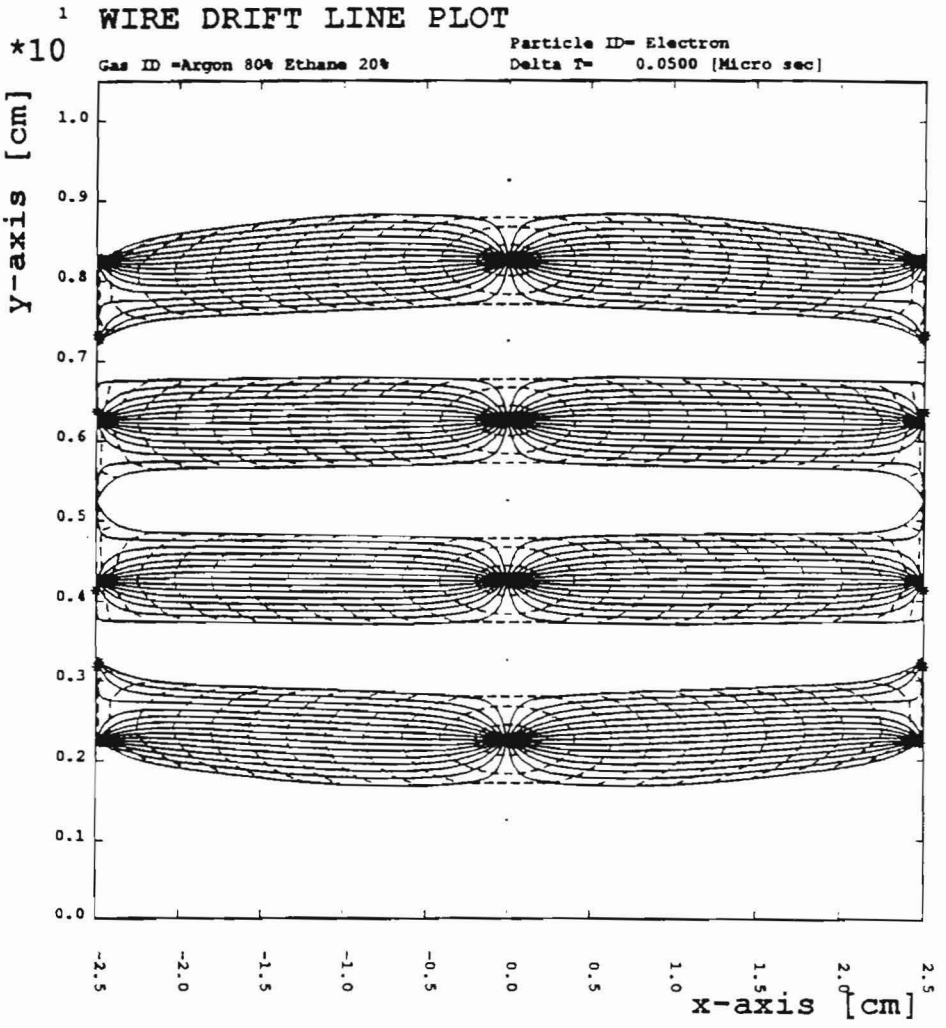

Figure 2.18: Electric field map and isochrone lines. The isochrone lines are separated by 50 ns and plotted up to 500 ns.

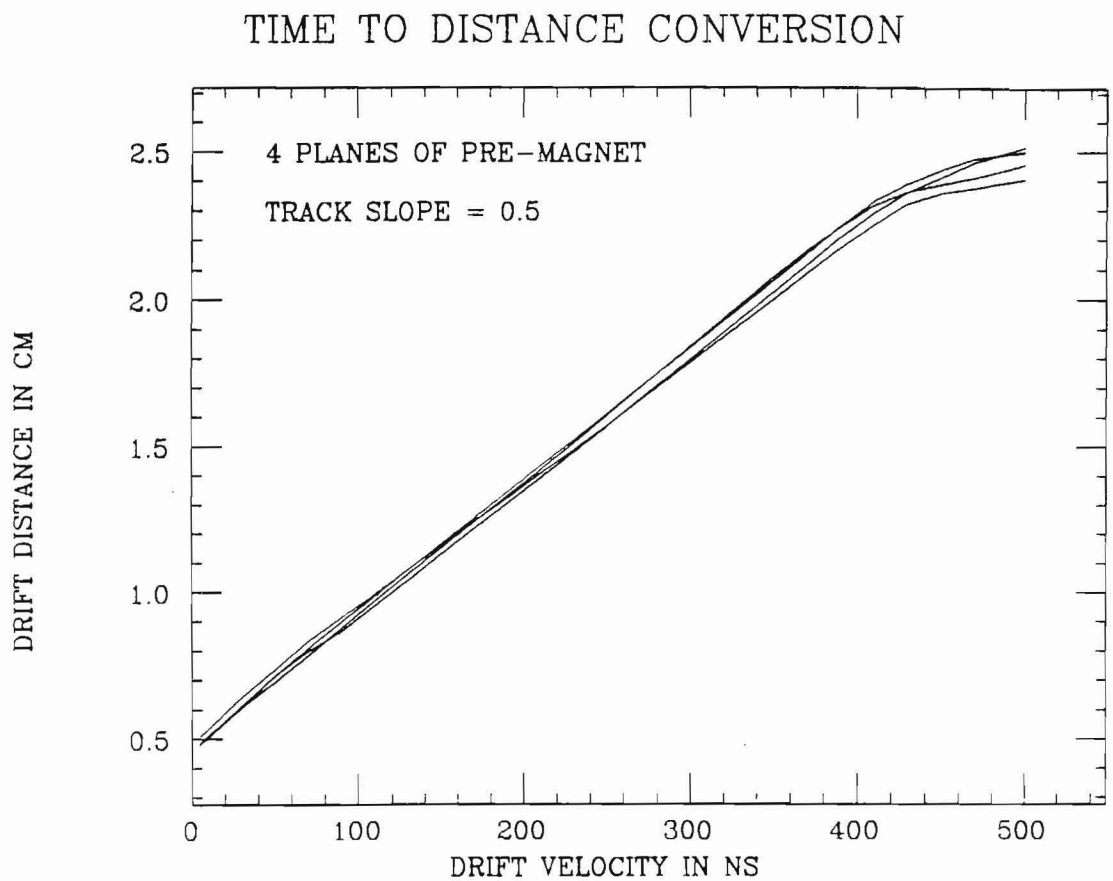

Figure 2.19: Time to distance conversion for the four pre-magnet chamber planes for a track slope of 0.5.

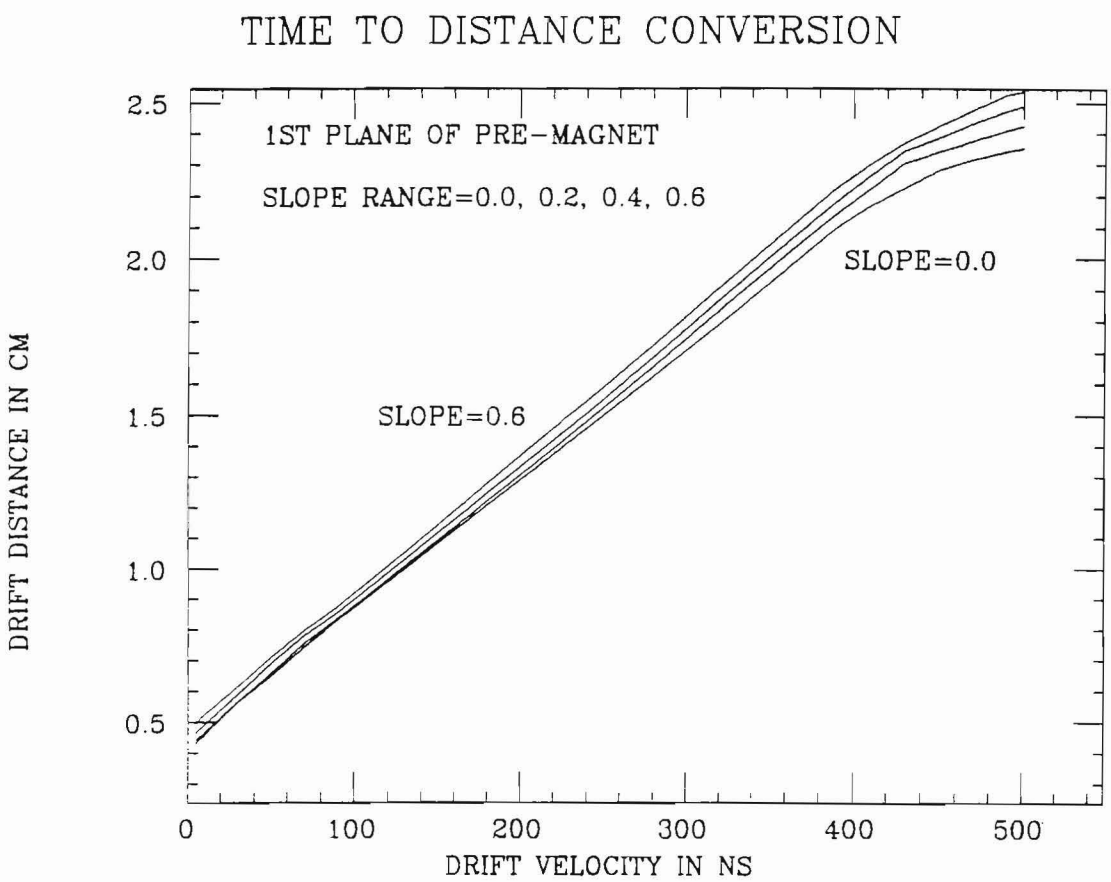

Figure 2.20: Time to distance conversion for the first pre-magnet chamber plane for a track slope range of 0.0-0.5.

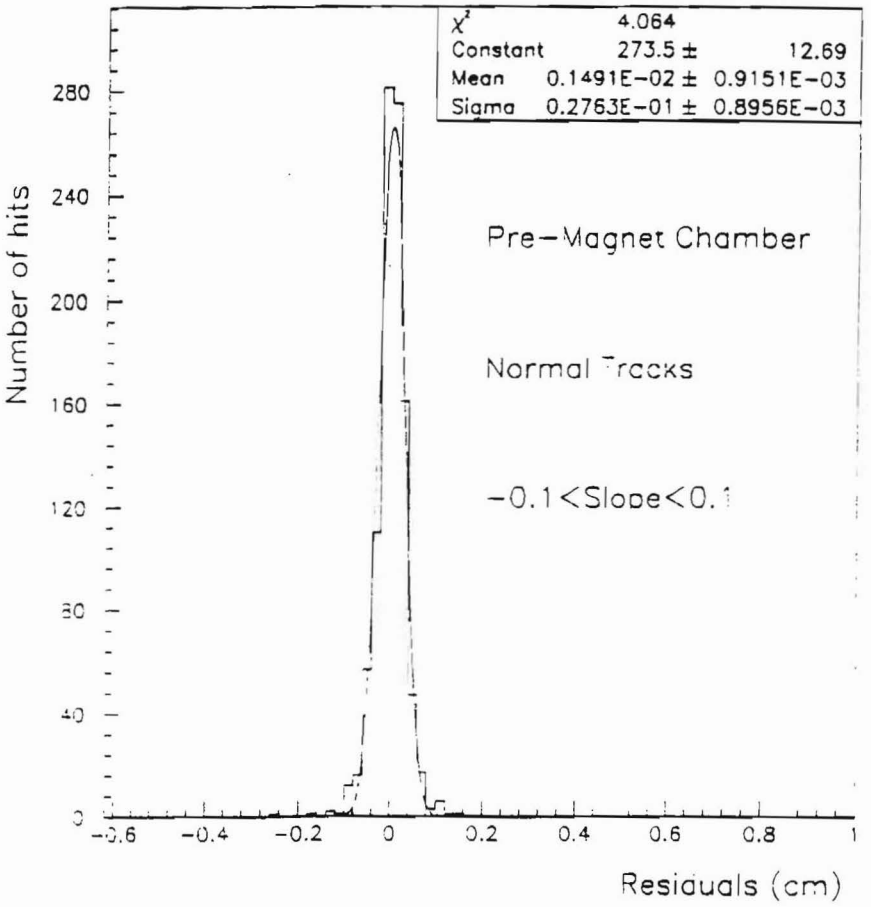

Figure 2.21: Measured pre-magnet residuals for normal tracks.

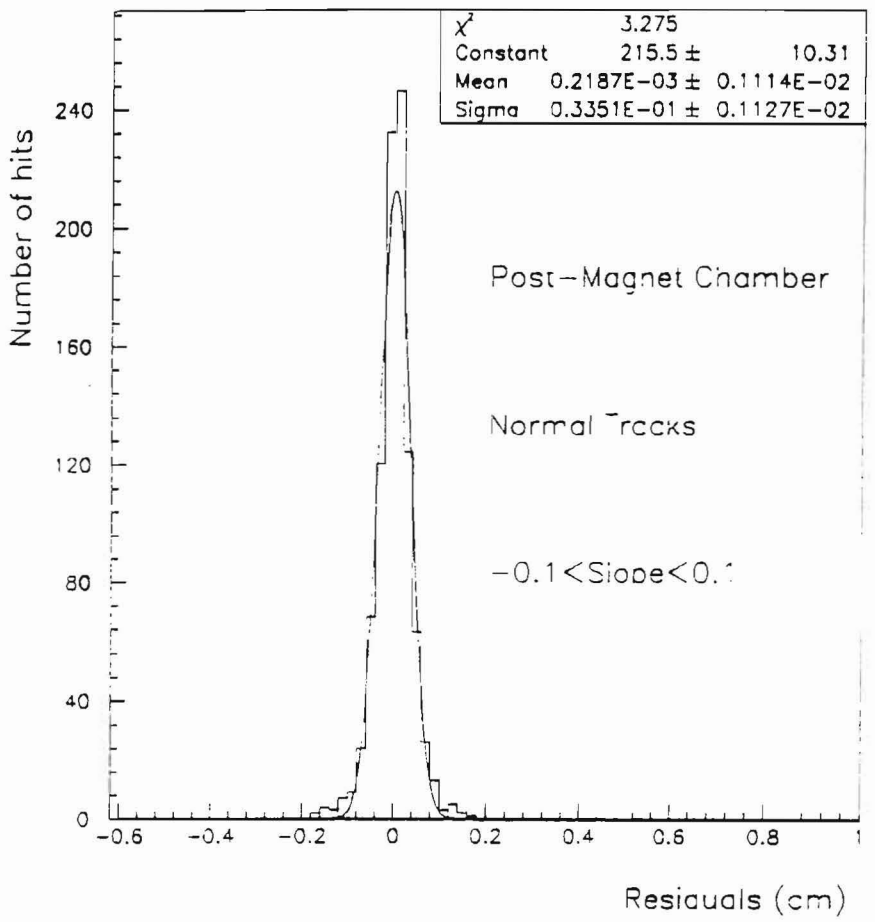

Figure 2.22: Measured post-magnet residuals for normal tracks.

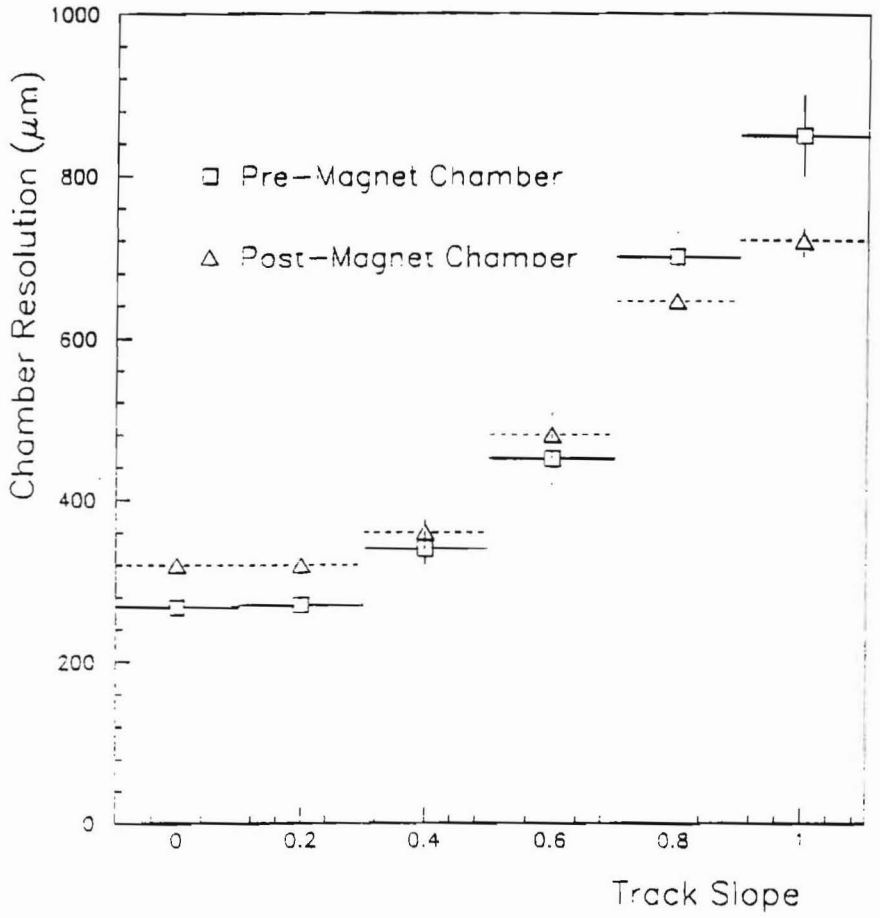

Figure 2.23: Pre- and post-magnet chamber hit resolution as a function of the track slope.

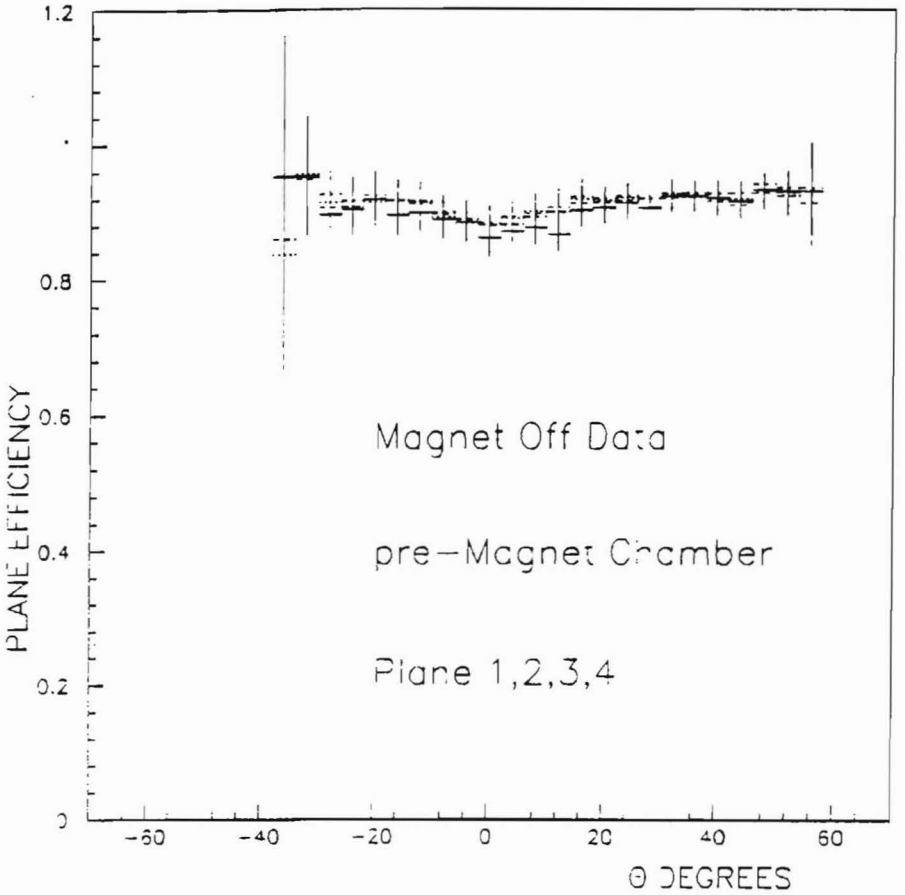

Figure 2.24: Measured pre-magnet chamber efficiency, $\epsilon^{meas.}$, as a function of θ for four planes of the pre-magnet chamber.

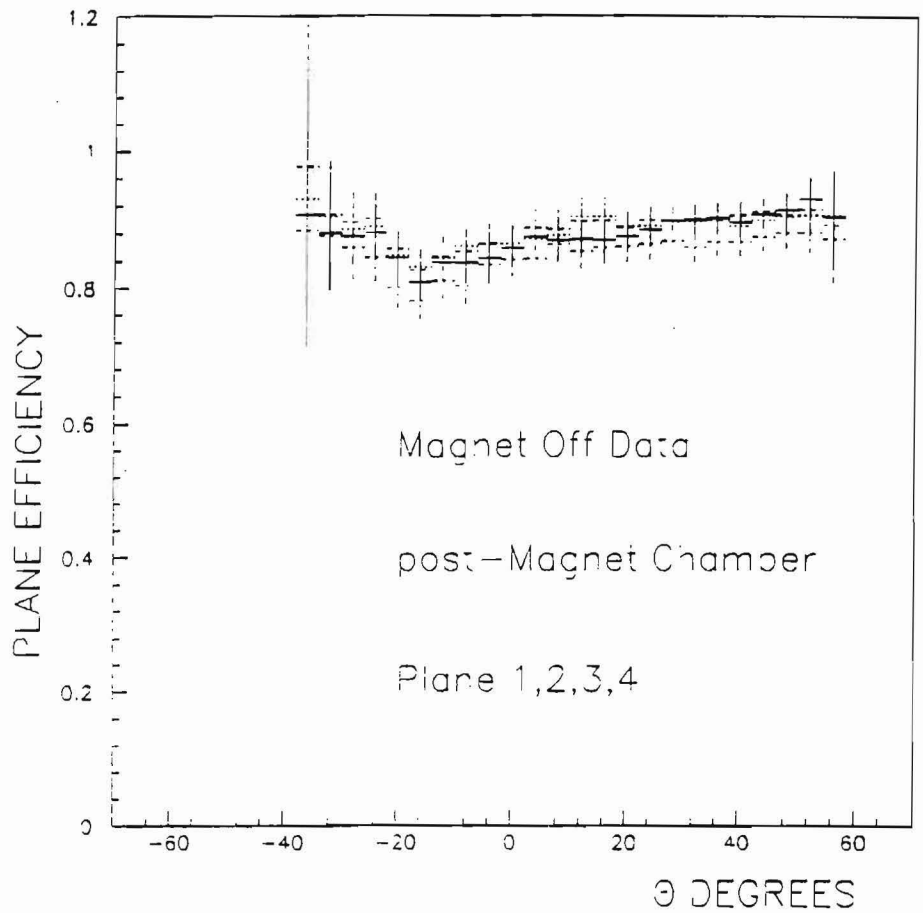

Figure 2.25: Measured post-magnet chamber efficiency, $\epsilon^{meas.}$, as a function of θ for four planes of the post-magnet chamber.

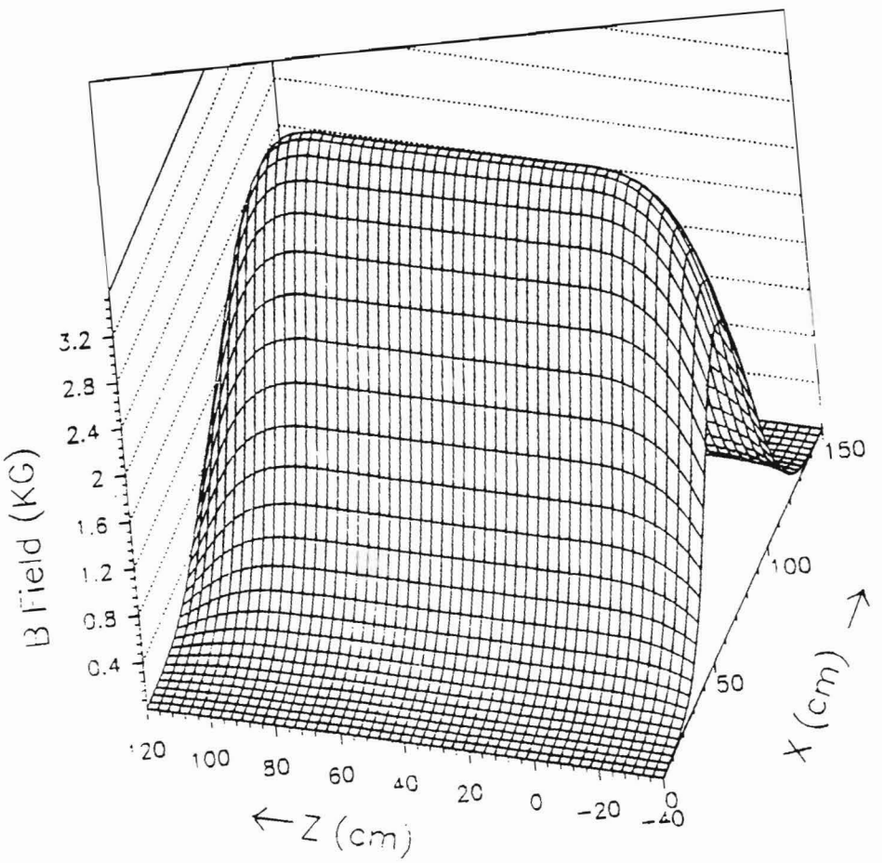

Figure 2.26: Calculated magnetic field, $B_y(x,z)$, at the center of the magnet y=15 cm.

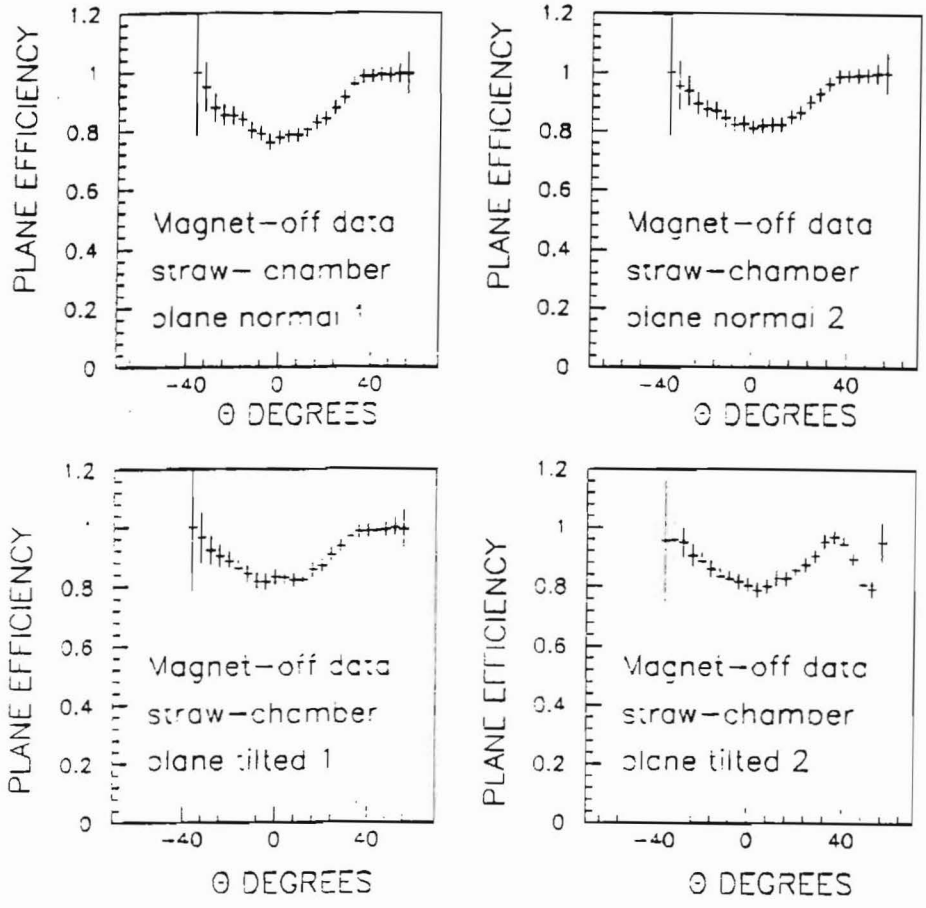

Figure 2.27: Straw chamber measured efficiency as a function of the angle, θ, defined in the text.

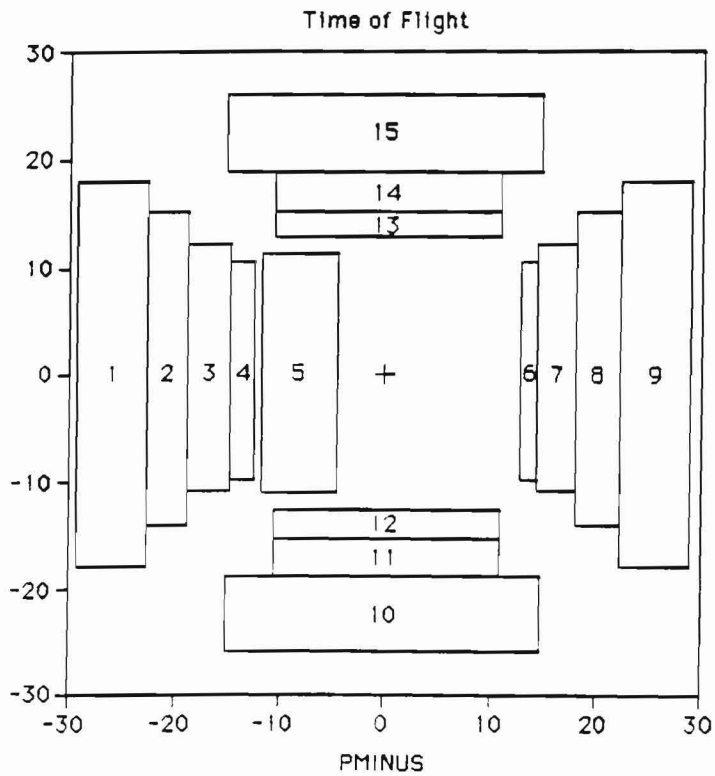

Figure 2.28: Layout of the trigger counters TOF_p and $TOF_{\bar{p}}$.

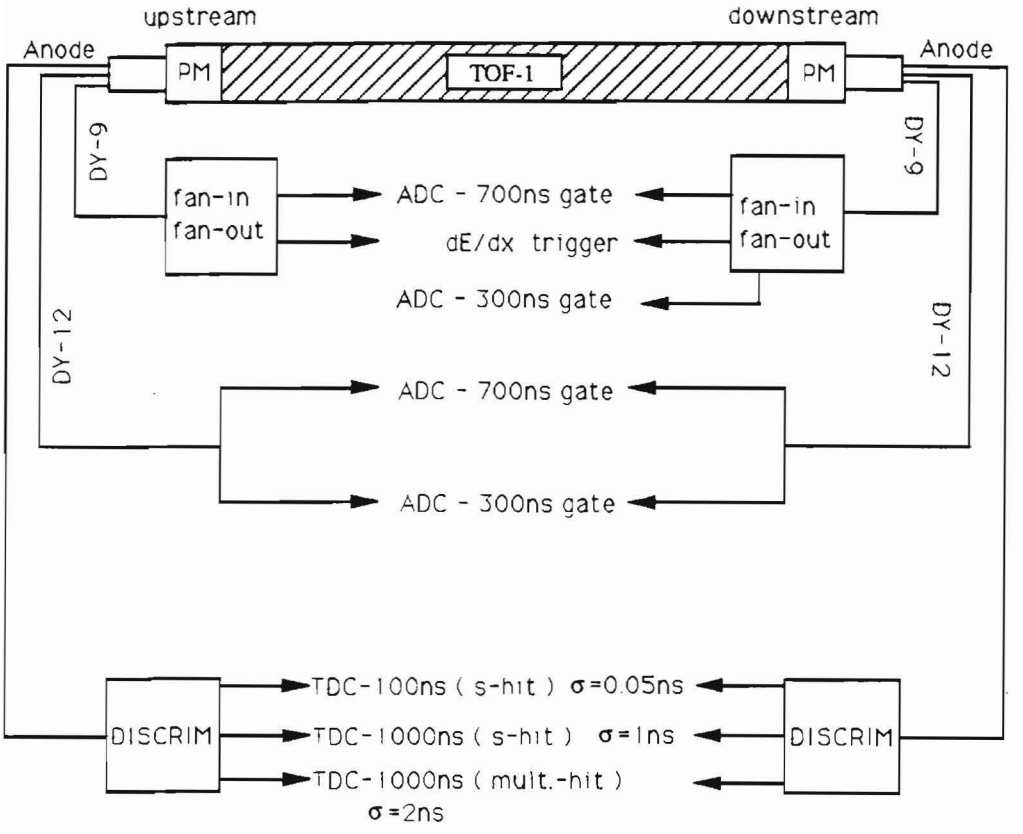

Figure 2.29: ADC and TDC configuration of the TOF_1 system.

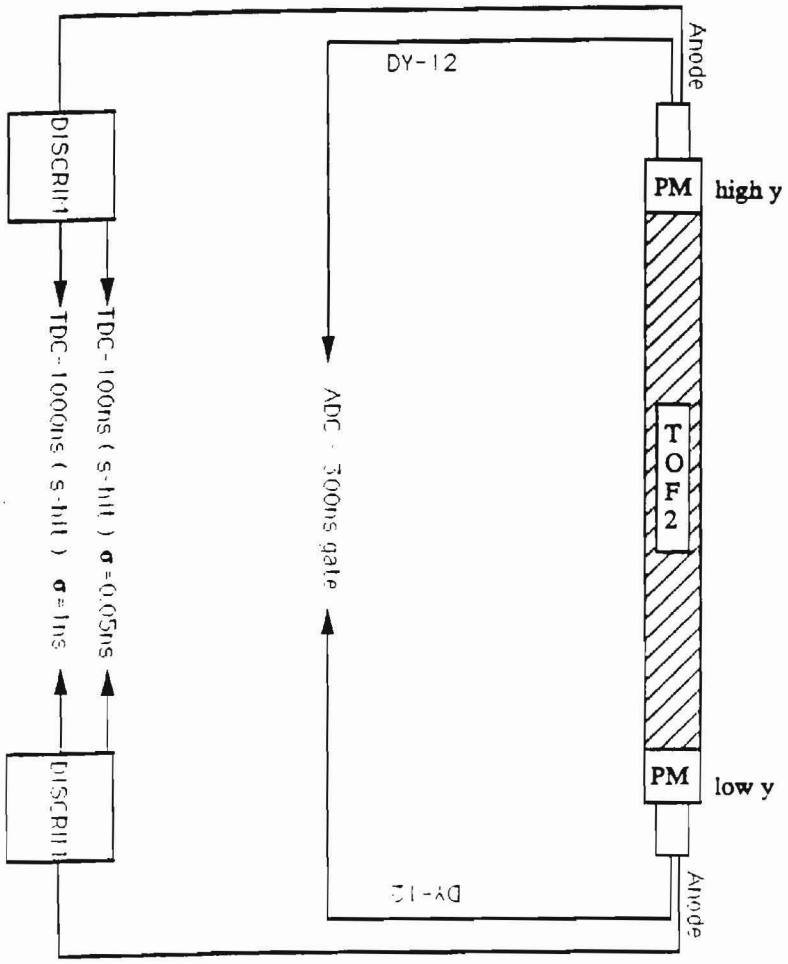

Figure 2.30: ADC and TDC configuration of the TOF_2 system.

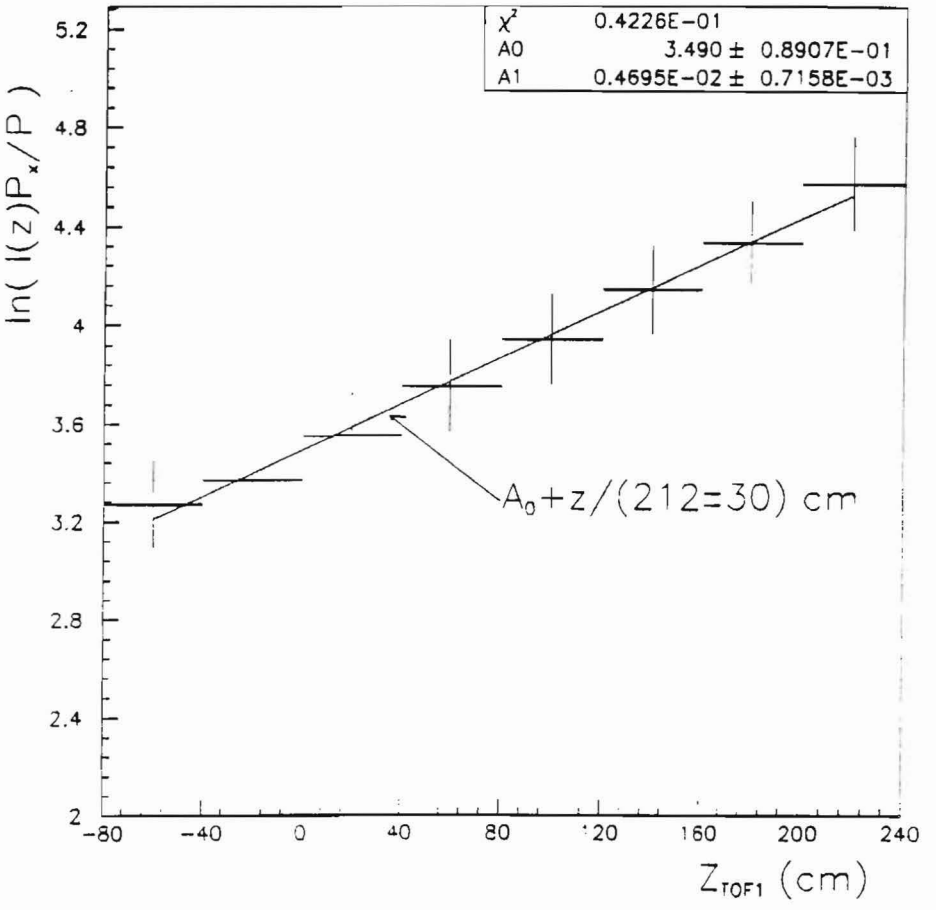

Figure 2.31: Measured attenuation length, λ, of counter number 5 of the TOF_1 system.

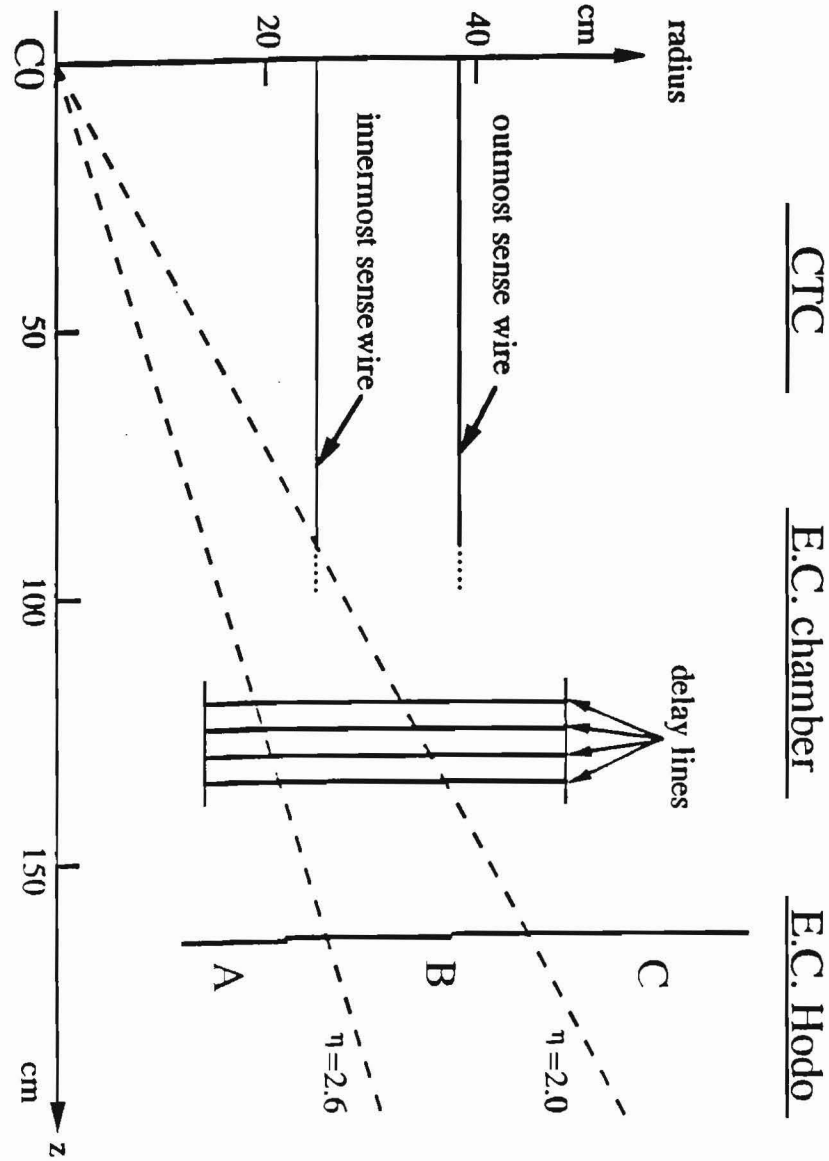

Figure 2.32: Cross section through C0 along the beam line. The CTC, downstream endcap chamber, and the endcap hodoscope are shown.

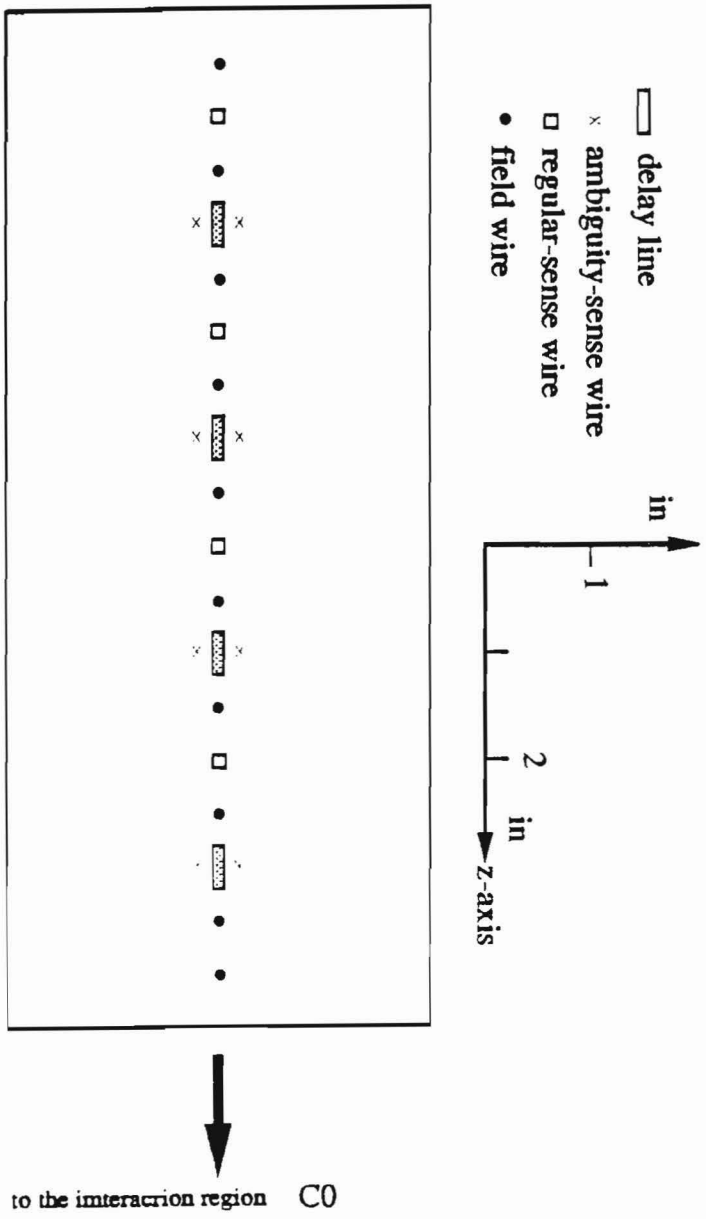

Figure 2.33: Top view of an endcap segment. Dimensions are to scale.

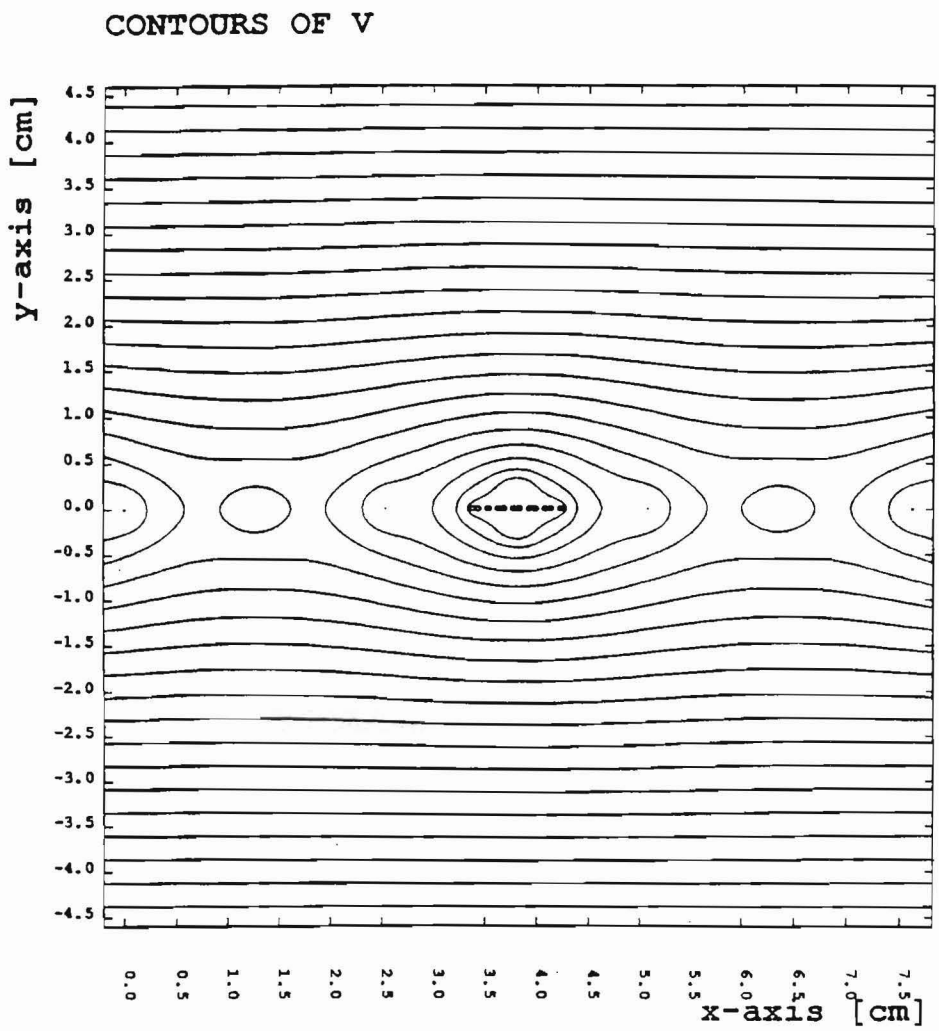

Figure 2.34: Equipotential lines of an endcap delay line drift chamber cell for every 100 volts from -4000 volts to 1300 volts.

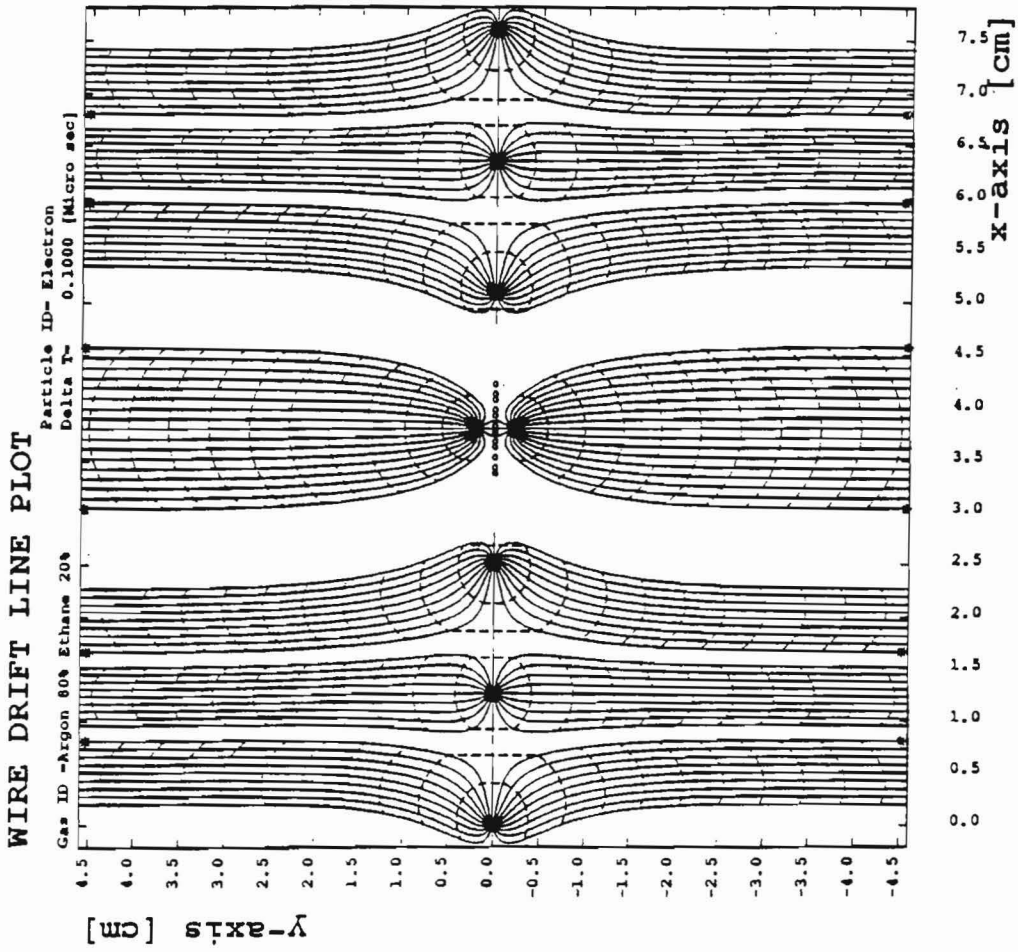

Figure 2.35: Isochrones and drift lines of endcap delay line drift chamber cell. The isochrones were plotted every 100 ns.

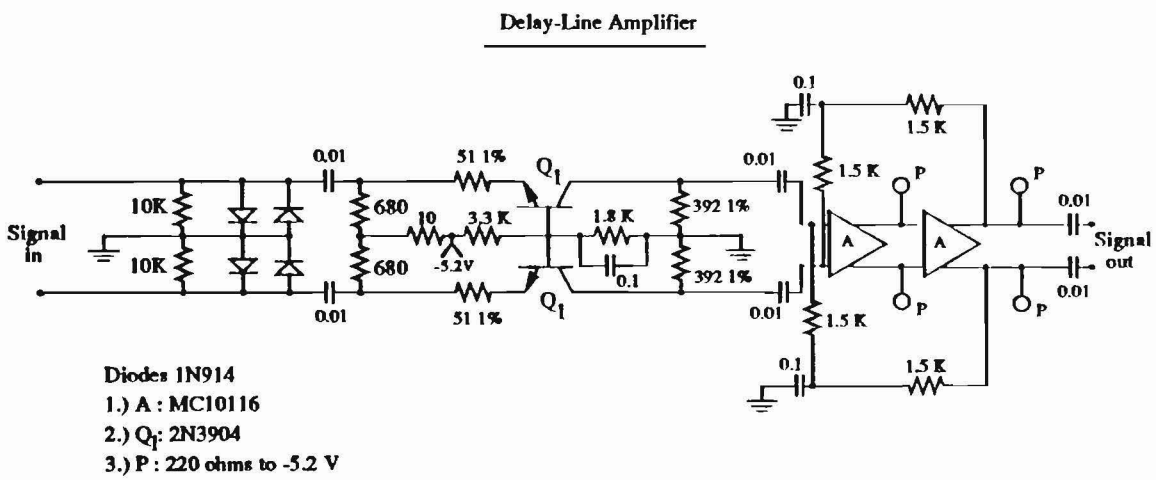

Figure 2.36: Delay line endcap amplifier.

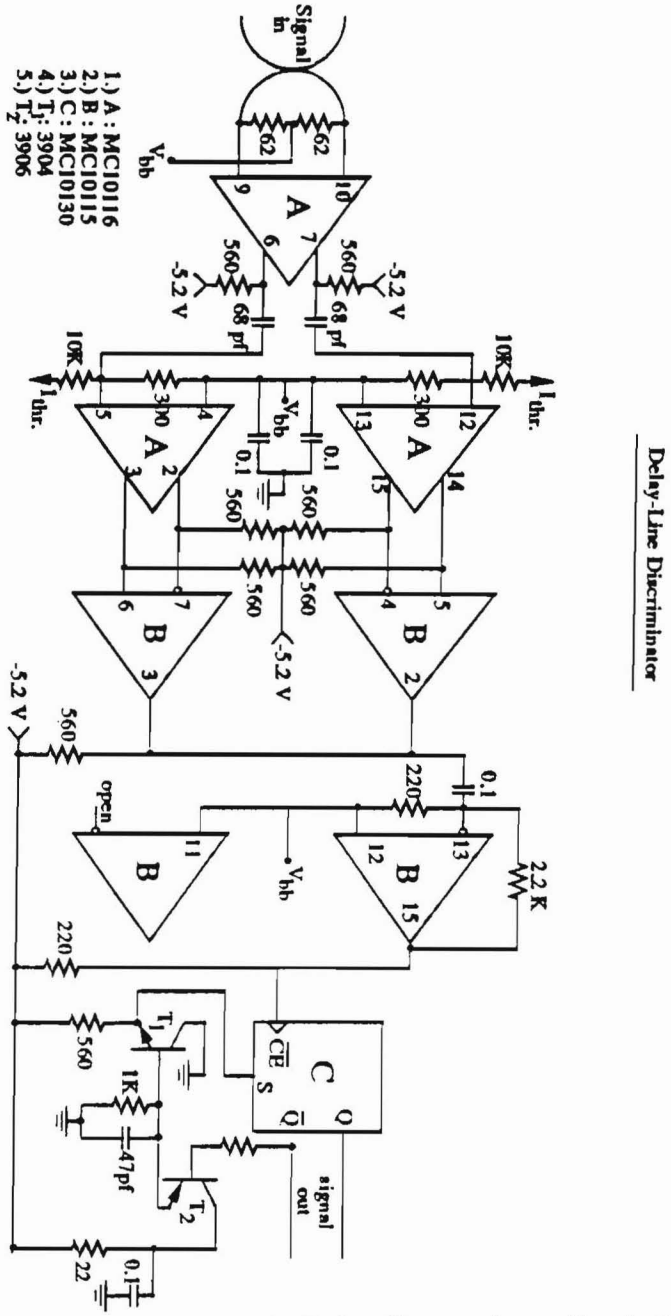

Figure 2.37: Delay line endcap discriminator.

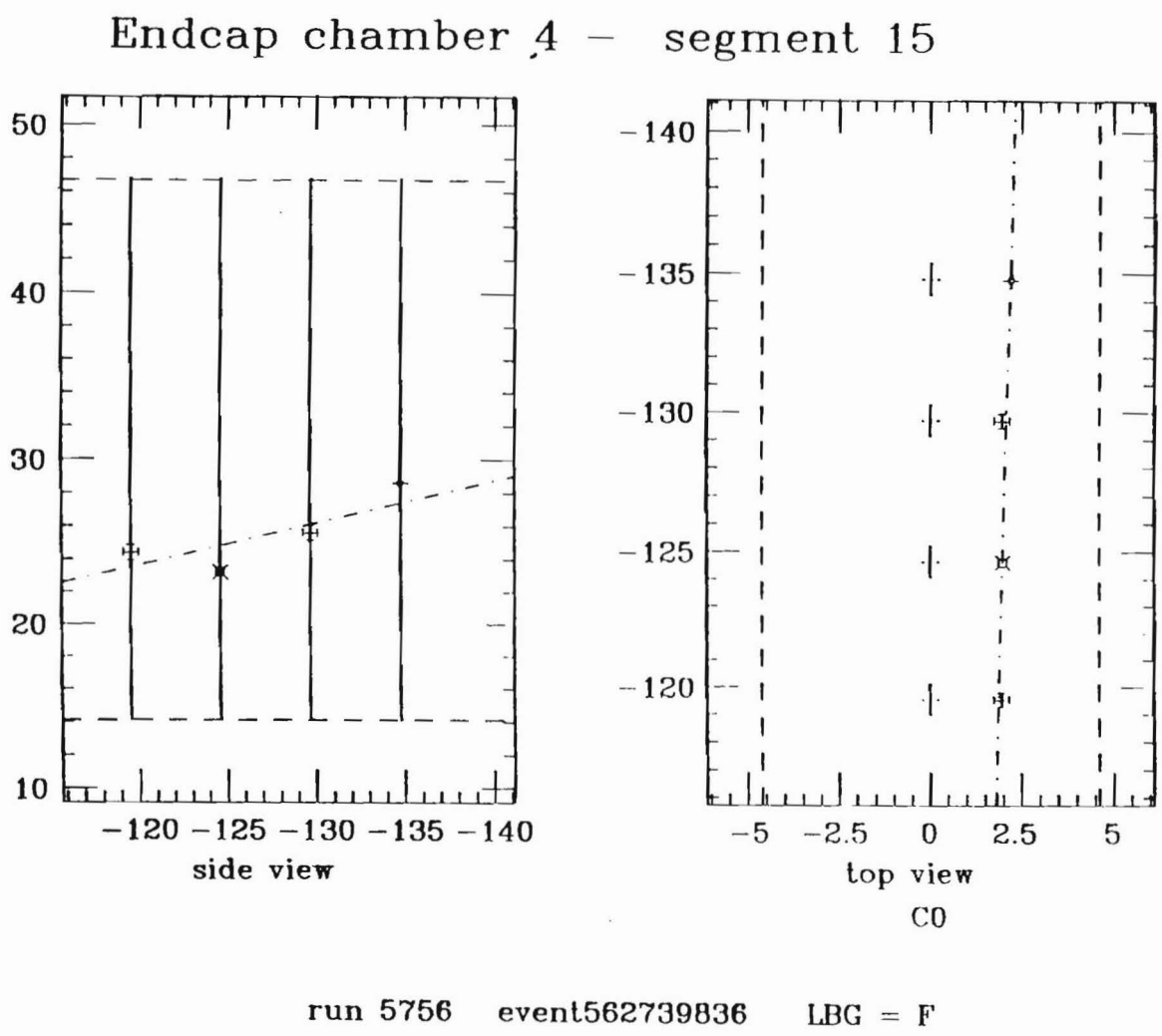

Figure 2.38: A typical track through an endcap segment.

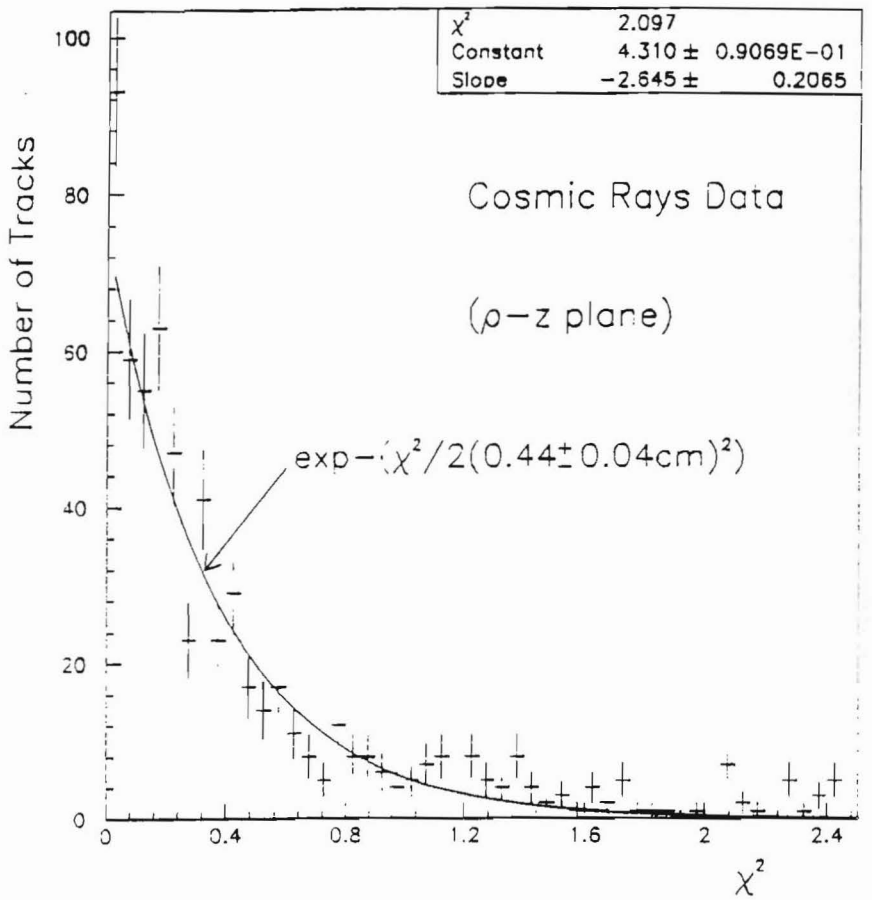

Figure 2.39: χ^2 distribution for tracks through four points in the endcap chamber using cosmic ray data.The straight line fit is with the drift distance ρ and z.

Chapter 3

Data Acquisition and Triggers

In this chapter the flow of the data from the various parts of the E735 detector will be discussed, and the different kinds of trigger logic schemes constructed in order to enhance the various physics objectives will be described.

During the 1988-1989 collider period 15×10^6 events were recorded on tape at center of mass energies of $\sqrt{s}$ = 0.3, 0.54, 1.0, and 1.8 TeV. The maximum luminosity of the accelerator at C0 was 1×10^{28} cm^{-2}sec^{-1} and the integrated luminosity [62] was 20 nb^{-1}.

3.1 Data Acquisition

If any of the various trigger requirements (will be discussed in next section) set by the physics goals were met, data collection from all E735 detector components began.

For online data taking and monitoring, two computers, a PDP 11/45 and a PDP 11/50, were used. The data were then transferred to a VAX 750 and from there to tape.

Data from the z-chamber, pre-magnet, post-magnet, and endcap chambers

were read through FASTBUS by the PDP-11/50 computer. The rest of the E735 detector components were read through CAMAC by the PDP-11/45 computer. The above processes were done simultaneously. When the PDP-11 readout was completed, the data were read out over a DR11-W communication line to the VAX 750, which was dedicated to data acquisition. Once the two parts (PDP-11/45 and PDP-11/50) of an event were recorded in the memory on the VAX 750, merging was achieved by comparing the event time clocks of these two event parts. Diagnostic routines provided information during a run to help spot hardware failures and various other problems. All triggered events were written to magnetic tape for later offline analysis.

Each tape contained one run with about 10,000 events. The recorded time of a typical "spectrometer trigger" tape (see next section) was 20-30 min. Our detector was inactive 20% of the time due to gating out the first 0.5 second of the 2.4 second main ring cycle. High voltage supplies for the chambers, trigger, and multiplicity hodoscopes were lowered for this period in order to avoid damage from high doses of radiation associated with the Main Ring proton injection.

3.2 Triggers

The trigger scheme was designed by taking into account the physics to be studied as well as the individual detector components. A bunch crossing occurred every 3.5 μs. This long time interval between the bunch crossings can be used for the trigger logic. In principle, new information becomes available for each bunch crossing and hardware logic must determine whether the event is to be accepted

or rejected. If the event is rejected all the logic elements are reset to prepare for the next bunch crossing.

In order for an event to get recorded onto tape, it had to satisfy a type of trigger based on the trigger hodoscope (TOF_p, $TOF_{\bar{p}}$) or the TOF_1 counters, or the pre and post-magnet chambers. A review of the different types of triggers will be given in the following sections.

3.2.1 $T0$ Trigger

The $T0$ trigger, the most basic trigger used in the E735 experiment, was used to study unbiased interactions between protons and antiprotons. This trigger occurred whenever a main proton bunch and a main antiproton bunch crossed the C0 interaction region. The signal produced by this beam crossing (refered to as $T0$) was provided by the Tevatron Beam Synchronous clock (TBS). This T0 signal generated the appropriate TDC start, ADC gates, FC (fast clear) signals, etc. for all detector components.

3.2.2 PT Trigger

The trigger hodoscopes (TOF_p, $TOF_{\bar{p}}$) were responsible for this trigger. An event was recorded as a PT trigger if hits were detected in both trigger hodoscopes were in coincidence with the beam crossing signal $T0$ under the application of the following vetos:

- The ETV (Early Time Veto) removes events in which the TOF_p or $TOF_{\bar{p}}$ trigger hodoscope had a counter hit before the bunch crossing T0. This

veto excludes background events that occurred before the proper trigger hodoscope time by the main bunch interacting either with gas particles inside the beam pipe or with beam satellites (± 20 nsec either side of the main bunch).

- The SBG (Satellite Beam Gas) veto removes events in which TOF_p was hit 14 ns before the $TOF_{\bar{p}}$ trigger hodoscope. (The time-of-flight difference of TOF_p and $TOF_{\bar{p}}$ was 14 ns.). This veto excludes events resulting from the trailing satellite part of the beam interacting before reaching the trigger array.

These events constitute our "minimum-bias" sample. In order to avoid beam-gas interactions (between the proton beam and a molecule inside the beam pipe or the wall of the the beam pipe) in low luminosity events, the number of $TOF_{\bar{p}}$ hits had to be greater than 1 ($TOF_{\bar{p}} > 1$). This trigger was called a standard trigger (ST). High multiplicity events were enhanced with an online trigger processor which scaled events in different multiplicity regions. Some data were taken with the magnet turned off in order to study off-line chamber calibration, resolution, etc. Furthermore, some data were collected with the magnet in its opposite polarity in order to study possible acceptance asymmetry for positive and negative particles.

3.2.3 TOF_1 Trigger

In order to insure one or more tracks in the spectrometer, a TOF_1 trigger was imposed. This required at least one hit in the seven TOF_1 scintillator counters. The TOF_1 trigger was used together with the PT trigger. Many times a hit in

the TOF_1 counter was not due to a real track in the spectrometer, but rather was due to the electronic noise in the TOF_1 system. In order to enhance the number of events with one or more tracks in the spectrometer, a trigger based in the pre- and post-magnet chambers was built, called a spectrometer trigger. It will be described in the next section.

3.2.4 Spectrometer Trigger

The spectrometer trigger formed on from charged tracks traversing the drift chambers. The only components used for this trigger were the pre- and post-magnet chambers. The purpose of this trigger was to take a large percentage of events with one or more tracks in the spectrometer arm in order to increase the statistics of the two-track events for Bose-Einstein correlation or resonance studies, like Λ's, K^0's, etc.

The enhancement of the multiple track events in the spectrometer was obtained by requiring that at least three out of a possible four planes in each magnet chamber record one or more hits. This was the one-track spectrometer trigger. The spectrometer trigger idea is shown schematically in Figure 3.1.

A two-track spectrometer trigger was implemented by requiring two tracks in both the pre- and post-magnet chambers. A track in either the pre- or post-magnet chamber consisted in hits three of the four planes of the magnet chamber. Figure 3.2 shows the logic of the two-track spectrometer trigger. The two-track trigger was not used because it added too many events with background clutter.

The spectrometer trigger consists of the following:

- The Pre- and Post-magnet chambers (Section 2.3.4).
- The Current Summing Unit per chamber plane which sums up all contributions from the sense wires of a magnet chamber plane (Figures 3.3 and 3.4).
- The Gating Unit which enables the Current Summing Unit (Figures 3.3 and 3.5).
- The Discriminator Spectrometer Unit which discriminates the total current from the Current Summing Unit, thus providing information about the number of hits per plane, as shown in Figures 3.3 and 3.6.

3.2.5 dE/dx Trigger

The purpose of the ionization density trigger, or dE/dx trigger was to generate a signal which was proportional to the ionization density dE/dx produced from a single charged track which passed through one of the seven TOF_1 scintillator counters. The goal was to search for heavy ionization particles produced at the interaction point: ie. tritium (t), α, Helium (He^3), Helium (He^4), etc. since these particles have a relatively high dE/dx. For example, fast α particles have a $dE/dx = 4 \times minimum$, where $minimum$ is the ionization density of a MIP charged particle (minimum ionization energy for a particle of charge $1e$).

A signal was generated which was proportional to the ionization density dE/dx, seen for single charged tracks which pass through the scintillators. A trigger was generated when any of the seven scintillator signals exceeded a com-

mon threshold ($dE/dx = threshold$), where the threshold was set at about five times *minimum*. The attributes of the trigger were:

- The seven circuits (for each TOF_1 counter) were identical.
- A common OR at the end gave a NIM level trigger if any of the seven circuits indicated $dE/dx > threshold$.
- A produced particle passed through a scintillator at an angle which varied from about -20 degrees to 55 degrees relative to the normal of the scintillator plates and thus, $\cos\theta$ correction was formed ranging from 1.0 to 0.57. The light was also attenuated exponentially as it traveled each direction in the scintillator by as much as a factor of $e(= 2.72)$ over the 3 m length of the TOF_1.
- Each of the seven scintillators produced two signals (one from each end) called P_u (upstream side of the counter) and P_d (downstream side of the counter). Using these signals, the necessary $\cos\theta$ and exponential corrections were calculated in order to produce the best estimate of the actual ionization density, dE/dx, of the passing charged particle.
- The decision to determine whether $dE/dx > Threshold$ was carried out with about 10% accuracy for a threshold of five times *minimum* to clearly separate 4.0×, 5.0×, 6.0× *minimum*.
- The trigger was produced within 300 ns of pulse arrival.

The ionization density was derived using the upstream P_u and downstream P_d signals of a TOF_1 counter. Suppose a charged particle crosses a TOF_1 counter (with attenuation length λ at distance x_t) at a position z and with angle θ with respect to the x-axis (see Figure 3.7). The light produced by the charged particle is:

$$I = (\frac{dE}{dx})/\cos\theta. \tag{3.1}$$

The two signals P_u and P_d are given by:

$$P_u = G_u I e^{-(l+z)/\lambda} = G_u e^{-(l+z)/\lambda}(\frac{dE}{dx})/\cos\theta, \tag{3.2}$$

and

$$P_d = G_d I e^{-(m-z)/\lambda} = G_d e^{-(m-z)/\lambda}(\frac{dE}{dx})/\cos\theta, \tag{3.3}$$

respectively, where $l + m$ is the total length of a TOF_1 counter G_u and G_d are the gains of the upstream and downstream analog electronics systems, which are defined by the following equations:

$$G_u = \cos\theta_u, \tag{3.4}$$

and

$$G_d = \cos\theta_d, \tag{3.5}$$

where the θ_u and θ_d are the upstream and downstream angles, as shown in Figure 3.7. It was assumed that each pulse height was measured in units of the pulse height seen by the MIP particle passing at the expected angle next to the photocathode. By dividing P_u by P_d the z position and $\cos\theta$ correction factor can be derived. Namely:

$$z = (m - l - \lambda\ln(\frac{P_u G_d}{P_d G_u}))/2, \tag{3.6}$$

and the $\cos\theta$ correction term is given by:

$$\cos\theta = x_t/\sqrt{x_t^2 + z^2}. \tag{3.7}$$

By multiplying P_u by P_d the ionization density is:

$$dE/dx = \sqrt{P_u P_d \cos^2\theta e^{(l+m)/\lambda}/G_u G_d}. \tag{3.8}$$

Equation 3.8 gives an estimate of the produced ionization density as a function of the measured upstream, P_u, and downstream, P_d, signals.

The dE/dx trigger consists of:

- Seven TOF_1 scintillator counters. (Section 2.3.7.)
- Fourteen PMT's (photomultipliers). (Section 2.3.7.)
- Two NIM analog modules with 14 stretching or integrating modules. One integrator circuit is shown in Figure 3.8.
- Four NIM trigger modules with eight trigger circuits (used only seven circuits of the trigger modules) and a "control module". These trigger circuits were built by the U.W.-Madison PSL [63].

The P_u, P_d signals were passed to integrating modules in order to stretch the signal over a range of 0 to +2 Volts. This stretched signal was accepted by trigger modules via an internal series 50 Ω resistor and a parallel 40 pF capacitor to smooth any high frequency noise picked up on the cables between the integrator and the trigger module. Input signals above 2 volts were treated as 2 volts. Two 8 bit flash ADCs (ADC_u and ADC_d inside the trigger module)

measured the stretched P_u and P_d signals. After the flash ADCs, two subtractors obtained the difference between the flash ADC outputs before and after the pulse. They expressed the differences as 7 bit integers. The calculation of Equation 3.8 was done for all permutations of the above subtractor outputs and the results were stored in a ROM which gave a 7 bit output value which was proportional to dE/dx. An 8 bit comparison compared the ROM output with an 8 bit preset threshold.

Figures for Chapter 3

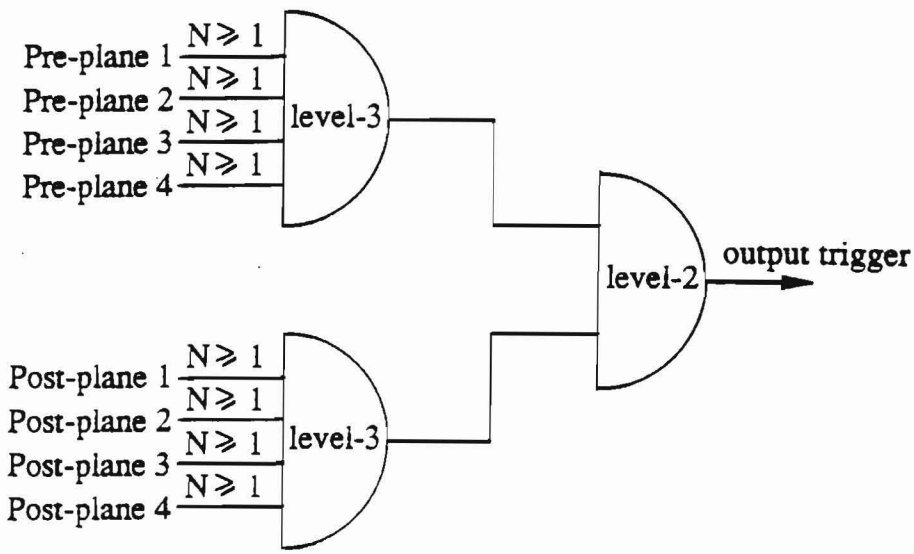

N : number of hits per plane

level-3 : output = 1 for any 3 inputs = 1

level-2 : output = 1 for any 2 inputs = 1

Figure 3.1: Spectrometer one-track trigger logic.

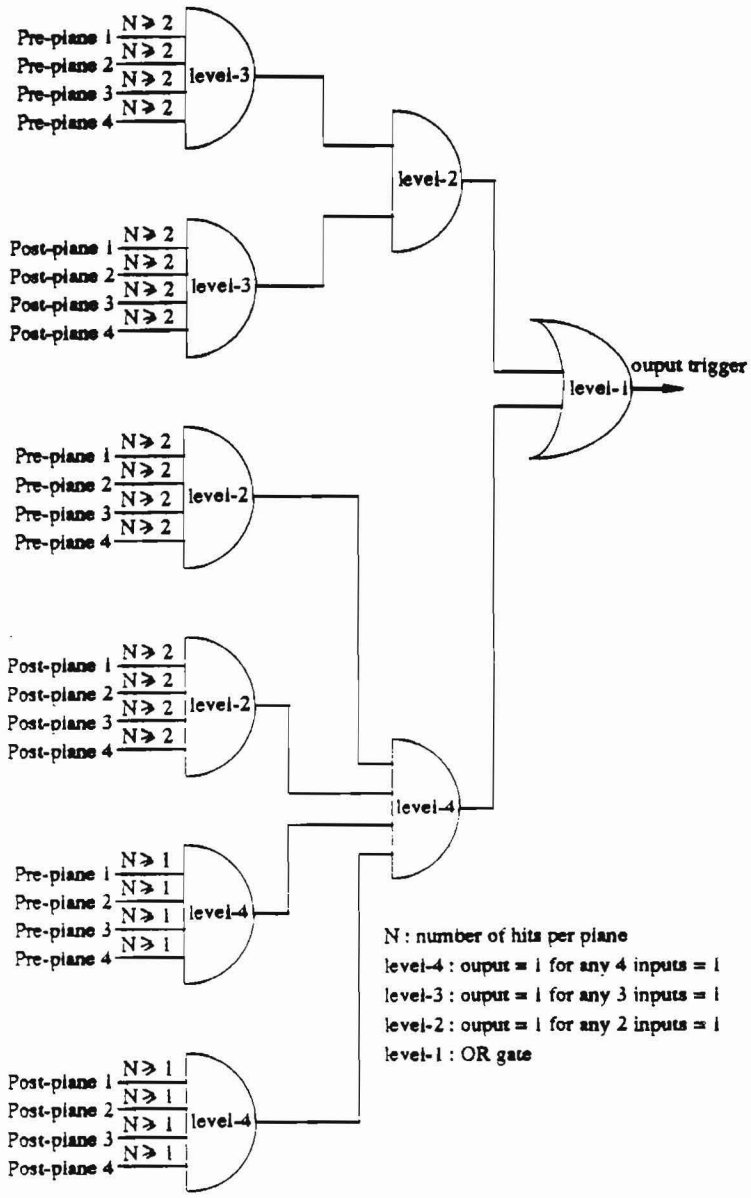

Figure 3.2: Spectrometer two-track trigger logic.

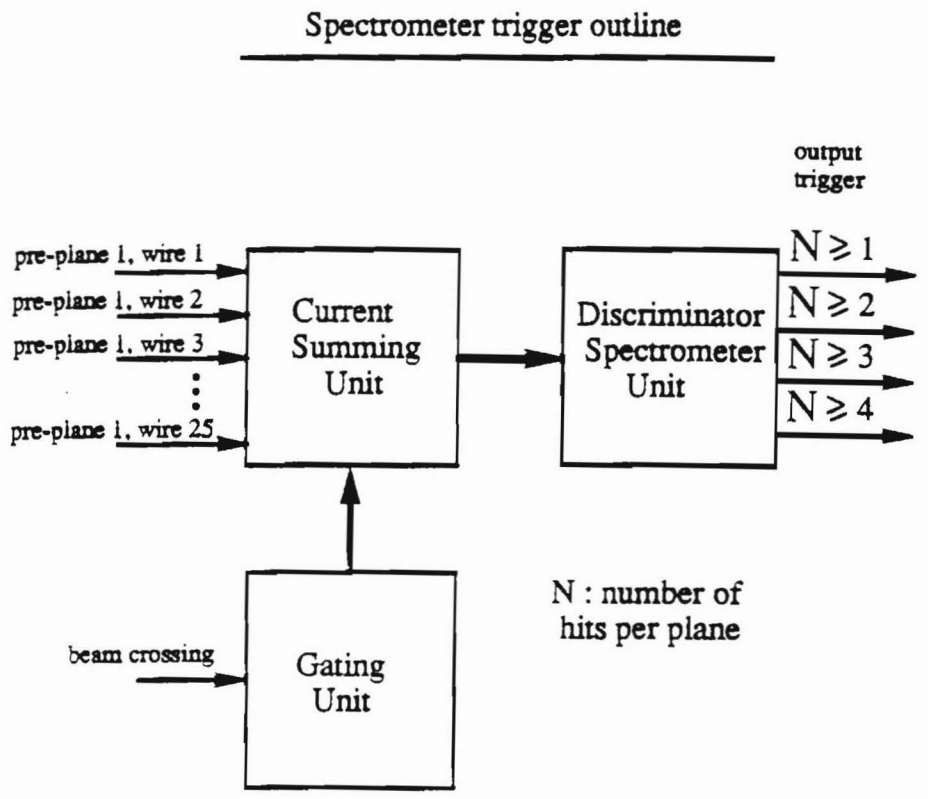

Figure 3.3: Spectrometer trigger outline.

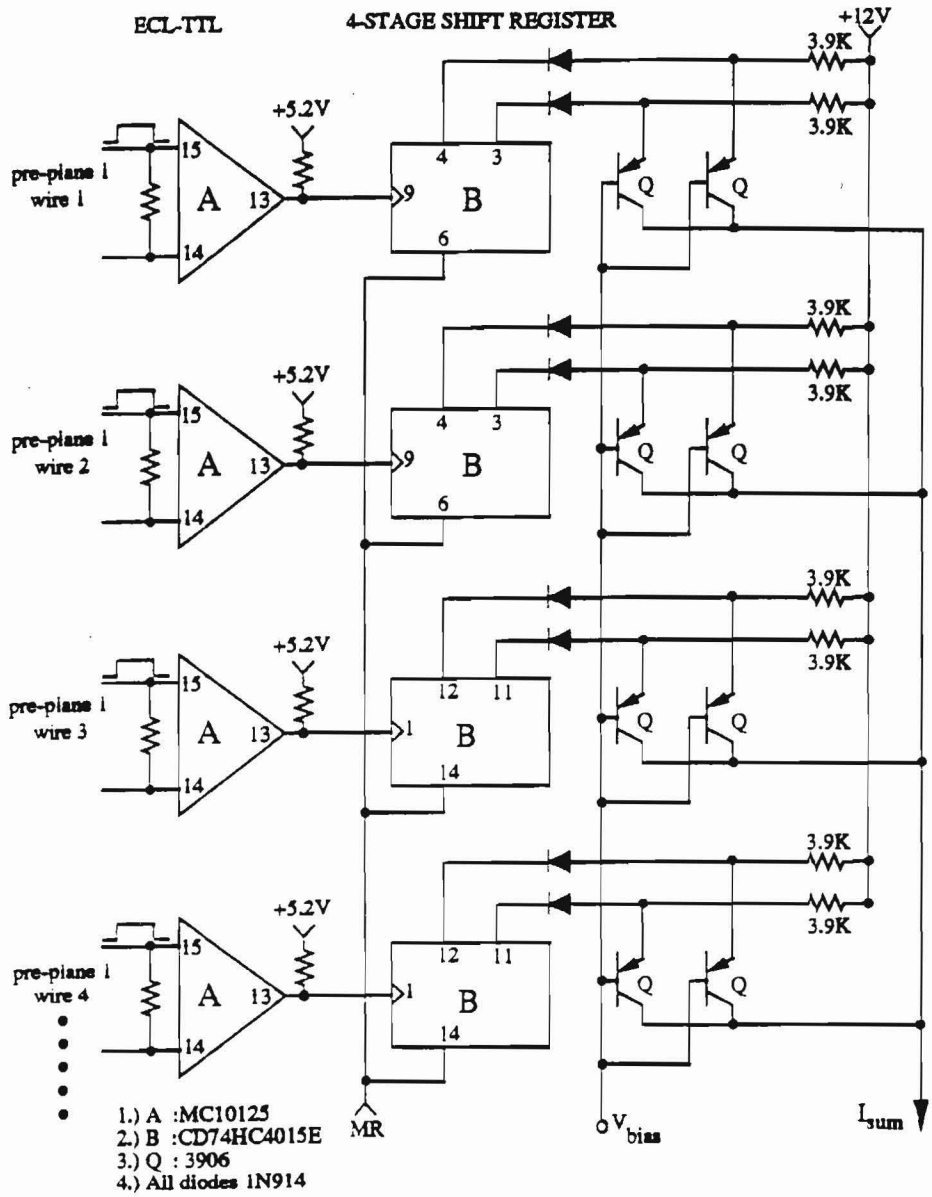

Figure 3.4: Current summing unit.

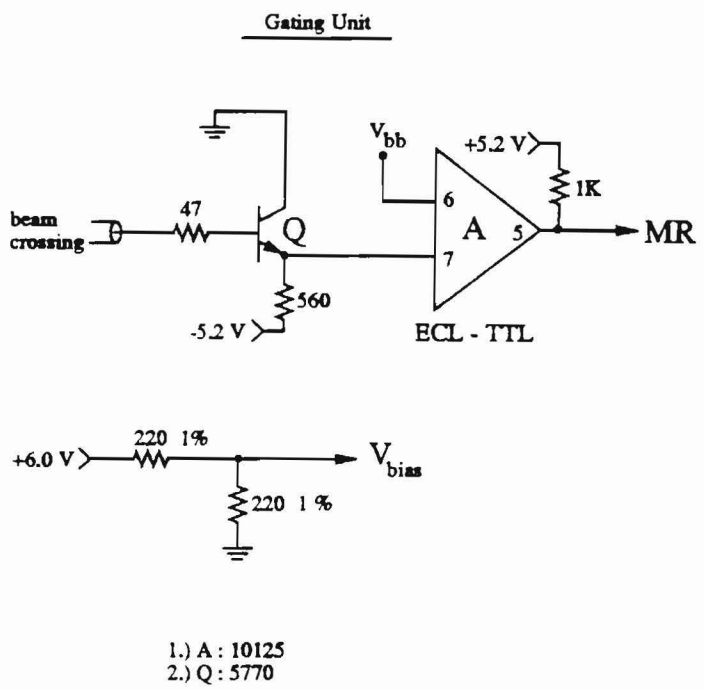

Figure 3.5: Gating unit for the spectrometer trigger.

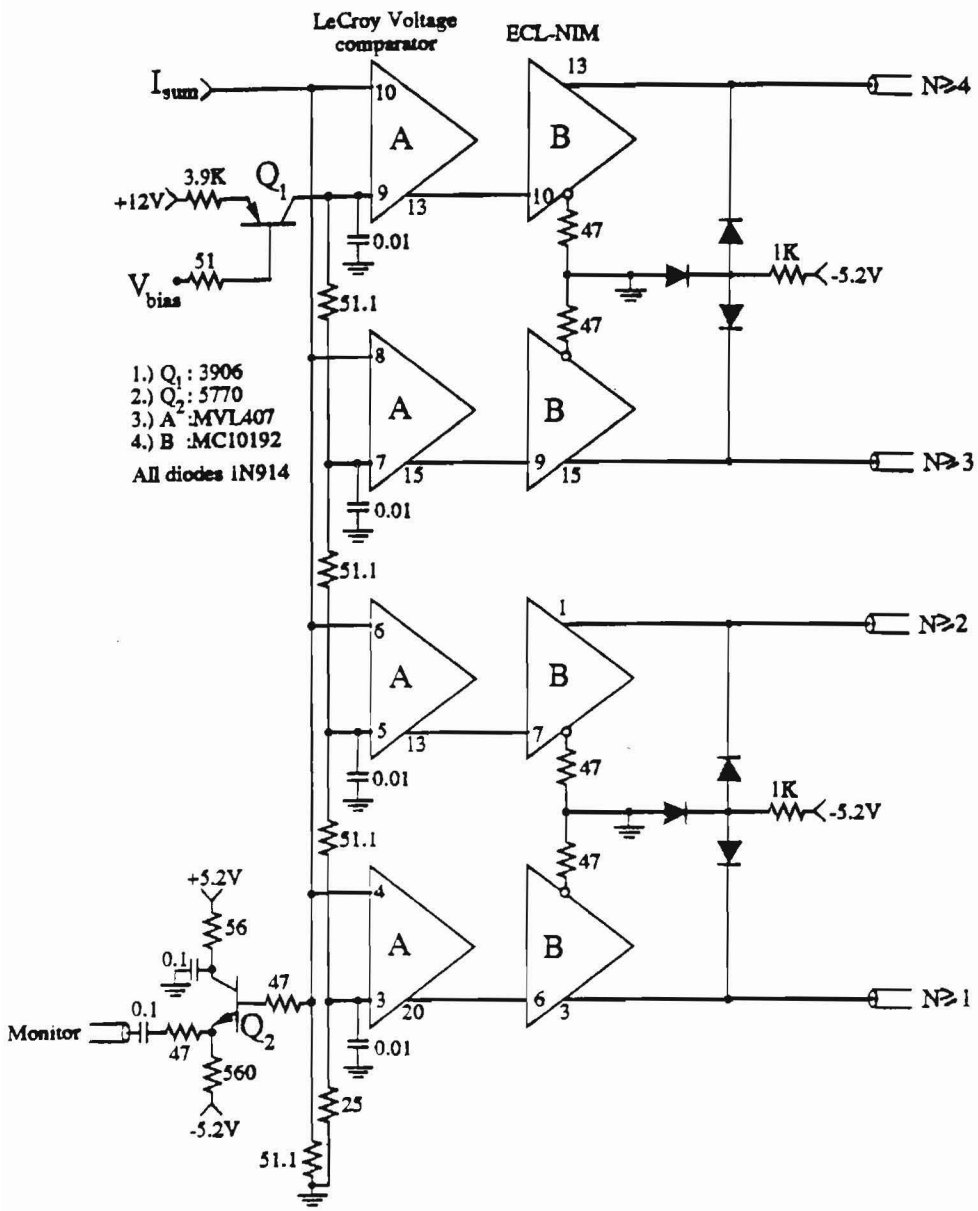

Figure 3.6: Discriminator spectrometer trigger.

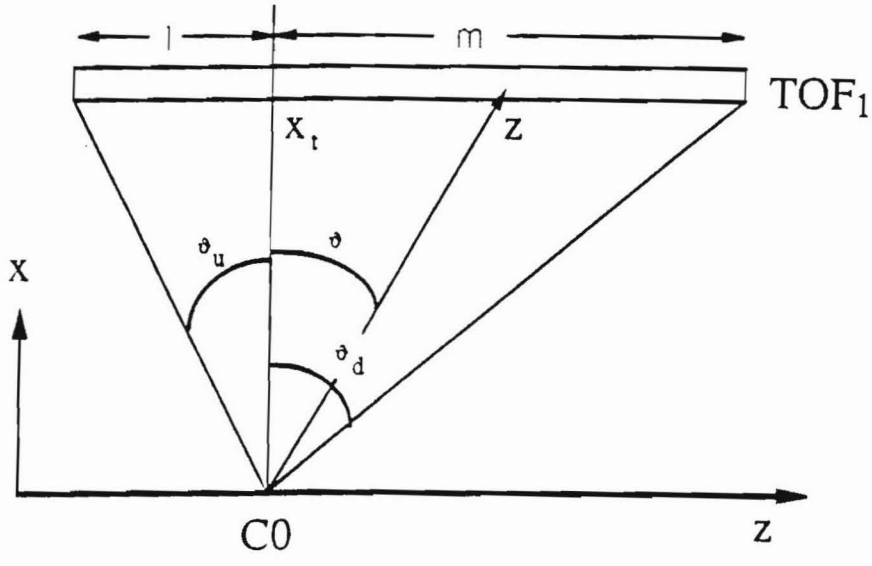

Figure 3.7: Description of variables used in the dE/dx trigger.

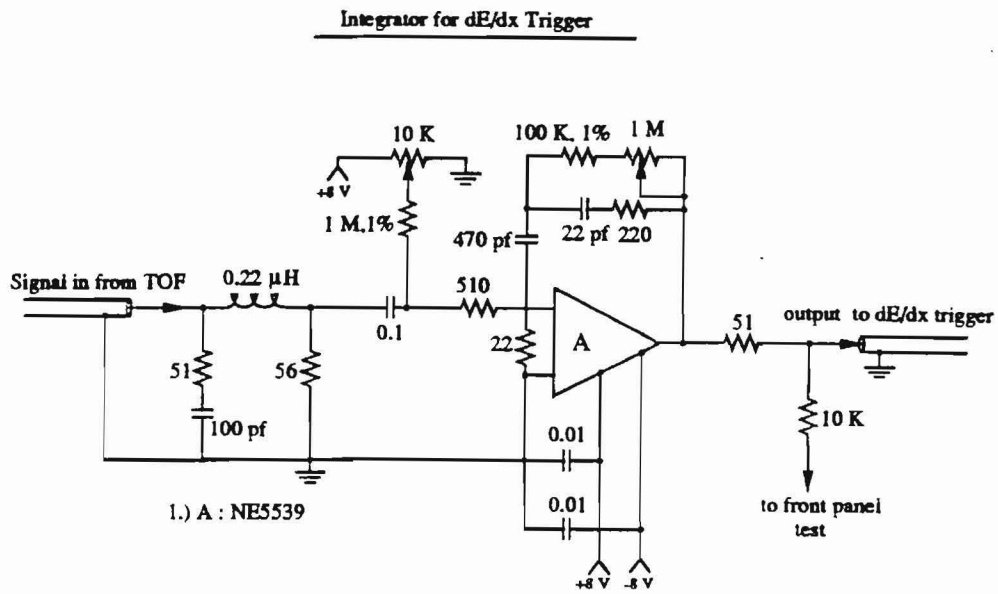

Figure 3.8: Integrator circuit used in the dE/dx trigger.

Chapter 4

Event Reconstruction

The raw data were written on data tapes, and a reconstruction program processed these data in order to create the data summary event record or the so-called DST tapes. Because of the large number of events, the processed event information is heavily compressed to yield the smallest event record while still retaining all relevant event information that might be needed in later event analysis and selection.

Several other record types were produced from the DST record. For example, a DSL record duplicates the most relevant information carried on the DST record in a much smaller record size. The DSL record only carried the parameters of the reconstructed charged tracks, the event vertex, event number, charged multiplicity, and particle mass calculated from the TOF_1, and TOF_2 devices. The size of the DSL record is approximately one-tenth of the corresponding DST record. From the DSL a $DSLDBL$ record was written including only events with more than one track in order to study the HBT phenomenon and resonance search.

Before a reconstruction of the data was performed, detector calibration was performed including pedestal subtraction for the hodoscope ADC's and TDC's

and the time to distance conversion for each drift chamber hit. The reconstruction of an event includes the calculation of the initial momentum (at the beam line), final momentum (at the final point of the track), initial point (at x=0 cm), final point, χ^2 per degree of freedom, momentum error of the fit, etc., of each track. The vertex of an event was calculated using the z-chamber. The mass of each particle and the vertex of an event were calculated with the use of the time-of-flight system ($TOF_p, TOF_{\bar{p}}, TOF_1, TOF_2$). The multiplicity of an event was calculated using the multiplicity hodoscope.

In summary, the event reconstruction procedure was divided into several steps:

- The transformation and decoding of the raw data.
- The calibration of various parts of the detector.
- The event vertex calculation using the z-chamber.
- The pattern recognition algorithm that reconstructs the particle trajectories.
- The packing of the resulting information into a DST data record that is stored for subsequent analysis.

In this chapter the track reconstruction will be described via the different components of the E735 detector. The vertex finding algorithm used in this reconstruction method will be described. Off-line data selection criteria used in this analysis will be given in order to remove background events and tracks. In

addition, three different ways of calculating the experimental momentum error of a track will be discussed.

4.1 Event Vertex

Because of its proximity to the beam line and its relatively long z dimension, the vertex chamber or z-chamber almost always contained hits from several tracks per recorded event. Through a succession of steps the chamber was initially used to obtain an approximate vertex derived from global hit information without explicit tracking. Ultimately a constrained vertex was calculated using a sample of the best quality track fits. Two different methods (both based on one Global idea) allowed one to construct distribution functions for the determination of the vertex position without the previous reconstruction of all trajectories.

4.1.1 Global Method A

As a first step, a z coordinate along the beam line, z_g, was estimated for a vertex using the vertex chamber hits in a global method without benefit of tracking. The method is a variation of one suggested by Yatsunenko [64]. Namely, one defines a distribution function $G(z)$ which is derived by first dividing the vertex range ($-100 < Z < +100$ cm) into 1 cm bins. Beginning from one end of the vertex range, a track is formed between a z-bin and a hit in the outermost layer of the z-chamber. The residuals between the track and all hits in the other two layers are found (including both left-right possibilities for every hit). Similarly, the residuals are found for all other tracks between the z-bin and the remaining

of the hits in the outermost layers. The negative of the sum of the squares of these residuals is entered into an exponential whose value is assigned to that z-bin. This process is repeated for all other z-bins. Mathematically one defines z_g as the z-coordinate which maximizes the summation over all hits in the vertex chamber:

$$G(z) = \sum_{k,\ell,m,n} g_{k,\ell,m,n}, \tag{4.1}$$

where

$$g_{k,\ell,m,n} = \exp(-[(z - z_{\ell,k,3})(x_3 - x_n)/x_3 + z_{\ell,k,3} - z_{\ell,m,n}]^2/2\sigma^2). \tag{4.2}$$

The quantity σ defines the sharpness with which one expects to resolve hits. In our case a value of $\sigma = 0.5$ cm, about a half cell width, gave satisfactory results. The subscript m ($m = 1, ...m_{max}(n)$) is the number of a hit sense wire in plane n ($n = 1, 2, 3$), and ℓ denotes each of the two ambiguities used. The coordinate of plane n is x_n cm from the beam line at $x = 0$. The index k steps through the hits of plane three only (Figure 4.1).

The global algorithm typically locates z_g to within ± 1.2 cm (rms) relative to the vertex along the beam axis as found by the whole spectrometer (Figure 4.2). Two maxima in G(z) having the same magnitude within 10% constitute good evidence for the presence of a second vertex in the event (Figure 4.3).

4.1.2 Global Method *B*

In this second global method, the hit position was used to reconstruct the event vertex. For any pair of hits (both hits in different z-chamber planes), the intercept of the line that connects these two z-chamber hits with the beam line is

reconstructed (Figure 4.4). This intercept, z_v, is given by:

$$z_v = (z_i(n)x_j(m) - z_j(m)x_i(n))/(x_j(m) - x_i(n)), \tag{4.3}$$

where $(z_i(n), x_i(n))$, $(z_j(m), x_j(m))$ are the coordinates of hit n, in plane i, and hit m in plane j, respectively. This also takes into account the z-chamber resolution for these two hits. Thus, a smearing (AB) of the intercept z_v can be defined as shown in the above figure.

$$(AB) = 2\sigma(x_j(m) + x_i(n))/|x_j(m) - x_i(n)|, \tag{4.4}$$

where σ is the z-chamber hit resolution. A Lorentzian function $L_{i,j}(n,m)$ is constructed for these two z-chamber hits:

$$L_{i,j}(n,m) = 1/((z - z_v)^2 + ((AB)/2)^2), \tag{4.5}$$

where z_v and (AB) are defined as above. This procedure was repeated for each pair of hits which were in different planes of the z-chamber. By summing all contributions, $L_{i,j}(n,m)$, for all possible pairs of hits, a global function $G(z)$ which is the probability of the vertex point is defined :

$$G(z) = \sum_i^3 \sum_j^3 \sum_n^{N_i} \sum_m^{N_j} L_{i,j}(n,m), \tag{4.6}$$

where N_i and N_j are the number of hits in the z-chamber plane $(i = 1,..,3)$, $(j = 1,..,3)$, respectively. The maximum of the global function $G(z)$ defines the vertex of an event z_g. Figures 4.5, 4.6, and 4.7 show the reconstruction of the event vertex (using z-chamber points, via method B, as described in the text) for three high charged track multiplicity events.

The determination of the vertex point, z_g, on the beam line was studied using Monte Carlo methods. In this Monte Carlo simulation, a number of pion tracks are generated uniformly in azimuth and rapidity range following a Poisson distribution, with mean particle multiplicity three and originating at a common vertex point, z_{gen}. Each particle is followed through the z-chamber to simulate z-chamber hits. The vertex z_{rec} is reconstructed from the simulated z-chamber hits (assigning ambiguity hits too) using global method B. Figure 4.8 shows the $z_{gen} - z_{rec}$ distribution for a radial hit resolution of $\sigma_r = 0$ cm. It seems this method reconstructs the vertex point, z_g, very well. Figure 4.9 shows the $z_{gen} - z_{rec}$ for a radial hit resolution of $\sigma_r = 500\ \mu m$. From this Monte Carlo study, one could conclude that the vertex z_g or z_{rec} can be located to within ± 0.6 cm (rms) relative to the generated vertex point.

A final vertex coordinate, z_A, was determined for an event by using all of the selected track candidates (which will be described later in Section 4.2) in a constrained fit to a common origin along the beam axis. The following χ^2 function was minimized to find a new set of track slopes, B_j, and a common intercept, z_A, at the beam line.

$$\chi^2 = \sum_{i=1,3} \sum_{j=1,N} (z_{ij} - z_A - B_j x_{ij})^2, \tag{4.7}$$

where N is the total number of selected tracks used. The coordinates x_{ij}, z_{ij} belonged to the ambiguity-resolved hit of the j-th track in the i-th plane. Namely, the minimization of the χ^2 function was carried out with respect to the z_A and B_j parameters:

$$\partial\chi^2/\partial z_A = 0, \tag{4.8}$$

$$\partial\chi^2/\partial B_j = 0 \quad \forall\, j = 1, ..., N, \tag{4.9}$$

or

$$3Nz_A + \sum_{i,j} B_j x_{ij} = \sum_{i,j} z_{ij}, \tag{4.10}$$

$$z_A \sum_{i=1}^{3} x_{ik} + B_k \sum_{i=1}^{3} x_{ik}^2 = \sum_{i=1}^{3} z_{ik} x_{ik}, \tag{4.11}$$

where $k = 1, ..., N$ and N is the total number of z-chamber reconstructed tracks. By solving the above $N+1$ system of equations, the z_A and B_j parameters were calculated.

4.2 Track Reconstruction

Due to the geometry of a z-chamber cell and the resulting isochrone configuration (Figure 2.6), a hit produces a drift circle around a sense wire. Tracks in the z-chamber are located by forming 0.5 cm wide roads using paired combinations of hits in planes one and three. Since the magnetic field is low at the z-chamber, only straight tracks were considered. Four possible roads were formed from the tangents to the drift circles in the first and third planes, as shown in Figure 4.10. These roads were used to select the best hit ambiguity in plane two in order to form a three-point track candidate. The selection of a track candidate was based on the χ^2 of the fit and on the distance of closest approach to z_g obtained above with the global vertex calculation. The same tracking idea was applied in the reconstruction of straw chamber tracks.

For each wire hit in the pre-magnet chamber, a left and right ambiguity hit is considered. Tracks in the pre-magnet chamber were located by forming four 0.5

cm wide roads using paired combinations of hits in two of the four planes and by using the left right ambiguity hits. The first pair hit combination tried was from plane one and four. In case, plane one or four was inefficient, the rest of the pair combinations were considered out of the four planes. These roads were used to select the best hit ambiguity in the remaining planes in order to form a three or four-point track candidate. The selection of a track candidate was based on the χ^2 of the fit and on the distance of closest approach. Only straight tracks were formed. The same tracking idea was tried in the post-magnet chamber as well.

When track reconstruction is complete three classes of tracks, based on the number of track segments involved for each track, were created. These three classes are:

RCT1. These tracks are the ones which traverse all chambers in the spectrometer arm. They are formed from track segments found in the straw, pre-magnet, post-magnet, and z-chamber.

RCT2. These are tracks which formed track segments in the pre-magnet, post-magnet, and z-chambers and used hits in the first three straw chamber boxes (six first straw chamber planes). These tracks arise either from particles which do not traverse the entire spectrometer arm due to low energy or from inefficiencies in the straw chamber as studied, in the following paragraph.

RCT3. RCT3 tracks are formed from unused straw chamber track segments and any hits found near a physical trajectory which aligns with the track

segment in the straw chambers and also passes through the event vertex found using the z-chamber.

The RCT2 tracks, as mentioned above are the ones which arise either from straw chamber inefficiencies or from missing track segments within the entire track. Figure 4.11 shows the z-coordinate distribution at TOF_1 for extrapolated tracks in the spectrometer. Within the distribution of tracks obtained from the tracking algorithm, RCT1 and RCT3 show large gaps at around z = +30 cm and z = -40 cm. The fact that the RCT2 tracking algorithm shows a surfeit of tracks in the same region implies that the straw chamber planes were suffering some losses in this region (as shown in the middle plot of Figure 4.11). RCT1 and RCT3 were unable to reconstruct some of the tracks corresponding to z = +30 cm and z = -40 cm, however RCT2 was able to reconstruct many of these missing RCT1 and RCT3 tracks as well as the wide angle tracks, as shown in Figure 4.11.

Figures 4.12, 4.13, and 4.14 show some typical events with tracks in the spectrometer. The curves drawn are from the track reconstruction fit. The track reconstruction efficiency was studied by scanning 2000 real events and compared with the results of the reconstruction program. The reconstruction efficiency was about 94% on average.

In this thesis all classes of tracks were used for the resonance studies. In the Bose-Einstein correlation studies, RCT1 and RCT2 were used as well as RCT1, RCT2, and RCT3 tracks in order to increase the statistics of two track events especially for the studies of the Bose-Einstein correlation function as a

function of the charged multiplicity, n_{ch}, and total momentum, P_{tot}, of the pair. In order to avoid poorly reconstructed low momentum RCT3 tracks a 0.100 GeV/c momentum cut was applied ($|\vec{p}| > 0.100$ GeV/c).

Each recognized track was fit using an iteritive least-squares algorithm based on Bock's [65] work. The five initial track parameters were determined from a fit of the straw track segment. These parameters were:

- The slope of the track in $x - z$ plane, $\tan\theta$.
- The z-coordinate of the track at the TOF_1 system, z_0.
- The curvature of the track k/p, where p, k are the momentum and the charge of the fitted track, respectively.
- The slope of the track in $x - y$ plane, $\tan\phi$.
- The y-coordinate of the track at the TOF_1 system.

For the track momentum calculation $\vec{p}$ Runge-Kutta integration method [66] was performed through the magnetic field $\vec{B}(x, y, z)$.

4.3 Event and Track Selection

The first step in data reduction is done via off-line analysis for all raw data. Events and tracks are subjected to a list of cuts in order to remove background events. This selection was carried out in two steps: (1) the event selection and (2) the track selection.

4.3.1 Event Selection

The events recorded in our interaction region are not only from pure $p\bar{p}$ collisions, but may also result from beam-gas interactions. Background tracks could come from the interaction of the beam (proton or antiproton) with the wall of the beam pipe and the magnets. These background events were referred to as beam-gas events. The study of beam-gas events was done by using missing $\bar{p}$ bunches in the collider or by using proton beam only. In order to remove these background events, a list of cuts (called LBG cuts) was applied to the data:

- $N_p > 1$ and $N_{\bar{p}} > 1$, where N_p and $N_{\bar{p}}$ are the number of hits in the upstream and downstream trigger hodoscope, respectively. These were found by studying the number of hits per event in the up-stream and down-stream hodoscope triggers for two classes of events: the beam-gas events, where no $\bar{p}$ bunches are present in the collider, and beam-beam events, where both p and $\bar{p}$ bunches were present in the collider.

- Endcap upstream-downstream asymmetry cut $|A| < 0.6$. For statistical reasons, the asymmetry cut is used for the events with $n_{ch} > 80$. The symmetry cut removes most beam-gas events that are fixed target interactions, and thus produce most particles along the projectile direction. The asymmetry variable A is defined as:

$$A = \frac{N_u - N_d}{N_u + N_d}, \tag{4.12}$$

  where N_u and N_d are the number of hits in the upstream and downstream multiplicity hodoscope, respectively. Figure 4.15 shows this asymmetry

variable for a set of minimum bias triggers with charged particle multiplicity greater than 80 (n_{ch}) as measured by the hodoscope multiplicity counters. As shown there is a good separation between the beam-gas events and the $p\bar{p}$ events.

- Averaged time cut on the hodoscope, upstream and downstream endcap multiplicity hodoscope. This timing cut was derived by studying the hit time of the upstream endcap multiplicity counter versus the downstream endcap multiplicity counter hit time. The timing cut removed beam-gas events which occurred not only outside the E735 detector, but also between the trigger hodoscope and the multiplicity hodoscope.

- The event vertex calculated from the TOF system was required to be within $-40 < z_{vertex} < 60$ cm in order to remove events that occurred outside the detector.

4.3.2 Track Selection

After the reconstruction of all RCT1, RCT2, and RCT3 tracks a list of quality cuts was applied in order to reject the poorly reconstructed and background tracks. Background tracks in our data come from secondary interactions in the 3 mm Aluminum pipe width, in the magnet yoke, and inside each chamber.

- The reconstructed momentum of each track had to have $p > 0.100$ GeV/c in order to reject electron tracks and poorly reconstructed tracks. By studying the mass identification of low momentum track data ($p < 0.100$ GeV/c), it was found that these were mostly electron tracks.

- The χ^2 per degree of freedom, χ^2/dof, of each track was required to be less than 8. This cut eliminates most poorly reconstructed RCT3 tracks. RCT1 and RCT2 tracks were almost unaffected.

- The momentum resolution of each track dp/p is given by:

$$\frac{dp}{p} = p\sigma_{1/p}, \tag{4.13}$$

  where $\sigma_{1/p}$, is the curvature $(1/p)$ error of the fitted track given by the tracking program, was limited to $dp/p < 10\%$.

- The single charged track intercept at the beam line ($x = 0$ cm) was limited to $|z_{interc.}| < 50$ cm in order to remove upstream and downstream low momentum tracks.

- Single charged tracks were required to come from the identified event vertex. (This requirement was not imposed in the search of the various resonance studies, as will be discussed later). Figure 4.2 shows the difference between the event vertex reconstructed by the z-chamber, z_{vertex}, and the track intercept, $z_{interc.}$, along the beam pipe. The RMS error of this plot is 1.2 cm. A 5 cm cut was imposed on this $z_{vertex} - z_{interc.}$ distribution (accepted tracks with $|z_{vertex} - z_{interc.}| < 5$ cm).

- For events with more than one track (in the study of Bose-Einstein correlations) the relative intercept of a pair at the beam line, $z_1 - z_2$, was studied. Figure 4.16 shows the difference between the two track intercepts at the beam line. The RMS of this distribution was 3 mm after using a Gaussian

fit to the peak of this distribution. Notice the deviation of the tail of the above distribution from the Gaussian fit. A 3 cm cut was imposed to this $z_1 - z_2$ distribution (accepted tracks with $|z_1 - z_2| < 3$ cm).

- In the study of the Bose-Einstein pion correlation, all particles which are not well identified kaons or protons are assigned the mass of a pion. Well identified kaons or protons are defined as follows: $0.4 < M_{TOF1} < 1.5$ GeV/c^2 or $0.4 < M_{TOF2} < 1.5$ GeV/c^2, where M_{TOF1} and M_{TOF2} are the masses calculated using TOF_1 and TOF_2 systems, respectively.

4.4 Multiplicity Calculation

The true charged particle multiplicity, n_{ch}, of the $p\bar{p}$ collisions was calculated using the 240 scintillator hodoscope counters (Section 2.3.3) that determine the number of hodoscope hits, n_h, for pseudorapidity range $3.25 < \eta < +3.25$. The determination of the relation between the true charged particle multiplicity and the hodoscope hit multiplicity, n_h, was done by studying the number of tracks accepted by the spectrometer as a function of hodoscope hit multiplicity as described in Section 2.3.3. The conversion from the measured number of hits in the hodoscope, n_h, to the true charged multiplicity, n_{ch}, produced in a $p\bar{p}$ interaction was parametrized, as described in references [8,67]:

$$n_{ch} = 0.875 n_h - 0.608 \times 10^{-3} n_h^2 + 0.141 \times 10^{-4} n_h^3, \tag{4.14}$$

for $0 < n_h < 200$, since the hodoscope is affected by background tracks as well as by saturation effects due to the finite number of the hodoscope counters. All

of the above problems were taken into account in a Monte Carlo simulation of the hodoscope counters, as described in reference [54].

4.5 Particle ID and Mass

Particles were identified by measuring the time-of-flight between the interaction time, t_0, and the arrival time at the TOF_1 system or the TOF_2 system as described in Section 2.3.7.

The corresponding time for a track was found by extrapolating the track in the spectrometer to TOF_1 or TOF_2. By comparing the predicted position on TOF_1 or TOF_2 from tracking to the position calculated from the time measurement from each end of the scintillator counter, the corresponding time-of-flight of the track was considered. Figures 4.17 and 4.18 show the distribution of $Y_{trk} - Y_{TOF1}$ and $Z_{trk} - Z_{TOF1}$, respectively, of each track in the spectrometer for all the possible TOF_1 hits. Y_{trk}, Y_{TOF1} are the y-spatial component of the extrapolated track to the TOF system and the y-spatial component of a hit on the TOF_1 system, respectively. Similarly, Z_{trk}, Z_{TOF1} are the z-spatial components of the extrapolated track to the TOF system and the z-spatial components of a hit on the TOF_1 system, respectively. There is a long tail in the distribution of Y_{trk}, Y_{TOF1} due to poor y track reconstruction as well as the lack of y information within a TOF_1 counter width. Studying the above figures, the y-intercept of a track at TOF_1 must be within 25 cm of the hit position reconstructed from the TOF_1 timing information while the z-intercept of the extrapolated track at TOF_1 must be within 15 cm of the reconstructed hit position reconstructed via

the TOF_1 timing. The above cuts for the y-intercept and z-intercept are plotted on Figures 4.17 and 4.18.

By matching each track to a TOF_1 hit, the velocity, $\beta = v/c$, is determined.

$$\beta = s/tc, \tag{4.15}$$

where s is the arc length from the intercept of the track at the beam line to the TOF counter, t is the corresponding time provided by the TOF system, and c is the velocity of light.

The mass of the track now was defined by using the reconstructed momentum of the track:

$$m^2 = p^2/\beta^2\gamma^2, \tag{4.16}$$

where m is the mass of the particle, and $\gamma = 1/\sqrt{1-\beta^2}$.

4.6 Single Track Momentum Resolution

The single track momentum error was due to measuring and multiple scattering errors. It is expected that each contribution is independent and thus adds in quadrature to form the momentum error δp. $\delta p/p$ can then be written as:

$$(\delta p/p)^2 = (ap)^2 + (b/\beta)^2, \tag{4.17}$$

where a and b are the coefficients that characterize the contribution of the measuring and multiple scattering errors, respectively.

In finding the coefficients a and b, four independent calculations were used:

- The m^2 widths were measured as a function of momentum for pions (π), kaons (K), and protons (p), using TOF1 and TOF2. All three m^2 widths were combined into a single fit from which the coefficients were extracted.

- The $K^0 \rightarrow \pi^+\pi^-$ mass width which was obtained by studying K^0 decays in the E735 detector was compared with the Monte Carlo K^0 mass width.

- The $\Lambda^0 \rightarrow p\pi^-$ and $\bar{\Lambda}^0 \rightarrow \bar{p}\pi^+$ mass widths were measured and compared with the Monte Carlo Λ^0 mass widths.

- Spectrometer points in magnet-off runs were tracked using the same tracking program as used in tracking the magnet-on runs. These produced a *momentum spectrum* for hits which matched TOF1 hits and used all three z-chamber points. This *momentum spectrum* was compared to a simple model for multiple scattering of pions with a fixed measuring error, δz, in each plane. From this comparison, assuming a momentum error with the form of Equation 4.17, the coefficients a and b can be extracted.

4.6.1 Pion, Kaon, and Proton Mass Widths

An effort was made to study the m^2 widths as a function of momentum for π's, K's, and p's and to fit the momentum dependence of these widths with a form suggested by TOF errors, multiple scattering errors, and drift chamber errors.

The functional form of the width dependence on momentum was assumed to be that obtained from the differential of m^2:

$$m^2 = p^2/(\beta\gamma)^2, \tag{4.18}$$

where p is the momentum of the particle, $\beta = L/T$ (L is the distance that the particle traveled, and T is the corresponding particle time of flight), and $\gamma = 1/\sqrt{1-\beta^2}$. The above differentiation gives:

$$(\delta m^2/m^2) = 2(\delta p/p) + 2\gamma^2(\delta T/T), \tag{4.19}$$

where $\delta(1/\beta^2\gamma^2) = (2/\beta^2)(\delta T/T)$. Independent contributions from measuring error and multiple scattering add in quadrature to form $\delta p/p$ (Equation 4.17). Similarly, random values of $\delta T/T$ should add in quadrature to those of $\delta p/p$, Thus, the functional form for the momentum dependence of m^2 can be expressed as:

$$\delta m^2 = 2m^2\sqrt{(ap)^2 + (b/\beta)^2 + g^2\gamma^4}, \tag{4.20}$$

where $g = (\delta T/T)$ is the TOF system timing error. The first term in the square root refers to position measurement error, the second to multiple scattering, and the third to time-of-flight errors.

The data used in this calculation were subjected to the following cuts:

- Beam gas cut was applied for each event.
- Tracks reconstructed in RCT1, RCT2, and RCT3 methods.
- The m^2 values were calculated using TOF1.
- The track originated within 5 cm of the constrained z-chamber vertex.
- The z-intercept with the Tevatron beam line was between -50 and +50 cm.
- The $\chi^2_{pdf} \leq 8$.

- Positive and negative tracks were plotted together without distinguishing charge in order to increase statistics.

All widths were obtained from Gaussian fits to the data. Sometimes these were multiple Gaussian fits, as in Figures 4.19 and 4.20. These plots cover the $1.3 < p < 1.4$ GeV/c and $0.4 < p < 0.5$ GeV/c, respectively. In other cases, the Gaussian fits were used in combination with assumed forms for the local background. Each m^2 was obtained several ways over each momentum interval, and various m^2 intervals were included or excluded from the fits tried. The range of answers for the widths was noted and used to estimate the systematic error to be associated with the answer finally selected as best for a particular momentum interval.

Figure 4.21 shows the momentum behavior of the pion, kaon, and proton widths. The three m^2 widths are combined into a single fit and the results are plotted in Figure 4.21. There is an upturn in the widths at low momentum for protons which can be accommodated by the expected functional form. For some reason the proton widths appear smaller at intermediate momenta than the other points would imply. The combined fit is not especially good, but it follows the trend of the data. The extracted values of errors to a, b, and g are $a = 5.8\%$, $b = 4.4\%$, and $g = 2.55\%$. These are shown in Figure 4.21.

The m^2 widths as a function of momentum calculated using the TOF2 system were studied [68]. The data used in this calculation were subjected to the following cuts in order to get a cleaner sample of tracks:

- Tracks reconstructed via RCT1, RCT2, and RCT3 methods.

- The m^2 values were calculated using TOF2.
- The track originated within 3 cm of the constrained z-chamber vertex.
- The z-intercept with the Tevatron beam line was between -35 and +35 cm.
- Azimuthal angles were between 5 to 15 degrees in order to avoid magnet pole tips.
- The $\chi^2_{pdf} \leq 8$.
- Positive and negative tracks were plotted together without distinguishing charge in order to increase statistics.

Figure 4.22 shows the momentum behavior of the pion, kaon, and proton widths. All three m^2 values were combined into a single fit, and the results are shown in Figure 4.22. The extracted values of a, b, and g errors are $a = 4.4\%$, $b = 4.3\%$, and $g = 1.25\%$, as shown in the Figure 4.22. Note that the error coefficient g for TOF1 (Equation 4.21) is twice as big as the TOF2 result (Equation 4.22) because of the geometric position of the TOF1 and TOF2 systems. The feature to note is that the TOF1 (Figure 4.21) data points do not have the upturn in width at low momentum which was observed in the TOF2 widths (Figure 4.22). This anomalous low momentum upturn is characteristic of all TOF2 widths. It is presumably a manifestation of dispersion in the threshold for reaching various TOF2 counters after passing through a trajectory-dependent thickness of TOF1. This upturn for kaons and protons at the momentum cannot be explained by the assumed functional form of Equation 4.20. However, by excluding these points,

one can find a fit that is not completely unreasonable. If the coefficients a, b, and g are interpreted literally, our best momentum resolution is not quite as good as we might expect, and the time resolution is $\delta T \simeq 165$ picoseconds. The momentum error is multiple scattering limited at low momentum tracks and is limited by the measuring error at high momentum.

4.6.2 K^0 Mass Width

An experimental estimate for the value of δp can be obtained from the observed width of the K^0 decay to $\pi^+\pi^-$. Figure 4.23 shows the invariant mass M of unlike-signed pions in our spectrometer under the following list of cuts:

- only events with two or more tracks are accepted.
- each event should satisfy the Beam Gas cut.
- only RCT1, RCT2, and RCT3 tracks are accepted.
- all particles which are not well identified as kaons or protons by TOF1 or TOF2 are assigned the pion mass. Well identified kaons or protons are defined as follows: $0.4 < M_{TOF1} < 1.2$ GeV/c or $0.4 < M_{TOF2} < 1.2$ GeV/c, where M_{TOF1}, M_{TOF2} are the identified masses of a charged particle using TOF_1 and TOF_2 system, respectively.
- the momentum of each track should be $|\vec{p}| \geq 0.100$ GeV/c^2.
- $\chi^2_{pdf} \leq 8$.
- $dp/p \leq 0.1$, where dp (momentum error) is calculated from the error matrix.

- opening angle of a pair should be $\geq 10^0$ in order to eliminate misidentification of e^+e^- pairs from γ conversion.
- total momentum of a pair $P \geq 0.8$ GeV/c.
- $q_t \leq 0.350$ GeV/c, where q_t is given by Equation B.5.
- $|\vec{p}_1 - \vec{p}_2| \geq 0.4$ GeV/c. (The above four cuts are calculated from a Monte-Carlo study of K^0 decays in our spectrometer.)
- $0 \leq x_0 \leq 55$ cm, where x_0 is the decay point of a pair in $x - z$ plane.
- |zvertex - z_v| ≤ 10 cm.
- |zinterc| ≤ 50 cm for each track in the observed pair.

The zvertex is the reconstructed vertex of the events using the z-chamber, while zinterc is the z-intercept of the individual track at the beam line, and z_v is the vertex point of the pair at $x = 0$.

A clear K^0 mass peak is found around 0.500 GeV/c^2 in the invariant mass plot (Figure 4.23). The invariant mass of like-signed pions under the application of the same list of cuts is shown in Figure 4.24. There is no indication of a fake K^0 near 0.500 GeV/c^2. Suppressing the K^0 background by applying a cut of P_{tot} >1.3 GeV/c^2 (P_{tot} is the total momentum of a pair), a clearer K^0 peak (Figure 4.25) was observed. The experimental mass resolution is obtained from the fit to the K^0 peak (Figure 4.26) and is estimated to be $\Delta M_{K^0} = 0.017 \pm 0.002$ GeV/c^2. This is close to the predicted value, ($\Delta M_{K^0} = 0.016$), from the K^0 Monte Carlo (Figure 4.27) using the momentum error of Equation 6.24 with

$a = 4\%$ for the measuring error and $b = 4\%$ for the multiple scattering error. Finally, the measured mass of the K_0 is 0.4964 GeV/c^2, in excellent agreement with the accepted mass reported in the Particle Properties Data Booklet [69].

In Figure 4.28 the proper decay length ($L_0 = L/\beta\gamma$) of the K^0 is plotted, where L is the space intercept of the two $\pi's$. Since a K^0 cannot be identified on an event-by-event basis, we plot separately the proper decay length distribution of events both from the signal and background mass distributions, as defined above. In addition, a mass cut of $0.460 \leq M \leq 0.540$ MeV/c^2 was applied. The background decay length distribution was normalized to have the same number of background events found within the K^0 mass cut under the K^0 peak. This normalized distribution was subtracted from the K^0 decay length distribution to obtain the final distribution shown in Figure 4.28.

The exponential curve drawn is the fit curve through the experimental points. The extracted decay length ($c\tau = 2.51 \pm 0.3$ cm) is within the expected decay length ($c\tau = 2.67$ cm) from the Particle Properties Data Booklet [69].

4.6.3 Λ^0 Mass Width

An experimental estimate for the value of δp can be obtained from the observed width of the Λ^0 and $\bar{\Lambda}^0$ decay to $p\pi^-$ and $\bar{p}\pi^+$, respectively. Figure 4.29 shows the invariant mass, M, of $p\pi^-$, $\bar{p}\pi^+$ pairs (signal) superimposed with the invariant mass, M, of $p\pi^+$, $\bar{p}\pi^-$ pairs (background) after appropriate scaling and under the following list of cuts:

- only events with two or more tracks are accepted.

- each event should satisfy the Beam Gas cut (LBG cut 4.3.1.)
- only RCT1, RCT2, and RCT3 tracks are accepted.
- one particle in the pair should be either a proton, p, or an antiproton, $\bar{p}$, as identified by the TOF1 or TOF2 system. A proton or antiproton is defined by $0.650 < M_{TOF} < 1.4$ GeV/c^2. Particles not identified as protons or antiprotons are assigned the pion mass.
- the momentum of each track should be $|\vec{p}| \geq 0.080$ GeV/c in order to eliminate low momentum electrons.
- $\chi^2_{pdf} \leq 8$.
- $dp/p \leq 0.1$, where dp is calculated from the error matrix.
- $q_t \leq 0.350$ GeV/c, where q_t is given by Equation B.5.
- The pion momentum is required to be less than that of the proton and less than 1.0 GeV/c.
- The production vertex calculated from the extrapolation of the decay vertex to the colliding beam axis is required to be within ± 10 cm of the event vertex calculated from the z chamber.

  The above three cuts were the result of a Monte-Carlo study of Λ^0 and $\bar{\Lambda}^0$ decays in our spectrometer.
- $-5 \leq x_0 \leq 55$ cm, where x_0 is the decay point of a pair in the $x - z$ plane.

A clear Λ^0 and $\bar{\Lambda}^0$ peak is found at 1.115 GeV/c^2 in the invariant mass plot (Figures 4.29 and 4.30, after subtracting background from signal). The experimental mass resolution is obtained from the fit to the Λ^0 peak (Figure 4.30) and is estimated to be $\Delta M_{\Lambda^0} = 0.006$ GeV/c^2, close to the predicted value ($\Delta M_{\Lambda^0} = 0.0055$ GeV/c^2) from the Λ^0 Monte Carlo (Figure 4.31) using momentum error of Equation 6.24 with $a = 4\%$ for the measuring error and $b = 4\%$ for the multiple scattering. The measured mass of the Λ_0 is 1.115 GeV/c^2, in excellent agreement with the true mass reported in the Particle Properties Data Booklet [69]

The number of Λ's is taken as the number of entries above the background for the mass range between $1.100 < M < 1.130$ GeV/c^2. There are 10,800$\pm$ 500 $\Lambda^0 + \bar{\Lambda}^0$ and in our sample and the ratio of Λ^0 to $\bar{\Lambda}^0$ is 1.03$\pm$0.05.

In Figure 4.32 the proper decay length ($L_0 = L/\beta\gamma$) of the Λ^0 and $\bar{\Lambda}^0$ is plotted, where L is the space intercept of the $p\pi^-$ or $\bar{p}\pi^+$pair. Since the Λ^0 cannot be identified on an event-by-event basis, the proper decay length distribution of events, both from within and outside the lambda mass cut, was plotted again separately. The latter distribution is normalized to the same number of background events found within the Λ^0 and $\bar{\Lambda}^0$ mass cut and under the Λ^0 peak. This normalized length distribution was subtracted from the Λ^0 decay length distribution to obtain the final distribution shown in Figure 4.32.

The exponential curve drawn is the fit curve through the experimental points. The extracted decay length ($c\tau = 8.3 \pm 0.3$ cm (*stat.*)) is close to the expected decay length ($c\tau = 7.9$ cm) in the Particle Properties Data Booklet [69].

The transverse momentum distribution p_t (Equation 2.8) of the lambdas was studied. To get the momentum distribution of lambdas, the proton-pion invariant mass ($p\pi^-$ and $\bar{p}\pi^+$, *signal distribution*) was found for 11 p_t intervals, from 0.5 GeV/c to 3.0 Gev/c. The background invariant mass of a proton-pion ($p\pi^+$ and $\bar{p}\pi^-$) was plotted for the same 11 p_t intervals. The number of lambdas was calculated by subtracting the signal distribution from a normalized background distribution. The number of lambdas was corrected by the acceptance correction curve of Figure 4.33, which was derived using Monte Carlo $\Lambda + \bar{\Lambda}$ decays in the E735 detector. Figure 4.34 shows the corrected momentum distribution, dn/dp_t^2, for the lambdas. The $< p_t >$ was derived by fitting the dn/dp_t^2 using an exponential function, $exp(-bp_t)$. From the above fit, $b = 2.58 \pm 0.05$, which corresponds to a $< p_t >= 780 \pm 16$ MeV/c for lambdas. The above mean transverse momentum value is not calculated from minimum biased data, but it is expected than the corrections to minimum bias experiment will yield 5% lower.

4.6.4 Magnet-Off Data

Spectrometer points in magnet-off runs were tracked using the same tracking program used in tracking magnet-on runs producing a "momentum spectrum".

The data used in this calculation were subjected to the following list of cuts:

- Beam gas cut was applied for each event.
- Tracks reconstructed in RCT1 and RCT2 methods.
- Each track matches with a TOF_1 hit.

- The track originated within 5 cm of the constrained z-chamber vertex.
- The z-intercept with the Tevatron beam line was between -50 and +50 cm.
- The $\chi^2_{pdf} \leq 8$.
- Each track uses all three z-chamber hits.

Tracks using z-chamber points have an obvious difference in the character of their momentum spectrum from those without z-chamber points. This appears to be true for the magnet-off spectrum (Figure 4.35 a, b, and c). Differences appear to exist at the low momentum end as well as at the high momentum end of the spectrum. Use of the z-chamber points tends to eliminate many of the low momentum electron tracks.

Field-Off Monte Carlo

A Monte Carlo was run for pion tracks using simple models to describe "deflections" generated by multiple scattering and measuring errors. For simplicity the spectrometer was assumed to be symmetric about a magnet at x=1.0 meter midway between the origin and TOF1. For later reference, the steps that were used to generate an apparent momentum spectrum will be outlined below.

1. Obtain a pion with "true" momentum p_t from a spectrum generated by

$$dN/dp_t = Ap_t\, e^{-E_t/T}.$$

$T = 0.16$ GeV throughout this study. This temperature parameter, T, is close to the observed one in E735 experiment (Reference [2]).

2. Calculate an rms scattering angle for the spectrometer arm over its entire length. Express the length as a fraction of a radiation length, x/x_R . The rms angle θ_o is a function of p_t and velocity β.

$$\theta_o = [14.1(MeV)/\beta p_t] Z_{inc} \sqrt{x/x_R}[1 + 0.11 log_{10}(x/x_R)].$$

(See the Particle Properties Data Booklet [69])

3. Choose a θ_{xz} in the xz plane from a Gaussian distribution

$$dN/d\theta_{xz} \simeq e^{-\theta_{xz}^2/2\theta_o^2}$$

Keep track of the sign of θ_{xz}. Use geometry to estimate an effective deflection angle 2α from θ_{xz}. ($2\alpha \simeq \theta_{xz}/2$).

4. Choose a measuring error, s_m centimeters, from a Gaussian distribution with mean value s_o. Compute a deflection angle, θ_m, using $\theta_m = \tan^{-1}(s_m/X)$ and X=1 meter. (This will be justified later.) Keep track of the sign of θ_m.

5. Combine the two theta's with signs. $\theta = \theta_m + 2\alpha$.

Compute an apparent momentum $p = 50(\text{MeV/c})/\theta$.

6. Return to **1.** to generate another event.

Models for Momentum Errors

Two sources of errors are assumed, the projected rms scattering angle, θ_{xz}, and a z-coordinate measuring error per chamber plane, s_m. For a Monte Carlo track, each of these is generated from a Gaussian distribution and used to construct

an apparent magnet deflection. It is necessary to understand how the apparent deflection is estimated in order to relate the Monte Carlo result to a predicted momentum error for the real data.

- θ_{xz}: Figure 4.36(a) shows a field-free track which is bent along a "circular" path through an angle θ_{xz}. The tracking program effectively fits a chord (translated for best fit) to each half of the path and computes the deflection angle at the center, 2α, between the two chords. The apparent momentum returned by the tracking program is approximately $p = 50(\mathrm{MeV/c})/2\alpha$. With simple geometry one finds $\tan\alpha = (1 - \cos\theta)/\sin\theta$ from which $\tan 2\alpha = 2\tan\alpha/(1 - \tan^2\alpha)$. For small deflections $2\alpha = \theta_{xz}/2$, as one expects.

- Measuring Error s_o: Figure 4.36(b) shows two tracks whose slopes are effectively determined by clusters of points at each end of a track with each point having the same measuring error, $s_o = \delta z$. The errors in the end points at z_A and z_B are reduced by averaging the cluster of measurements so that for seven data points $\alpha_1 = (\delta z/X_1)\sqrt{(1/N_A) + (1/N_B)} = 0.76(\delta z/X_1)$. In desperation only, three points are assigned to the straw chamber to compensate for the reduced effectiveness of internal points in determining the lever arm for the slope. Then $2\alpha = (\delta z/X)\sqrt{2(3/4)^2} = 1.06(\delta z/X) \simeq s_o/(1.0\ \mathrm{meter})$.

Admittedly, this is not a correct argument because the fitting program does not allow the two track segments to be independent of each other. However, almost any argument, even a units argument, will suggest parameterization of

the deflection angle $\delta\theta$ due to measurement error should be of the form $\delta\theta = \tan^{-1}(s/X)$. This seems to work well in the Monte Carlo and allows us to estimate the effect of measuring the error on the momentum once we determine a value for s_o.

Comparison of Monte Carlo to Data

Figure 4.37 shows the Monte Carlo p_t spectrum compared to a transverse momentum (p_T) spectrum from the magnet-off data which uses the z-chamber in tracking. In the remaining figures, real data are always represented by a smooth curve. For this figure the Monte Carlo assumes the spectrometer has 0.052 radiation lengths (e.g. 2 grams of N_2) of material after the beam pipe and before TOF1. The measuring error, s_o, is assumed to be 500 microns. The match between the Monte Carlo and data is not so good for such crude assumptions.

The cumulative matter in the spectrometer after the aluminum beam pipe is 0.04 radiation length. The distribution is not uniform in x [70]. About 3/4 of the scattering material appears in the sturdily constructed straw chambers. A guess is that the effective spectrometer length might be somewhat shorter than the full extent of the straw chambers, hence 0.030 radiation lengths was the number used in the Monte Carlo. The comparison of the p_t (generated) and p_T (measured) distributions appears in Figure 4.38. The abscissa, and subsequent ones, are simply labeled with a generic P, but transverse momentum is being examined.

The agreement in Figure 4.38 is as good as we might hope to get with such methods. No particle types other than pions were tried.

Estimate of Momentum Error

Momentum $p = 50$ (MeV/c)/θ, where θ is the deflection angle found by the tracking program was assumed. This implies $\delta p/p = \delta\theta/\theta$.

- a) For multiple scattering $\delta\theta = 2\alpha = \theta_o/2$ (θ_o defined above). From the Monte Carlo we found the effective radiation length of the spectrometer to be ~ 0.030, so we use this to calculate $\delta\theta = \theta_o/2 = 0.0203/(2\beta p)$. Then

$$\delta p/p = (1.015/\beta p)(1/\theta) = (1.015/\beta)(1/50.0) = 0.02/\beta.$$

  The above momenta are all in units of MeV/c.

- b) For measuring errors, the Monte Carlo agreed with $\delta\theta = s_o/X = 0.05/100$. Since the tracking program finds 0.05 cm to be the approximate error per plane, we use this even though "error per plane" may not be quite the correct interpretation for the parameter s_o. Therefore,

$$\delta p/p = \delta\theta/\theta = 0.0005/\theta = (0.0005/0.05)p \text{ (GeV/c)}, \tag{4.21}$$

$$\delta p/p = 0.01\, p \text{ (GeV/c)}. \tag{4.22}$$

- If the errors in parts (a) and (b) combine quadratically,

$$\delta p/p = \sqrt{(0.01p)^2 + (0.020/\beta)^2}. \tag{4.23}$$

Sensitivity of the Method

Some idea of how sensitive the method is to the two types of errors can be seen in the Monte Carlo data plotted in Figures 4.39 and 4.40 which use 0.03

radiation lengths and 500 micron measuring error. Figure 4.39 shows the no-field momentum spectrum to be expected if only the multiple scattering error is turned on. Only about 10% of the particles would appear to have momentum above 20 GeV/c. Figure 4.40 shows the no-field momentum spectrum to be expected if only the measurement errors are turned on. In that case most particles would appear to have momenta above 20 GeV/c.

Unless the real no-field momentum spectrum has tracks above 20 GeV/c, our measurememnts cannot be very sensitive to the measuring errors. The real no-field transverse momentum spectrum of Figure 6 shows that around 10% of the no-field tracks are above 20 GeV/c, and there are still many tracks ($\sim 1\%$) at 100 GeV/c. Thus we can have some sensitivity to the measuring errors.

Variations in the radiation length also change the Monte Carlo spectrum with respect to the field-off data. The range of 0.025-0.038 radiation lengths corresponds to the multiple scattering error [70] range of $(0.018/\beta)^2$ to $(0.023/\beta)^2$. The mechanical length of the spectrometer is more like 0.038 radiation lengths.

The Monte Carlo used above assumed no true magnet-off spectrometer particles below 50 MeV/c could reach TOF1. By changing this lower limit assumption to 80 MeV/c, a better fit to the data is achieved by changing the radiation length from 0.030 to 0.024 or 0.026, giving a momentum error term of $\sim (0.018/\beta)^2$ instead of $(0.020/\beta)^2$.

We have also studied how the variation of the measuring error parameter, s_o, affects the Monte Carlo spectrum. Monte Carlo spectra are plotted for measuring errors that range from 0.025 to 0.40 cm. For s_o below 1 mm the multiple

scattering error is so large that changes in s_o do not affect the spectrum shape. Using $s_o = 1$ mm changes our momentum error formula to

$$\delta p/p = \sqrt{(0.02p)^2 + (0.020/\beta)^2}. \tag{4.24}$$

Values of s_o larger than 1 mm rapidly become more difficult to accept when the Monte Carlo is compared with real data. Tracking residuals imply s_o could not be significantly below 0.5 mm.

Best Estimate of Momentum Error Formula

If the momentum error formula has the form

$$\delta p/p = \sqrt{(ap)^2 + (b/\beta)^2}, \tag{4.25}$$

then the above Monte Carlo comparisons suggest $a = 0.015 \pm 0.005$ and $b = 0.020 \pm 0.003$.

This can be compared to the formula derived using the other two previous methods of

$$\delta p/p = \sqrt{(0.04p)^2 + (0.04/\beta)^2}.$$

Figures for Chapter 4

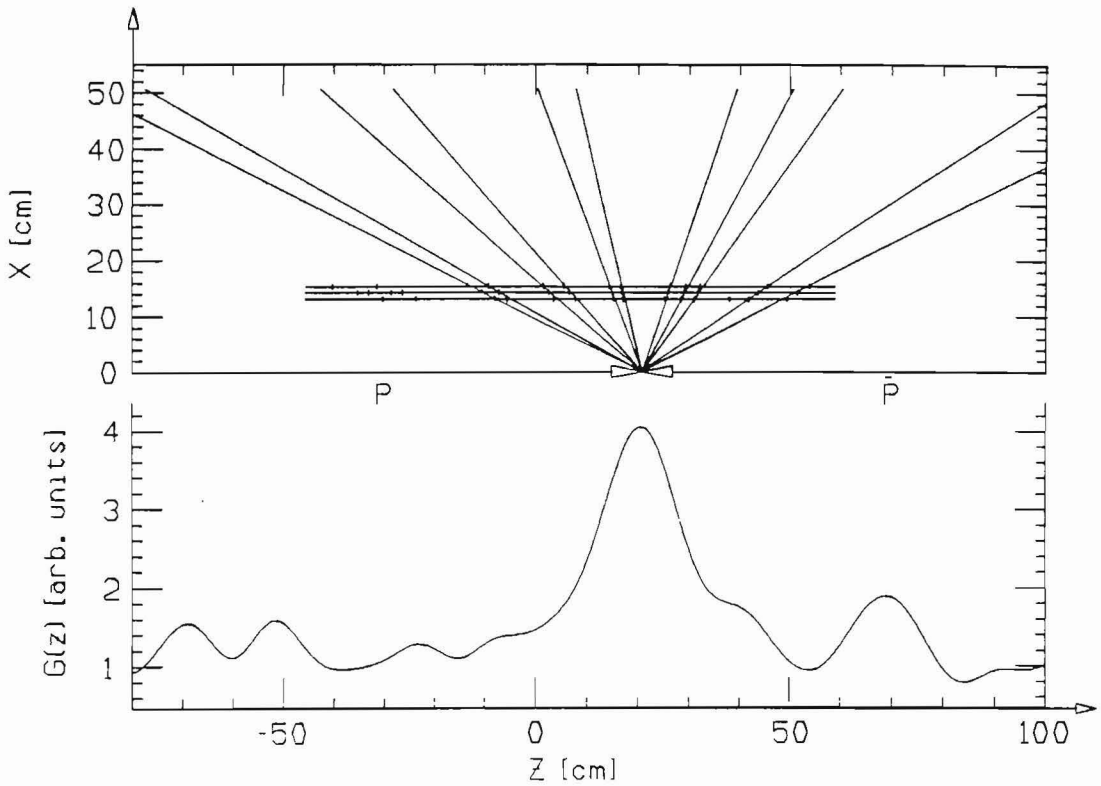

Figure 4.1: Example of the vertex reconstruction. For the G(z) definition see the text. The tracks indicated are those which were selected and constrained to a common vertex coordinate z_A.

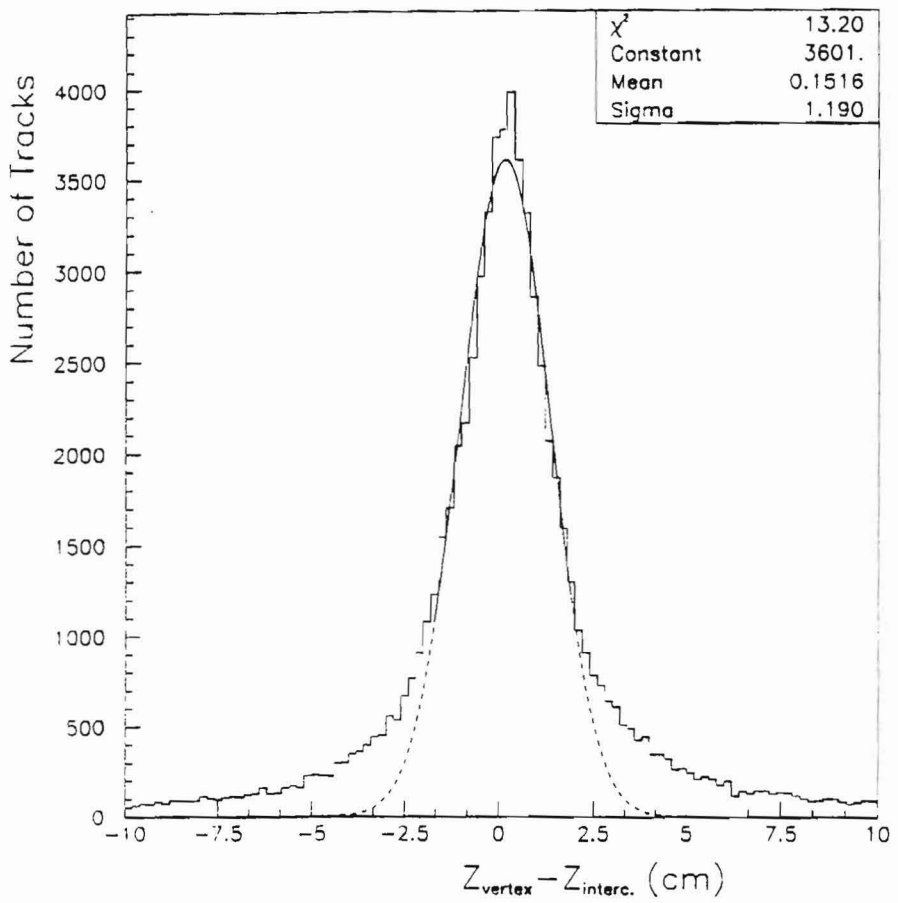

Figure 4.2: The distribution of the difference between the event vertex found by the z-chamber z_{vertex} and the track intercept at the beam line $z_{interc.}$, also shown is a superimposed Gaussian fit of the peak part of this distribution.

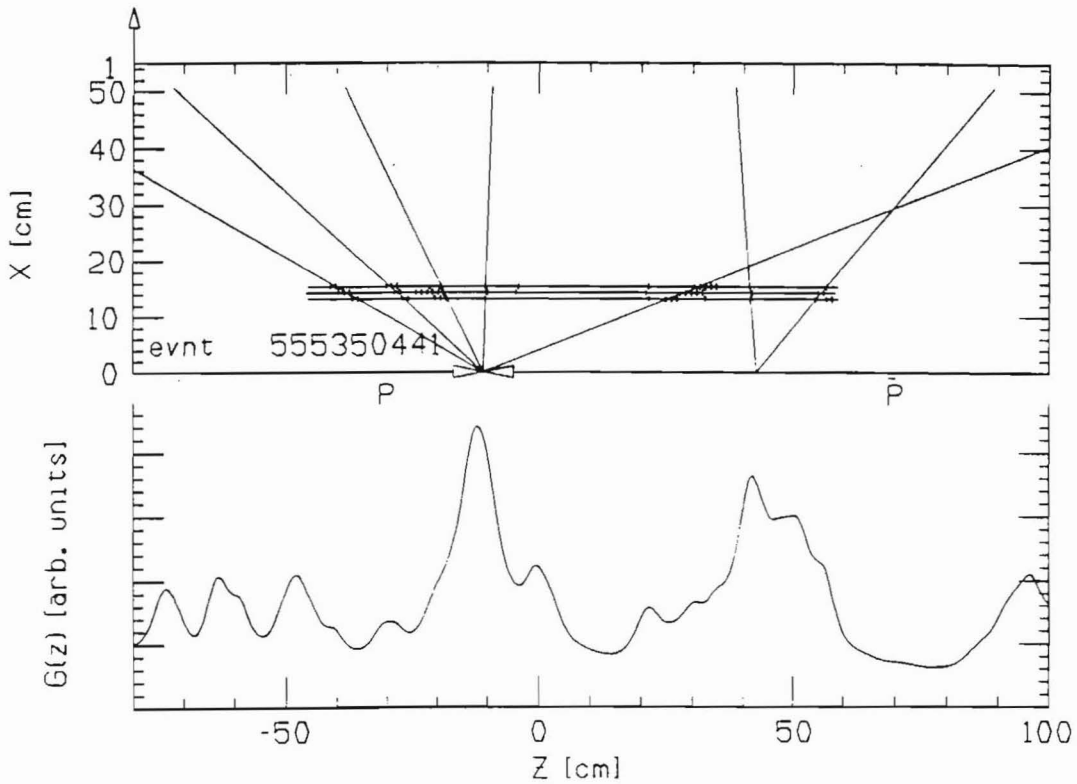

Figure 4.3: Example of two-vertex reconstruction. For the G(z) definition see the text. The tracks indicated are those which were selected and constrained to a common vertex coordinate z_A.

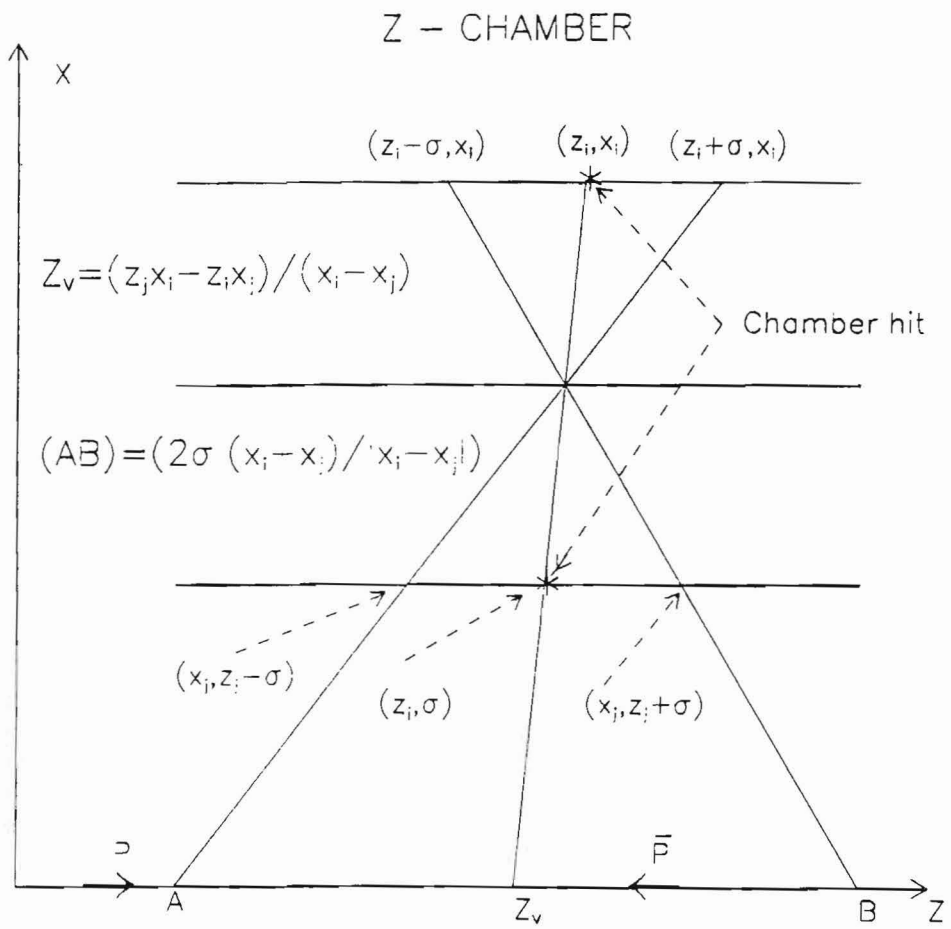

Figure 4.4: Two hits in the z-chamber in the first and last plane, respectively. Definition of z_v and (AB).

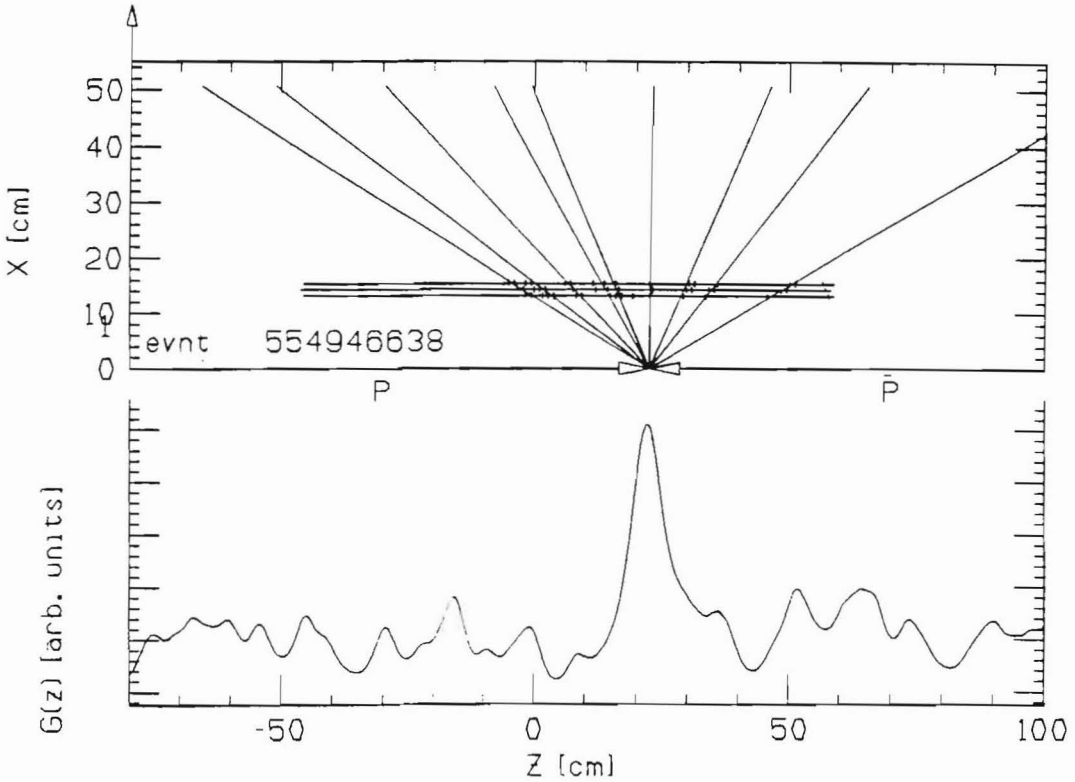

Figure 4.5: Z-chamber points used to reconstruct the event vertex of a typical high multiplicity event using method B.

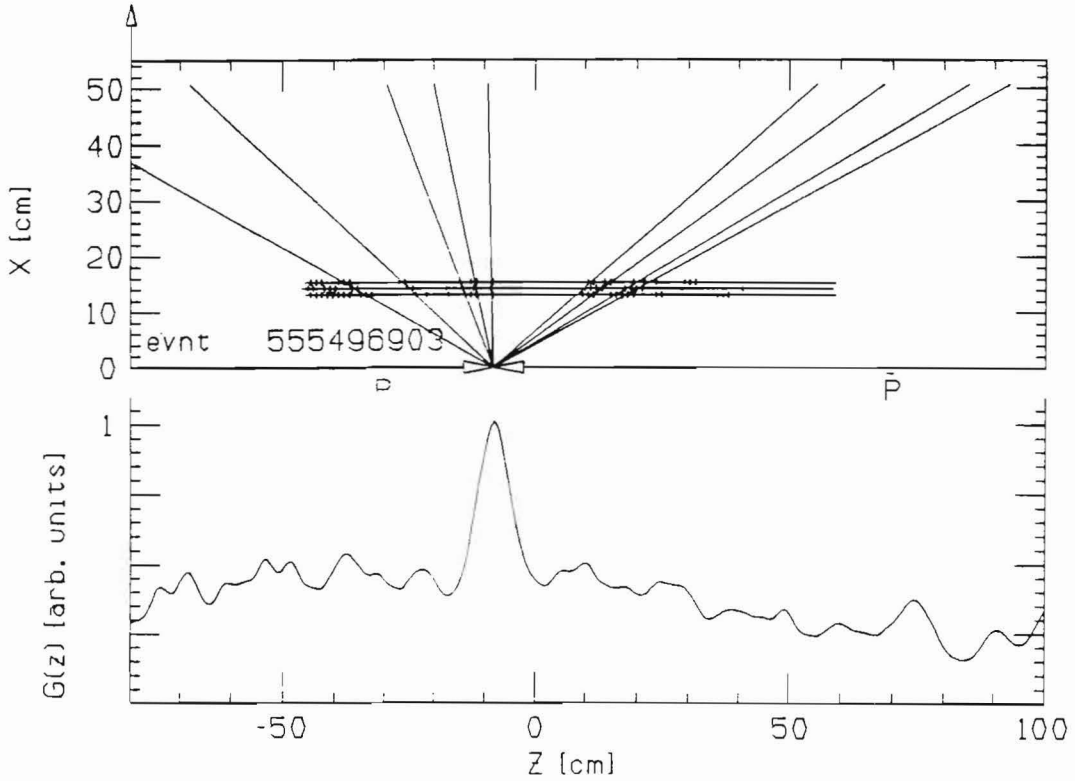

Figure 4.6: Z-chamber points used to reconstruct the event vertex of a typical high multiplicity event using method B.

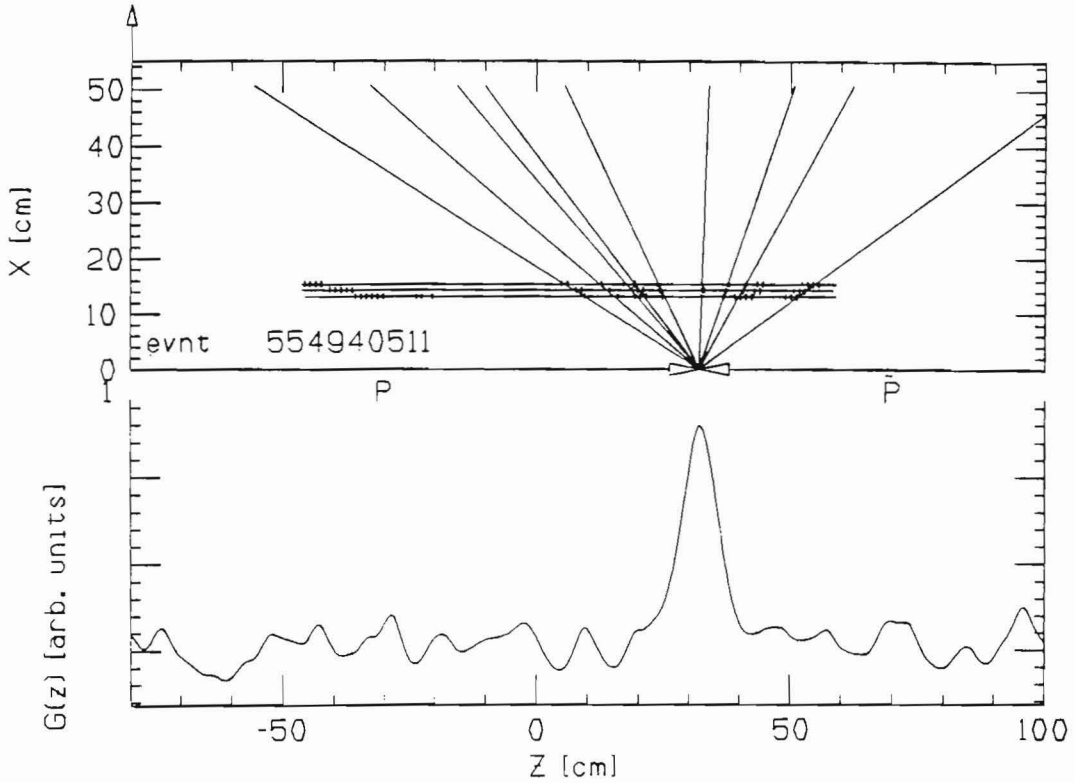

Figure 4.7: Z-chamber points used to reconstruct the event vertex of a typical high multiplicity event using method B.

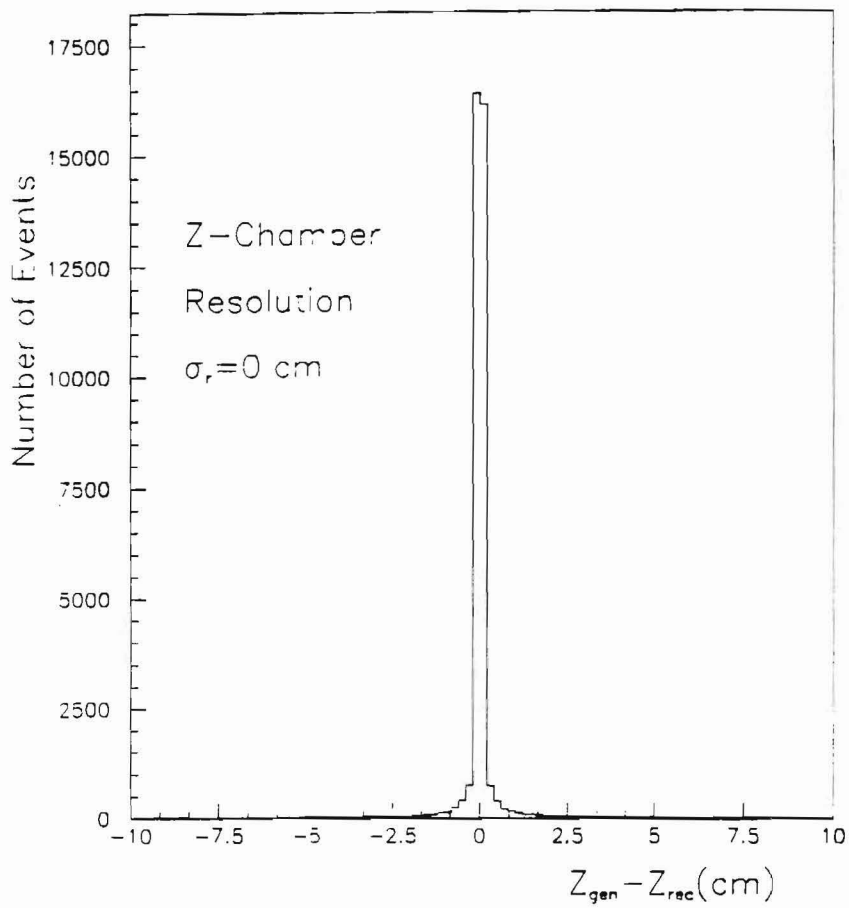

Figure 4.8: $z_{gen} - z_{rec}$ distribution using Monte Carlo data for z-chamber resolution $\sigma = 0$ cm.

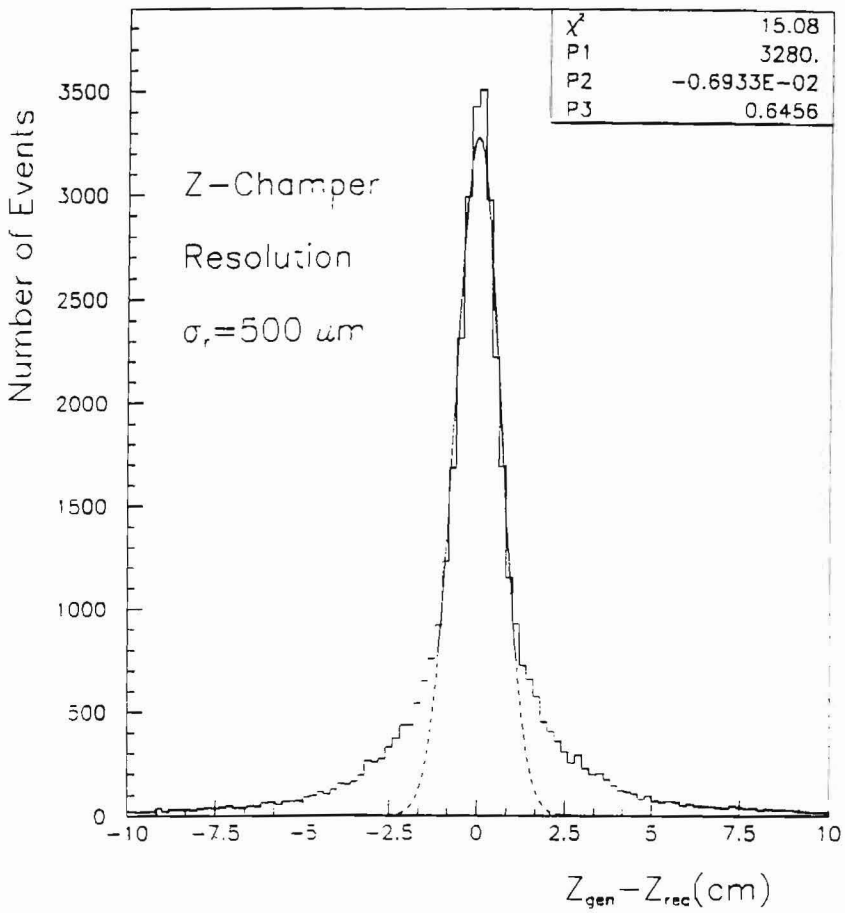

Figure 4.9: $z_{gen} - z_{rec}$ distribution using Monte Carlo data for z-chamber resolution $\sigma = 0.05$ cm

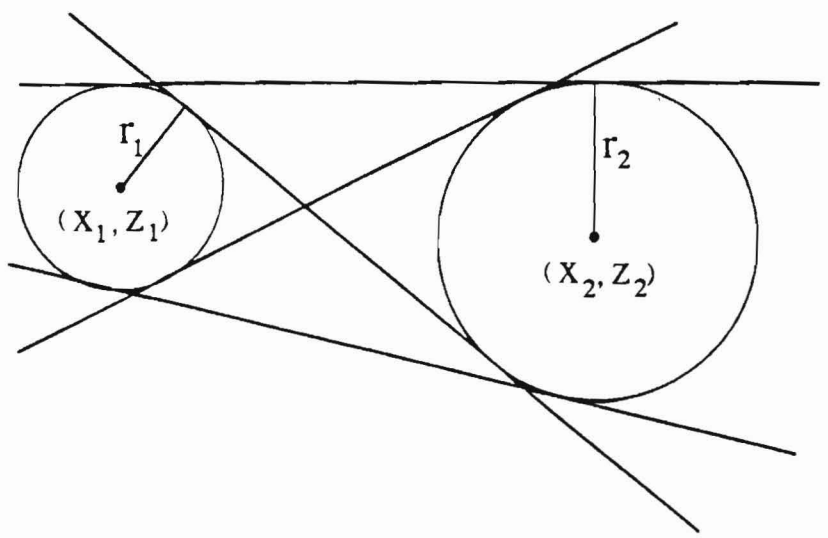

Figure 4.10: Four possible tangential lines are defined for two circles created by two corresponding hits in the z-chamber for first and third planes.

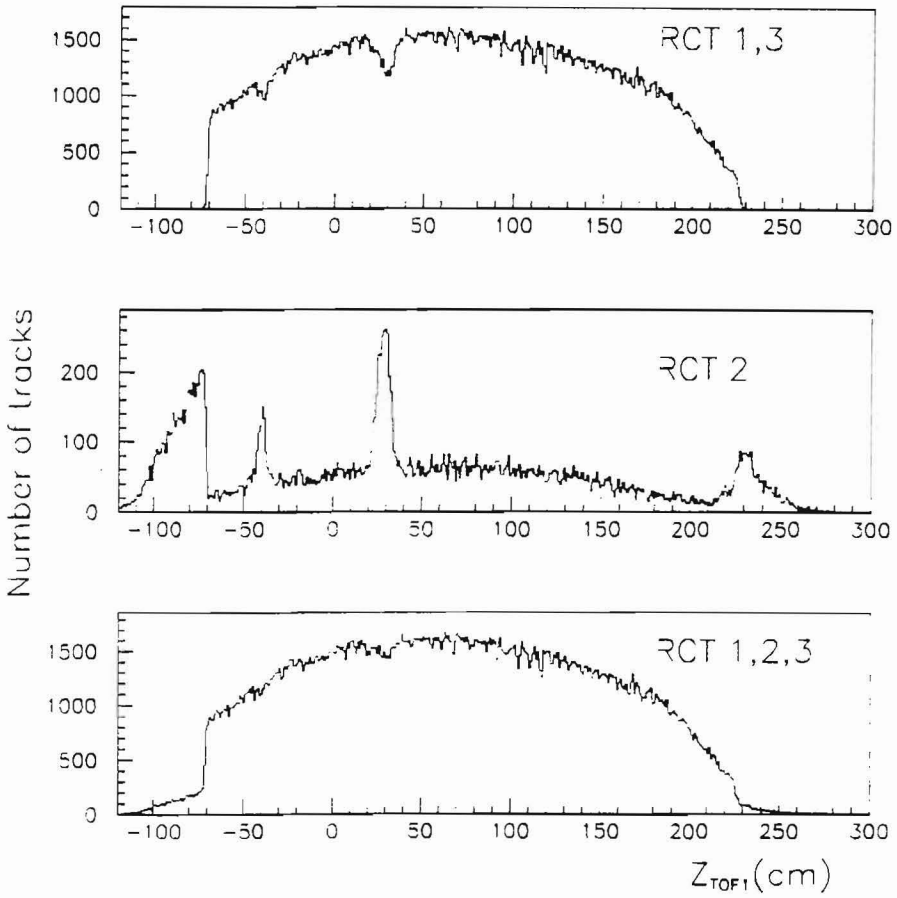

Figure 4.11: Z coordinate distribution at TOF_1 for tracks. The coordinate is estimated by extrapolating a spectrometer track to the TOF_1 plane. Upper: RCT1 and RCT3 tracks, Middle: RCT2 tracks, Lower: All tracks (RCT1, RCT2, and RCT3).

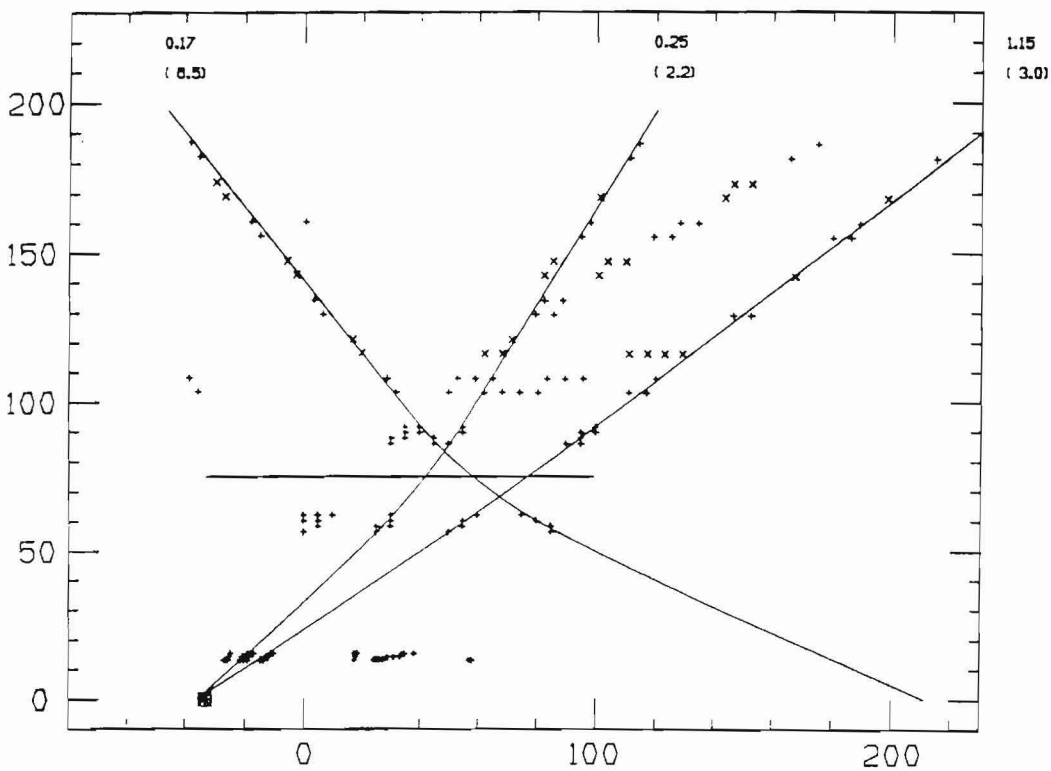

Figure 4.12: A typical high multiplicity event.

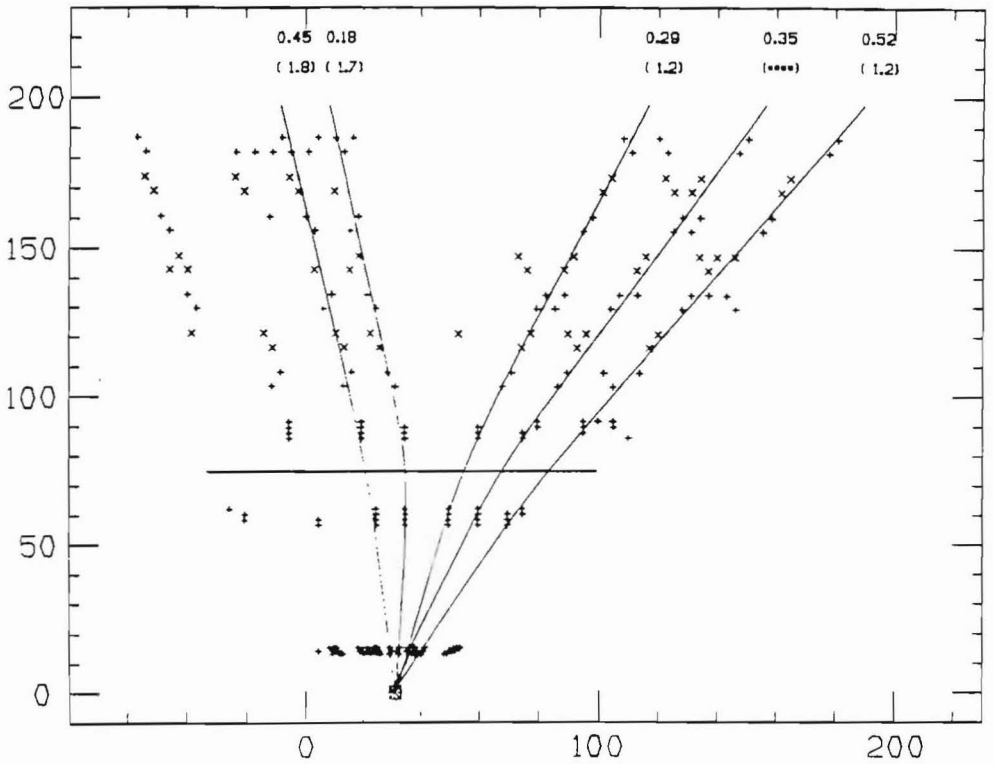

Figure 4.13: A typical high multiplicity event.

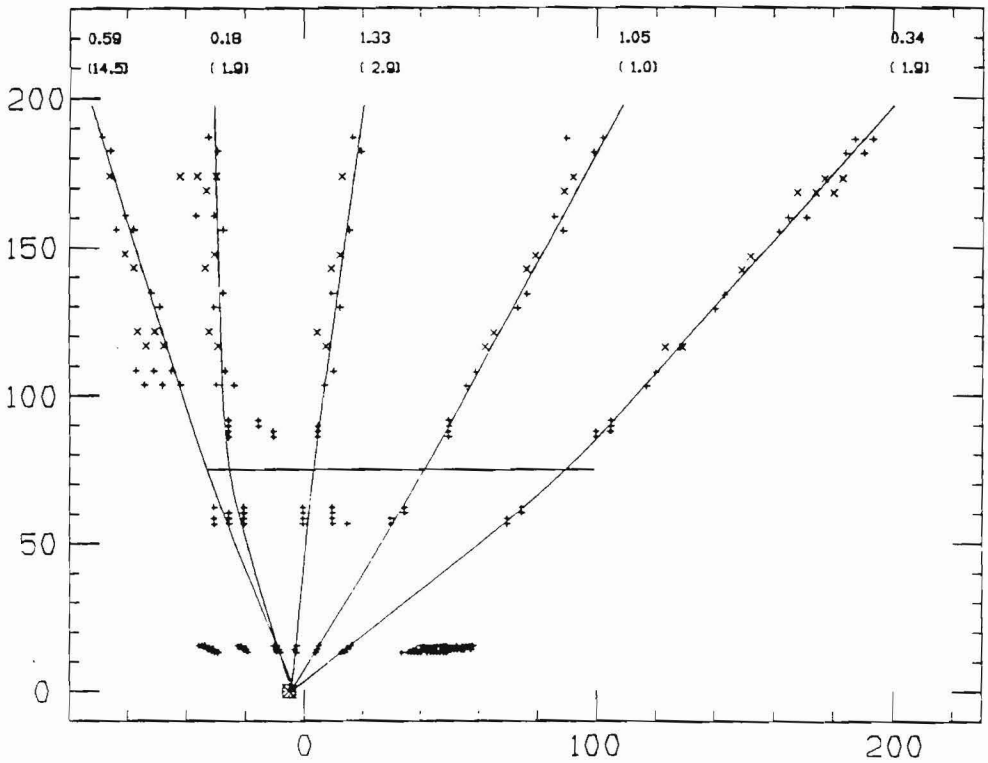

Figure 4.14: A typical high multiplicity event.

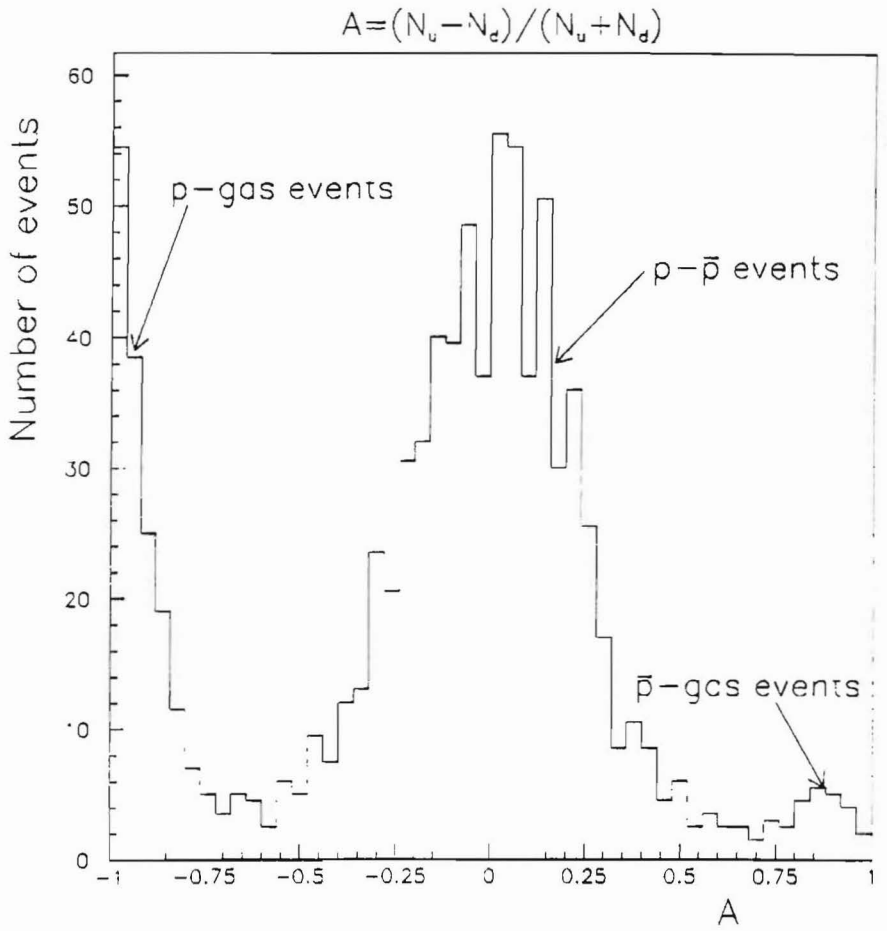

Figure 4.15: Asymmetry plot defined as $A = (N_u - N_d)/(N_u + N_d)$, where N_u, N_d are the number of hits in the upstream and downstream end cap multiplicity hodoscope.

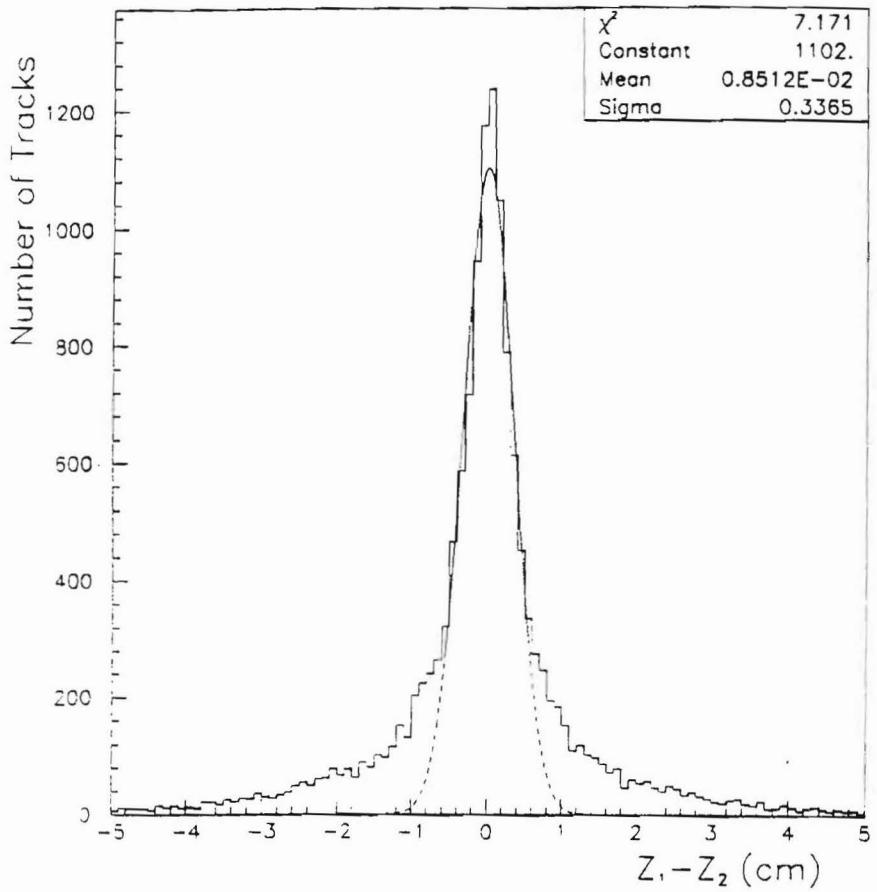

Figure 4.16: The distribution of the difference between two track intercepts $z_1 - z_2$. A superimposed Gaussian fit of the peak part of this distribution also is shown.

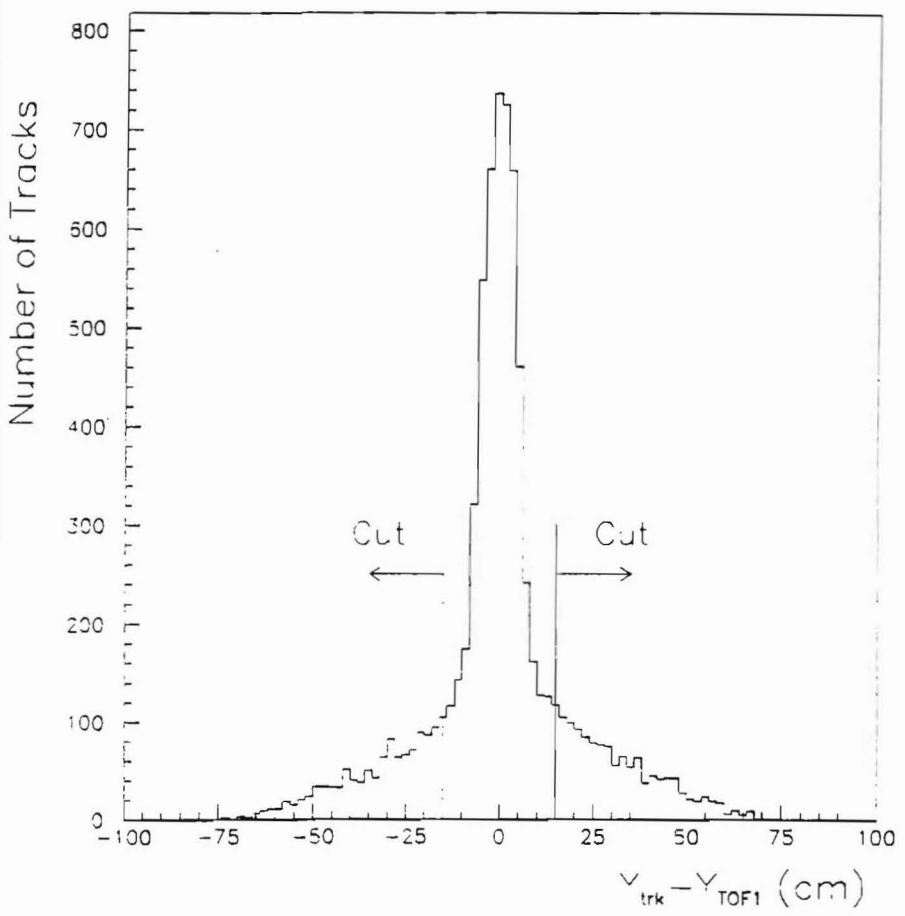

Figure 4.17: $Y_{trk} - Y_{TOF1}$ distribution of tracks at TOF_1.

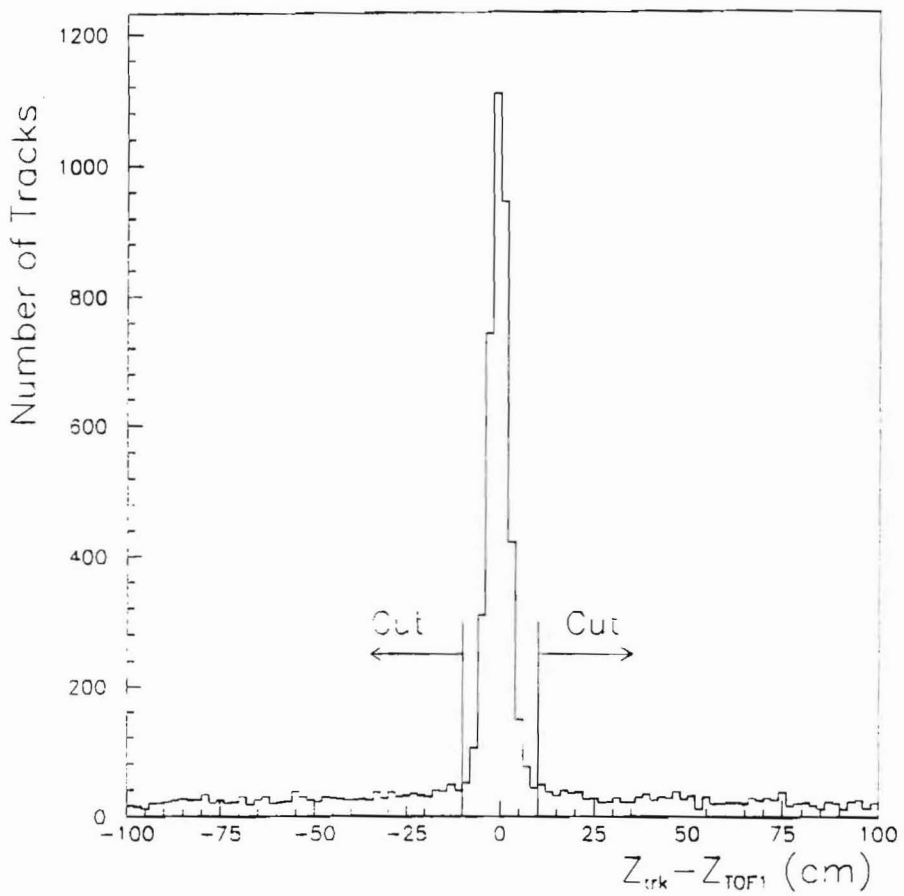

Figure 4.18: $Z_{trk} - Z_{TOF1}$ distribution of tracks at TOF_1 system.

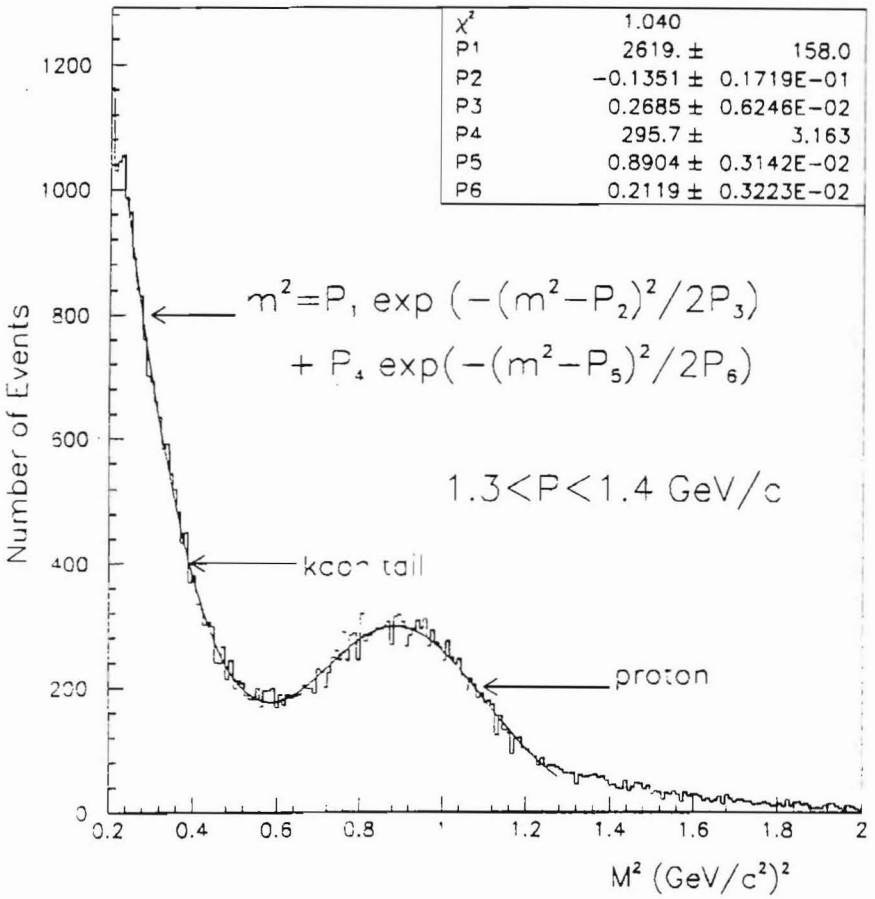

Figure 4.19: m^2 spectrum using TOF1 for the momentum range: $1.3 < m^2 < 1.4$ GeV/c.

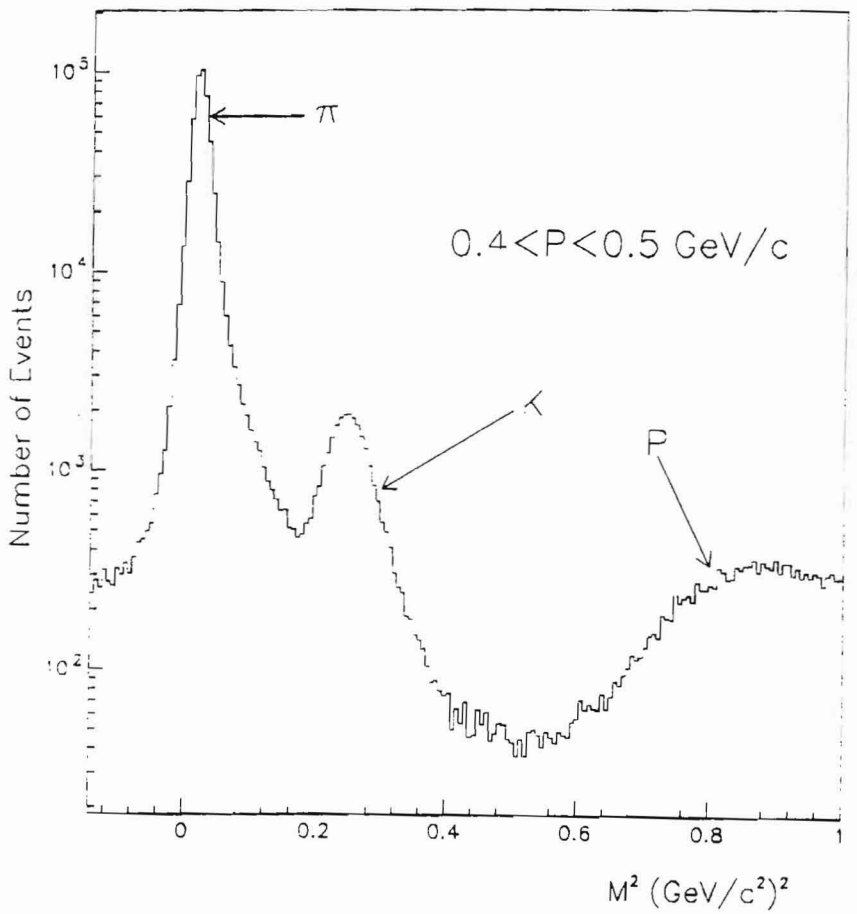

Figure 4.20: m^2 spectrum using TOF1 for the momentum range: $0.4 < m^2 < 0.5$ GeV/c. The vertical axis is plotted on a log scale.

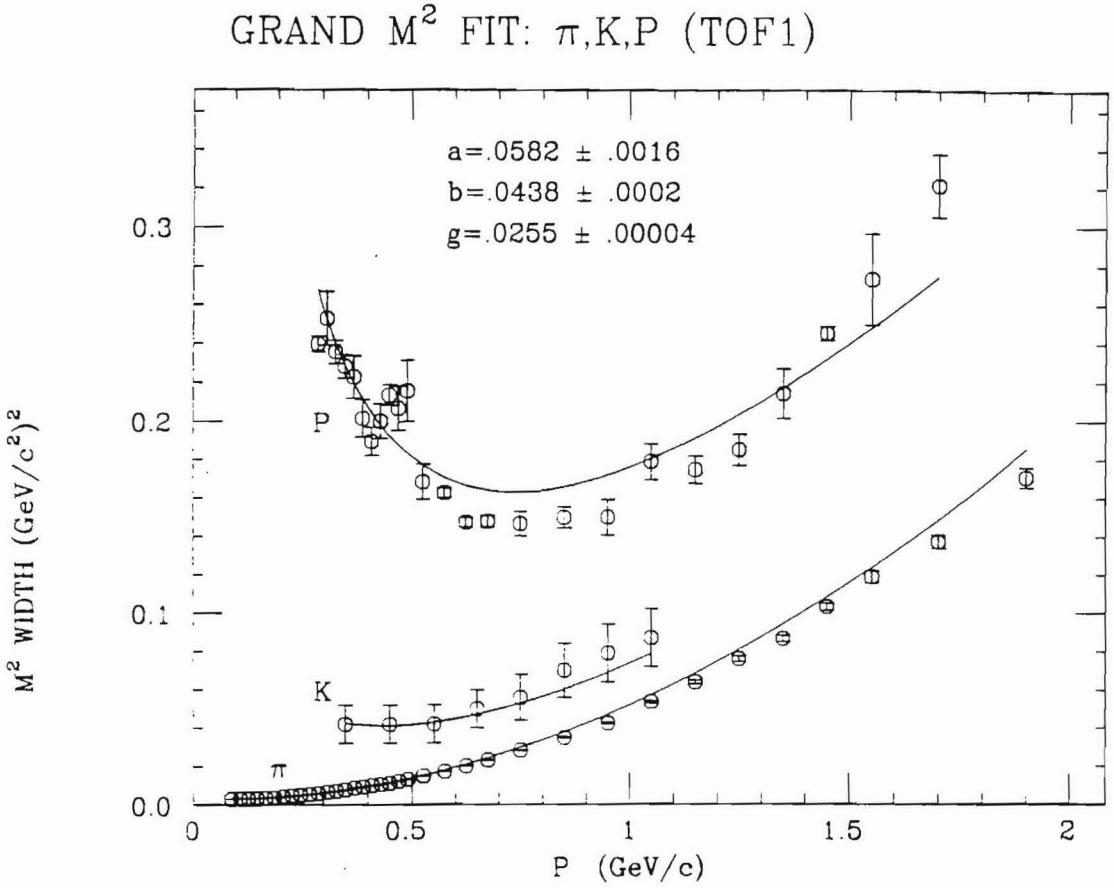

Figure 4.21: Pion, kaon, and proton m^2 widths computed with TOF_1 system.

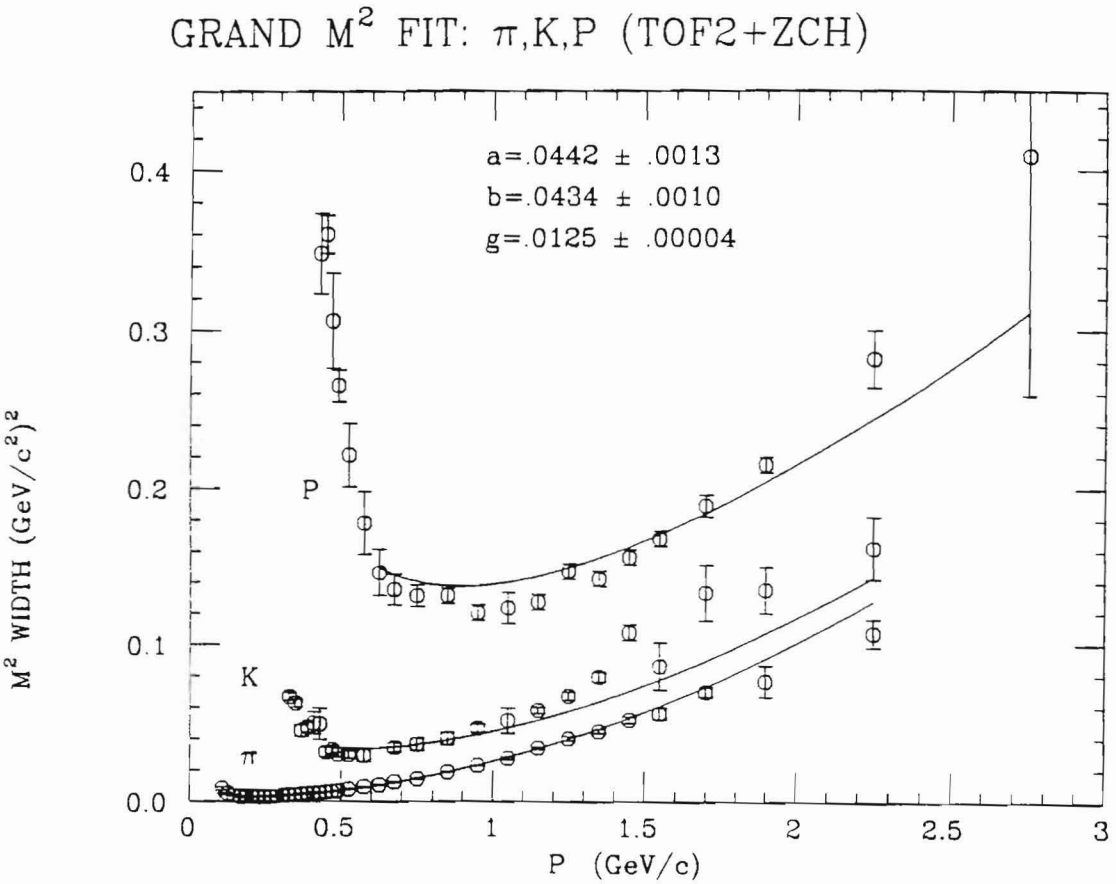

Figure 4.22: Pion, kaon, and proton m^2 widths computed with TOF_2 system. Each track in this plot uses at least one z-chamber hit.

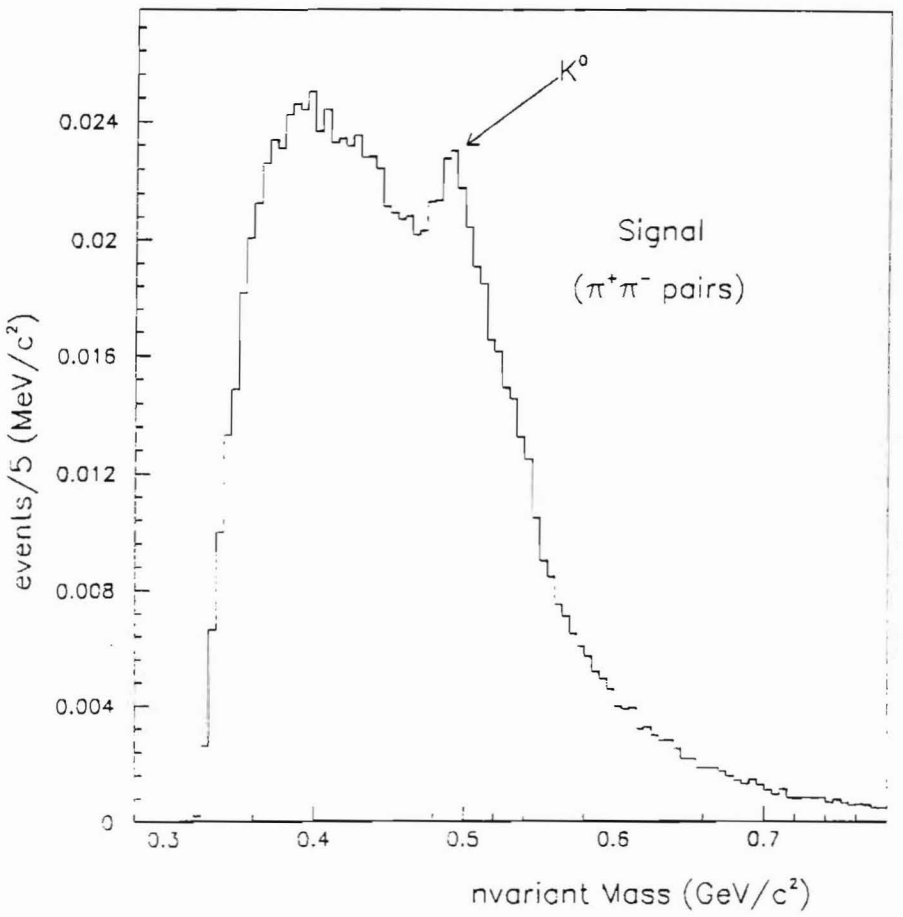

Figure 4.23: Invariant mass distribution of $\pi^+\pi^-$ pairs under the application of the cuts mentioned in the text. A clear K^0 peak appears around 0.5 GeV/c^2.

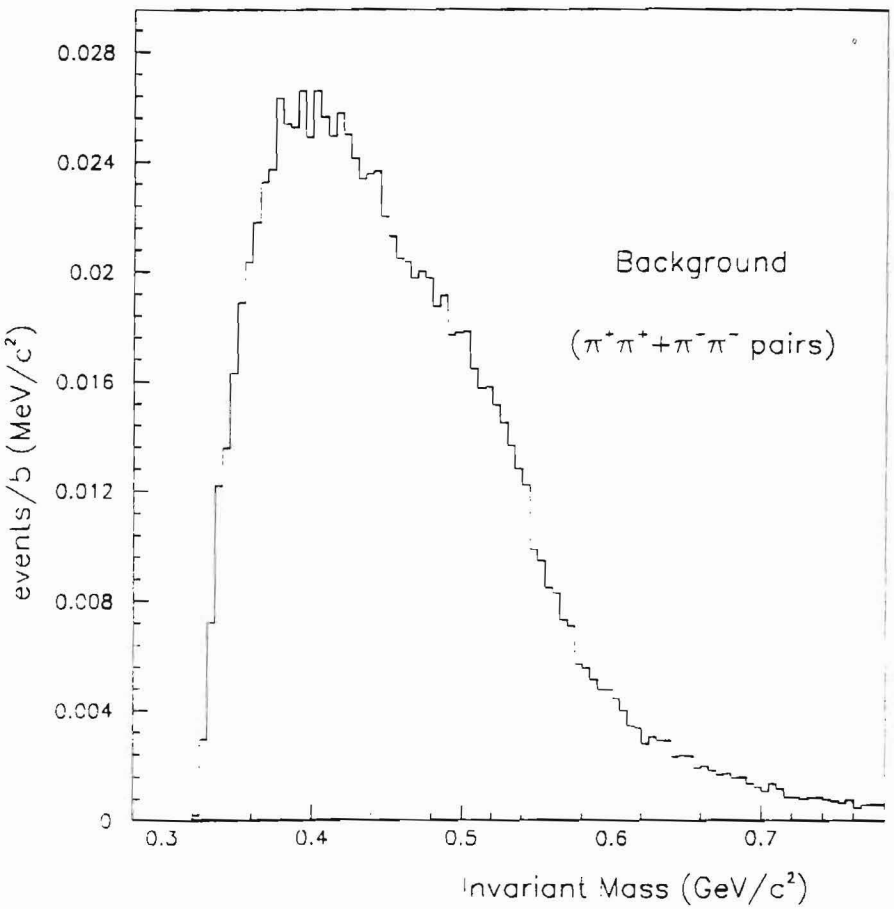

Figure 4.24: Invariant mass distribution of $\pi^+\pi^+$ and $\pi^-\pi^-$ like-sign pairs under the application of the cuts mentioned in the text. There is no indication of a fake K^0 peak around 0.5 GeV/c^2.

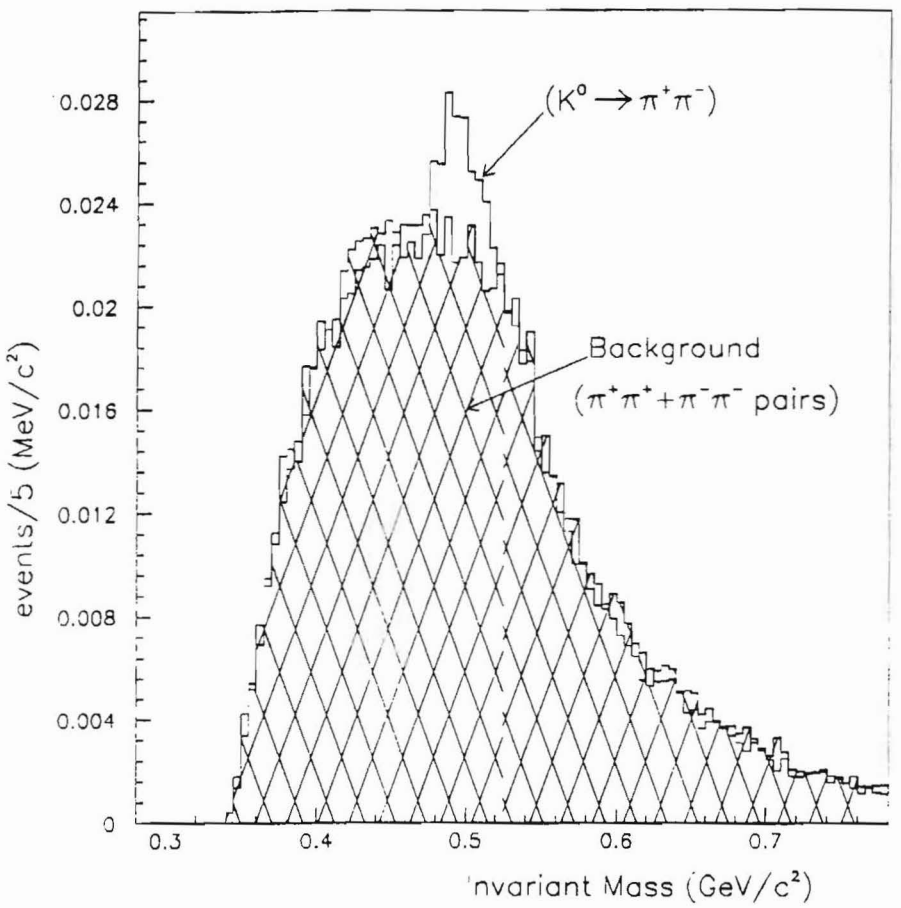

Figure 4.25: Invariant mass distribution of $\pi^+\pi^-$ pairs under the application of the cuts mentioned in the text and with total pair momentum $\geq$1.3 GeV/c superimposed with the corresponding invariant mass distribution of $\pi^+\pi^+$ and $\pi^-\pi^-$ pairs.

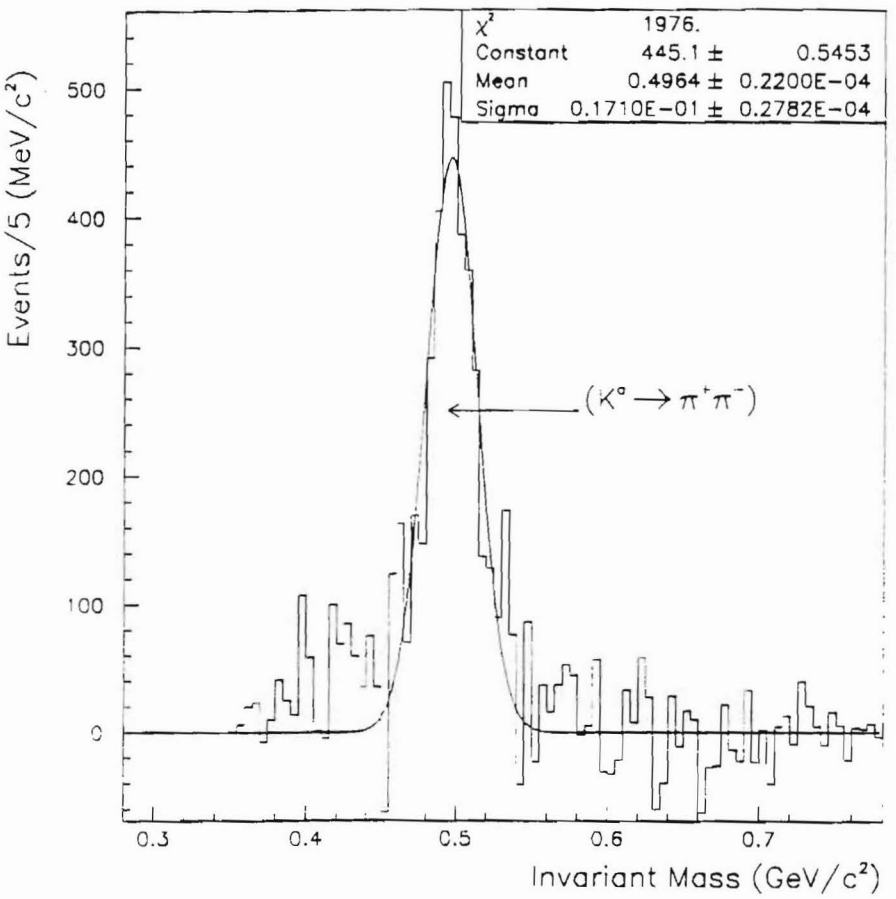

Figure 4.26: Invariant mass distribution of pion pairs after subtracting the background from the signal mass distribution.

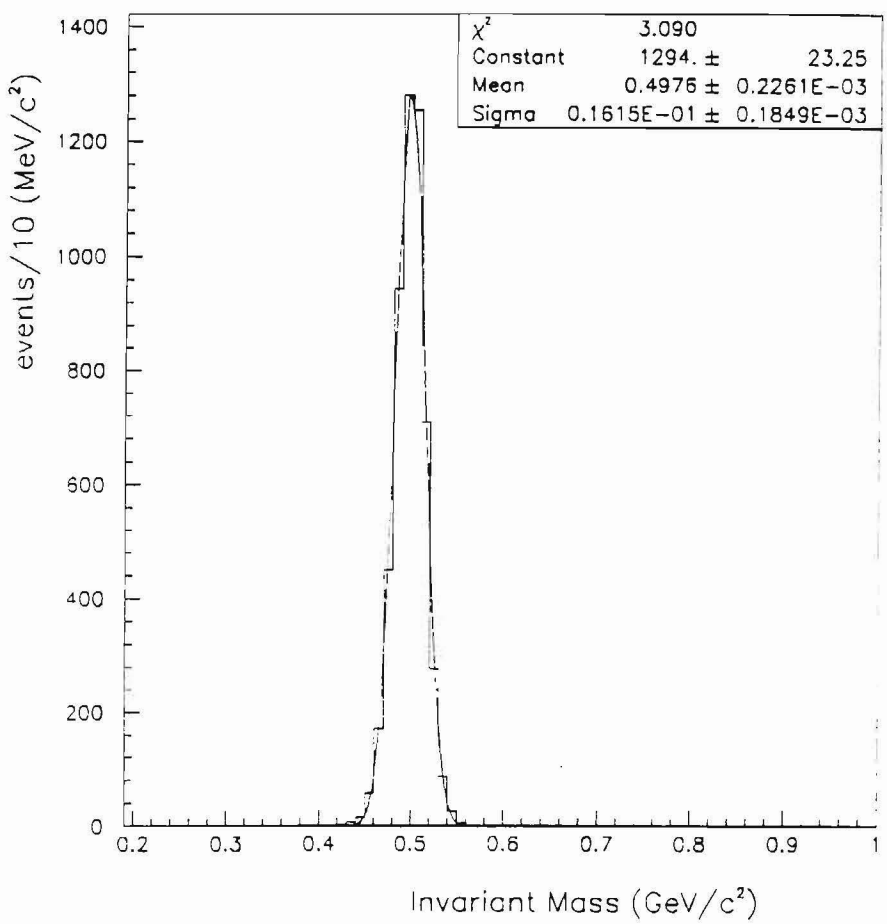

Figure 4.27: Invariant mass distribution of pion pairs using Monte Carlo K^0 decay data in the E735 detector.

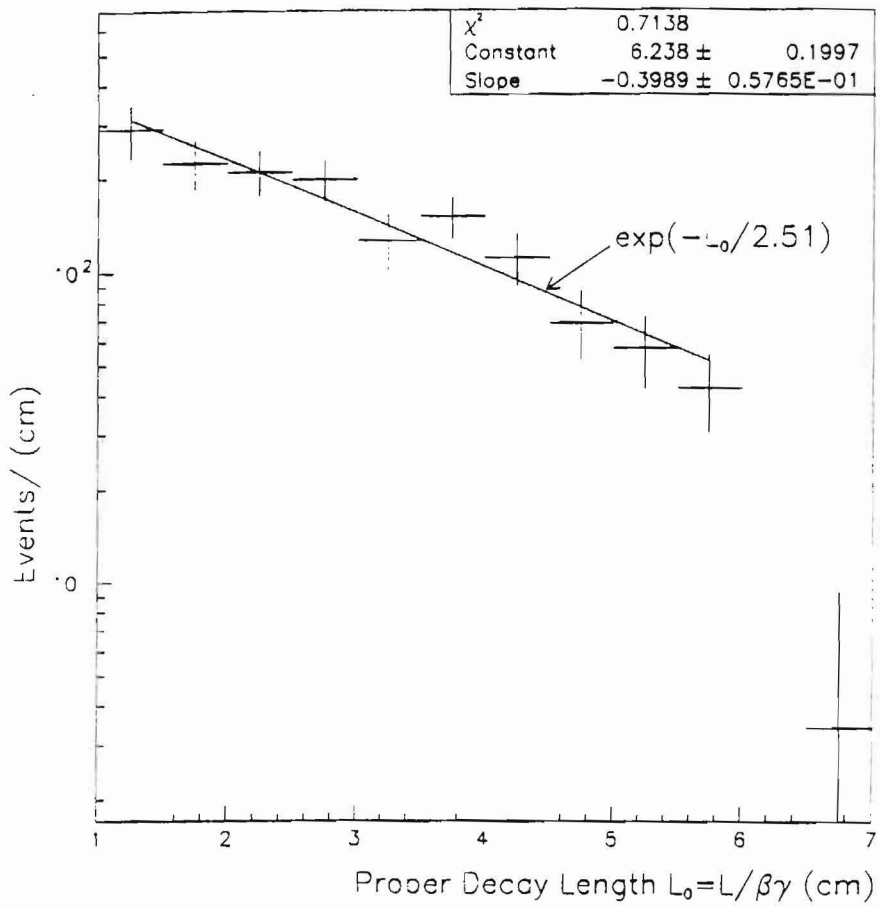

Figure 4.28: Proper decay-length ($L_0 = L/\beta\gamma$) distribution of K^0 measured from our data.The fitted curve is $\exp(-L_0/c\tau)$, where $c\tau$ is the K^0 lifetime of 2.5 ± 0.4 cm.

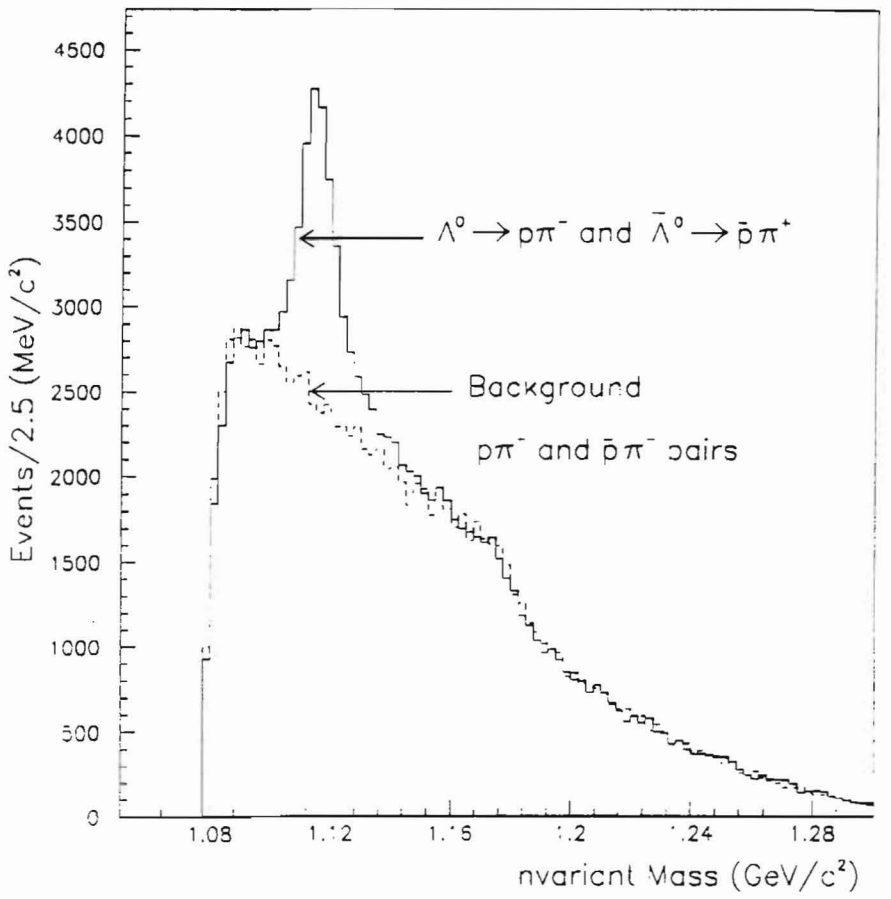

Figure 4.29: Invariant mass distribution of $p\pi^-$ and $\bar{p}\pi^+$ pairs (signal) superimposed with the invariant mass distribution of $p\pi^+$ and $\bar{p}\pi^-$ pairs (background) under the application of the cuts mentioned in the text. A clear $\Lambda^0 + \bar{\Lambda}^0$ peak appears around 1.115 GeV/c^2.

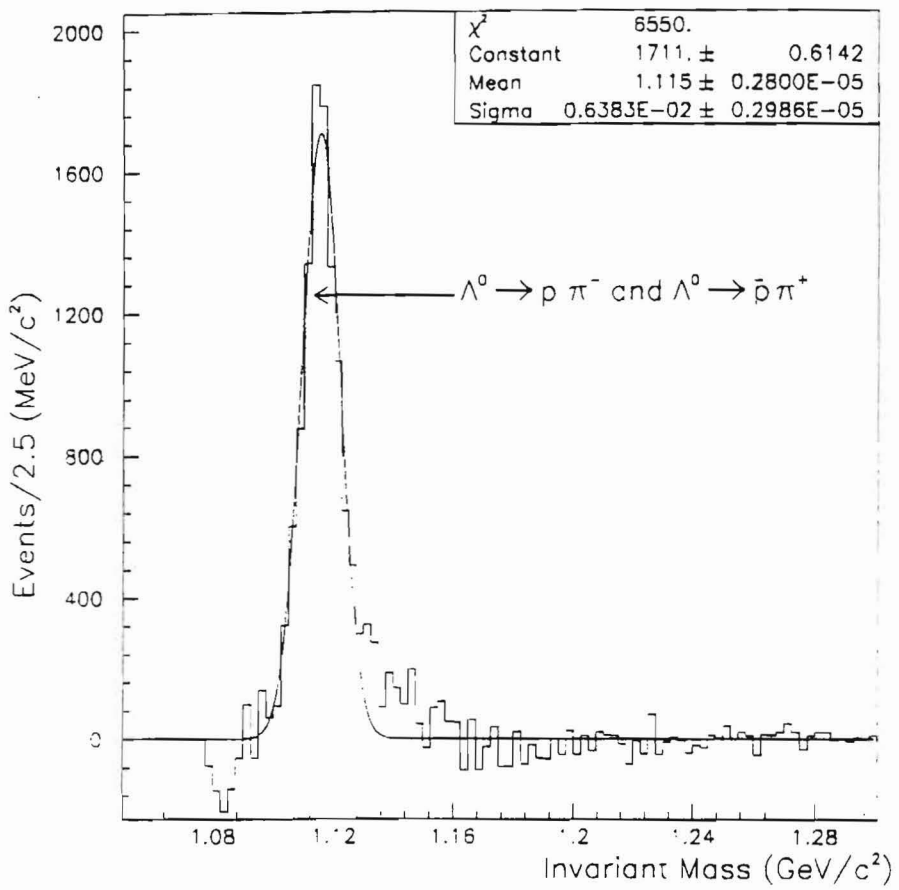

Figure 4.30: Invariant mass distribution of $p\pi^-$ and $\bar{p}\pi^+$ pairs after subtracting the background from the signal mass distribution.

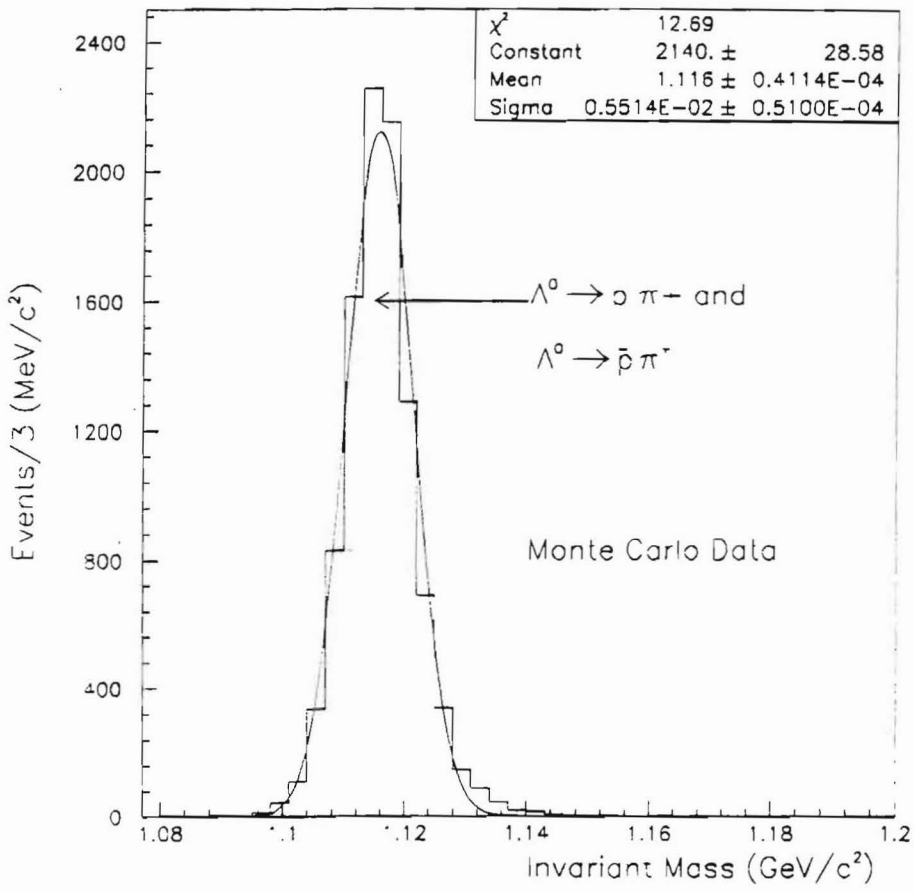

Figure 4.31: Invariant mass distribution of $\Lambda^0 + \bar{\Lambda}^0$ using Monte Carlo decays in the E735 detector.

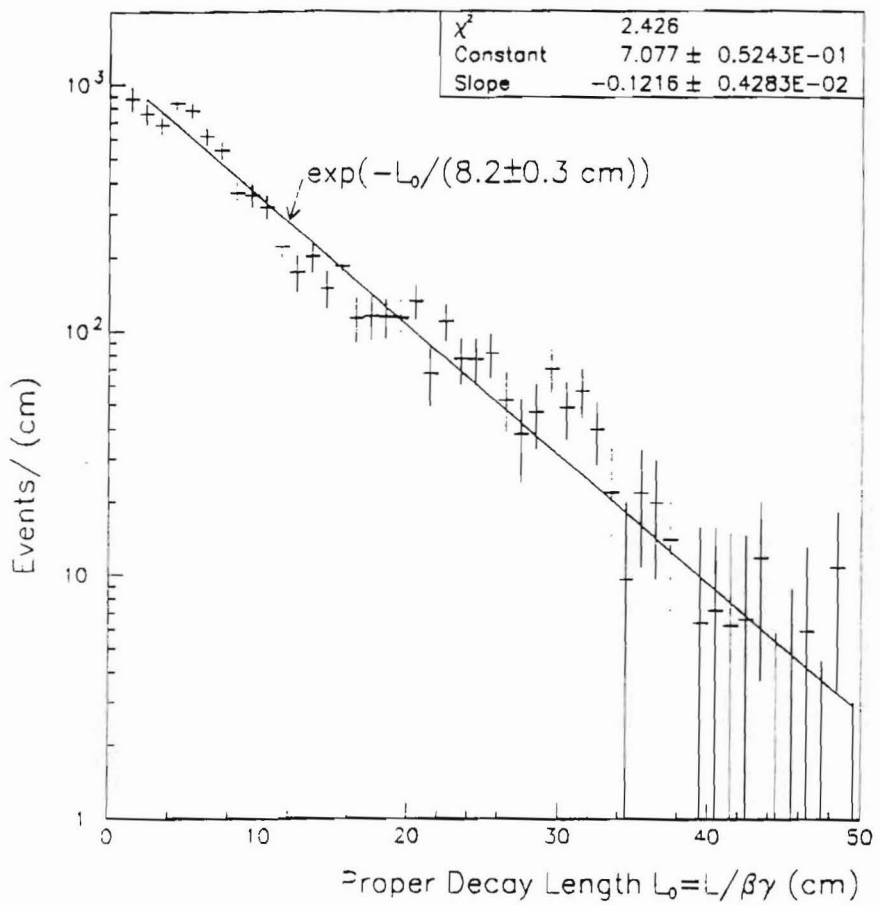

Figure 4.32: Proper decay-length ($L_0 = L/\beta\gamma$) distribution of $\Lambda^0 + \bar{\Lambda}^0$ measured from our data. The fitted curve is $\exp(-L_0/c\tau)$, where τ is the lifetime of $\Lambda^0 + \bar{\Lambda}^0$.

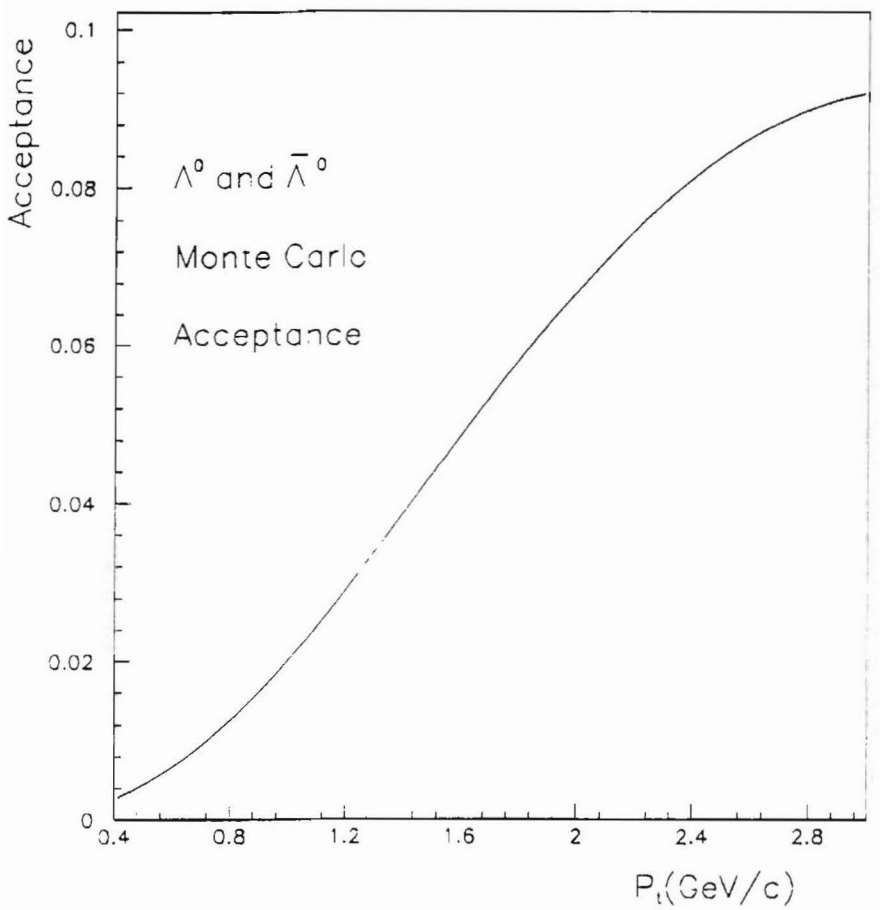

Figure 4.33: P_t acceptance curve of lambdas in the spectrometer.

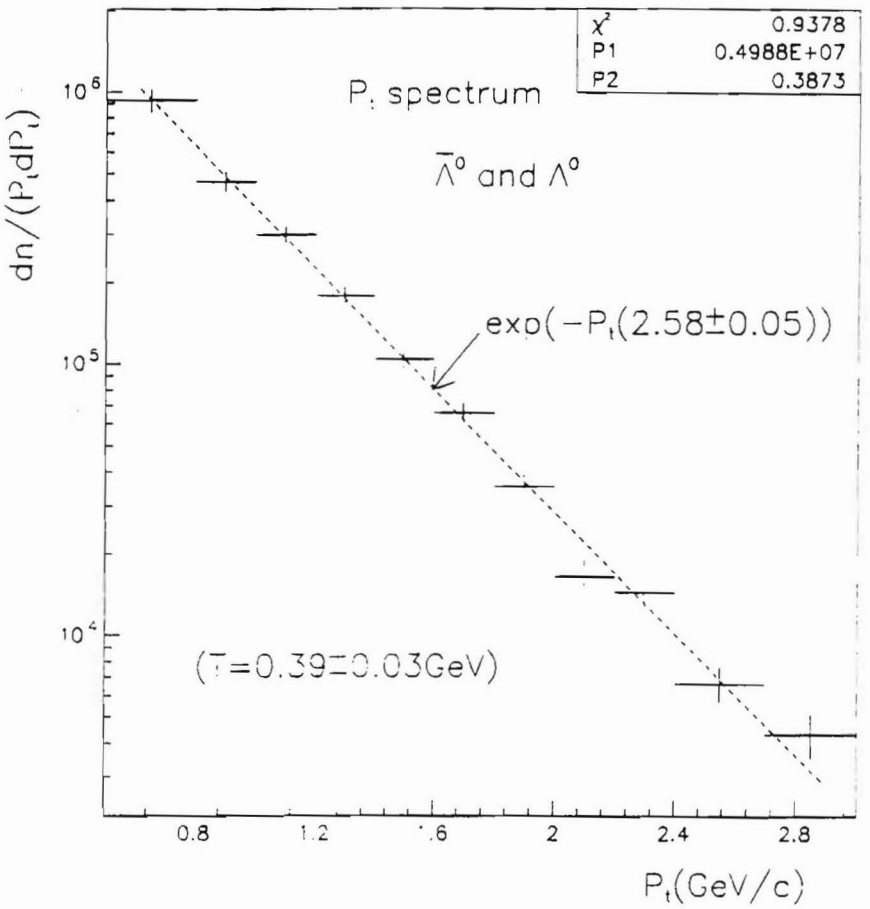

Figure 4.34: Momentum distribution dn/dp_t^2 for $\Lambda^0 + \bar{\Lambda}^0$. The fitted curve is an exponential curve, as described in the text.

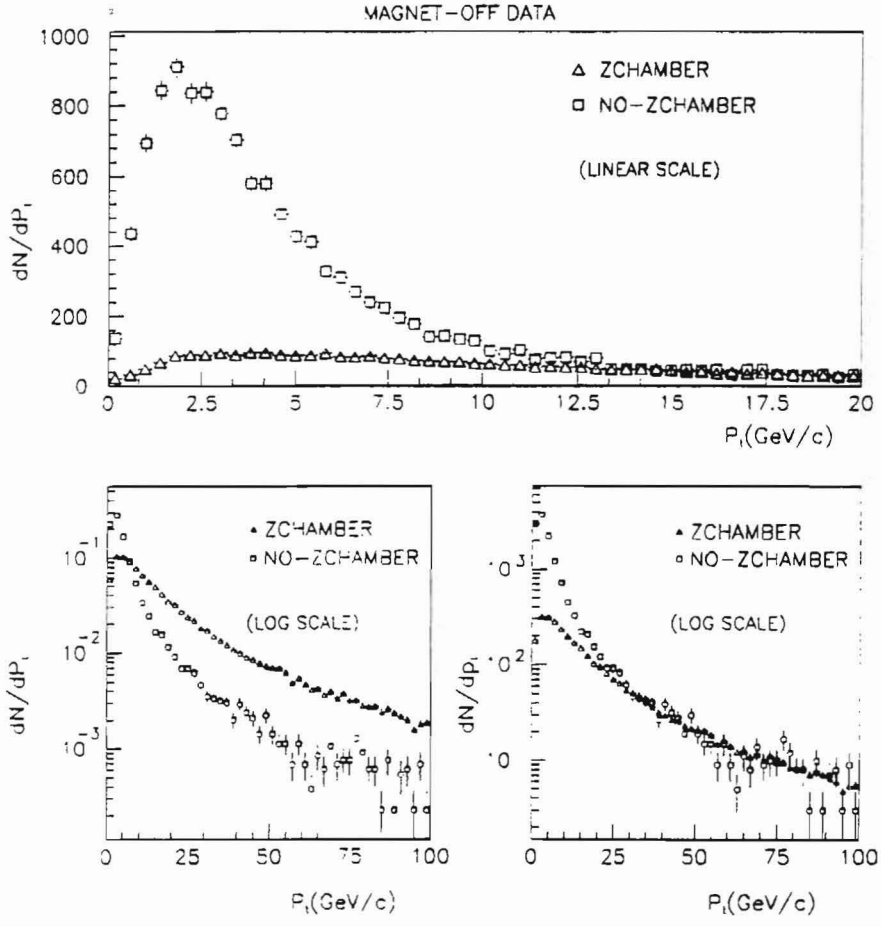

Figure 4.35: p_t spectrum using tracked Magnet-off data. All three figures use the same data, however, the difference is in the normalization constant and in the p_t scale.

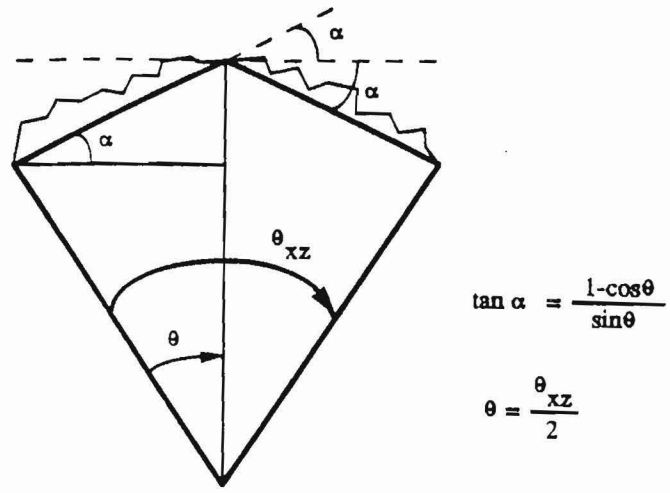

(a)

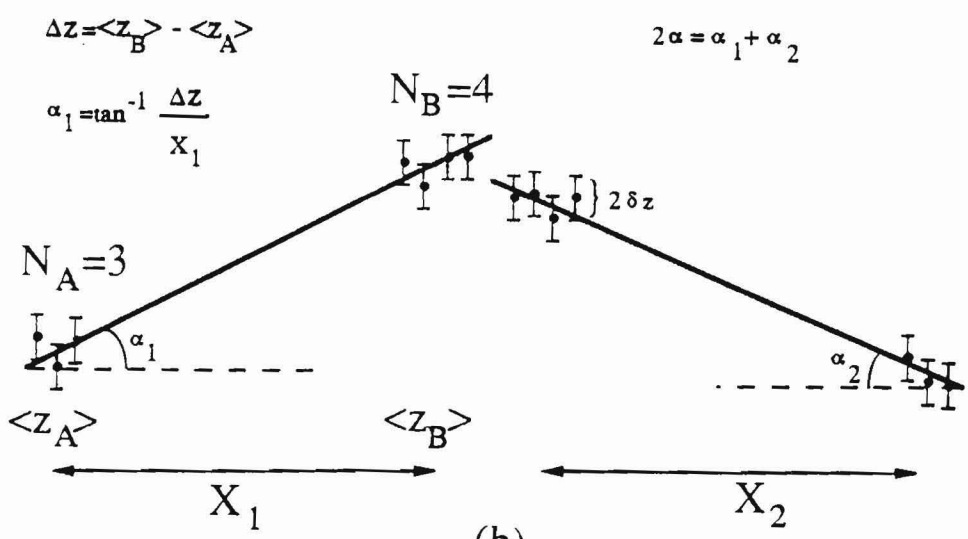

(b)

Figure 4.36: (a) Field-free track which is bent due to multiple scattering. (b) Two tracks whose slopes are effectively determined by clusters of points at each end of a track with each point having the same measuring error, δz.

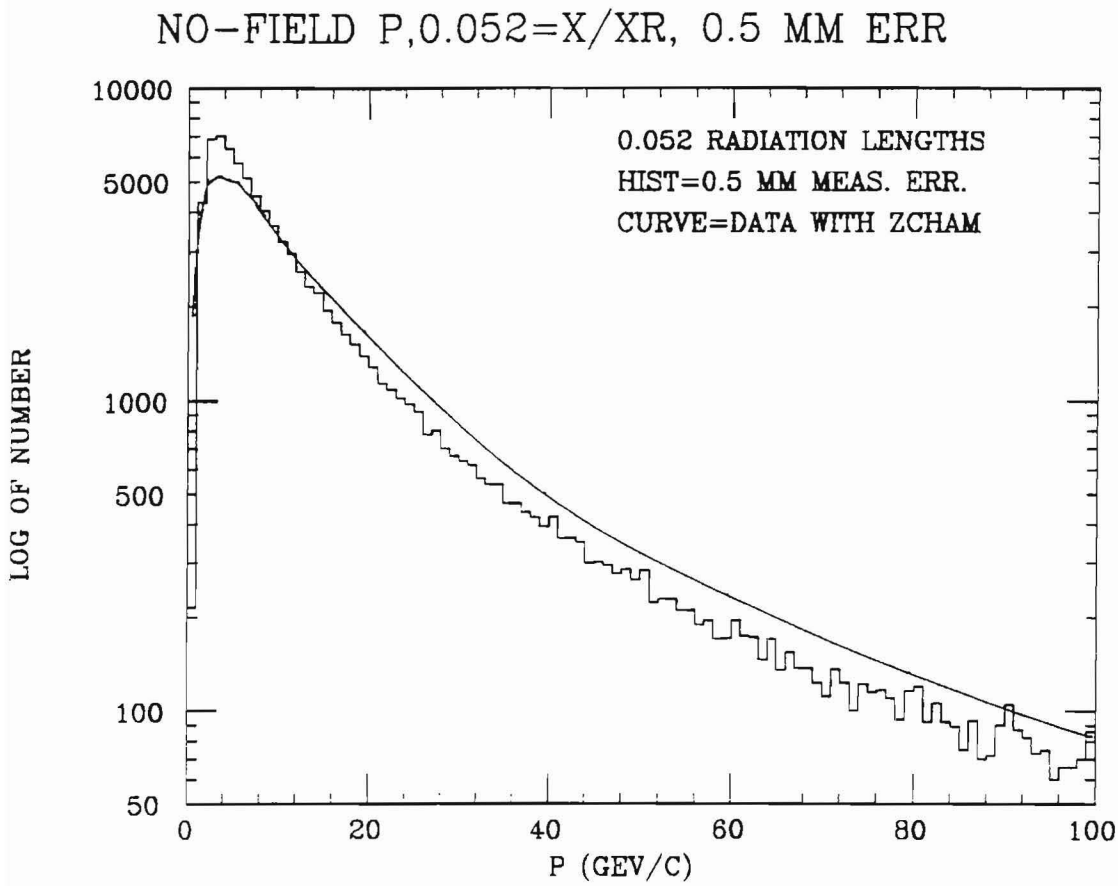

Figure 4.37: Monte Carlo p_t spectrum compared to a transverse momentum, P_T, spectrum from magnet-off data.

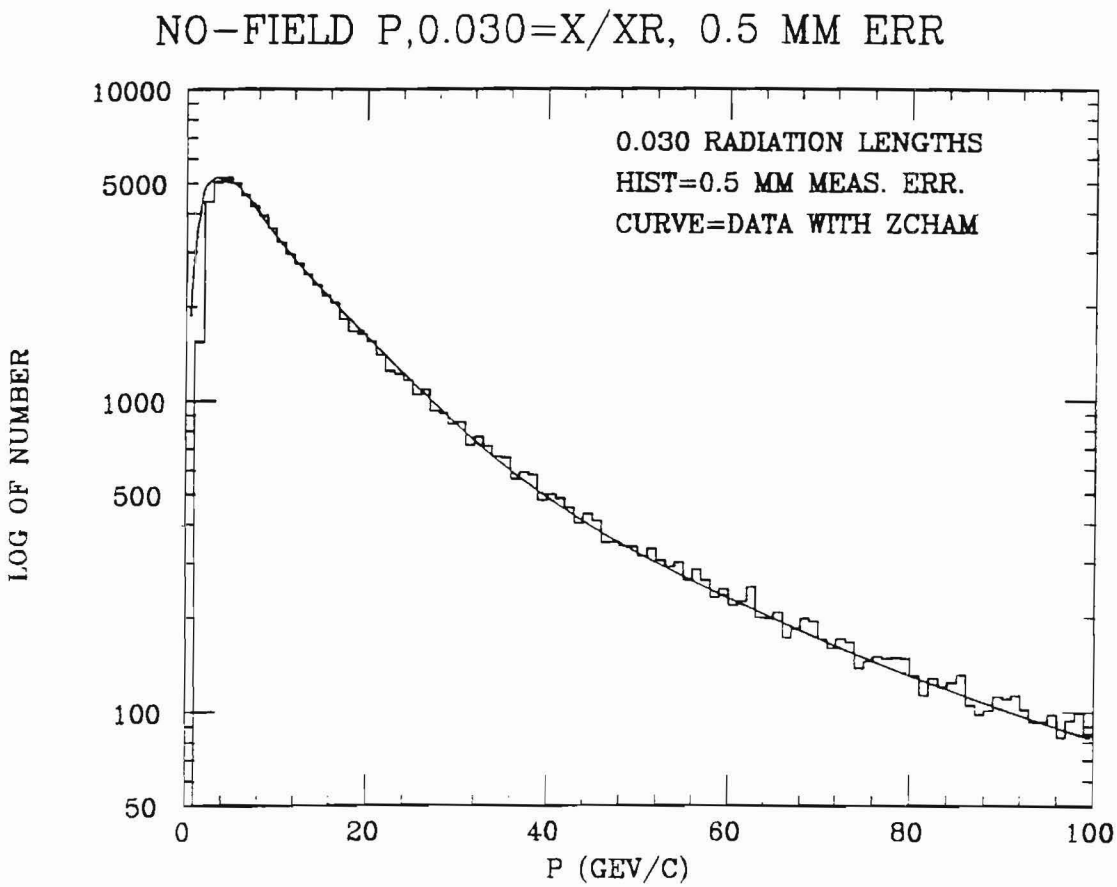

Figure 4.38: Monte Carlo p_t spectrum using 0.030 radiation lengths compared to a transverse momentum P_T spectrum from magnet-off data.

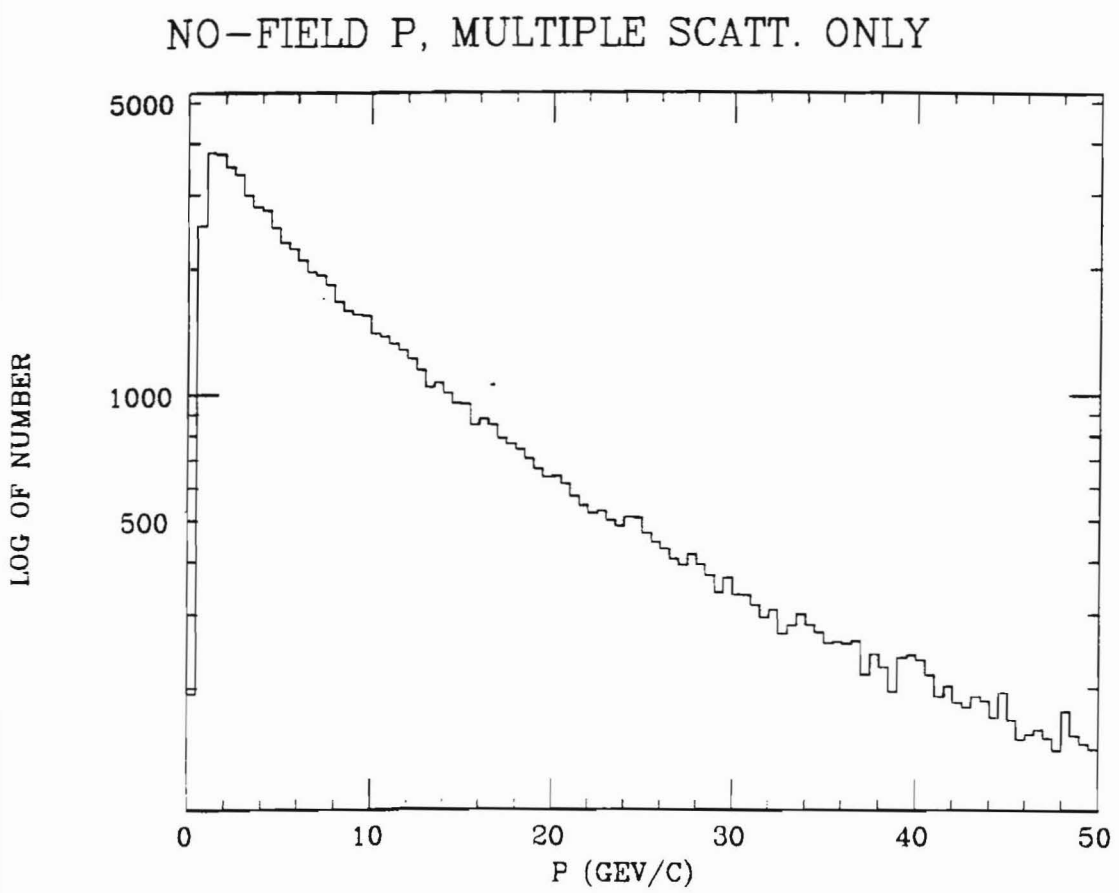

Figure 4.39: Monte Carlo no-field momentum spectrum using only multiple scattering from 0.030 radiation lengths.

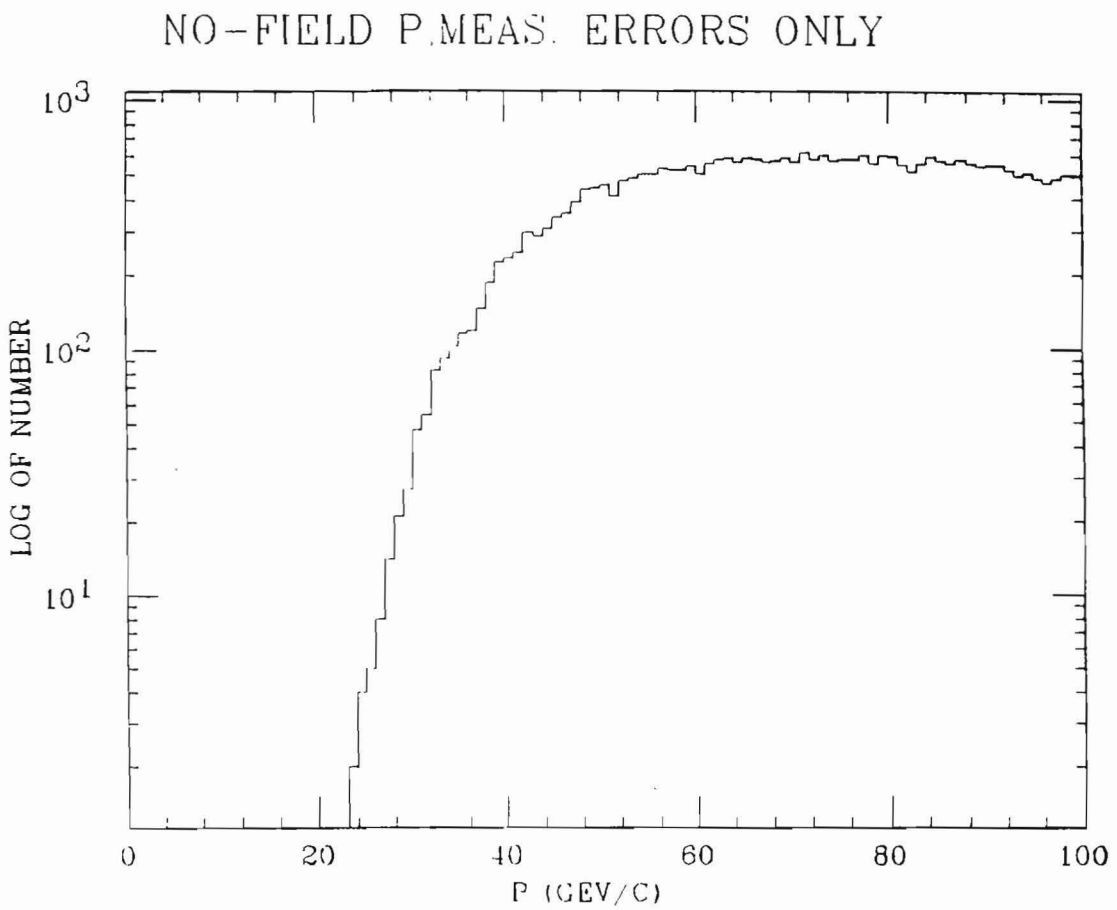

Figure 4.40: Monte Carlo no-field momentum spectrum using only a 500 micron measuring error.

Chapter 5

Resonance Search Using Neural Network Method

In this chapter a neural network method for identifying particle resonances is studied. A feed-forward neural network is used to construct an efficient mapping between certain observed kinematical variables and the resonance and background characteristics. The technique is applied to K^0, ρ^0, K^{*0}, and Λ^0 resonance searches revealing strong peaks in the invariant mass distributions. Due to our limited spectrometer acceptance, the search for the above mentioned resonances is quite a difficult problem. Figure 5.1 shows the invariant mass distribution of $\pi^+\pi^-$ pairs after track selection cuts. There is no indication of a K^0 or ρ^0 peak. The neural network method provides a way to eliminate the background events by selecting track pairs with the correct signal characteristics.

A short description of the feed-forward Neural Networks (NN) method will be presented in the next section and the so-called "backpropagation" technique will be analyzed. Furthermore, a series of resonance searches will be performed in order to test the NN method.

5.1 Neural Network Method

Neural Networks (NN) have come into use lately on a wide variety of pattern recognition applications in high energy physics such as track reconstruction, electron identification, B-jet recognition, problem of correctly pairing photons from π^0, η, and higher resonance decays in the presence of a high background of photons resulting from many simultaneous decays [71] etc. Here a Neural Network method for identifying resonances in the presence of a high background environment is examined. Using a feed-forward network structure, it is possible to obtain an efficient mapping between certain observed kinematical variables of resonance (signal) and background characteristics. The network analysis technique presents a promising alternative to the problem of identifying resonances through conventional cuts for various characteristic variables for the specific decay.

The Neural Network analysis gives a method of constructing a mapping, f, between a set of observable input quantities, $\vec{x} = (x_1, ..., x_k, ...)$, and output variables, $\vec{y} = (y_1, ..., y_i, ...)$, such that $\vec{y} = f(\vec{x})$. This is done by fitting $f(\vec{x})$ to a set of M known training patterns $(x_k^{(p)}; y_i^{(p)})$, $p = 1, ..., M$. Once the parameters in $f(\vec{x})$ are fixed, one uses this parameterization to find the features of test patterns not included in the training set.

The existence of this mapping is stated for the first time in "Kolmogorov's Mapping Neural Network Existence Theorem" [72].

Kolmogorov's Theorem: Given any continuous function $f : [0,1]^n \rightarrow R^m$, $f(\vec{x}) = \vec{y}$, f can be implemented exactly by a three-layer feedforward Neural Network having n fanouts processing elements in the first ($\vec{x}$-input)

layer, $(2n+1)$ processing elements in the middle layer, and m processing elements in the top ($\vec{y}$-output) layer.

The proof of this theorem given by Kolmogorov in the 1950's is not constructive, so it does not tell us how to determine transfer functions between the various layers. It is simply an existence theorem. Kolmogorov's theorem was a first step towards determining the mapping problem. Robert Hecht-Nielsen showed in 1978 that the backpropagation network (which will be discussed later) could implement any function of practical interest to any desired degree of accuracy. The backpropagation theorem is given [72] as follows.

Backpropagation Approximation Theorem: Given any $\epsilon > 0$ and any square-integrable function $f : [0,1]^n \rightarrow R^m$, there exists a three-layer backpropagation Neural Network that can approximate f to within ϵ mean squared error accuracy.

The ϵ mean squared error accuracy of a function $f(\vec{x})$ given by:

$$\int_{[0,1]^n} |f(\vec{x}) - \hat{f}(\vec{x})|^2 d\vec{x} < \epsilon, \tag{5.1}$$

where $\hat{f}(\vec{x})$ is the output of the Neural Network for an input vector $\vec{x}$.

In this analysis a three-layered feed-forward Neural Network architecture with analog-valued neurons, shown in Figure 5.2, was used. Our Neural Network consists of seven input neurons. x_k; one hidden layer with six neurons, h_j; and one output y_i that can take a value between 0 and 1. The equations governing the state of the network are [73] :

$$h_j = f(a_j), \tag{5.2}$$

and

$$y_i = f(a_i), \tag{5.3}$$

where $f(x)$ is the standard sigmoid function

$$f(x) = (1 + e^{-2x/T})^{-1}, \tag{5.4}$$

and a_i, a_j are given by the expressions:

$$a_j = \sum_{k=1}^{7} \omega_{jk} x_k - \theta_j, \tag{5.5}$$

$$a_i = \sum_{j=1}^{6} \omega_{ij} h_j - \theta_i. \tag{5.6}$$

Finally w_{jk} are the synapses between layers k and j, while θ_j are the threshold potentials of the hidden neurons, and θ_i are the threshold potentials of the output neurons ($i = 1$ in this application). Training the network means that we demand that the synapses and threshold potentials be chosen for p patterns in the data such that the output deviation function,

$$D(w_{ij}, \theta_i, w_{jk}, \theta_j) = \frac{1}{2} \sum_p \sum_i (y_i^{(p)} - t_i^{(p)})^2, \tag{5.7}$$

becomes as small as possible, where $t_i^{(p)}$ is the desired *target* output for a specific pattern p and an output neuron i.

A very successful method, usually referred to as *error backpropagation*, is used to search for a minimum of the error surface defined by the above relation. For this purpose one computes the gradient of D with respect to every parameter and then changes the value of the parameters according to steepest descent method [74]. In the first step, the only synaptic connections defined are those at

the output neurons:

$$\delta w_{ij} = -\eta \frac{\partial D}{\partial w_{ij}} = \eta \sum_p \delta_i^{(p)} h_j^{(p)} + \alpha \delta w_{ij}^{old}, \tag{5.8}$$

and

$$\delta \theta_i = -\eta \frac{\partial D}{\partial \theta_i} = \eta \sum_p \delta_i^{(p)} + \alpha \delta \theta_i^{old}. \tag{5.9}$$

This makes use of the abbreviation

$$\delta_i^{(p)} = (t_i^{(p)} - f(a_i^{(p)}))f'(a_i^{(p)}), \tag{5.10}$$

where η is a learning strength parameter, $\alpha \delta w_{ij}^{old}$ is the so-called momentum term used in order to damp out oscillations and $f'(a_i^{(p)})$ is the first derivative of the function f. The learning parameter, η, should be chosen sufficiently small [73].

Correspondingly in the second step, the synaptic connections from the input to the hidden layer neurons are as follows:

$$\delta w_{jk} = -\eta \frac{\partial D}{\partial w_{jk}} = \eta \sum_p \delta_j^{(p)} x_k^{(p)} + \alpha \delta w_{jk}^{old}, \tag{5.11}$$

and

$$\delta \theta_j = -\eta \frac{\partial D}{\partial \theta_j} = \eta \sum_p \delta_j^{(p)} + \alpha \delta \theta_j^{old}, \tag{5.12}$$

with the abbreviation

$$\delta_j^p = (\sum_i \delta_i^{(p)} w_{ij}) f'(a_j^{(p)}). \tag{5.13}$$

$\eta = 0.001$ is the learning strength parameter and $\alpha = 0.5$ is the so called momentum term parameter. The procedure is repeated for each pattern p until the network has "learned" all patterns to a satisfactory level (as decided by the experimenter). The calculation of the weights of the neurons using the backpropagation technique was done by using the JETNET-1.1 software package [75].

5.2 $K^0 \rightarrow \pi^+\pi^-$ Signal

The above Neural Network technique was tested by searching a series of resonances. The first test was be the $K^0 \rightarrow \pi^+\pi^-$ search.

5.2.1 Training the Neural Network

Monte Carlo $K^0 \rightarrow \pi^+\pi^-$ events and background $\pi^+\pi^+$, $\pi^-\pi^-$ pairs through the E735 detetctor were used. (A complete description of the Monte Carlo simulation is given in Appendix A.)

Each K^0 event was created from a momentum distribution

$$\frac{dn}{dp_t} = e^{-p_t/T}, \tag{5.14}$$

where the transverse momentum $p_t = \sqrt{p_x^2 + p_y^2}$ and $T = 0.250$ GeV/c^2. In this simulation K^0's were generated uniformly in azimuth and rapidity within the range $0 < \phi < 20^0$ and $-2.1 < y < 2.1$, respectively. The vertex distribution of the generated K^0 comes from a Gaussian distribution with mean $z_v = 0$ cm and a standard deviation $\sigma_z = 35$ cm. Each K^0 decayed according to the following decay distribution:

$$\frac{dn}{dL} = e^{-L_0/2.7cm}, \tag{5.15}$$

where L_0 is the proper decay length of K^0 given by $L_0 = L/\beta\gamma$,

$$\beta = P_{K^0}/\sqrt{P_{K^0}^2 + M_{K^0}^2}, \tag{5.16}$$

and P_{K^0}, M_{K^0} are the total momentum and mass of the K^0, respectively. Each Monte Carlo K^0 event, (π^+ and π^- tracks) was followed through the E735 spec-

trometer. To each track a momentum error,

$$dp = 4\% p\sqrt{p^2 + \frac{1}{\beta^2}} \tag{5.17}$$

was assigned, where $\beta = p/\sqrt{p^2 + m_\pi^2}$. Each background event was generated by two tracks coming from a momentum distribution given by:

$$\frac{dn}{dp_t} = e^{-p_t/T}, \tag{5.18}$$

where the transverse momentum of the produced pion $p_t = \sqrt{p_x^2 + p_y^2}$, and $T = 0.150$ GeV/c^2. Both tracks were again followed through the entire E735 spectrometer. To each background track a momentum error given by Equation 5.17 was assigned. Each K^0 or background event represents a pattern that has to be learned by the Neural Network with the output neuron forced to be the desired as 1 or 0, respectively.

The input variables of the Neural Network are

$$(x_1, x_2, x_3, x_4, x_5, x_6, x_7) = (p_x^1, p_y^1, p_z^1, p_x^2, p_y^2, p_z^2, z_v), \tag{5.19}$$

where p_{x1}, p_{y1}, and p_{z1} are the three cartesian components of the momentum of the positive pion of the $\pi^+\pi^-$ pair, p_{x2}, p_{y2}, and p_{z2} are the three cartesian components of the momentum of the negative pion of the $\pi^+\pi^-$ pair and z_v is the vertex of the pair at the beam line. The output target value was assigned to be $t^{(p)} = 1$ for a K^0 pattern and 0 for a background event. The weights in the Neural Network are initialized at random with values in the interval $[-1, +1]$. For every pattern the connections and biases δw_{ij}, $\delta\theta_i$, δw_{jk}, and $\delta\theta_j$ are computed using the above expressions (Equations 5.8, 5.9, 5.11, and 5.12).

Figures 5.3 and 5.4 show the network performance vs training epoch. One training epoch is defined when the network has seen the entire training set once. It is clear that the Neural Network learns to recognize the features of a pattern after only a few epochs. If the output is greater than 0.5 a K^0 event was defined.

5.2.2 Test of K^0 Decays Using the Neural Network

Figures 5.5 and 5.6 show the invariant mass distribution of $\pi^+\pi^-$ (signal, real data) pairs identified as K^0 superimposed with the mass distribution of $\pi^+\pi^+$ and $\pi^-\pi^-$ pairs (background, real data) identified as K^0's for output neuron greater than 0.7 and 0.8, respectively. It is clear that the mass peak of the identified K^0 is around 500 MeV/c^2. By subtracting the background from the signal distribution, a clean Gaussian mass peak of K^0 was observed (Figures 5.7 and 5.8) with $M = 496$ MeV/c^2.

5.3 $\rho^0 \rightarrow \pi^+\pi^-$ Signal

Another example of a resonance search made using the Neural Network method is the $\rho^0 \rightarrow \pi^+\pi^-$ decay.

5.3.1 Training the Neural Network

Monte Carlo $\rho^0 \rightarrow \pi^+\pi^-$ signal events and background $\pi^+\pi^+$, $\pi^-\pi^-$ pairs were used. For this study, decays coming from $K^0 \rightarrow \pi^+\pi^-$ constituted part of the background.

First ρ^0 events from a delta function mass distribution centered at $M_{\rho^0} =$

0.770 GeV/c^2 were generated by

$$\frac{dn}{dM} = \delta(M - M_{\rho 0}), \tag{5.20}$$

where $M_{\rho 0}$ = 0.770 GeV/c^2 was the ρ^0 mass. (Subsequent reference to this analysis is Trial 1.)

A different Neural Network was studied for ρ^0 events created from a Gaussian mass distribution

$$\frac{dn}{dM} = e^{-(M-M_{\rho 0})^2/\sigma^2_{\rho 0}}, \tag{5.21}$$

(where $M_{\rho 0}$ = 0.770 GeV/c^2 was the ρ^0 mass, $\sigma_{\rho 0}$ = 0.065 GeV/c^2 was the intrinsic mass width of the ρ^0 decay). (Subsequently refer to this analysis as Trial 2.)

The transverse momentum distribution of the ρ^0 is assumed to be given by:

$$\frac{dn}{dp_t} = e^{-p_t/T}, \tag{5.22}$$

where $p_t = \sqrt{p_x^2 + p_y^2}$ and T = 0.300 GeV/c^2. In this simulation ρ^0 events were generated uniformly in azimuth and rapidity within the range $0 < \phi < 20^0$, and $-2.1 < y < 2.1$, respectively. Each ρ^0 was generated from the beam line with a Gaussian vertex distribution with mean z_v = 0 cm and a standard deviation σ_z = 35 cm. Each of the (π^+ and π^-) tracks was followed through the E735 spectrometer. To each track a momentum error given by Equation 5.17 was assigned. Each background event was generated from two tracks coming from a momentum distribution given by Equation 5.18. Again, both of these tracks were followed through the E735 spectrometer.

Each ρ^0 or background event represents a pattern that has to be learned by the Neural Network as in the previous example. Using the signal and background events, the network is "trained" to discriminate the ρ^0 pattern from the background pattern.

Figure 5.9 shows the network performance vs training epoch for trial 1. One training epoch is defined as one run through the complete data Monte Carlo set as in the case of the K^0 training section. It is clear that the Neural Network learns to recognize the feature of a pattern after only a few epochs.

5.3.2 Test of ρ^0 Decays Using the Neural Network

Figures 5.10 and 5.11 show the mass distribution of $\pi^+\pi^-$ (signal) pairs of the pairs identified as a ρ^0 superimposed with the mass distribution of $\pi^+\pi^+$ and $\pi^-\pi^-$ pairs (background) identified as ρ^0's for output neuron greater than 0.8 and 0.9, respectively. (Figure 5.14 shows the distribution of the output neuron of Trial 1.) It is clear that the mass peak of the identified ρ^0 is around 770 MeV/c^2. By subtracting background from the signal distribution a clean mass peak of ρ^0 (Figures 5.12 and 5.13) was observed.

Figure 5.15 shows the distribution of the output neuron of Trail 2. Figure 5.16 shows the subtracted background mass distribution of $\pi^+\pi^+$ and $\pi^-\pi^-$ pairs from the signal mass distribution of $\pi^+\pi^-$ pairs. Again, a clean ρ^0 mass is found for output neuron greater than 0.7. A K^0 peak also appears in this plot. The K^0 in the ρ mass plot appears as a consequence of the large overlap of the K^0 and ρ^0 patterns. Requiring a greater value of the network output neuron (shown in

Figure 5.15) reduces the magnitude of the K^0 peak.

5.4 $K^{*0} \rightarrow \pi K$ Signal

One more example of resonance searches made using the Neural Network method is the $K^{*0} \rightarrow \pi K$ decay.

5.4.1 Training the Neural Network

Monte Carlo $K^{*0} \rightarrow \pi^- K^+$ and $\bar{K}^{*0} \rightarrow \pi^+ K^-$ were used for signal events and $\pi^+ K^+$, $K^- \pi^-$ pairs for background events.

K^{*0} events from a delta function mass distribution were generated, centered at $M_{K^{*0}} = 0.892$ GeV/c^2

$$\frac{dn}{dM} = \delta(M - M_{K^{*0}}), \tag{5.23}$$

where $M_{K^{*0}} = 0.892$ GeV/c^2 is the K^{*0} mass.

The transverse momentum distribution of the K^{*0} is assumed to be given by:

$$\frac{dn}{dp_t} = e^{-p_t/T}, \tag{5.24}$$

where $p_t = \sqrt{p_x^2 + p_y^2}$ and $T = 0.250$ GeV/c^2. In this simulation K^{*0} events were generated uniformly in azimuth and rapidity within the range $0 < \phi < 20^0$ and $-2.1 < y < 2.1$, respectively. Each K^{*0} was generated from the beam line with a Gaussian vertex distribution with mean $z_v = 0$ cm and a standard deviation $\sigma_z = 35$ cm. Each of the (K and π) tracks was followed through the E735 spectrometer. To each track a momentum error of Equation 5.17 was assigned. Each background event was generated from two tracks coming from a momentum

distribution given by Equation 5.18. Again, both of these tracks were followed through the E735 spectrometer. To each background track a momentum error of Equation 5.17 was assigned.

Each K^{*0} or background event represents a pattern that has to be learned by the Neural Network, as in the previous example. Using the signal and background events the network is "trained" to discriminate the K^{*0} pattern from the background pattern.

5.4.2 Test of K^{*0} Decays Using the Neural Network

Figure 5.17 shows the subtracted signal mass distribution of $K^+\pi^-, K^-\pi^+$ pairs from the background mass distribution of $K^+\pi^+$ and $K^-\pi^-$ pairs. A clean K^{*0} mass is found for output neuron greater than 0.7. The width of the K^{*0} is close to the one predicted by the convolution of the intrinsic mass width with the the mass width obtained from the momentum resolution.

5.5 $\Lambda^0 \rightarrow \pi p$ Signal

Finally, $\Lambda^0 \rightarrow \pi^- p^+$ resonance search was made using the Neural Network method.

5.5.1 Training the Neural Network

Monte Carlo $\Lambda^0 \rightarrow \pi^- p^+$ and $\bar{\Lambda}^0 \rightarrow \pi^+ \bar{p}$ for signal events and $p^+\pi^+$, $\bar{p}\pi^-$ pairs for background events were generated.

Λ^0 events from a delta function mass distribution were generated centered at

$M_{\Lambda^0} = 1.115$ GeV/c^2.

$$\frac{dn}{dM} = \delta(M - M_{\Lambda^0}). \tag{5.25}$$

The transverse momentum distribution of the Λ^0 is assumed to be given by:

$$\frac{dn}{dp_t} = e^{-p_t/T}, \tag{5.26}$$

where $p_t = \sqrt{p_x^2 + p_y^2}$ and $T = 0.400$ GeV/c^2. In this simulation Λ^0 events were generated uniformly in azimuth and rapidity within the range $0 < \phi < 20^0$ and $-2.1 < y < 2.1$, respectively. Each Λ^0 was generated from the beam line with a Gaussian vertex distribution with mean $z_v = 0$ cm and a standard deviation $\sigma_z = 35$ cm. Each of the (p and π) tracks was followed through the E735 spectrometer. To each track a momentum error of Equation 5.17 was assigned. Each background event was generated from two tracks coming from a momentum distribution given by Equation 5.18. Again, both of these tracks were followed through the E735 spectrometer. To each background track a momentum error of Equation 5.17 was assigned.

Each Λ^0 or background event represents a pattern that has to be learned by the Neural Network, as in the previous example. Using the signal and background events the network is "trained" to discriminate the Λ^0 pattern from the background pattern.

5.5.2 Test of Λ^0 Decays Using the Neural Network

Figure 5.18 shows the subtracted signal mass distribution of $p^+\pi^-$, $\bar{p}\pi^+$ pairs from the background mass distribution of $p^+\pi^+$ and $p^-\pi^-$ pairs. A clean Λ^0 mass is found for output neuron greater than 0.5. The number of lambdas found

with this method is 8,000. Note that the number of lambdas found with the conventional method of Section 4.6.3 is 10,000. This can be easily explained due to inefficiency of the neural network. Examination of the learning curve reveals for Monte Carlo lambda events an identification efficiency of only 80%.

Figures for Chapter 5

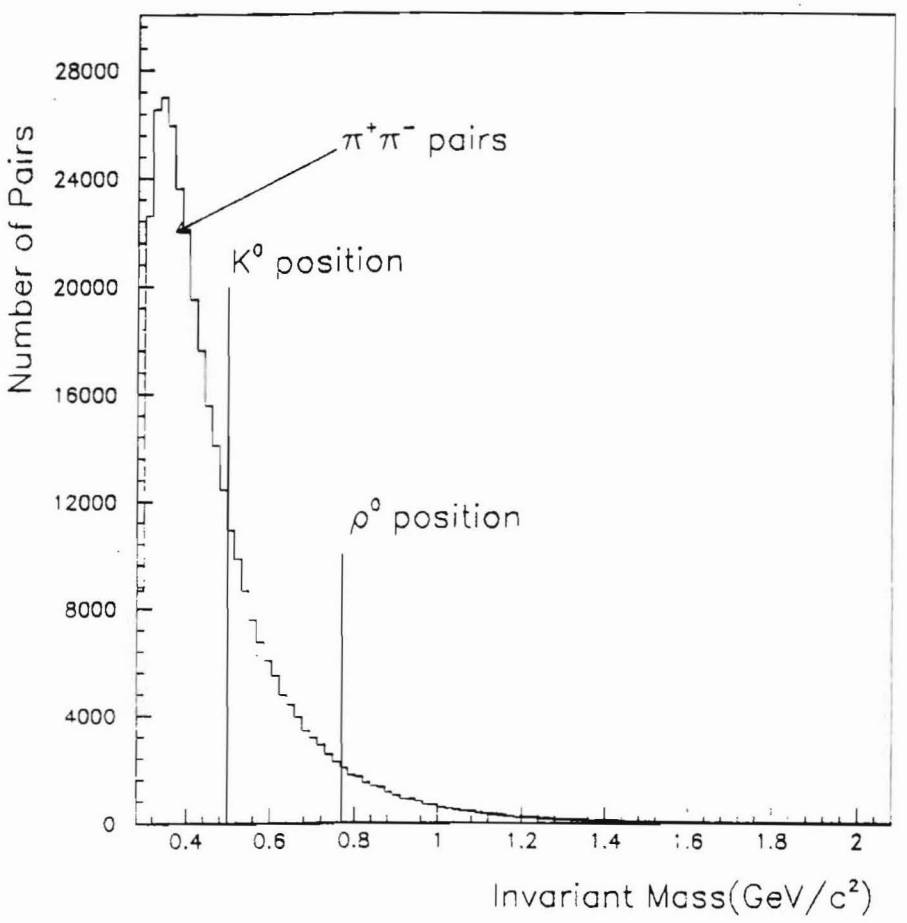

Figure 5.1: Invariant mass distribution of $\pi^+\pi^-$ pairs accepted by the E735 spectrometer.

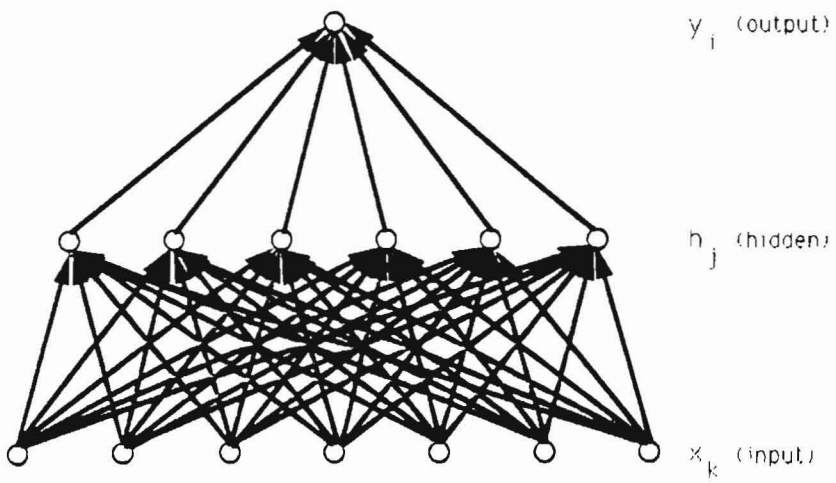

Figure 5.2: Architecture of a three layer feed-forward neural network.

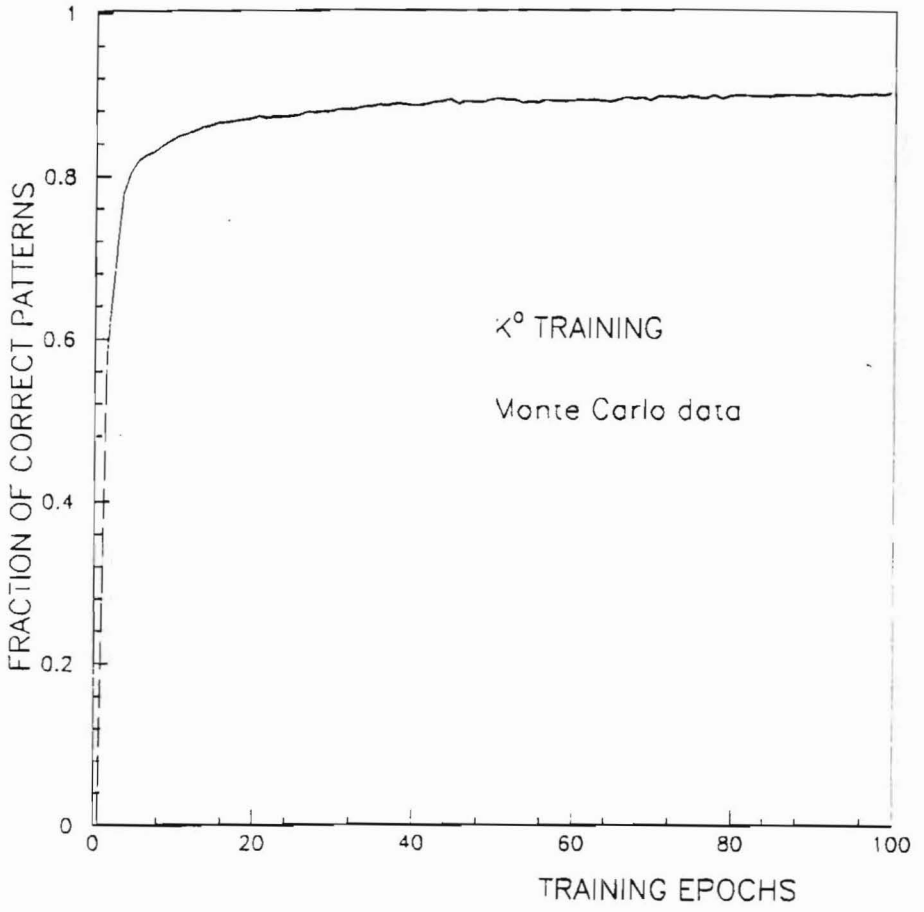

Figure 5.3: Fraction of correct classifications versus training epochs for the first 100 epochs in the K^0 search.

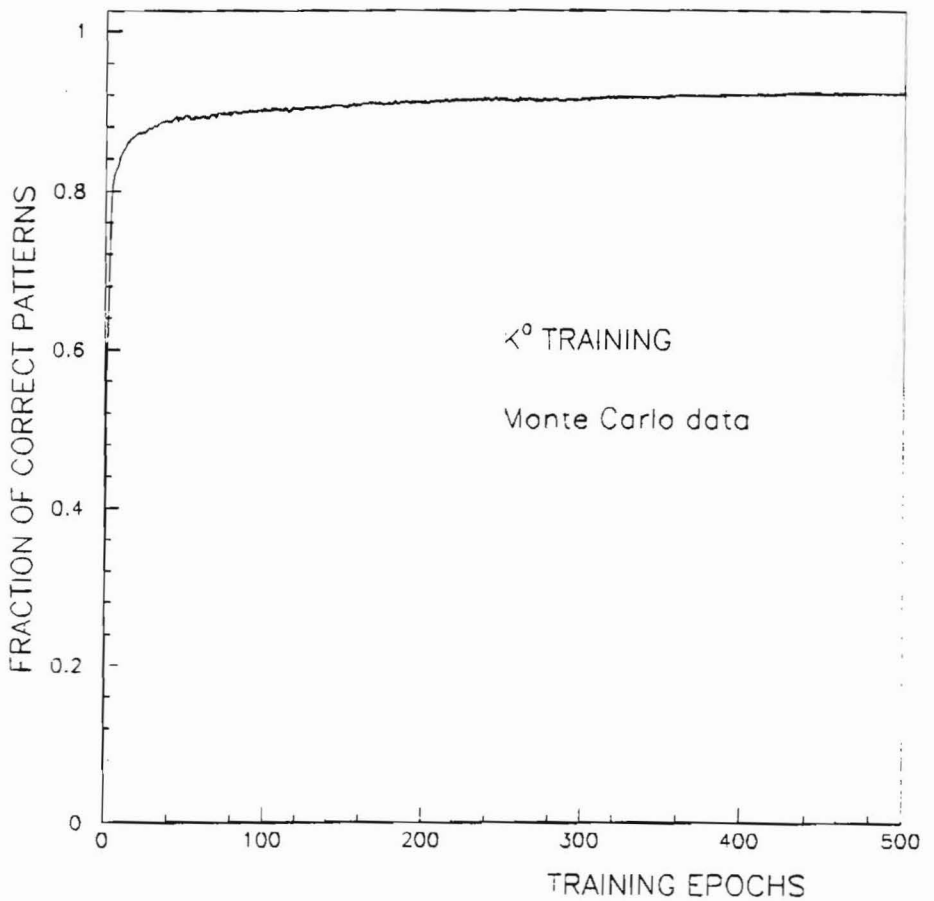

Figure 5.4: Fraction of correct classifications versus training epochs for the first 500 epochs in the K^0 search.

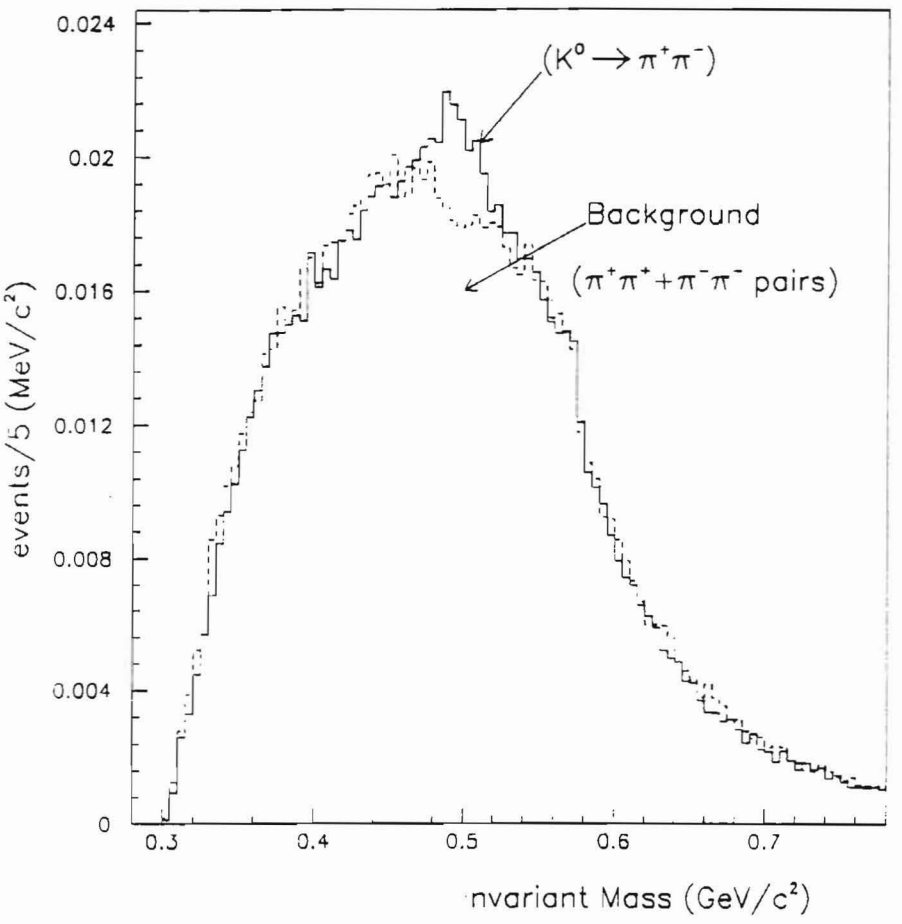

Figure 5.5: Invariant mass distribution of $\pi^+\pi^-$ pairs (signal) superimposed with the invariant mass distribution of $\pi^+\pi^+$, $\pi^-\pi^-$ pairs (background) with the neuron output value greater than 0.7.

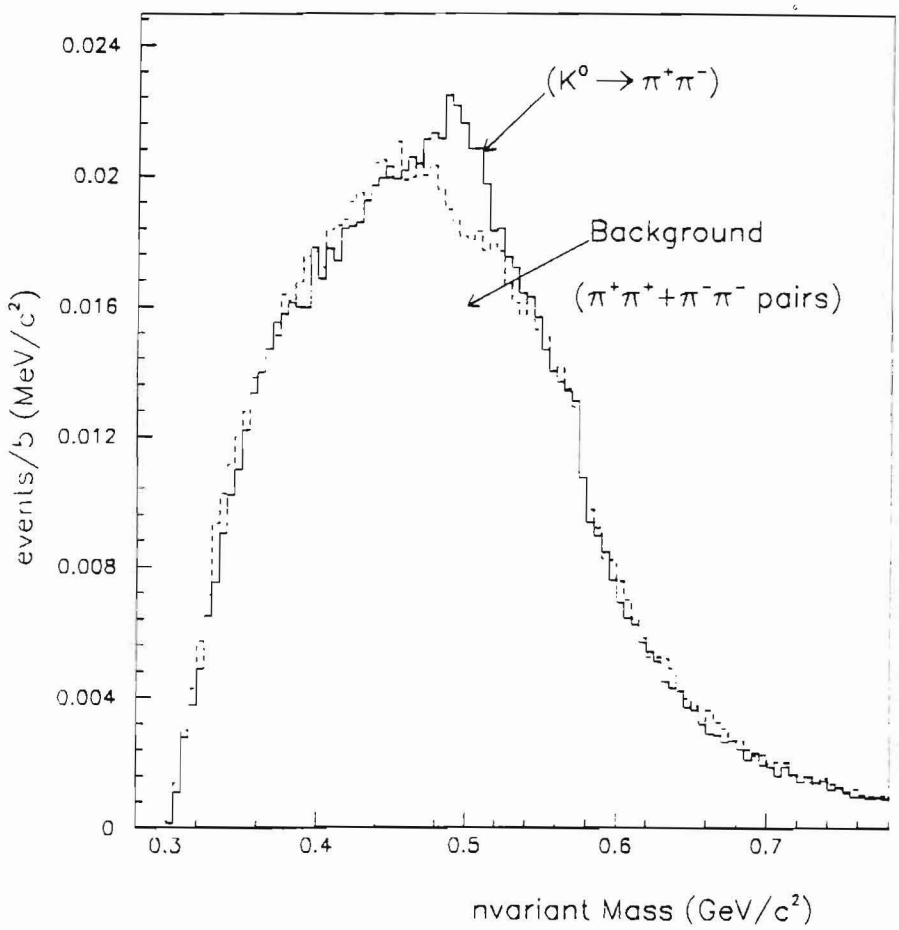

Figure 5.6: Invariant mass distribution of $\pi^+\pi^-$ pairs (signal) superimposed with the invariant mass distribution of $\pi^+\pi^+$, $\pi^-\pi^-$ pairs (background) with the neuron output value greater than 0.8.

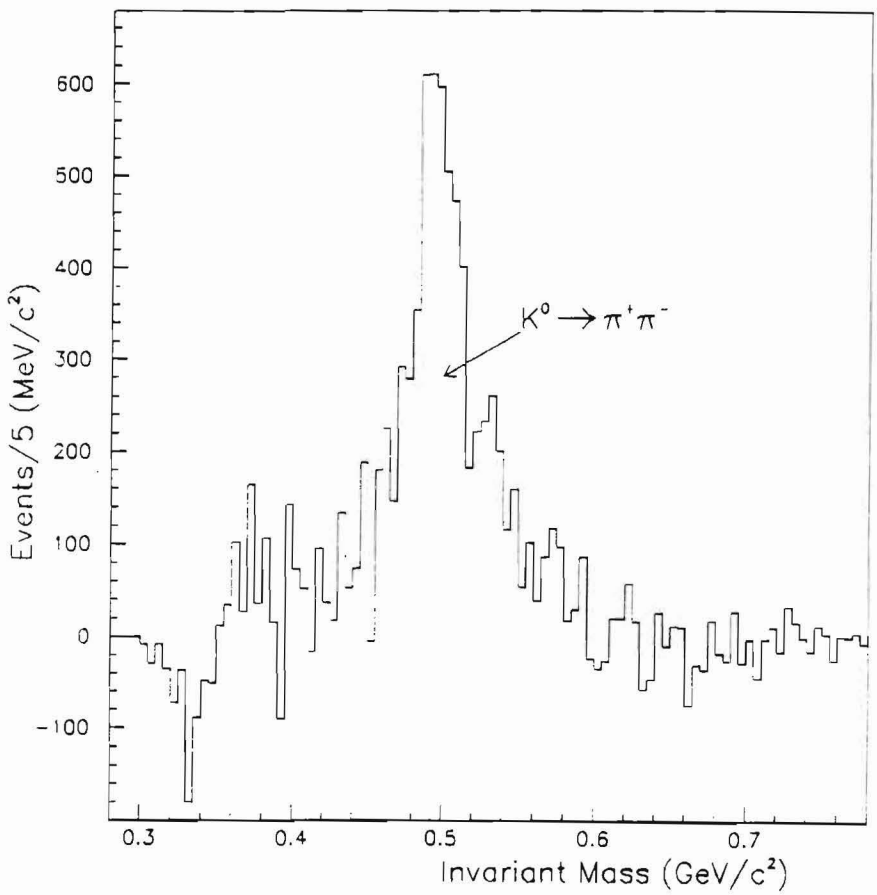

Figure 5.7: Invariant mass distribution of K^0 coming from $\pi^+\pi^-$ after subtracting the background invariant mass distribution of $\pi^+\pi^+$, $\pi^-\pi^-$ pairs with the neuron output value greater than 0.7.

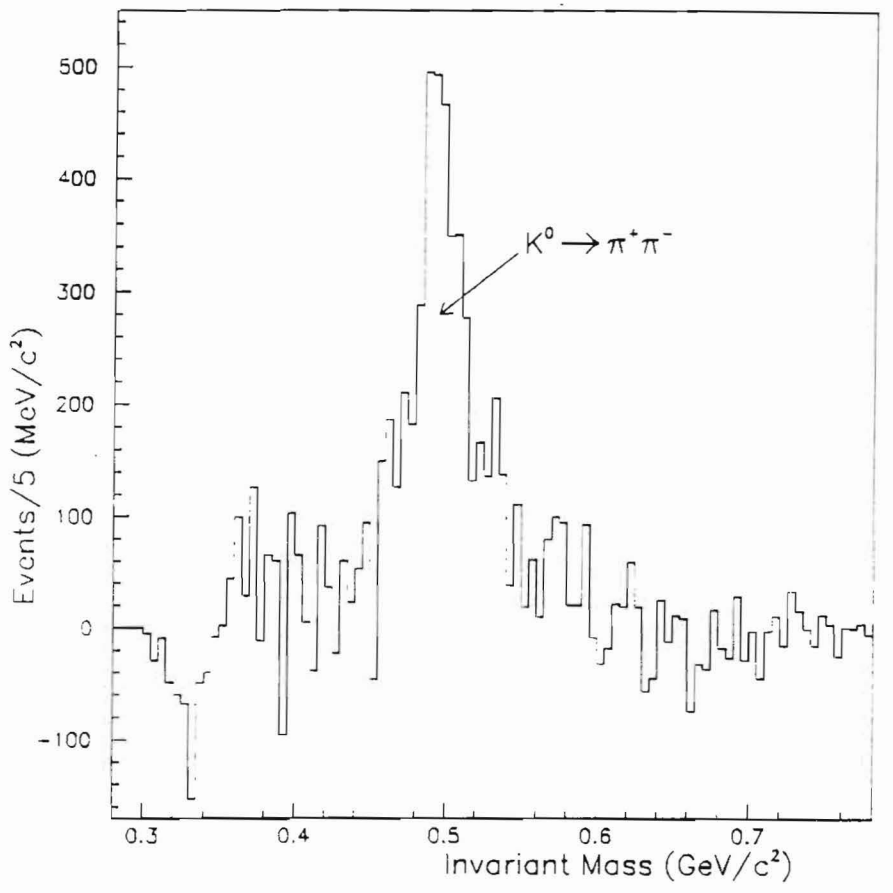

Figure 5.8: Invariant mass distribution of K^0 coming from $\pi^+\pi^-$ after subtracting the background invariant mass distribution of $\pi^+\pi^+$, $\pi^-\pi^-$ pairs with the neuron output value greater than 0.8.

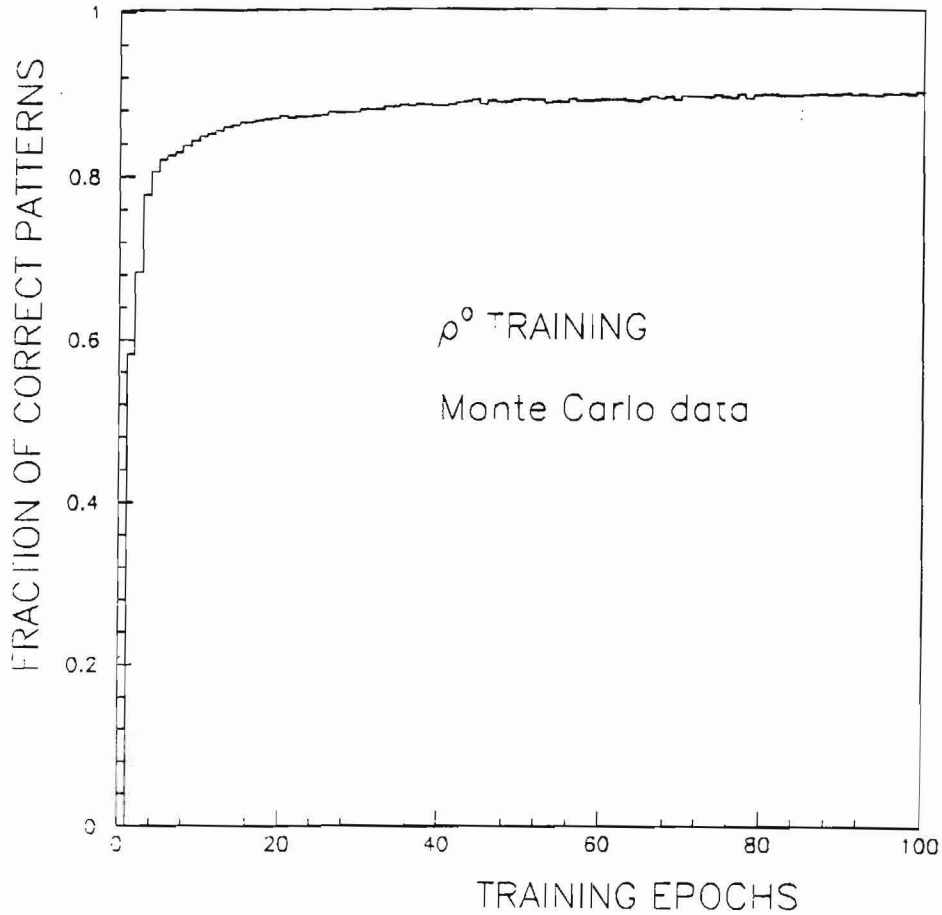

Figure 5.9: Fraction of correct classifications versus training epochs for the first 100 epochs in the ρ^0 search.

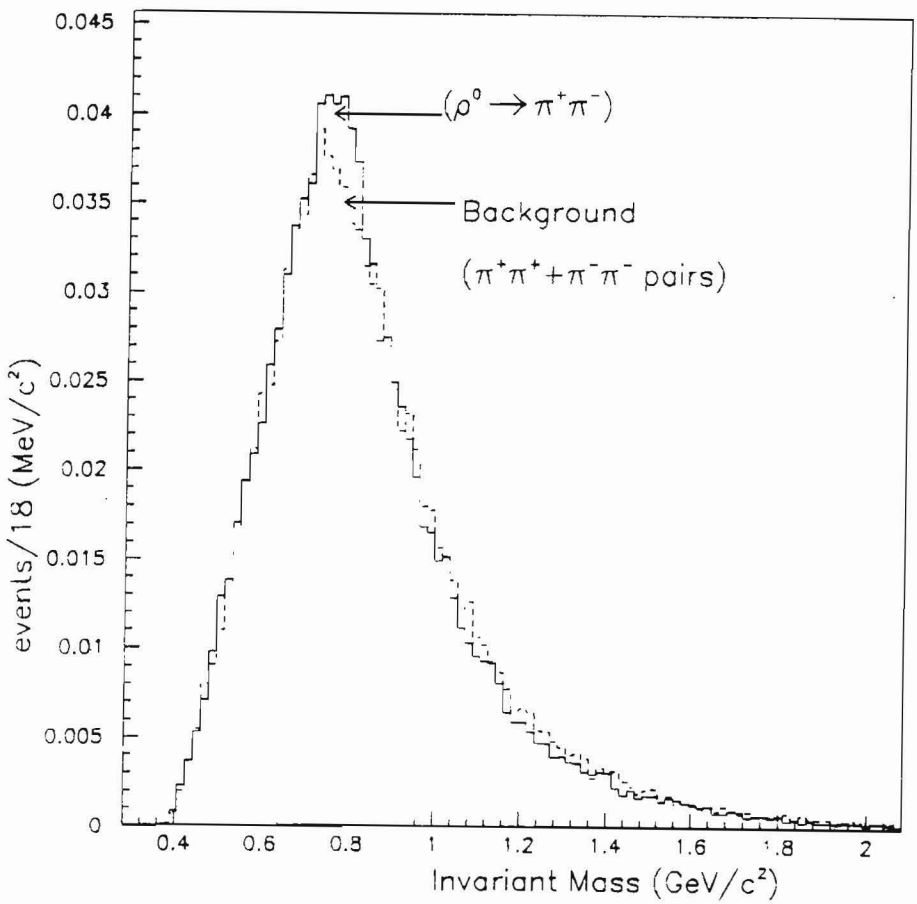

Figure 5.10: Invariant mass distribution of $\pi^+\pi^-$ pairs (signal) superimposed with the invariant mass distribution of $\pi^+\pi^+$, $\pi^-\pi^-$ pairs (background) with the Trial 1 neuron output value greater than 0.7.

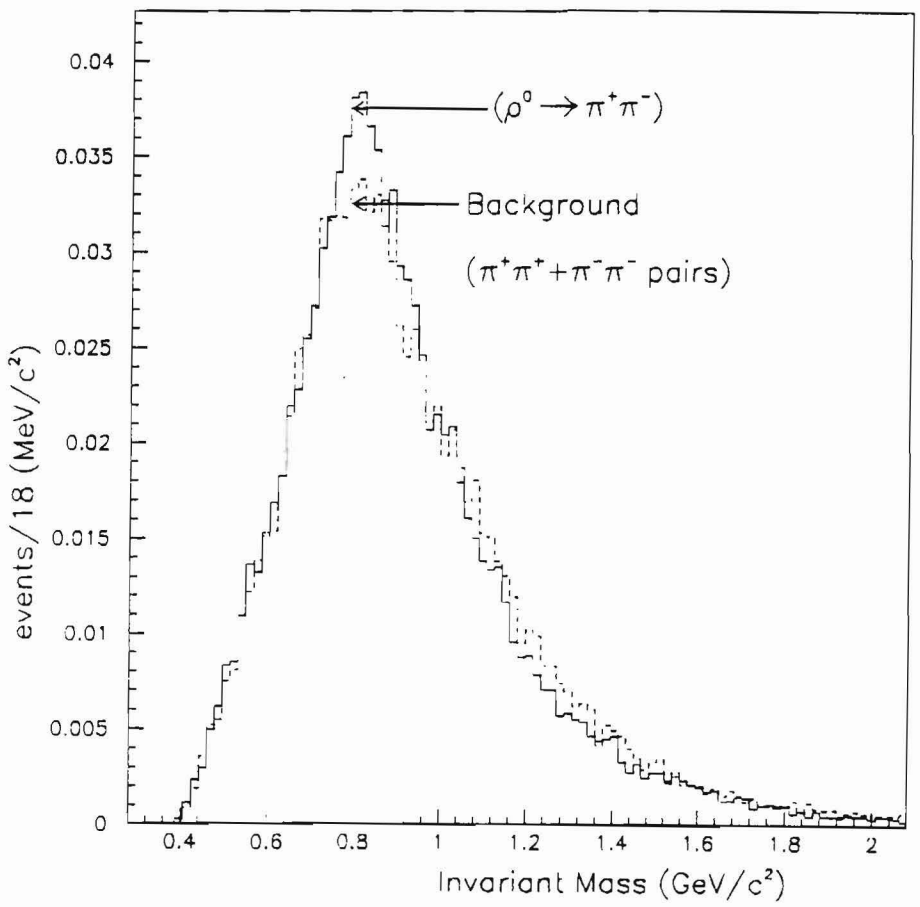

Figure 5.11: Invariant mass distribution of $\pi^+\pi^-$ pairs (signal) superimposed with the invariant mass distribution of $\pi^+\pi^+$, $\pi^-\pi^-$ pairs (background) with the Trial 1 neuron output value greater than 0.8.

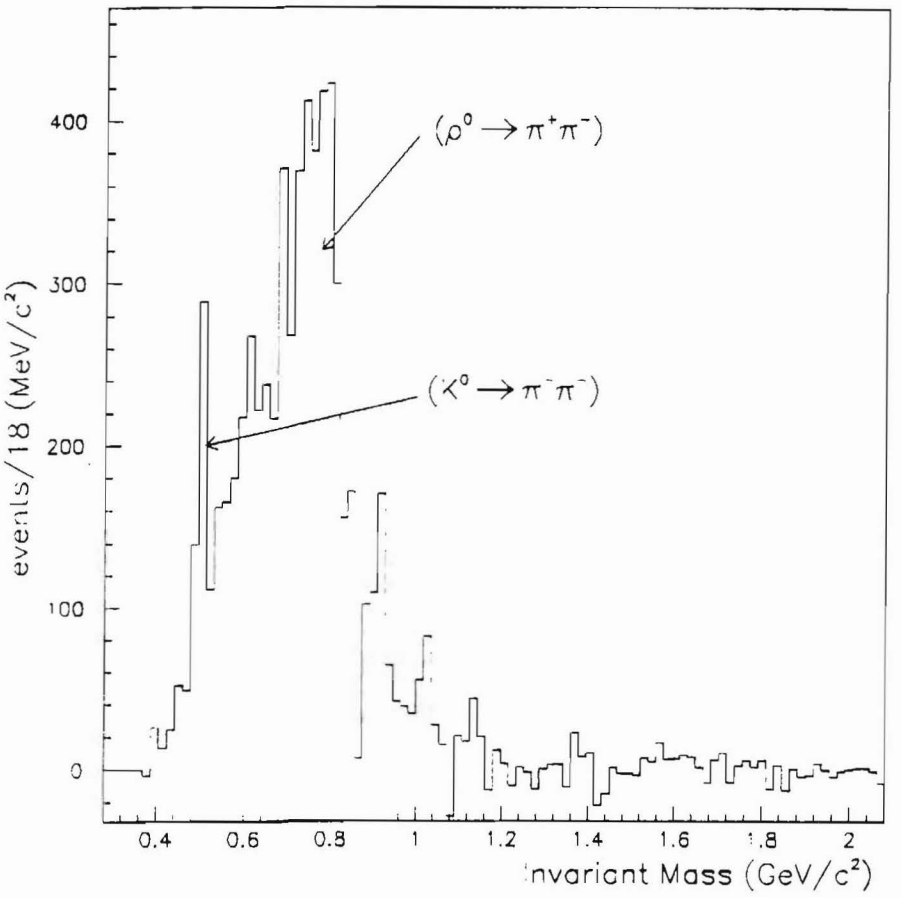

Figure 5.12: Invariant mass distribution of ρ^0 coming from $\pi^+\pi^-$ after subtracting the background invariant mass distribution of $\pi^+\pi^+$, $\pi^-\pi^-$ pairs with the Trial 1 neuron output value greater than 0.6.

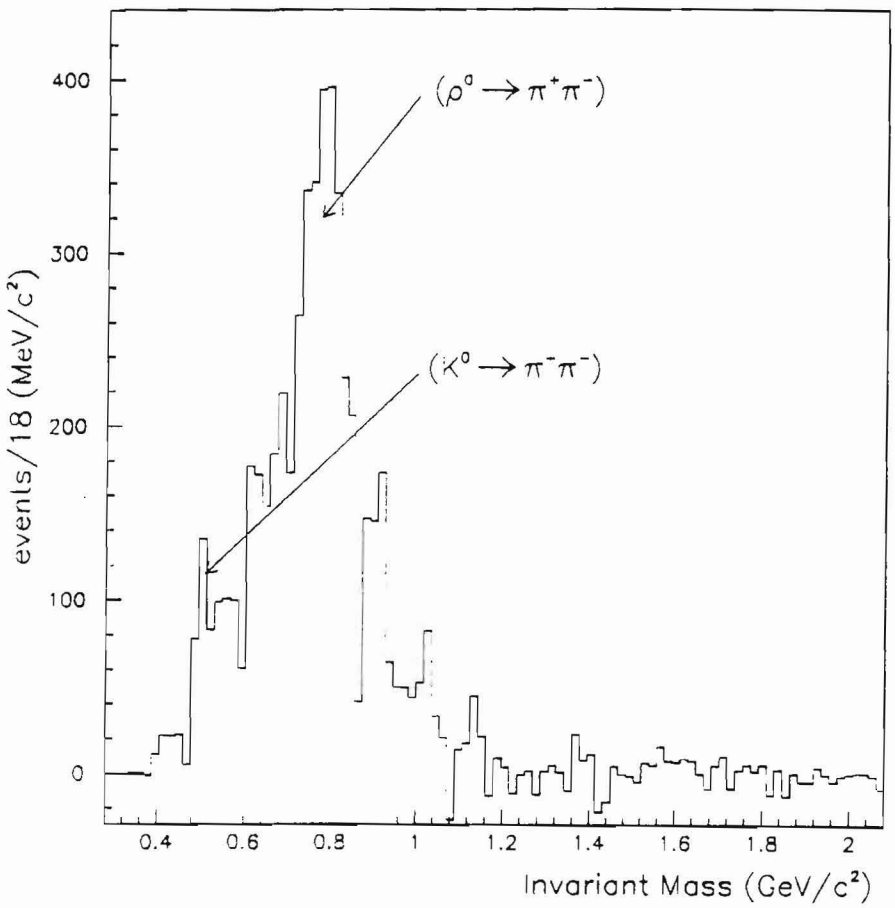

Figure 5.13: Invariant mass distribution of ρ^0 coming from $\pi^+\pi^-$ after subtracting the background invariant mass distribution of $\pi^+\pi^+$, $\pi^-\pi^-$ pairs with the Trial 1 neuron output value greater than 0.7.

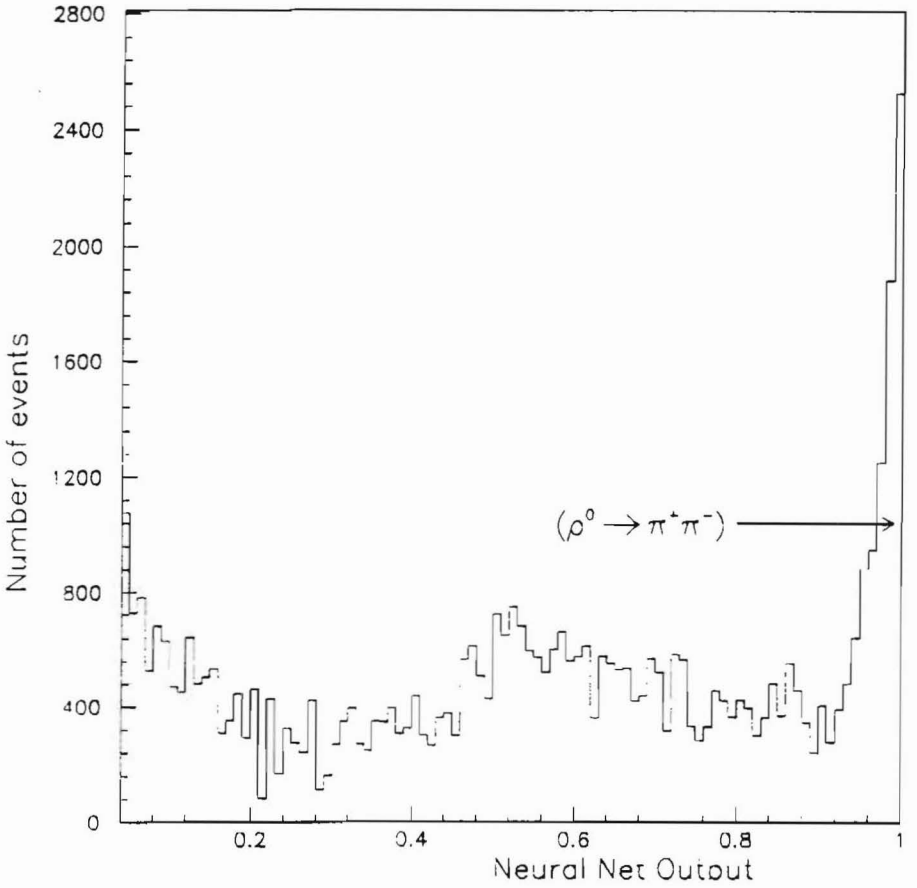

Figure 5.14: Output response of the neural net Trial 1.

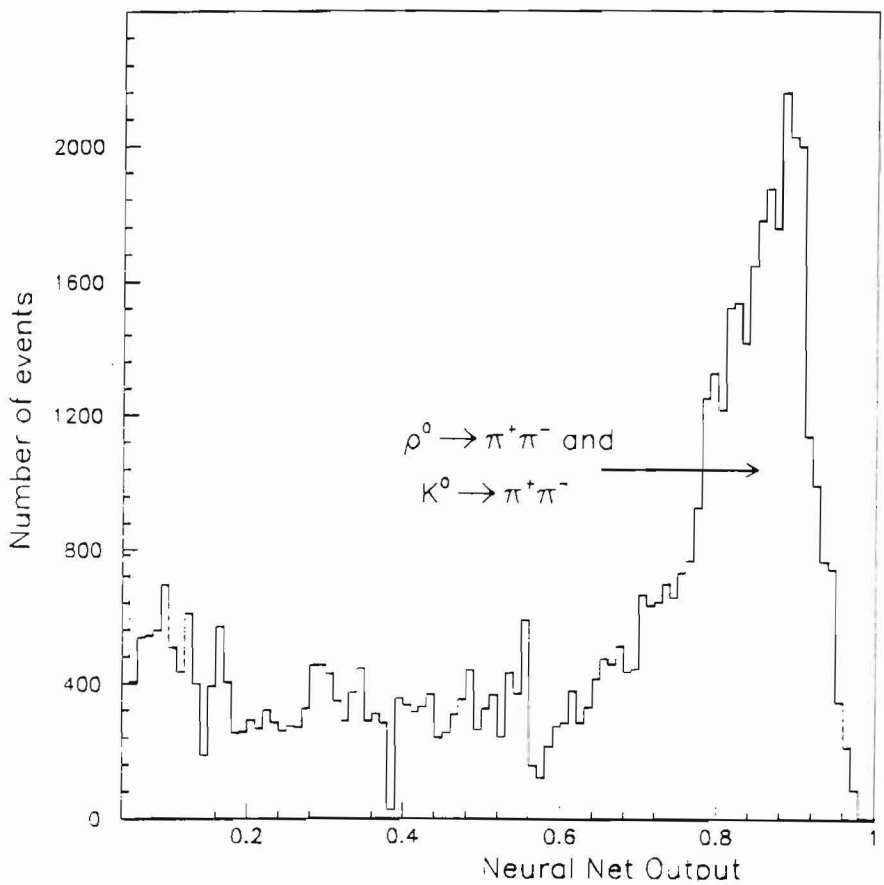

Figure 5.15: Output response of the neural net Trial 2.

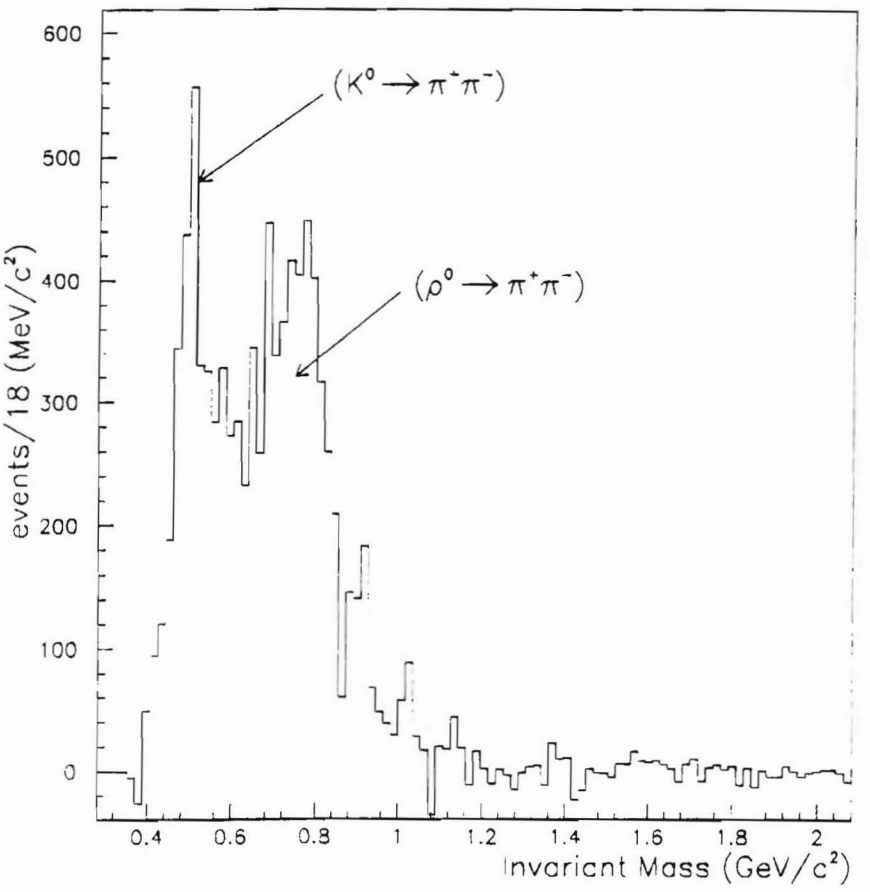

Figure 5.16: Invariant mass distribution of ρ^0 coming from $\pi^+\pi^-$ after subtracting the background invariant mass distribution of $\pi^+\pi^+$, $\pi^-\pi^-$ pairs with the Trial 2 neuron output value greater than 0.7.

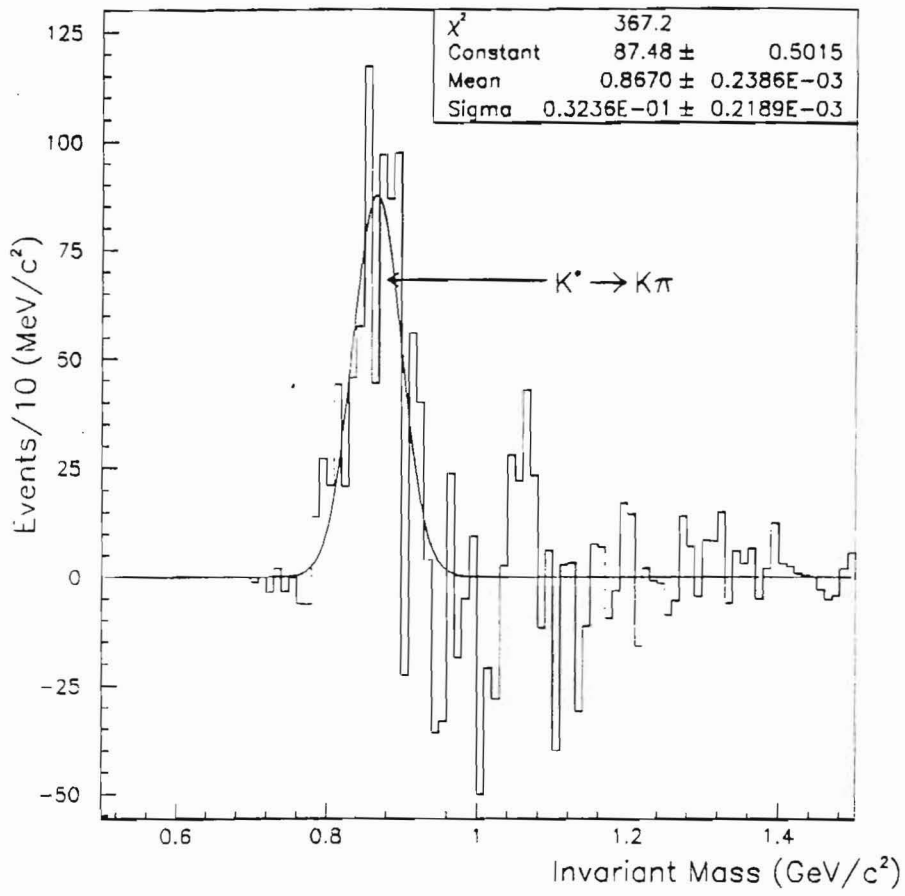

Figure 5.17: Invariant mass distribution of K^{*0} coming from $K^+\pi^-$, $K^-\pi^+$ after subtracting the background invariant mass distribution of $K^+\pi^+$, $K^-\pi^-$ pairs with the neuron output value greater than 0.7.

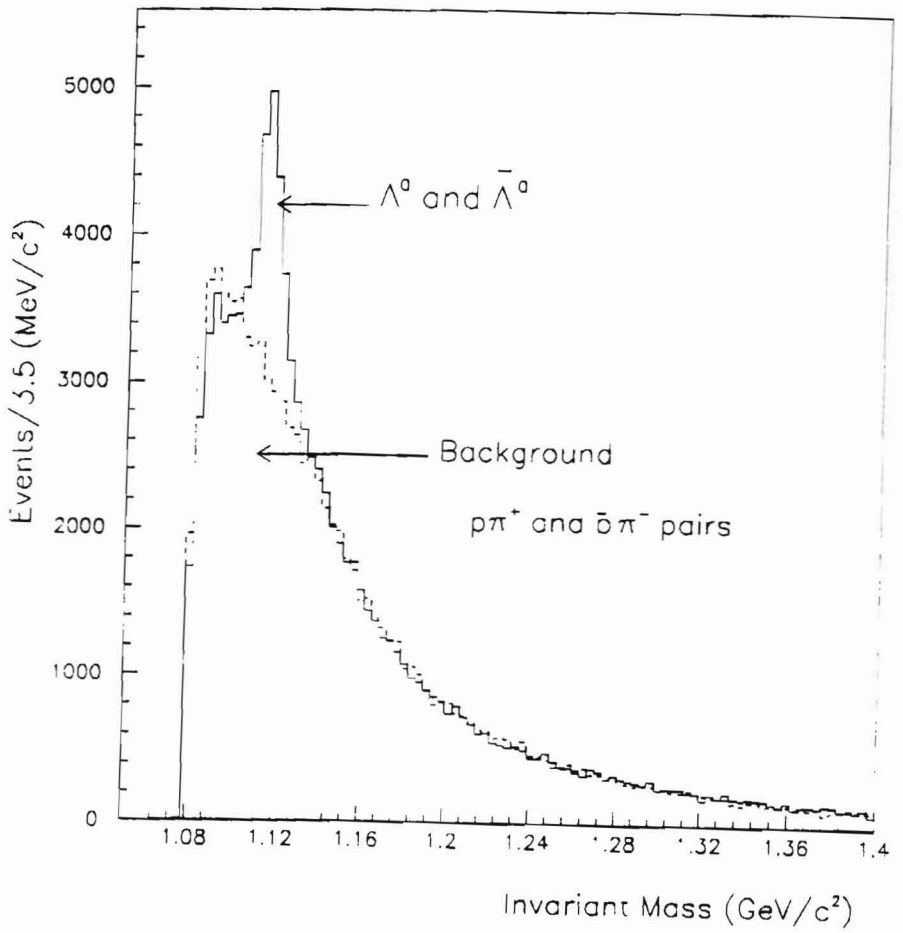

Figure 5.18: Invariant mass distribution of $\Lambda^0 + \bar{\Lambda}^0$ coming from $p\pi^-$, $\bar{p}\pi^+$ superimposed with the background invariant mass distribution of $p\pi^+$, $\bar{p}\pi^-$ pairs with the neuron output value greater than 0.5.

Chapter 6

HBT Data Analysis

In this chapter the structure of the Bose-Einstein effect will be studied in detail using two pion events from the E735 detector at a center of mass energy of $\sqrt{s} = 1.8$ TeV using the HBT method pointed out by Kapylov, Podgoretsky [23] and, independently, Cocconi [24]. The space-time structure (radius and lifetime) of the pion source will be studied as a function of charged particle multiplicity, n_{ch}.

The pure interference Bose-Einstein correlation of two like-sign charged particles can be distorted by other correlations which are present in hadronic production or by correlations resulting from the acceptance of the detector or reconstruction of the non-interference sample (background sample). In order to isolate the above biases a series of studies using Monte Carlo and real two-pion events was performed.

6.1 Measurement of the BE Correlation

The Bose-Einstein correlation function, C_2, is defined as the probability for observing correlated pairs of real bosons relative to uncorrelated pairs. This corre-

lation can be expressed (following Kopylov formalism [23]) as a function of the energy difference, q_0, of the two particles and q_t (Equation B.5) the projection of the three momentum difference ($\vec{q} = \vec{p}_1 - \vec{p}_2$) onto the plane normal to the sum of the momenta $\vec{p} = \vec{p}_1 + \vec{p}_2$ (Figure 6.1). Experimentally, C_2 is presented as a ratio between actual distributions of pairs $S(q_t, q_0)$ (signal) and a corresponding uncorrelated distribution $B(q_t, q_0)$ (background):

$$C_2 = \frac{S(q_t, q_0)}{B(q_t, q_0)}, \tag{6.1}$$

where $B(q_t, q_0)$ is normalized to $S(q_t, q_0)$.

In the case of no correlation this ratio should be flat over all q_t and q_0. If there are correlations present, identical particle statistics imply that there should be deviations from the flat value when q_t and q_0 are small (when the two particles that form the pair are close in phase-space).

An ideal background distribution is a copy of the signal distribution with the absence of the Bose-Einstein correlation. It is a rather difficult to construct an ideal background distribution due to problems analyzed in the following sections.

Before analyzing the correlation function, C_2, the functional dependence of the $S(|\vec{q}|, q_0)$ distribution is studied. Figure 6.2 shows the accepted momentum distribution, dn/dq^μ, ($q^\mu = (q_0, \vec{q})$) observed over the spectrometer acceptance of the E735 experiment. It is clear that only a limited region of the relative phase space $(q_0, \vec{q})$ is available in the diagonal region of the phase space due not only to spectrometer acceptance but also due to the kinematic constraints of the pion pair system (Equation B.15).

One consequence of the above study is that fixing q_0 restricts $|\vec{q}|$ to a narrow

band, a slice of q_0 (q_0 <0.200 GeV) had to be considered. In this case we define the two projections:

$$C_2(q_t) = \frac{\sum_{q_0<0.2} S(|\vec{q}|, q_0)}{\sum_{q_0<0.2} B(|\vec{q}|, q_0)}, \tag{6.2}$$

for the determination of the radius R, and

$$C_2(q_0) = \frac{\sum_{q_t<0.2} S(|\vec{q}|, q_0)}{\sum_{q_t<0.2} B(|\vec{q}|, q_0)}, \tag{6.3}$$

for the determination of the lifetime of the source τ, or the depth of the source.

It should be pointed out here that the determination of the lifetime, τ, can be done using $q_0 = |E_1 - E_2|$ (where E_1 and E_2 are the two energies of the two outgoing particles), but the depth of the source is related to q_l (Equation B.4). Because q_0 and q_l (Equation B.4 and Figure 6.3) are almost the same for fast moving particles (Equation B.30), it is impossible to distinguish between them. From Equation B.3, $|\vec{q}|$ can be written as:

$$|\vec{q}| = \sqrt{q_t^2 + q_l^2}, \tag{6.4}$$

which for small q_0 (q_0 <0.200 GeV, q_l small too) is $|\vec{q}| = q_t$. The invariant momentum difference, Q, (commonly used to express the correlation function, C_2) given by Equation B.11 and B.13 is almost the same as q_t (Figure 6.4 and Equation B.35).

6.1.1 Pairs from Different Events

The most common prescription used to generate the uncorrelated distribution or background distribution, $B(q_t, q_0)$, is that of different-event mixing, as first suggested by Kopylov [23]. This technique attempts to use the data directly

to obtain the expected phase space distribution for like-charged particle pairs in the absence of Bose-Einstein correlations. In our case, this background, B, is constructed of like-sign pairs mixed from two different events of the same multiplicity and vertex location while the signal, S, consists of like-sign pairs from the same event. By so constructing the background, the same geometrical acceptances and experimental biases as seen by the signal were incorporated, except those induced by BE correlations. Hence, there is little need to make any bias corrections to the *background* distribution.

It should be pointed out here that in this different-event mixing algorithm, the background distribution is free of resonances such as $K^0 \rightarrow \pi^+\pi^-$ (see Section 5.1), $\rho^0 \rightarrow \pi^+\pi^-$ (see Section 5.1), $\omega - \pi^+\pi^-\pi^0$, $\eta^0 \rightarrow \pi^+\pi^-\pi^0$, $\eta' \rightarrow \pi^+\pi^-\eta^0$, etc. These resonances distort the phase space of the unlike-charge pairs and may introduce further correlations. The use of $\pi^+\pi^+$, $\pi^-\pi^-$ mixed from different events may be complicated by the lack of four-momentum, $p^\mu = (E.\vec{p}\ )$, conservation in the overall event. This could be a problem in an experiment, where the small number of produced particles can lead to strong kinematic constraints. In our case the outgoing energy of the π's (of the order of 0.2 GeV) is a small fraction of the total available energy ($\sqrt{s}$ = 1.8 TeV), so there appears to be no problem with strong kinematic constraints.

6.1.2 Pairs from the Same Events

Another technique, attempting to make direct use of the data, to obtain background distributions free of the Bose-Einstein correlation consists of using $\pi^+\pi^-$

pairs from the same event. In this case $\pi^+\pi^-$ pairs from the same event do not obey a symmetrization requirement. Unfortunately, the $\pi^+\pi^-$ pairs are dominated by the above series of the resonances. Furthermore, there are two more hidden assumptions in this method:

- All geometrical acceptances should be the same for both $\pi^+\pi^-$ and $\pi^+\pi^+$, $\pi^-\pi^-$. This is not the case for our spectrometer. Our data are not charge symmetric and the two-particle distributions $\pi^+\pi^+$ and $\pi^-\pi^-$ are different. A common background distribution for both would introduce biases (see Section 6.2.1).

- All the detection efficiencies for two-track $\pi^+\pi^-$ and $\pi^+\pi^+$, $\pi^-\pi^-$ should be equal or at least well understood. It shall be shown that this is certainly not the case for our spectrometer due to the different two-track detection efficiencies of the z-chamber and straw chamber for both $\pi^+\pi^-$ and $\pi^+\pi^+$, $\pi^-\pi^-$ because of the way particles bend in the magnetic field (see Section 6.2.5).

6.2 Systematic Biases

All possible systematic biases influencing the correlation function, C_2, will be reviewed and studied in this section. Systematic biases are due to the limited acceptance of the E735 detector. finite resolution of the drift chambers, and the final state interaction of the pions.

6.2.1 E735 Aperture Problem

A Monte Carlo method (Appendix A) is used to generate two track events in the E735 spectrometer. It uses a flat rapidity distribution for $-2.1 < y < +2.1$ and a flat azimuthal distribution for $0.0 < \phi < 20°$. The transverse momentum spectrum is taken to be $dN/dp_t^2 \simeq \exp(-p_t/0.15)$ (Equation 6.14). The Monte Carlo introduces no deliberate correlation between the two tracks of an event. The same list of cuts we have applied to the data analysis were applied in the Monte Carlo study.

Figure 6.5 shows the z-coordinate vertex distribution of real events accepted by the E735 acceptance model just described. There are observable differences between $\pi^-\pi^-$, $\pi^+\pi^+$, and $\pi^+\pi^-$ events.

Figure 6.6 shows the q_t distributions for the three possible sign combinations. The HBT variable q_t is the component of the momentum difference that is perpendicular to the total pair momentum (Equation B.5. Also see Figure 6.1 for vector diagrams defining q_t.). All three distributions are different.

The next three figures present the usual HBT plot using Monte Carlo events with no Bose-Einstein correlation. Figure 6.7 shows the ratio of distributions for $(\pi^+\pi^+)/(\pi^+\pi^-)$ vs q_t, and Figure 6.8 shows the ratio of $(\pi^-\pi^-)/(\pi^+\pi^-)$ vs q_t. This ratio is used because only pairs of identical sign can exhibit the HBT effect. For completeness, Figure 6.9 is the sum of the two Figures 6.7 and 6.8. To be useful, however, the denominator of the ratio must experience the same acceptance bias as the numerator. This equivalence appears to be insufficiently true for the E735 spectrometer. In fact, for the case of either sign in Figures 6.7

and 6.8, the Monte Carlo enhancement at low q_t is a significant fraction of the maximum value of 2.0 allowed for the HBT effect. It can be demonstrated that the Monte Carlo events alone introduce a dominant correlation. For the above fits the Gaussian parameterization of the source was used (Equation 6.38).

From the above study, when the q_t distribution for like-sign pairs is divided by the q_t distribution of unlike-sign pairs, an apparent HBT enhancement occurs which implies an interaction radius of 1-2 fermi with a substantial (~ 0.5) chaoticity factor (Equation 1.40 for the Weiner representation) being indicated.

6.2.2 Fake Background Correlations

The Bose-Einstein correlation modifies the phase-space density of single pions, which in turn modifies the phase space of both the unlike-charge pion pairs and the different event background distribution. This has the effect of inducing a Bose-Einstein correlation which is applied in both of the above background calculation methods. Mathematically, this may be formulated by the following argument, as first described by W.A. Zajc [25]: The correlation function, C_2, (Equation 6.1) can be expressed as the ratio of the two-particle inclusive cross section to the product of the single-particle cross sections, so that:

$$C_2(q_t, q_l) = K \frac{d^6 n}{d^3\vec{p}_1 d^3\vec{p}_2} / \frac{d^3 n}{d^3\vec{p}_1} \frac{d^3 n}{d^3\vec{p}_2}, \tag{6.5}$$

where the normalization factor K involving the pion multiplicity, n_π is:

$$K = < n_\pi >^2 \; / \; < n_\pi(n_\pi - 1) > . \tag{6.6}$$

The background distribution $B(q_t, q_0)$ is normalized to the signal distribution $S(q_t, q_0)$ (Equation 6.1). The definition of the single particle inclusive momentum

distribution normalization is given by:

$$\int \frac{d^3n}{d^3\vec{p}} d^3\vec{p} =< n_\pi >, \tag{6.7}$$

and the two particle inclusive momentum distribution normalization:

$$\int \frac{d^6n}{d^3\vec{p_1} d^3\vec{p_2}} d^3\vec{p_1} d^3\vec{p_2} =< n_\pi(n_\pi - 1) > . \tag{6.8}$$

From quantum mechanics (Section 1.2), the correlation function can be expressed as:

$$C_2(q_t, q_l) = 1 + \rho_F(q_t, q_l, q_0), \tag{6.9}$$

where $\rho_F(q_t, q_l, q_0)$ is the square of the Fourier Transform of the pion source in space and time (from the formulation of Section 1.2), $\rho_F(q_t, q_l, q_0) = |F|^2$. This is the essential result of intensity interferometry (Section 1.2). Equation 6.5 may then be written, using Equation 6.9, in the following form (for a normalized background to signal distribution):

$$\frac{d^6n}{d^3\vec{p_1} d^3\vec{p_2}} = [1 + \rho_F(q_t, q_l, q_0)] \frac{d^3n}{d^3\vec{p_1}} \frac{d^3n}{d^3\vec{p_2}}. \tag{6.10}$$

The single pion background momentum distribution $dn_b/d\vec{p_1}$ is given by integrating the two-particle momentum distribution over all $\vec{p_2}$, so that:

$$\begin{aligned} \frac{d^3n_b}{d^3\vec{p_1}} &= \int_\Omega \frac{d^6n}{d^3\vec{p_1} d^3\vec{p_2}} d^3\vec{p_2} \\ &= \frac{d^3n}{d^3\vec{p_1}} \int_\Omega [1 + \rho_F(q_t, q_l, q_0)] \frac{d^3n}{d^3\vec{p_2}} d^3\vec{p_2} \\ &= \frac{d^3n}{d^3\vec{p_1}} [1 + \delta(\vec{p_1}; \rho_F(q_t, q_l, q_0))], \end{aligned} \tag{6.11}$$

where Ω is the region of integration which depends on the acceptance of the spectrometer and $\delta(\vec{p_1}; \rho_F(q_t, q_l, q_0))$ is expressed as:

$$\delta(\vec{p_1}; \rho_F(q_t, q_l, q_0)) = \int_\Omega \rho_F(q_t, q_l, q_0) \frac{d^3n}{d^3\vec{p_2}} d^3\vec{p_2}. \tag{6.12}$$

The single pion background momentum distribution, $dn_b/d\vec{p}_1$, is thus modified by a correction term, $\delta(\vec{p}_1;\rho_F(q_t,q_l,q_0))$. Similarly the single pion background momentum distribution, $dn_b/d\vec{p}_2$, is modified by a correction term $1+\delta(\vec{p}_2;\rho_F(q_t,q_l,q_0))$. The correlation function, C_2, thus becomes:

$$C_2 = C_2^{obs}[1+\delta(\vec{p}_1;\rho_F(q_t,q_l,q_0))][1+\delta(\vec{p}_2;\rho_F(q_t,q_l,q_0))]. \tag{6.13}$$

Monte-Carlo calculations show that the magnitude of this residual correlation δ is of the order of $3-4\%$ using the following calculation. This calculation assumes one had a priori knowledge of the correlation function. A C_2 of the form, $C_2 = 1+\lambda e^{-R^2q^2-\tau^2q_0^2}$, with chaoticity factor, $\lambda = 0.5$, lifetime $\tau = 0.5$ fm and radius of the source $R = 1$ fm, was assumed. To estimate this percentage, it was also assumed that the momentum distribution of the single particle was

$$\frac{dn}{dp_t} = e^{-p_t/T}, \tag{6.14}$$

where $p_t = \sqrt{p_x^2+p_y^2}$, $T = 0.150$ MeV and the distribution was flat in rapidity, y, and in azimuthal angle, ϕ.

6.2.3 Gamow Corrections

It is well known that the Coulomb interaction of two like-charged particles modifies the phase space density in relative momentum via the Gamow [78,20] factor $G(\eta)$. For like-charged and unlike-charged pairs, the inclusive momentum distributions in the presence of Coulombic interaction are given by $(dn/d\vec{p}_1d\vec{p}_2)_l$ and $(dn/d\vec{p}_1d\vec{p}_2)_u$, respectively.

$$(\frac{dn}{d\vec{p}_1d\vec{p}_2})_l = G_l(\eta)(\frac{dn}{d\vec{p}_1d\vec{p}_2}), \tag{6.15}$$

$$(\frac{dn}{d\vec{p}_1 d\vec{p}_2})_u = G_u(\eta)(\frac{dn}{d\vec{p}_1 d\vec{p}_2}), \tag{6.16}$$

where $dn/d\vec{p}_1 d\vec{p}_2$ is the pair inclusive distribution in the absence of the Coulomb force, and:

$$G_u(\eta) = \frac{2\pi\eta}{e^{2\pi\eta} - 1} = e^{-\pi\eta}(\frac{\pi\eta}{\sin h\pi\eta}), \tag{6.17}$$

$$G_l(\eta) = \frac{2\pi\eta}{1 - e^{-2\pi\eta}} = e^{+\pi\eta}(\frac{\pi\eta}{\sin h\pi\eta}), \tag{6.18}$$

$$\eta = \frac{\alpha m_\pi}{\sqrt{Q^\mu Q_\mu}}, \tag{6.19}$$

$\alpha = \frac{1}{137}$, $Q^\mu Q_\mu = M^2 - (2m_\pi)^2$, M is the invariant mass of the pion-pair, and m_π is the pion mass.

The corrections for Coulomb effects are made by weighting each like-pair by $1/G_l(\eta)$ and each unlike pair by $1/G_u(\eta)$. The correction factors for like-charged and unlike-charged pairs are small except for very small $Q^\mu Q_\mu$, as shown in Figure 6.10. If the background distribution is calculated from an unlike-charged pair from the same event, then in order to calculate the corrected correlation function, C_2, (the ratio of like-charged to unlike-charged pairs from the same event) in the absence of the Coulomb final-state interaction, the observed C_2 must be multiplied by the factor G_u/G_l. This ratio is shown in Figure 6.10 by the dashed line which is still small except in the region of very small $Q^\mu Q_\mu$.

If the background distribution is calculated from like-charge pairs from different events, the correlation function, C_2, (the ratio of like-charge (signal distribution) to like-charge pairs from different events (background distribution)) in the absence of the Coulomb final-state interaction is multiplied by the factor $1/G_l$, the solid line, which is in fact smaller than the dashed-line.

It is important here to note that the induced Gamow correction may be applied to the background events via the method in Section 6.2.2. This can be seen mathematically through the following argument: The single pion background momentum distribution, $(dn_b/d\vec{p}_1)_l$, generated by different-event mixing is calculated by integrating Equation 6.5 over all $\vec{p}_2$, so that

$$(\frac{dn_b}{d\vec{p}_1})_l = \int_\Omega G_l(\eta)\frac{dn}{d\vec{p}_1}\frac{dn}{d\vec{p}_2}d\vec{p}_2 = \frac{dn}{d\vec{p}_1}\epsilon_1, \tag{6.20}$$

where $d^3/d^3\vec{p}_i$ (i=1,2) is the single particle distribution from different events, and ϵ_1 is given by

$$\epsilon_1 = \int_\Omega G_l(\eta)\frac{dn}{d\vec{p}_2}d\vec{p}_2. \tag{6.21}$$

Similarly, the single pion background momentum distribution, $(dn_b/d\vec{p}_2)_l$, is modified by a correction factor, ϵ_2,

$$\epsilon_2 = \int_\Omega G_l(\eta)\frac{dn}{d\vec{p}_1}d\vec{p}_1. \tag{6.22}$$

The correlation function, C_2, (the ratio of like-charged (signal) to like-charged pairs from different events (background)) in the absence of the Coulomb final-state interaction should be multiplied by the factor $\epsilon_1\epsilon_2/G_l$. This effect is probably negligible, but cannot be totally removed by combining tracks from different events.

6.2.4 Momentum Error

The final systematic error in this analysis is the broadening of the Bose-Einstein enhancement due to the finite-momentum resolution. To study this effect, we

simulate the Bose-Einstein enhancement in the Monte Carlo data by weighting each like-charged pion pair (see Appendix C) by

$$C_2 = 1 + \lambda e^{-R^2 q_t^2}, \tag{6.23}$$

with $\lambda = 1$ and source radius, $R = 1$ fm. The distributions of $q_t^{gen,s}$ and $q_t^{gen,b}$ are made for weighted and non-weighted like-pion pairs, respectively. At the same time, a Gaussian momentum error with a mean value p and standard deviation σ was assigned to each track:

$$dp = 4\% p \sqrt{p^2 + \frac{1}{\beta^2}}, \tag{6.24}$$

where $\beta = p/\sqrt{p^2 + m^2}$ and m is the pion mass. A new set of distributions of $q_t^{obs,s}$ and $q_t^{obs,b}$ background are made for weighted and non-weighted like-pion pairs. For both $q_t^{obs,s}$ and $q_t^{gen,s}$ distributions a correlation function, C_2 was calculated and analytic functions were fit. Namely,

$$C_2(q_t^{obs}) = \frac{dn}{dq_t^{obs,s}} / \frac{dn}{dq_t^{obs,b}}, \tag{6.25}$$

and

$$C_2(q_t^{gen}) = \frac{dn}{dq_t^{gen,s}} / \frac{dn}{dq_t^{gen,b}}. \tag{6.26}$$

Comparing the fitted values of λ^{obs} and R^{obs} for $C_2(q_t^{obs})$ with the fitted values λ^{gen} and R^{gen} for $C_2(q_t^{gen})$, a systematic error of the order of 2-3% was assigned to R which is small compared to the observed statistical error (Table 6.1). Figure 6.11 shows the correlation function, $C_2(q_t^{obs})$, after applying the momentum error.

The relative error ($\delta R/R$) of the calculated radius, R^{gen}, due to the momentum error, (Equation 6.24) was studied. Figure 6.12 gives this calculated relative

radius error (δR) versus radius (R^{gen}). Figure 6.13 shows the relation between the observed radius, R^{obs}, of the source as a function of the generated radius R^{gen}.

Radius Resolution of the Source

In addition, the two-track momentum resolution determines how small of a Q can be resolved, which in turn limits the maximum size, R, of the source that can be measured. The resolution ΔQ can be calculated from the definition of Q (Equations B.12 and B.13) via Monte-Carlo calculations, provided enough is known about the spectrometer resolution. An experimental estimate for the value of ΔQ can be obtained from the observed width of the K^0 decay (as described in section 4.6.2) to $\pi^+\pi^-$.

From the observed K^0 mass width the Q resolution is

$$\Delta Q = M_{K^0} \Delta M_{k^0} / Q_{K^0} = 0.020 \text{ GeV}. \tag{6.27}$$

Given Equation 1.32, the ability of this experiment to measure the radius, R, deteriorates above

$$R = \hbar c / \Delta Q = 10 \text{ fm}. \tag{6.28}$$

This value is much larger than the value from a typical $\bar{p}p$ collision experiment (1 fm).

6.2.5 Opening Angle Problem

The effect of experimental biases in the opening angle in the x-z plane, θ_{xz}, of a pair was studied by examining S (signal) and B (background) independently

($C_2 = S/B$). Figure 6.14 shows tracking data taken in the magnet-off configuration. The plotted variable is the opening angle of the pair at the origin in the $x - z$ plane (θ^o_{xz}). It appears that the two-track resolution is not 100% efficient at angles less than $10 - 15^0$. This is due to the limited two-track resolution of z- and straw chamber. Figures 6.15 and 6.16 show tracking data taken in the magnet-on configuration. As can be noticed, first of all, the difference in the two-track efficiency between like-charged (Figure 6.15) and unlike-charged pairs (Figure 6.16) below 15^0. This is due to the different way the $\pi^+\pi^+ + \pi^-\pi^-$ and $\pi^+\pi^-$ bend in the magnetic field. In the calculation of the two-particle correlation function,

$$C_2 = \frac{(++) + (--)}{(+-)}, \tag{6.29}$$

or

$$C_2 = \frac{\text{like} - \text{charged} - \text{pairs}}{\text{unlike} - \text{charged} - \text{pairs}}. \tag{6.30}$$

The above difference must be removed in order to avoid self-generating the correlation. One may avoid the problem all together by requiring a minimum opening angle θ^o_{xz} cut for both like-charged and unlike-charged pairs. Figures 6.17 and 6.18 show the opening angle θ^o_{xz} at the origin (x = 0) for like-charged and unlike-charged pairs, respectively, (each particle in a pair coming from a different event). It was noticed that there is no two-track inefficiencies for either like-charged or unlike-charged pairs from different events. In this study we will not try to correct for the like-charged pair (from same events) inefficiency, but a minimum opening angle, θ^o_{xz}, cut of 12^0 (see Section 6.3.1) will be required in the calculation of the

two-particle correlation function

$$C_2 = \frac{(++)_S + (--)_S}{(++)_D + (--)_D}, \tag{6.31}$$

or

$$C_2 = \frac{\text{like} - \text{charged} - \text{pairs} - \text{same} - \text{events}}{\text{unlike} - \text{charged} - \text{pairs} - \text{different} - \text{events}}. \tag{6.32}$$

It will be shown that this does not especially limit our ability to measure large values of R.

6.2.6 Vertex Problem

In order to verify that the observed Bose-Einstein correlation is a result of the Bose-Einstein effect and not a result of any hidden systematic errors, a sample of Monte Carlo pairs without any Bose-Einstein correlations $(++)_S + (--)_S$ were generated. From this Monte Carlo sample, a mixing sample from different pairs was created in order to construct the background distribution $(++)_D + (--)_D$. The Monte Carlo events were analyzed in the same way as the real data. It was observed that the mixing technique does introduce an artificial correlation.

Figure 6.19 shows the calculated correlation function for Monte Carlo events,

$$C_2 = \frac{(++)_S + (--)_S}{(++)_D + (--)_D}, \tag{6.33}$$

as a function of q_t, while Figure 6.20 shows the same correlation function, C_2, as a function of the invariance difference Q. These two variables (q_t and Q) behave the same way for energetic pairs (Equation B.35).

This artificial correlation is a result of the vertex distribution of the mixing sample. Figure 6.21 shows the Monte Carlo event vertex (average z-intercept of

a pair) distribution of the $(++)_S + (--)_S$ sample (tracks from the same event). Figure 6.21 also shows the vertex distribution of the $(++)_D + (--)_D$ sample (tracks from the mixing algorithm). The difference between the two vertex distributions is clear. This is due to the fact that the vertex distribution of tracks from the mixing algorithm, $(dn/dz_v)_D$, is a function of the vertex distribution of tracks from the same event, $(dn/dz_v)_S$. Namely,

$$(\frac{dn}{dz_v})_D = (\frac{dn}{dz_v})_S^2. \tag{6.34}$$

In the case of a Gaussian vertex distribution, the standard deviation of $(dn/dz_v)_D$, differs from the the standard deviation of $(dn/dz_v)_S$ by a factor of $\sqrt{2}$.

In order to correct this systematic error we have accepted only mixing pairs that form a vertex distribution similar to the same-event pair vertex distribution. Figure 6.22 shows the vertex (average z intercept of a pair) distribution of the $(++)_S + (--)_S$ sample (tracks from the same event) superimposed with the modified vertex distribution of the $(++)_D + (--)_D$ sample (tracks from the the different event mixing algorithm). There is no difference between the two vertex distributions. Likewise, the Monte Carlo correlation function, C_2, as a function of q_t (Figure 6.23) and invariance difference Q (Figure 6.24) no longer has any artificial correlations like that in Figures 6.19 and Figure 6.20.

6.3 Control Experiment

A number of different "control" (test) experiments were performed using real data and the same analysis used in the like-sign charged correlation studies in

order to verify the nature of the like-sign charged correlation. Unlike-sign $K\pi$ combinations [79] as well as $+-$ combinations were considered as test experiments.

6.3.1 Unlike-sign $+-$, $K\pi$, etc., Correlations

A way, other than Monte Carlo studies, to test any artificial correlation or other systematic errors is to study charged $K\pi$, $p\pi$, Kp combinations identified by the TOF1 and TOF2 systems. Using uniquely identified $\pi^{\pm}$, $K^{\pm}$, p, and $\bar{p}$; the correlation function was formed,

$$C_2 = \frac{(\pi^{\pm}K^{\pm} + p^{\pm}K^{\pm} + \pi^{\pm}p^{\pm})_S}{(\pi^{\pm}K^{\pm} + p^{\pm}K^{\pm} + \pi^{\pm}p^{\pm})_D}. \tag{6.35}$$

Despite the fact that one of the particles is identified as a kaon or proton, we have assigned the π mass to both particles and analyzed them in the same way as pion pairs. Figures 6.25 and 6.26 show the correlation function, C_2, (Equation 6.35) versus q_t, for all q_0 and $q_0 < 0.200$ GeV, respectively. It is clear that there is no significant enhancement in the correlation function at low q_t for these non-identical particles.

Yet another way to verify the nature of the Bose-Einstein correlation is to study $\pi^{\pm}$ pairs from the real data in the same way as we have analyzed $\pi^+\pi^+$, $\pi^-\pi^-$ pairs. Again, Figures 6.27, 6.28, and 6.29 show there is no evidence of an enhancement in the correlation function, C_2, at low q_t, as a function of multiplicity n_{ch}.

$$C_2 = \frac{(+-)_S}{(+-)_D}, \tag{6.36}$$

where the pairs $(+-)_S$ come from the same event and $(+-)_D$ come from the different event mixing algorithm.

The opening angle cut was varied from 12^0 to 20^0 for these events. No Bose-Einstein enhancement was observed in the correlation function. Figures 6.30, 6.31, and 6.32 show the correlation function, as a function of q_t for opening angle $\theta_{xz} > 20^0$. It is clear there is no correlation for $\theta_{xz} > 12^0$ as well as $\theta_{xz} > 20^0$.

It is known that many two body resonance decays exist which result in unlike-sign pairs. Some of these were studied in Section 5.1. One might expect some effect of these decays on $C_2(+-)$ but there were only minimal contributions near $q_t = 0$.

6.4 Radius and Lifetime Measurement

In this section the space-time characteristics of the pion source will be studied using like-sign charged particle correlations as a function of the charged particle multiplicity, n_{ch}. The spatial shape of the region in which pion generation occurs will also be analyzed.

6.4.1 Correlation C_2 versus q_t

The correlation function, C_2, is studied as a function of the charged multiplicity, n_{ch}, taken from the Hodoscope in a region of pseudorapidity $|\eta| \leq 3.25$. All information for this analysis was obtained from reconstructed charged tracks measured in a region of pseudorapidity $-0.36 \leq \eta \leq 1.0$. All data were analyzed for fixed intervals of charged particle multiplicity, n_{ch}. The uncorrelated back-

ground reference sample was obtained from like-sign track pairs mixed different events, thus avoiding the artificial analysis correlations, as discussed in previous sections. Coulomb corrections are not applied. For small opening angles ($< 1^0$) of equally charged particles, the Coulomb interaction between the particles will influence the correlation function, C_2 (see Section 6.2.3). Our experimental requirement of $\theta_{xz} > 12^0$ will make such Coulomb corrections to the correlation function negligible.

The correlation function

$$C_2 = \frac{(++)_S + (--)_S}{(++)_D + (--)_D}, \tag{6.37}$$

for all data was normalized to be equal to unity in the region $0.6 \leq q_t \leq 1$ GeV/c. The above vertex correction (Section 6.2.6) and the minimum opening angle cut $\theta^o_{xz} \geq 12^o$ were applied. Figures 6.33, 6.34, and 6.35 show that there is little difference in the correlation function for a cut of $\theta^o_{xz} \geq 10^o$, $\theta^o_{xz} \geq 15^o$, or $\theta^o_{xz} \geq 20^o$. Figure 6.36 shows the observed radius as a function of the above θ^o_{xz} cut in the Gaussian representation (Equation 1.19 or Equation 6.38).

The normalized data in the region $q_0 \leq 0.2$ GeV were fitted with a Gaussian of the form (Equation 1.19)

$$C_2 = A(1 + \lambda e^{-\beta q_t^2}), \tag{6.38}$$

where A is a normalization factor and λ is the ad-hoc incoherence or chaoticity factor.(Note in the case of the Weiner (Section 1.2.7) parameterization, this chaoticity factor is denoted as p). The radius of the source is calculated by the parameter β: $R = \hbar c\sqrt{\beta}$.

Before we study the correlation function (Equation 6.37) as a function of the charged multiplicity, n_{ch}, we study the the following correlation functions:

$$C_2 = \frac{(++)_S}{(++)_D}, \tag{6.39}$$

and

$$C_2 = \frac{(--)_S}{(--)_D}, \tag{6.40}$$

separately. Figures 6.37 and 6.38 show that there is no difference in the determination of the radius R within the errors. The source radius, R, for the $\pi^+\pi^+$ pairs is 1.04 ± 0.1 fm and 1.08 ± 0.1 fm for $\pi^-\pi^-$ pairs for mean charged multiplicity $< n_{ch} >= 97$. The chaoticity factors, λ, are about the same.

Figures 6.39, 6.40, and 6.41 show the observed correlation, C_2, vs q_t for three multiplicity bins $0 \leq n_{ch} \leq 60$, $60 \leq n_{ch} \leq 100$, and $100 \leq n_{ch} \leq 240$ (Table 6.1). Figures 6.42, 6.43, and 6.44 show the observed correlation, vs q_t for three multiplicity bins $0 \leq n_{ch} \leq 80$, $80 \leq n_{ch} \leq 120$, and $120 \leq n_{ch} \leq 240$ (Table 6.4).

Figure 6.45 shows the source size as a function of the charged particle density, $dn_{ch}/d\eta$, (where η is the pseudorapidity) in the Gaussian representation (Equation 1.19). Figure 6.45 the UA1 [80] and CDF [81] data points, were plotted for comparison. We noticed a small disagreement between the two sets of data. Comparisons with other investigations on the same topic should be made cautiously because of differences in the types of reactions considered, the energy range, difference in phase space studied (for example in our limited spectrometer acceptance the available phase space, Figure 6.46, is only a part of the whole space), etc.

Figure 6.47 shows the chaoticity factor, λ, as a function of the mean charged multiplicity $< n_{ch} >$. The chaoticity parameter seems to decrease with increasing $< n_{ch} >$. This effect has been previously observed by UA1 [80] at center of mass energy $\sqrt{s} = 640$ GeV.

Figure 6.48 shows the dependence of the source size as a function of the charged particle density, $dn_{ch}/d\eta$, in the Podgoretsky representation, (Equation 1.37, Table 6.3). The relation between the two radii is plotted in Figure 6.49.

For comparison with the previous parameterizations, Figure 6.50 shows the dependence of the source size on the charged particle density, $dn_{ch}/d\eta$, in the Weiner representation, (Equation 1.40, Table 6.2). There is no difference between the Gaussian radius and the Weiner radius within the errors.

A limited attempt was made to study C_2 vs q_t as a function of the total momentum of the pair. Figures 6.51 and 6.52 show the correlation function vs q_t for $P_{tot} < 0.9$ GeV/c and $P_{tot} > 0.9$ GeV/c, respectively. The observed radius, R, is 0.95 fm and 0.55 fm for the two different regions of total pion pair momentum (Table 6.5).

All fits to the correlation function, C_2, were done by minimizing the χ^2 with the utility minimization routine MINUIT.

6.4.2 Correlation C_2 versus q_0

In this section, the relationship between the correlation function, C_2 and q_0 is studied as a function of the charged multiplicity taken from the hodoscope in a region of pseudorapidity $|\eta| \leq 3.25$. All information for this analysis was ob-

tained from reconstructed charged tracks measured in a region of pseudorapidity $-0.36 \leq \eta \leq 1.0$. All data were analyzed for fixed intervals of charged particle multiplicities, n_{ch}.

The uncorrelated background reference sample was obtained from like-sign track pairs mixed from two different events. The correlation function

$$C_2 = \frac{(++)_S + (--)_S}{(++)_D + (--)_D} \tag{6.41}$$

was normalized for all data to be equal to unity in the region $0.6 \leq q_0 \leq 1$ GeV. Only events with $q_t < 0.200$ GeV/c were used.

Figures 6.53, 6.54, and 6.55 show the observed correlation, C_2, versus q_0 for three multiplicity bins $0 \leq n_{ch} \leq 60$, $60 \leq n_{ch} \leq 100$, and $100 \leq n_{ch} \leq 240$ (Table 6.6). Figures 6.56, 6.57, and 6.58 show the observed correlation, C_2, vs q_0 for the multiplicity bins $0 \leq n_{ch} \leq 80$, $80 \leq n_{ch} \leq 120$, and $120 \leq n_{ch} \leq 240$ (Table 6.7). Figure 6.59 shows the dependence of the source lifetime as a function of the charged particle density, $dn_{ch}/d\eta$. It includes the multiplicity bins $0 \leq n_{ch} \leq 80$, $80 \leq n_{ch} \leq 120$ and, $120 \leq n_{ch} \leq 240$ (Table 6.7).

One can verify the nature of the Bose-Einstein correlation in q_0 by studying $\pi^{\pm}$ pairs in the same manner as $\pi^+\pi^+$, $\pi^-\pi^-$ pairs were analyzed. Figures 6.60, 6.61, and 6.62 show there is no evidence of an enhancement in the correlation function, C_2, vs q_0, as a function of multiplicity, n_{ch},

$$C_2 = \frac{(+-)_S}{(+-)_D}, \tag{6.42}$$

where the pairs $(+-)_S$ come from the same event and $(+-)_D$ come from the different event mixing algorithm.

C_2 vs q_0 was also studied as a function of the total momentum of the pair. Figures 6.63 and 6.64 show the correlation function vs q_0 for $P_{tot} < 0.9$ GeV/c and $P_{tot} > 0.9$ GeV/c, respectively. The observed radius R is 0.95 fm and 0.55 fm, respectively for the two different ranges of total pion pair momentum (Table 6.8).

It is claimed by S. Barshay [82] that the charged particle multiplicity, n_{ch}, increases with the transverse dimension of the overlapping region of the two colliding particles, and that this region is related to the radius of the source, R (Figure 6.45). Our results, (Figure 6.59) show that the depth or the lifetime or the transverse extension of the source increases with the charged multiplicity.

6.4.3 Directional Dependence of the Radius R

To study the directional dependence of the radius, R, it was assumed that the source might be rotationally symmetric around the collision z-axis, with an ellipsoidal shape [83]. In this case the correlation function, C_2, is expressed as:

$$C_2 = 1 + \lambda e^{-(R_{xy}^2 q_{xy}^2 + R_z^2 q_z^2)}, \tag{6.43}$$

where R_{xy}, R_z are the transverse and longitudinal dimensions of the pion source, $q_{xy} = \sqrt{q_x^2 + q_y^2}$, and q_z are the components of the $\vec{q}$ transverse to and along the z-axis.

The correlation function, C_2, was studied, in terms of the angle, α (Figure 6.65), the angle between the beam z-axis and the momentum difference $\vec{q}$ of the pion pair. Figure 6.66 shows the correlation function, C_2, as a function of q_t for $|\cos\alpha| > 0.80$. The fitted radius is 1.2 ± 0.1 fm compared to 1.0 ± 0.1 calculated using all angles α (Figure 6.33). This supports the idea of an ellipsoidal

source shape. Because of our limited angle spectrometer, we were limited to low statistics for $|\cos\alpha| < 0.80$.

Yet another way to study the directional dependence of the radius, R, is to study the correlation function, C_2, versus q_t as a function of the angle ϕ (Figure 6.67) which is given by:

$$\cos\phi = \frac{\hat{y}\cdot(\vec{p_1}\times\vec{p_2})_t}{|(\vec{p_1}\times\vec{p_2})_t|}, \tag{6.44}$$

where $\hat{y}$ is the unit vector along the y-axis, $\vec{p_1}$, $\vec{p_2}$ are the momentum of two particles, and $(\vec{p_1}\times\vec{p_2})_t$ is the transverse component of the $\vec{p_1}\times\vec{p_2}$ vector to x-axis. This angle ϕ describes the orientation of the pion plane. The limited opening angle of the spectrometer does not allow us to break the ϕ angle into many bins. Figure 6.68 shows the correlation function as a function of q_t for $\phi < 6^0$, while Figure 6.69 shows the correlation function C_2 as a function of q_t for $\phi > 6^0$. It was found that the radius, R, for $\phi < 6^0$ is $R = 1.2 \pm 0.1$, while for $\phi > 6^0$, $R = 0.9 \pm 0.1$. Once more, the extension of the pion source parallel to the beam axis is longer than that transverse to it. Thus there may be a ellipsoid shape to the pion source.

We can now try to determine the extreme extensions both parallel to and transverse to the beam z-axis. Using the above Gaussian parameterization of the pion source shape in 3-D (Equation 6.43), we study the correlation function, C_2, with respect to q_{xy} and q_z. Figure 6.70 shows this correlation function. The result of a 2-dimensional fitting of the correlation function, C_2, could give us R_{xy} and R_z the transverse and longitudinal radii of the pion source. It is clear with our limited opening angle spectrometer we could not do this 2-dimensional

fitting to the correlation function, C_2, as shown in Figure 6.70.

6.5 Tables

$< n_{ch} >$	$dn_{ch}/d\eta$	R (fm)	λ
$0 - 60$	6.75	0.62 ± 0.09	0.36 ± 0.05
$60 - 100$	12.5	1.00 ± 0.08	0.20 ± 0.01
$100 - 240$	18.2	1.52 ± 0.14	0.16 ± 0.02

Table 6.1: Fitted values of radius, R, and chaoticity, λ, for three multiplicity bins in the Gaussian parameterization. The coded errors are statistical.

$< n_{ch} >$	$dn_{ch}/d\eta$	R (fm)	p
$0 - 60$	6.75	0.60 ± 0.11	0.20 ± 0.04
$60 - 100$	12.5	0.98 ± 0.10	0.11 ± 0.01
$100 - 240$	18.2	1.48 ± 0.17	0.08 ± 0.01

Table 6.2: Fitted values of radius R and chaoticity, p, (Equation 1.40) for three multiplicity bins in the Weiner parameterization. The coded errors are statistical.

$< n_{ch} >$	$dn_{ch}/d\eta$	R (fm)	λ
$0 - 60$	6.75	1.17 ± 0.20	0.35 ± 0.06
$60 - 100$	12.5	1.92 ± 0.18	0.20 ± 0.01
$100 - 240$	18.2	2.79 ± 0.29	0.15 ± 0.01

Table 6.3: Fitted values of radius, R, for three multiplicity bins in the Podgoretsky parameterization. The coded errors are statistical.

$< n_{ch} >$	$dn_{ch}/d\eta$	R (fm)	λ
$0 - 80$	9.00	0.70 ± 0.09	0.28 ± 0.03
$80 - 120$	15.5	1.10 ± 0.1	0.18 ± 0.01
$120 - 240$	20.17	1.86 ± 0.35	0.14 ± 0.03

Table 6.4: Fitted values of radius, R, and chaoticity, λ, for three multiplicity bins in the Gaussian parameterization. (Bins are shifted with respect to Table 1). The coded errors are statistical.

P_{tot} (GeV/c)	R (fm)	λ
$0 - 0.9$	0.95 ± 0.37	0.22 ± 0.015
$0.9 - ...$	0.55 ± 0.21	0.23 ± 0.015

Table 6.5: Fitted values of radius, R, and chaoticity, λ, for two ranges of total momentum, P_{tot}, of the pair bins in the Gaussian parameterization. The coded errors are statistical.

$< n_{ch} >$	$dn_{ch}/d\eta$	τ (fm)	λ
$0 - 60$	6.75	0.53 ± 0.07	0.32 ± 0.04
$60 - 100$	12.5	0.86 ± 0.12	0.14 ± 0.01
$100 - 240$	18.2	0.99 ± 0.15	0.11 ± 0.04

Table 6.6: Fitted values of lifetime, τ, and chaoticity, λ, for three multiplicity bins in the Gaussian parameterization. The coded errors are statistical.

$< n_{ch} >$	$dn_{ch}/d\eta$	τ (fm)	λ
$0 - 80$	9.00	0.65 ± 0.06	0.22 ± 0.02
$80 - 120$	15.5	0.89 ± 0.12	0.13 ± 0.01
$120 - 240$	20.17	0.88 ± 0.2	0.09 ± 0.02

Table 6.7: Fitted values of lifetime, τ, and chaoticity, λ, for three multiplicity bins in the Gaussian parameterization. (Bins are shifted with respect to the previous table). The coded errors are statistical.

P_{tot} (GeV/c)	τ (fm)	λ
$0 - 0.9$	0.94 ± 0.45	0.10 ± 0.008
> 0.9	0.45 ± 0.21	0.13 ± 0.01

Table 6.8: Fitted values of lifetime, τ, and chaoticity , λ, for two total momenta, P_{tot}, of the pair bins in the Gaussian parameterization. The coded errors are statistical.

Figures for Chapter 6

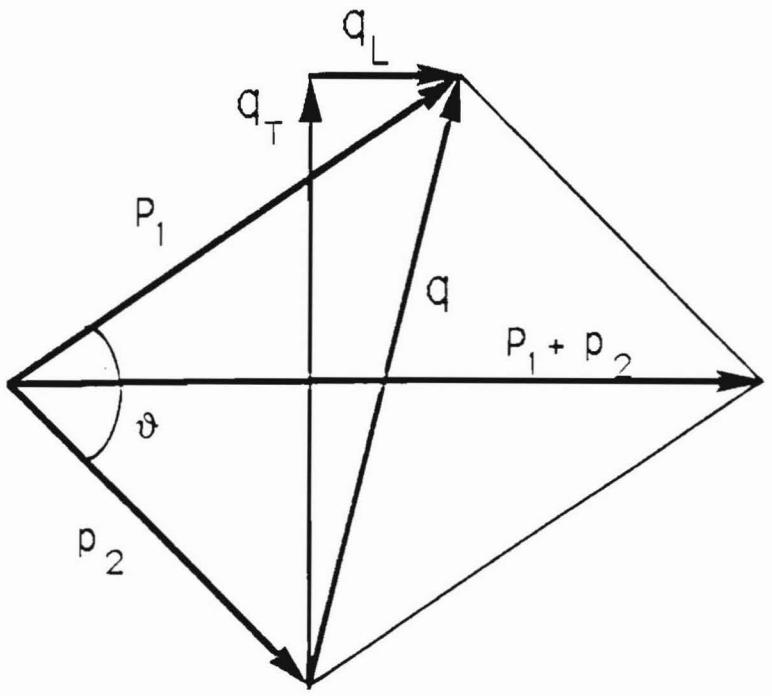

Figure 6.1: Total momentum $\vec{p}$, $\vec{q_t}$ and $\vec{q_l}$ vector definitions of a $\pi\pi$ pair.

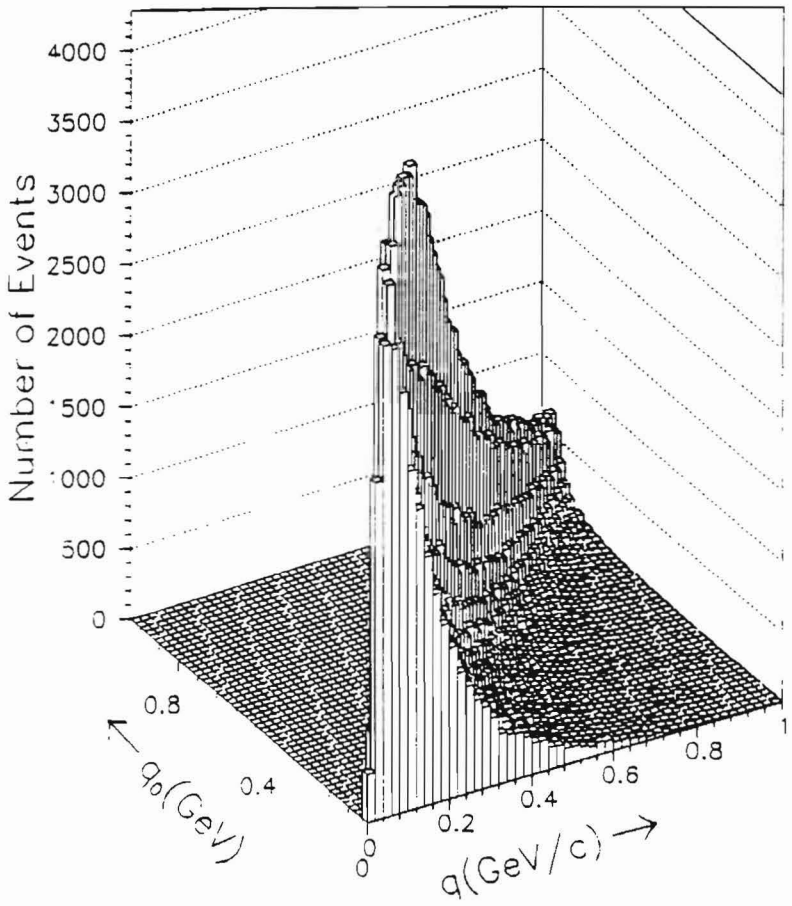

Figure 6.2: Momentum distribution, dn/dq_μ, as a function of $(|\vec{q}|, q_0)$ over the spectrometer acceptance used in this experiment.

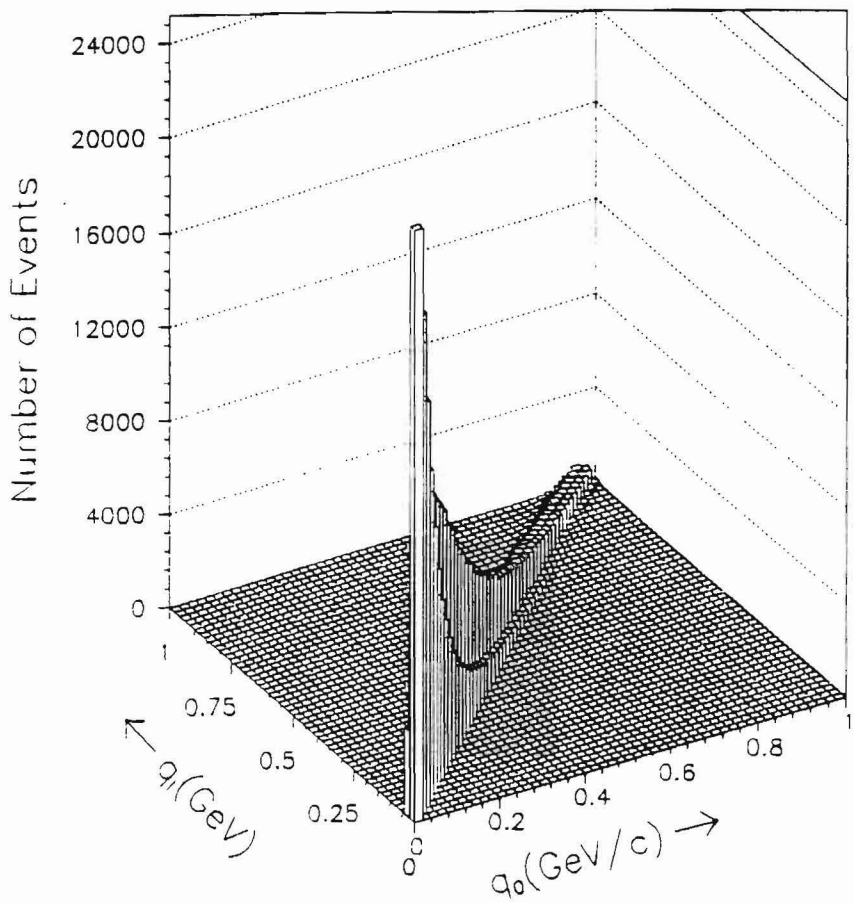

Figure 6.3: Relation of q_0 versus q_l for our data.

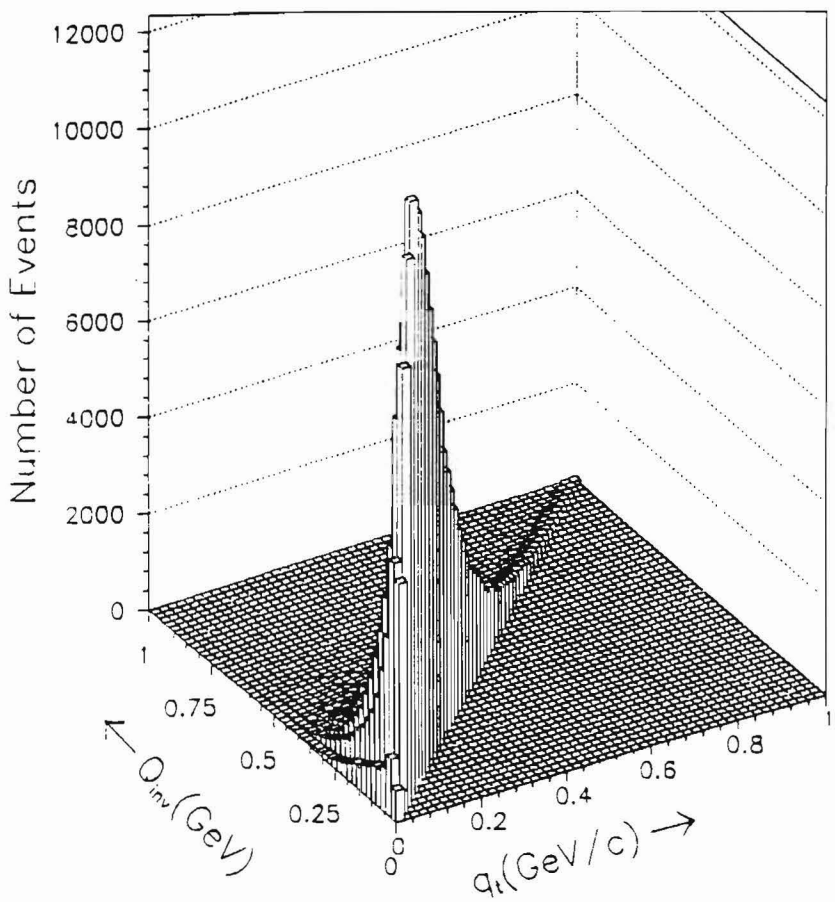

Figure 6.4: Relation of Q versus q_t for our data.

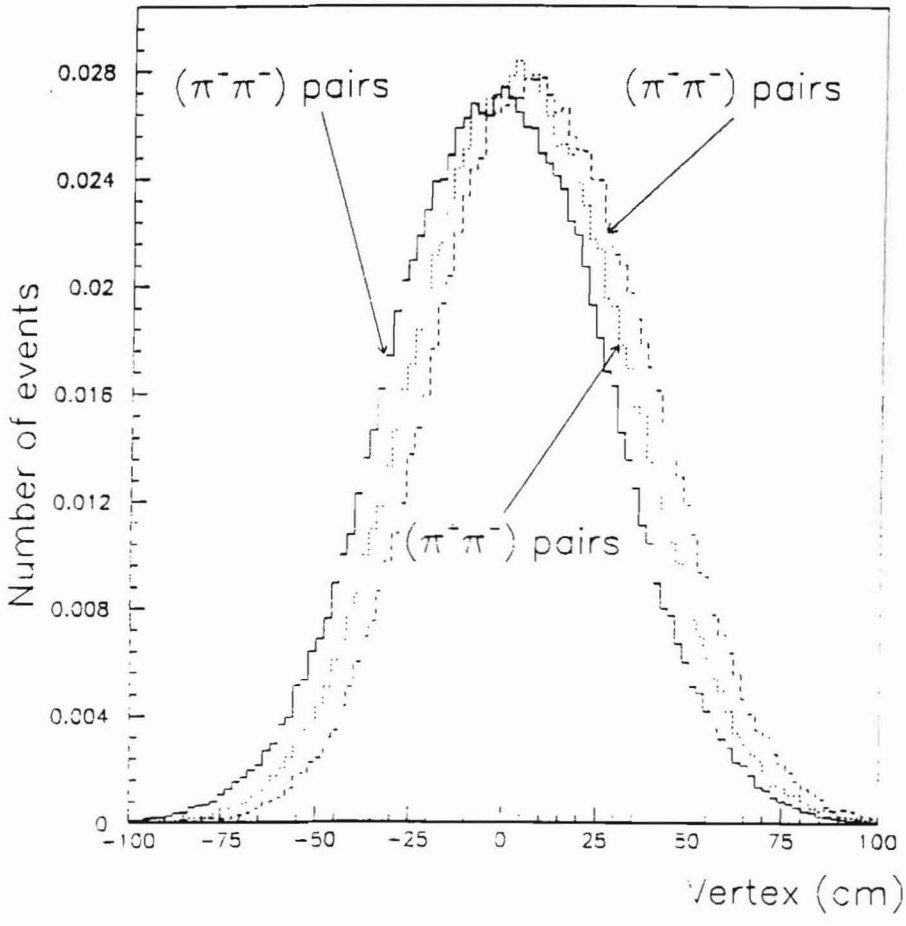

Figure 6.5: Vertex distribution of events accepted by E735 Monte Carlo analysis for $\pi^+\pi^+$, $\pi^-\pi^-$, and $\pi^+\pi^-$.

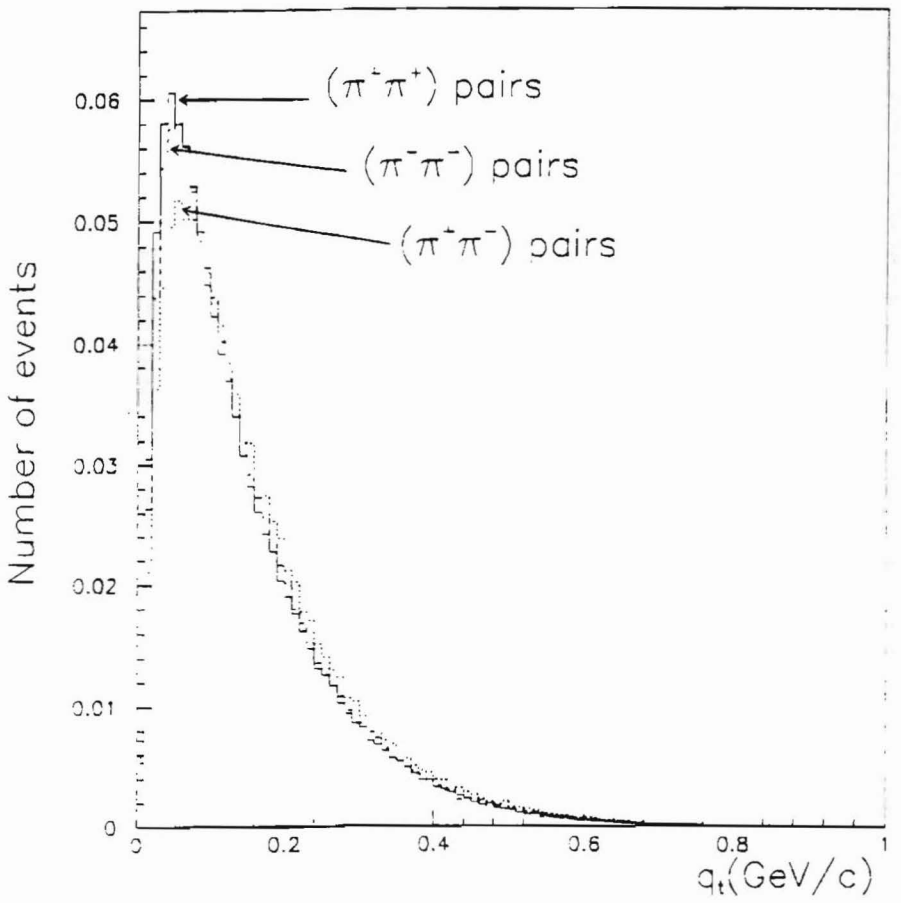

Figure 6.6: q_t distribution of events accepted by E735 Monte Carlo analysis for $\pi^+\pi^+, \pi^-\pi^-$, and $\pi^+\pi^-$ pairs.

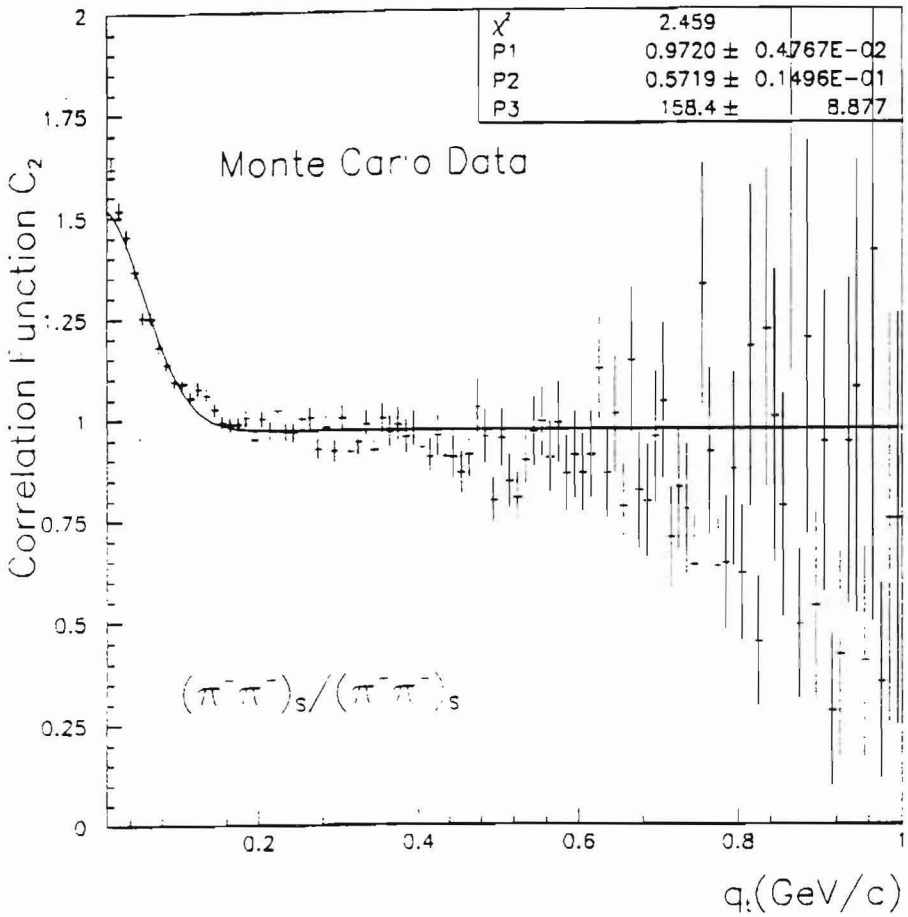

Figure 6.7: Correlation function, $C_2 = (\pi^+\pi^+)_S/(\pi^+\pi^-)_S$, versus q_t.

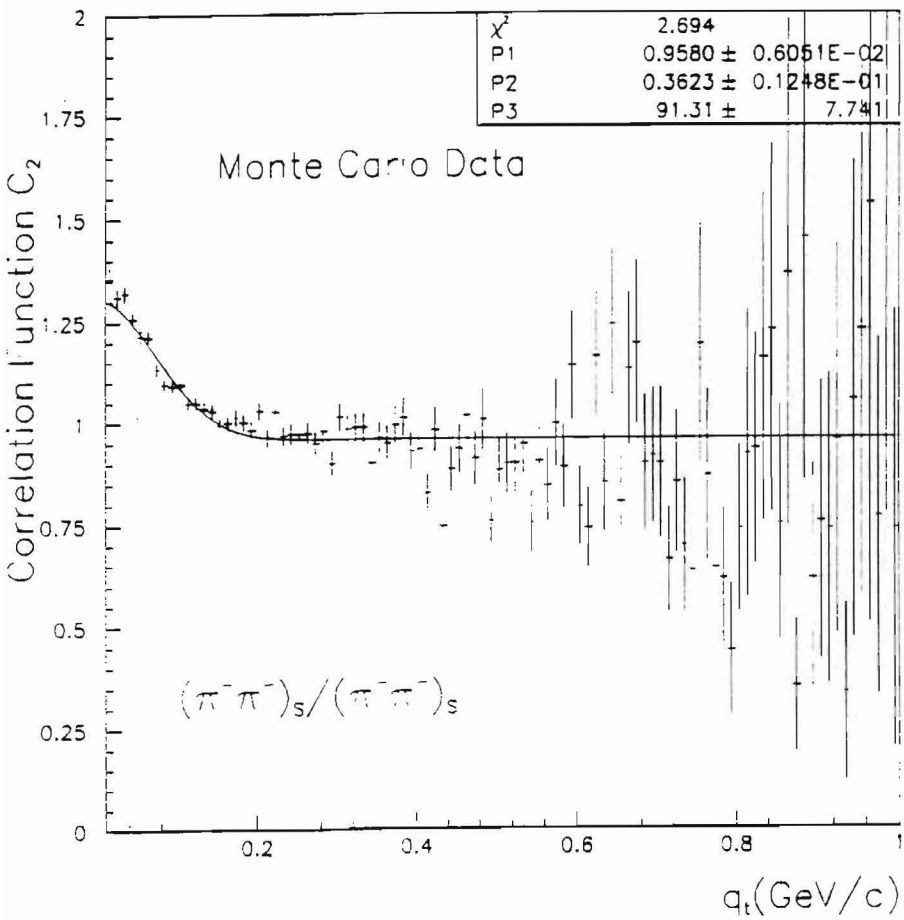

Figure 6.8: Correlation function, $C_2 = (\pi^-\pi^-)_S/(\pi^+\pi^-)_S$, versus q_t.

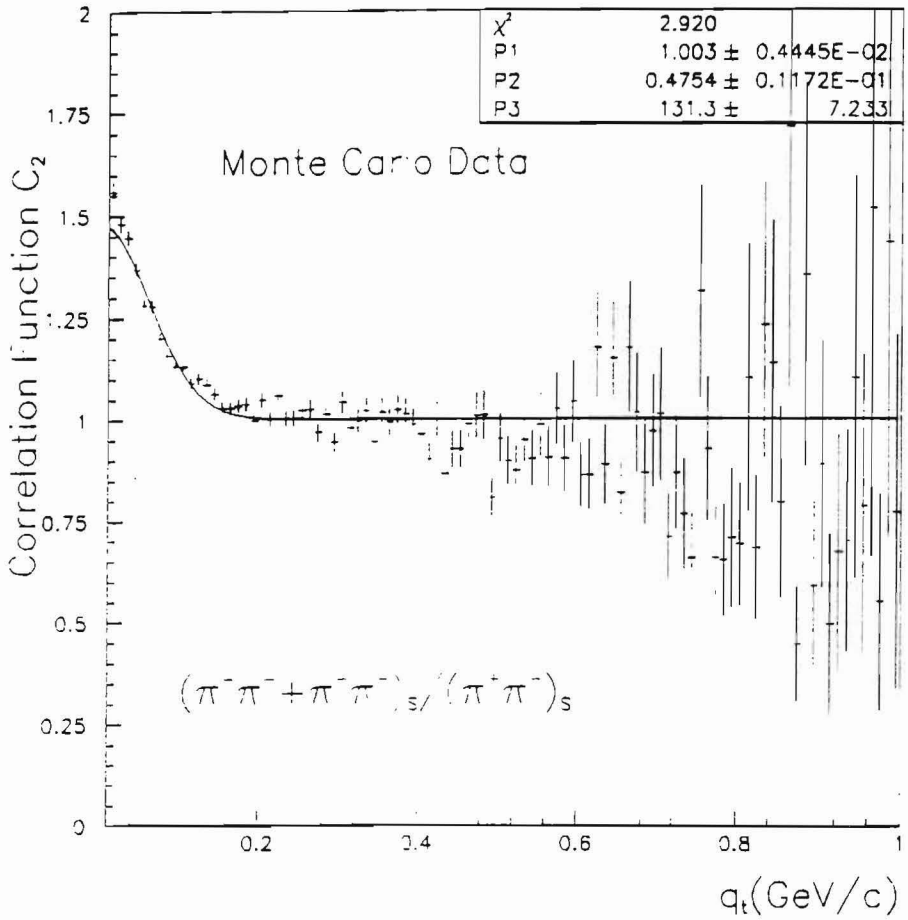

Figure 6.9: Correlation function $C_2 = (\pi^+\pi^+ + \pi^-\pi^-)_S/(\pi^+\pi^-)_S$ versus q_t.

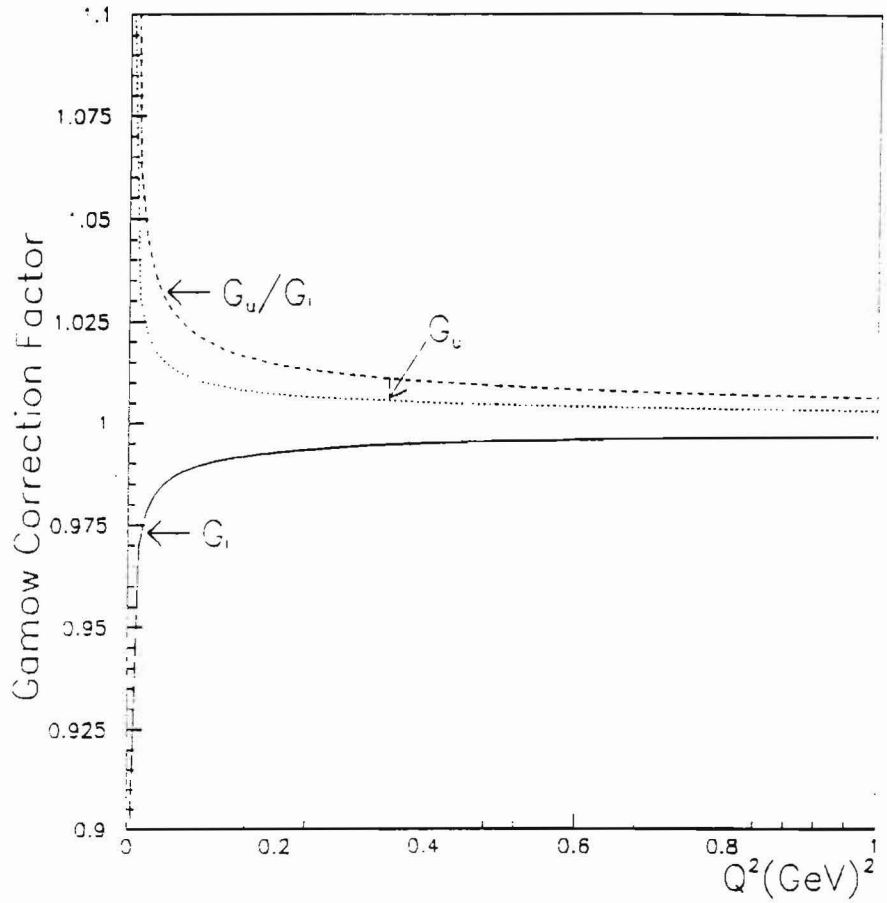

Figure 6.10: $G_u, G_l, G_u/G_l$ Gamow correction factors as a function of Q^2.

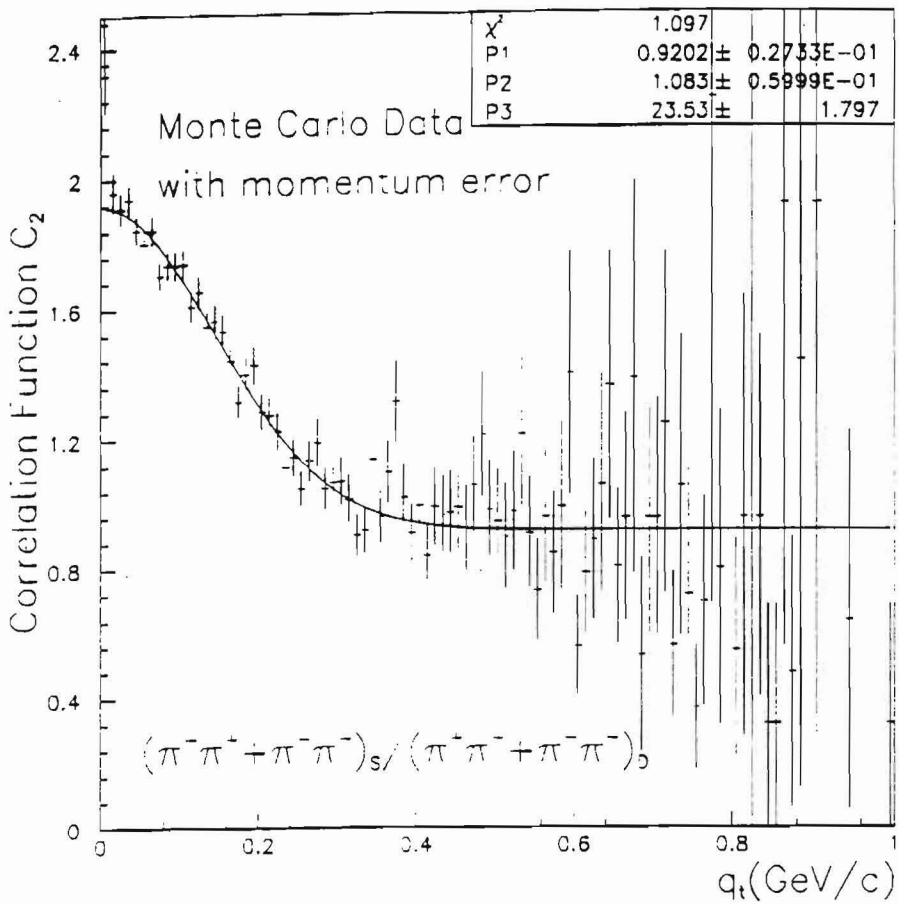

Figure 6.11: Monte Carlo correlation function, $C_2 = (\pi^-\pi^- + \pi^+\pi^+)_S/(\pi^-\pi^- + \pi^+\pi^+)_D$, as a function of q_t after momentum error. The fitted curve is of the form $C_2 = P_1(1 + P_2 \exp(-P_3 q_t^2))$.

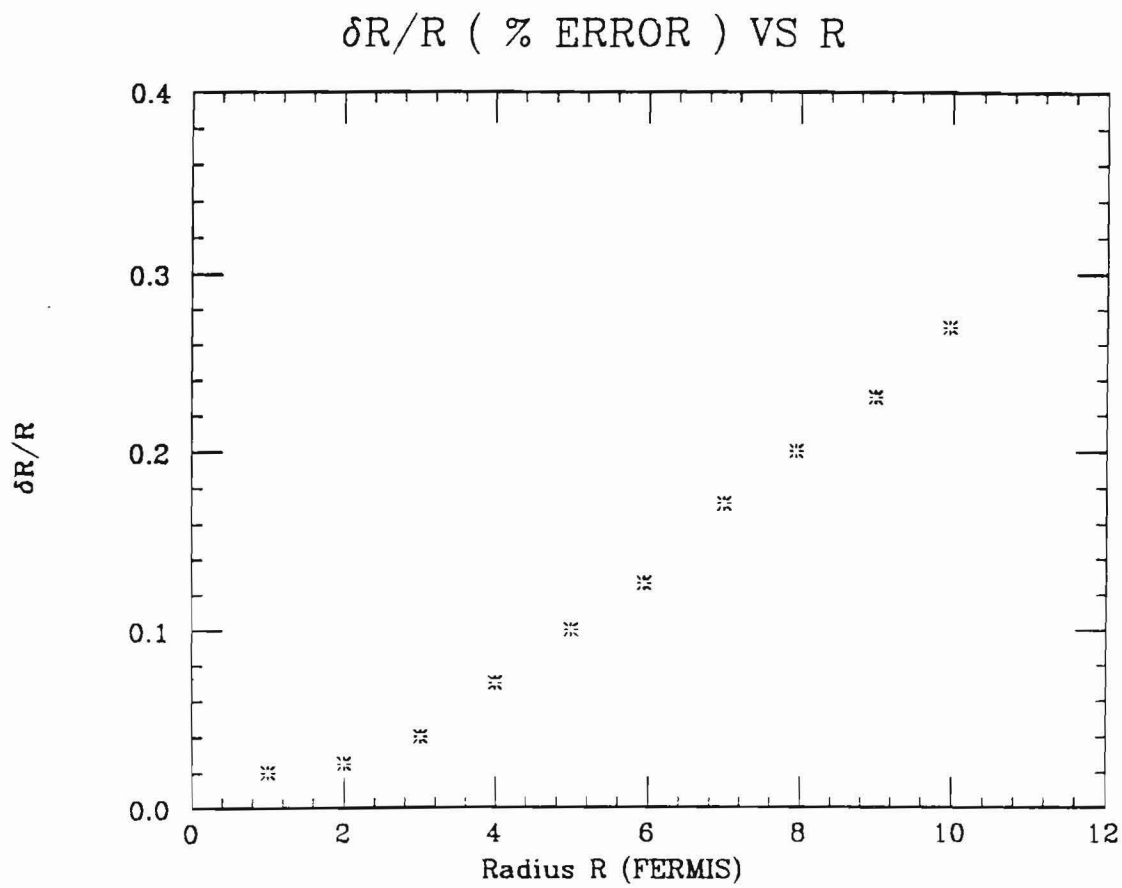

Figure 6.12: Relative radius error ($\delta R/R$) due to momentum single track error.

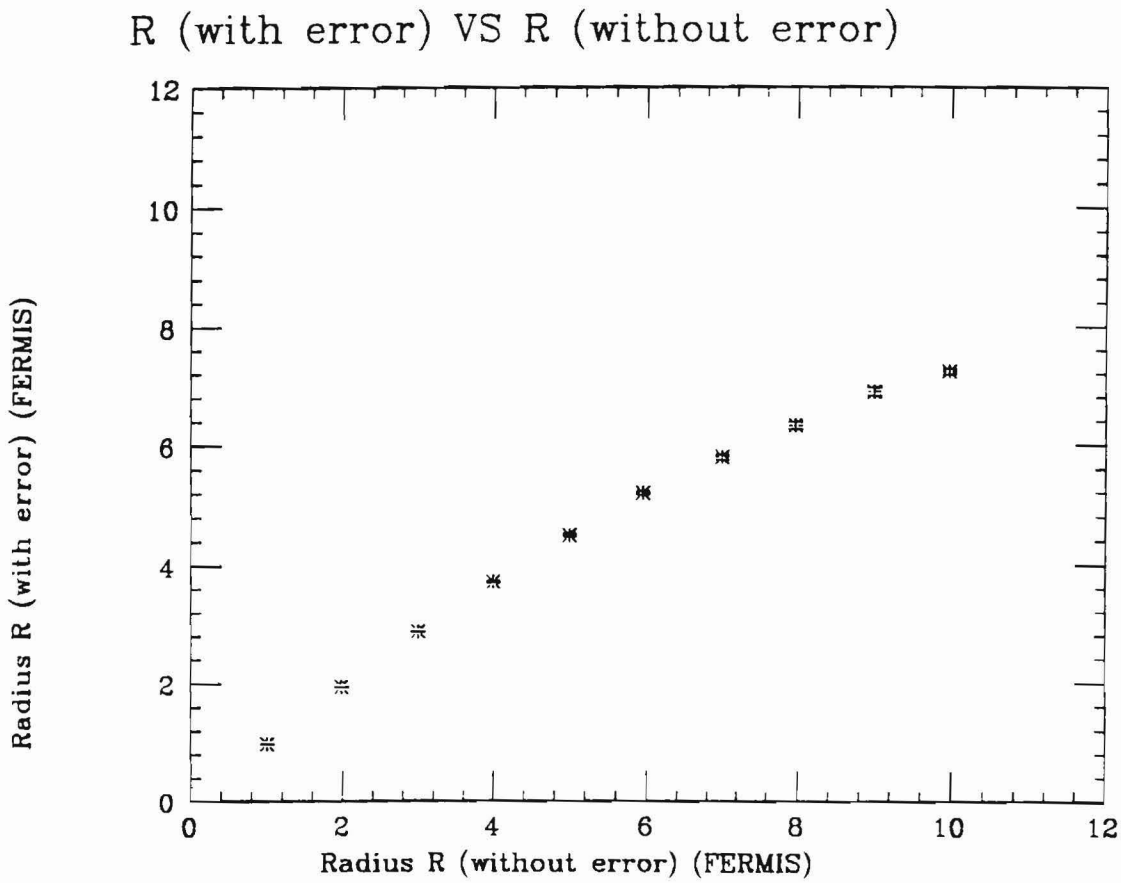

Figure 6.13: Radius with momentum error versus radius without momentum error.

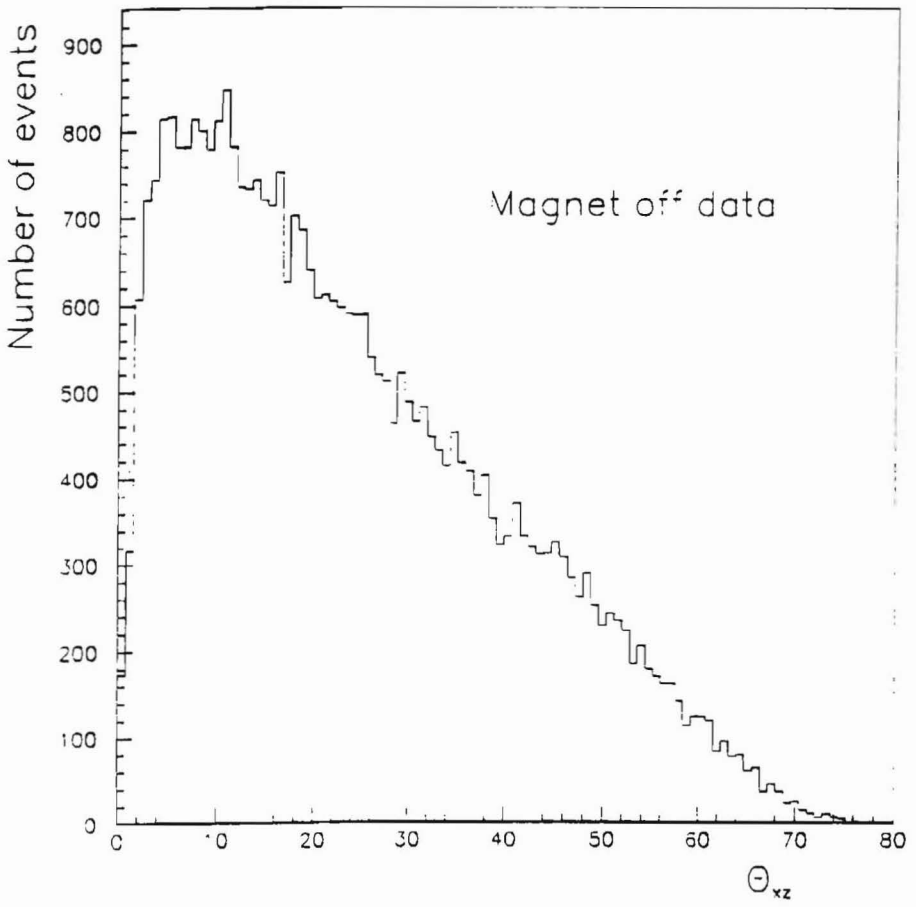

Figure 6.14: Input opening angle (θ_{xz}) distribution using tracking data taken in the magnet-off configuration.

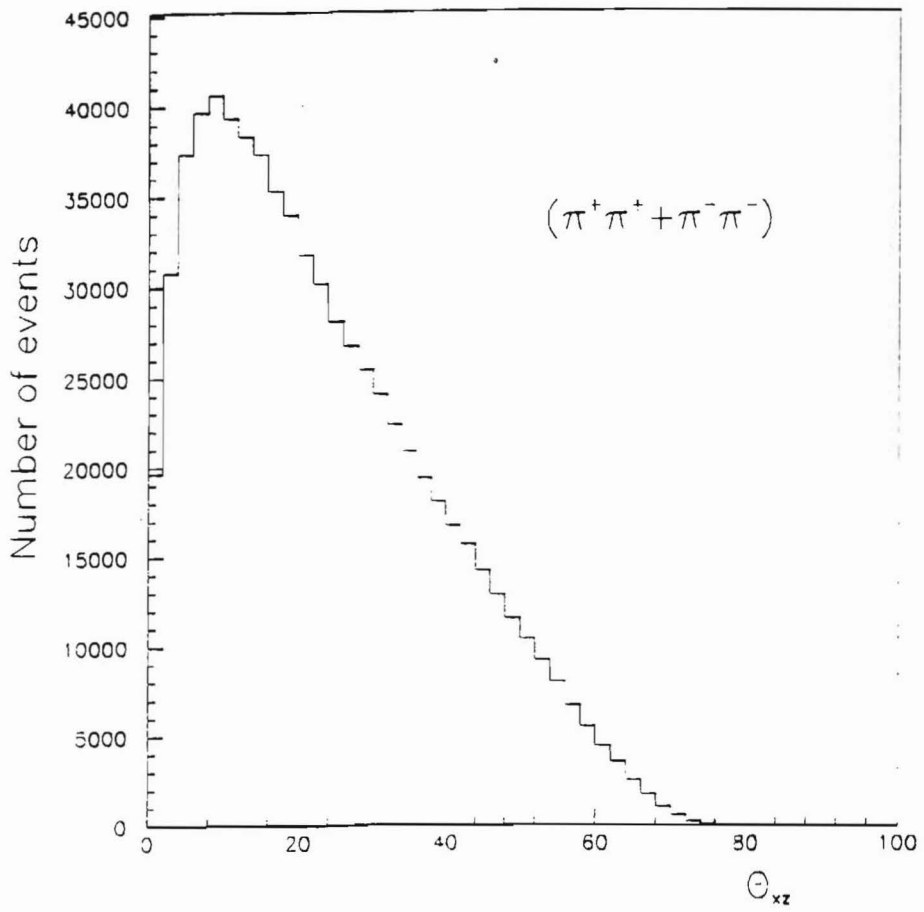

Figure 6.15: Input opening angle (θ_{xz} at the beam line) distribution using $\pi^+\pi^+ + \pi^-\pi^-$ tracking data taken in the magnet-on configuration.

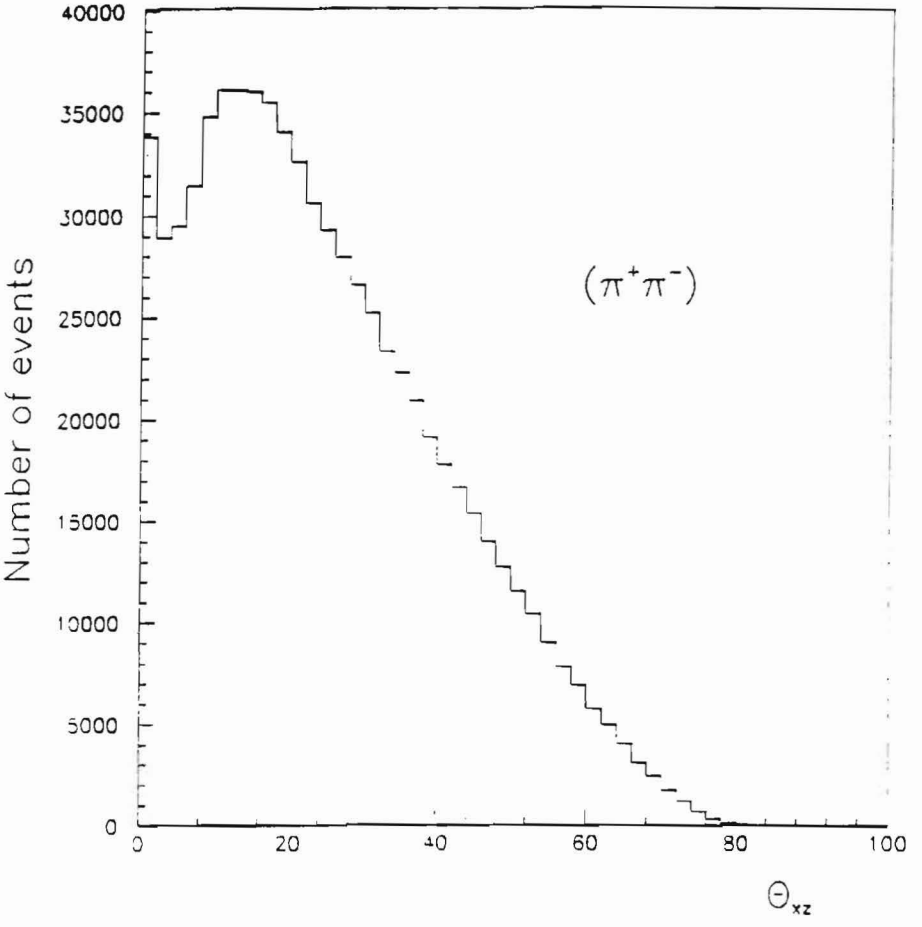

Figure 6.16: Input opening angle (θ_{xz} at the beam line) distribution using $\pi^+\pi^-$ tracking data taken in the magnet-on configuration.

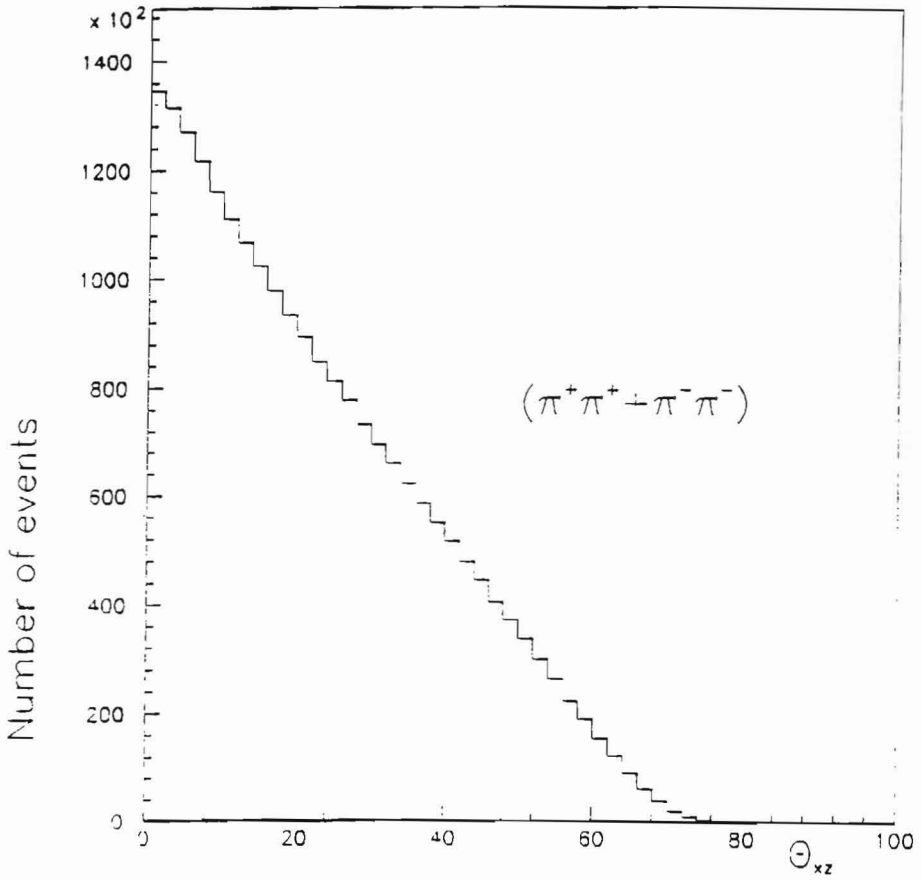

Figure 6.17: Input opening angle (θ_{xz} at the beam line) distribution using $\pi^+\pi^+ + \pi^-\pi^-$ tracking data taken in the magnet-on configuration, but the two tracks in the pair are taken from different events.

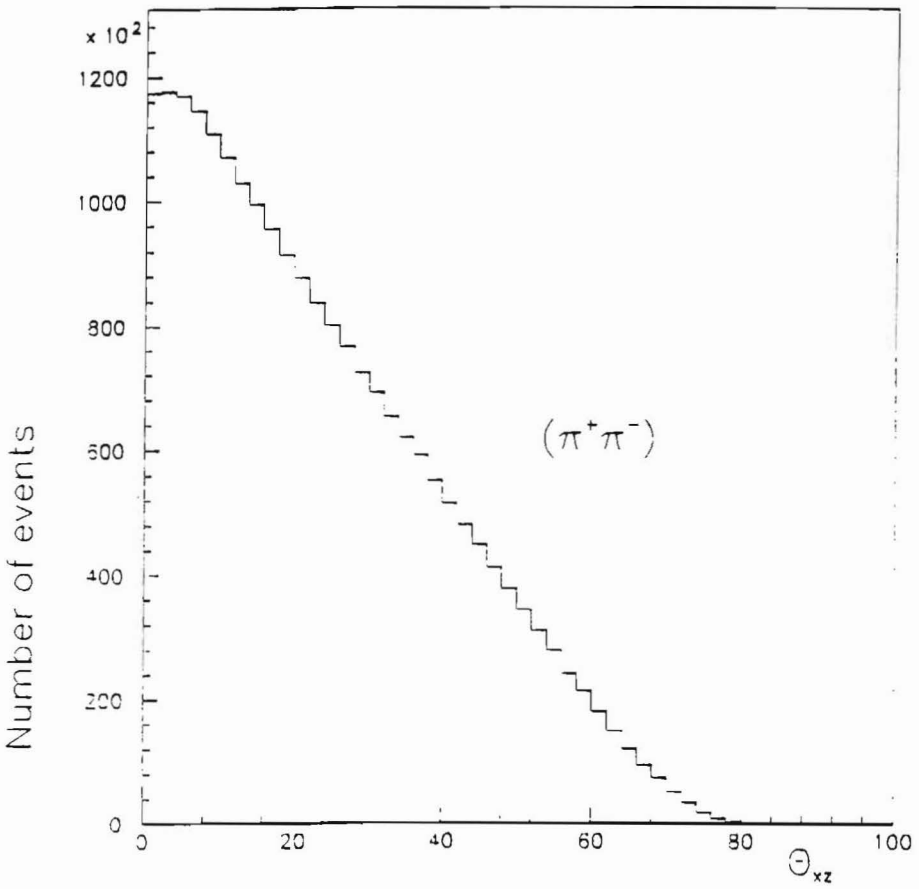

Figure 6.18: Input opening angle (θ_{xz} at the beam line) distribution using $\pi^+\pi^-$ tracking data taken in the magnet-on configuration, but the two tracks in the pair are taken from different events.

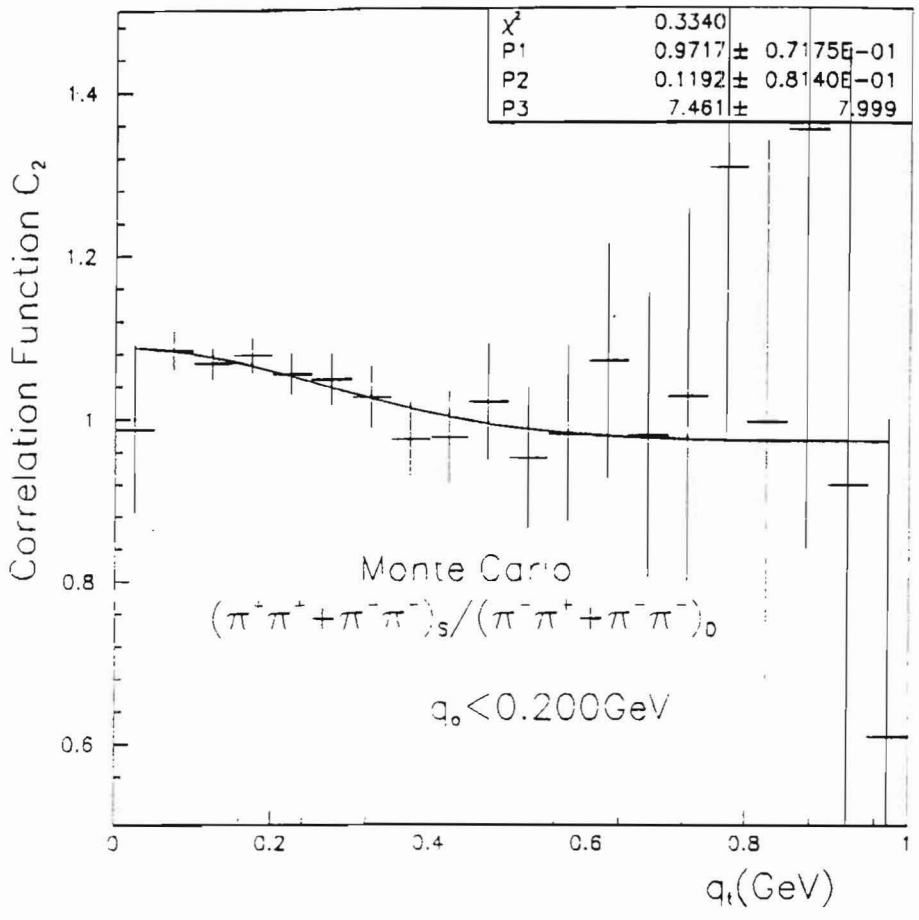

Figure 6.19: Correlation function, C_2, vs q_t using Monte Carlo $\pi^+\pi^+ + \pi^-\pi^-$ data without Bose-Einstein correlations.

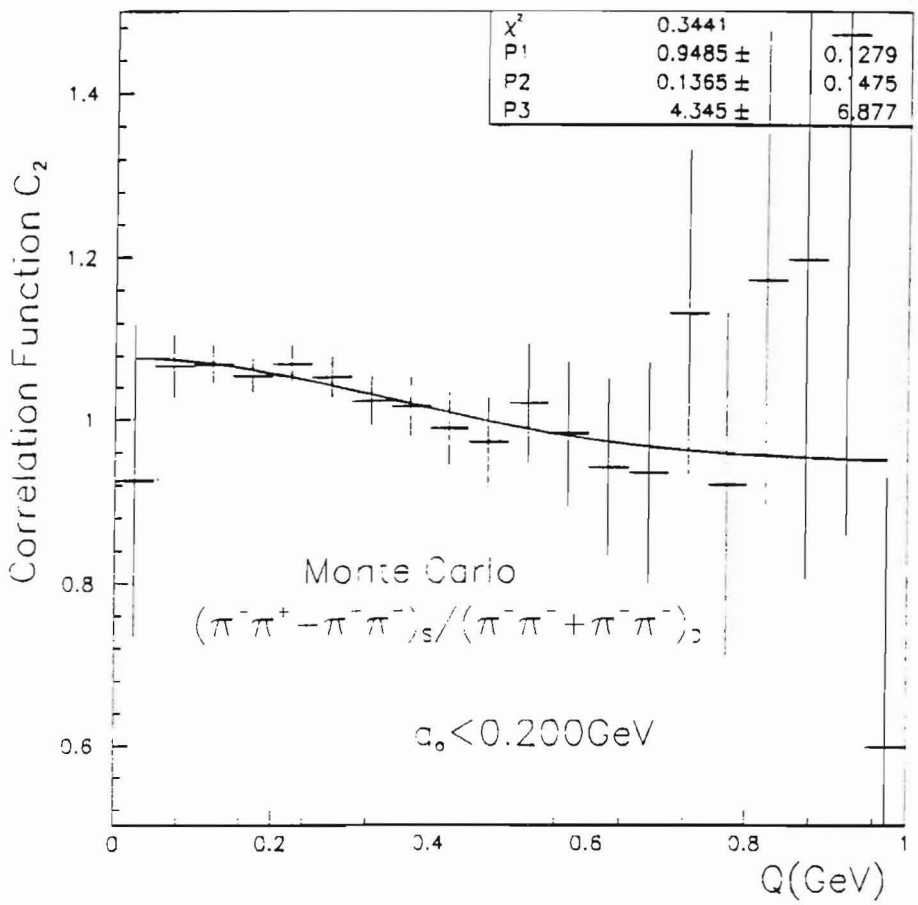

Figure 6.20: Correlation function, C_2, vs Q using Monte Carlo $\pi^+\pi^+ + \pi^-\pi^-$ data without Bose-Einstein correlations.

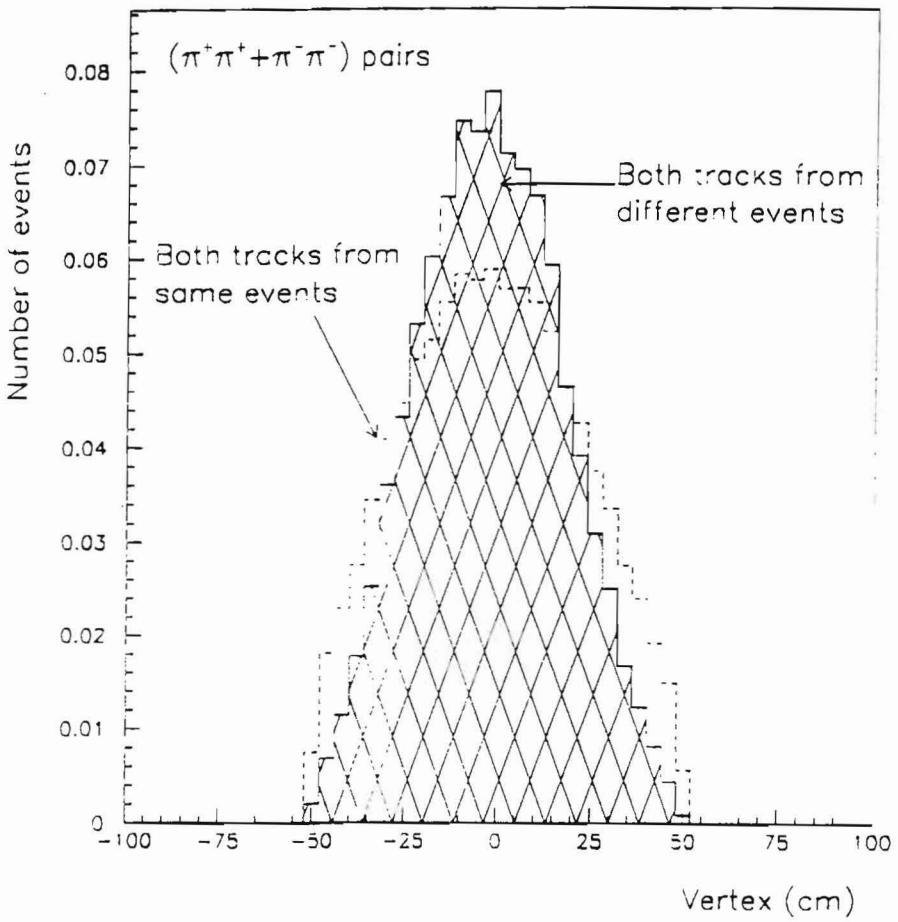

Figure 6.21: Vertex distribution for tracks coming from the same and different Monte Carlo $(\pi^+\pi^+ + \pi^-\pi^-)$ events.

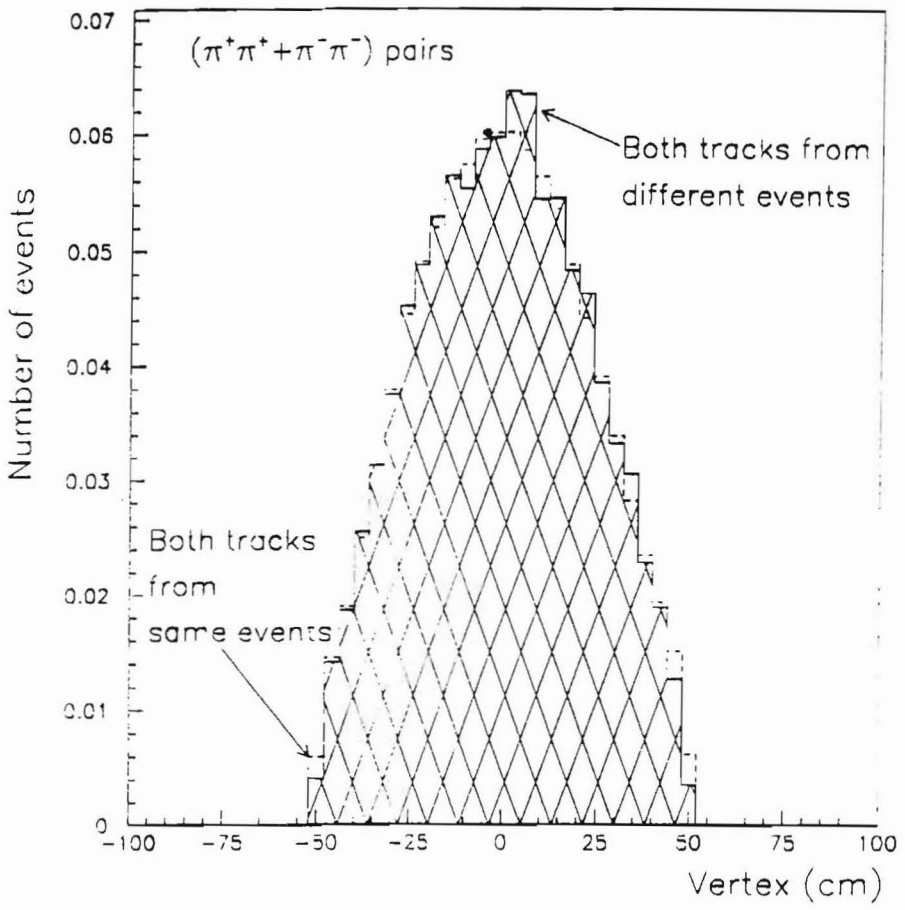

Figure 6.22: Vertex distribution for tracks coming from the same and different Monte Carlo $(\pi^+\pi^+ + \pi^-\pi^-)$ events.

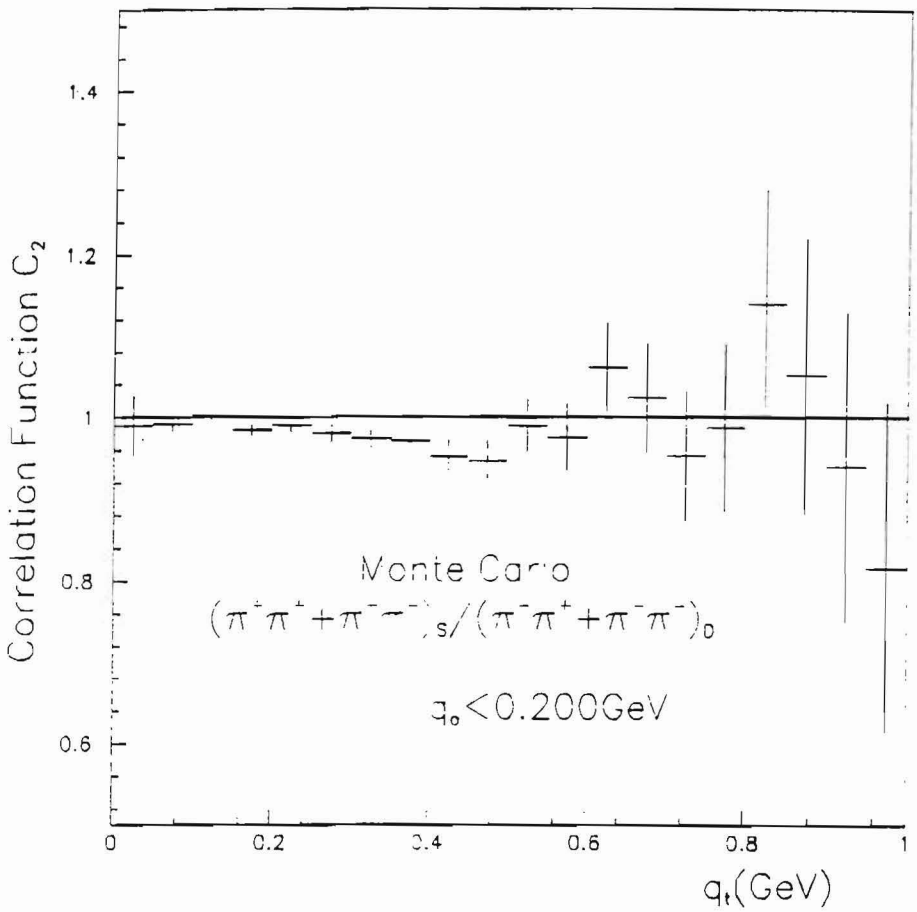

Figure 6.23: Correlation function, C_2, vs q_t using Monte Carlo $\pi^+\pi^+ + \pi^-\pi^-$ data without Bose-Einstein correlations.

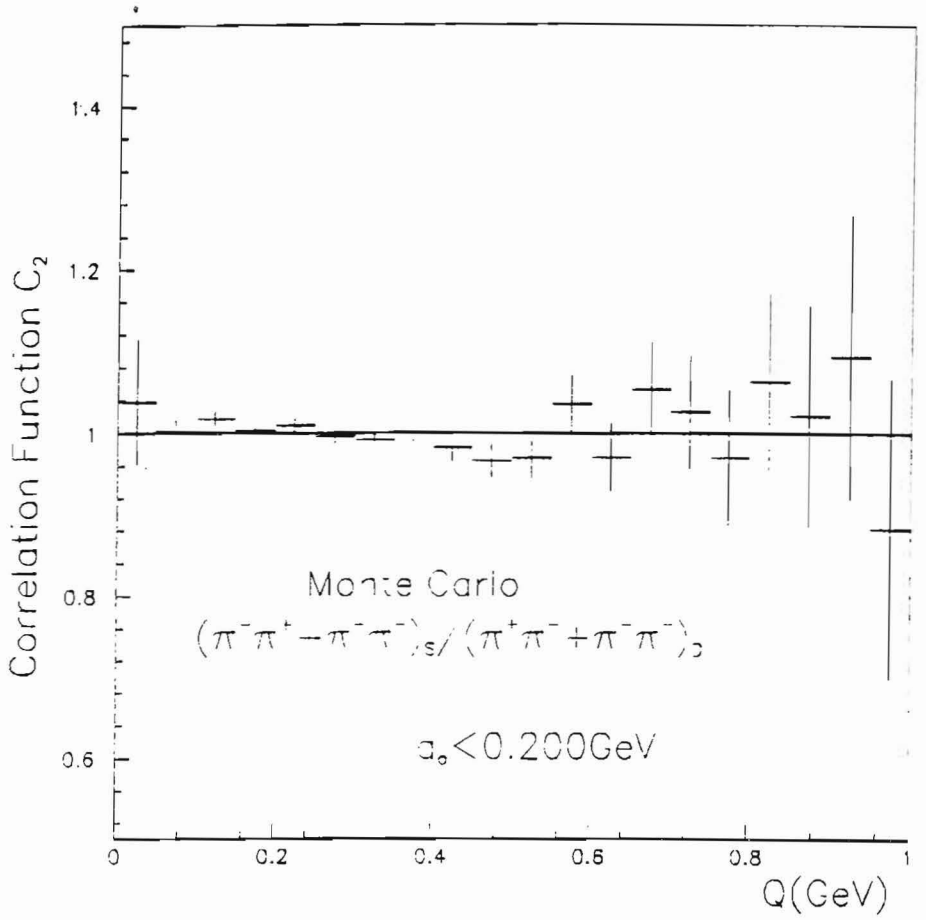

Figure 6.24: Correlation function, C_2, vs Q using Monte Carlo $\pi^+\pi^+ + \pi^-\pi^-$ data without Bose-Einstein correlations.

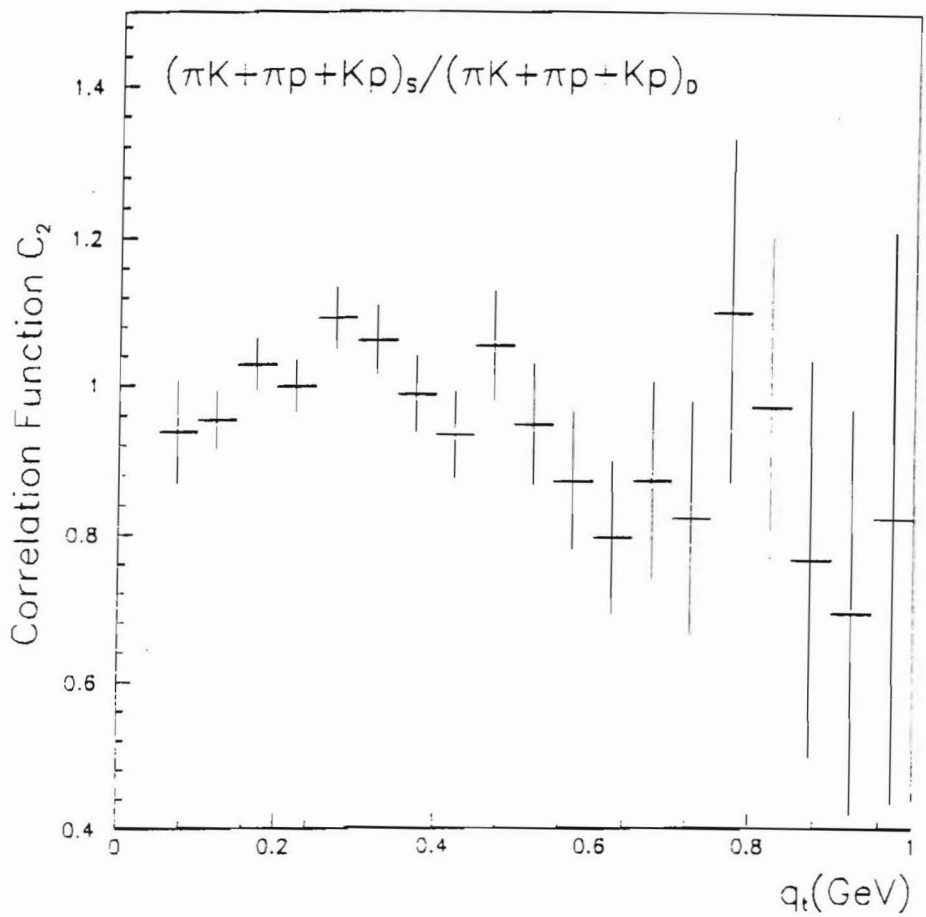

Figure 6.25: Correlation, function $C_2 = (\pi^{\pm}K^{\pm} + p^{\pm}K^{\pm} + \pi^{\pm}p^{\pm})_S/(\pi^{\pm}K^{\pm} + p^{\pm}K^{\pm} + \pi^{\pm}p^{\pm})_D$, as a function of q_t. This correlation function should be flat since the above pairs can not exhibit Bose-Einstein symmetrization.

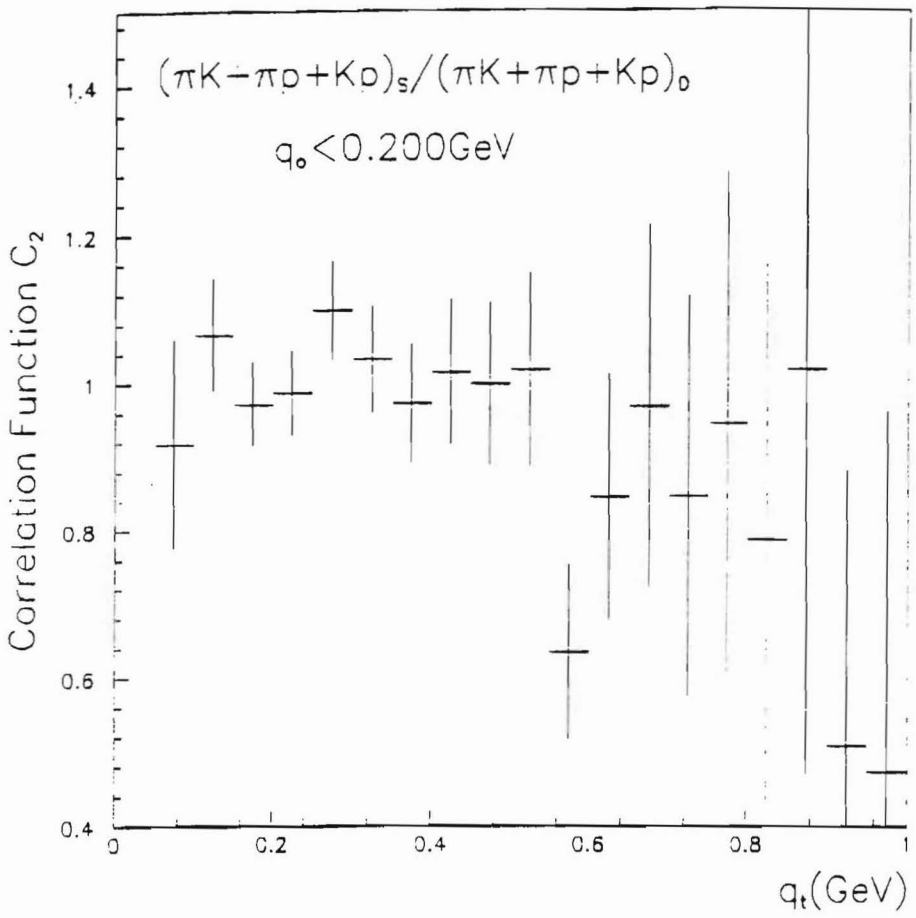

Figure 6.26: Correlation function, $C_2 = (\pi^{\pm}K^{\pm} + p^{\pm}K^{\pm} + \pi^{\pm}p^{\pm})_S/(\pi^{\pm}K^{\pm} + p^{\pm}K^{\pm} + \pi^{\pm}p^{\pm})_D$, as a function of q_t for $q_0 < 0.200$ GeV. This correlation function should be flat because the above pairs can not exhibit Bose-Einstein symmetrization.

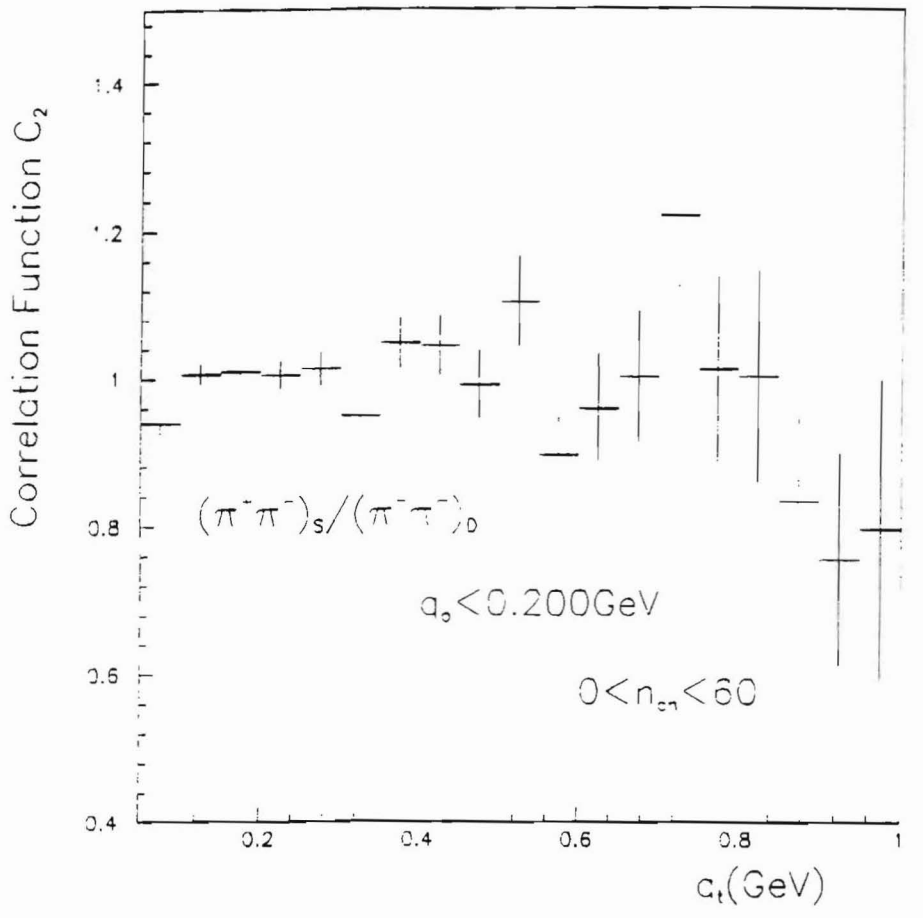

Figure 6.27: Correlation function $C_2 = (\pi^+\pi^-)_S/(\pi^+\pi^-)_D$ as a function of q_t for charged multiplicity $0 < n_{ch} < 60$ and $q_0 < 0.200$ GeV.

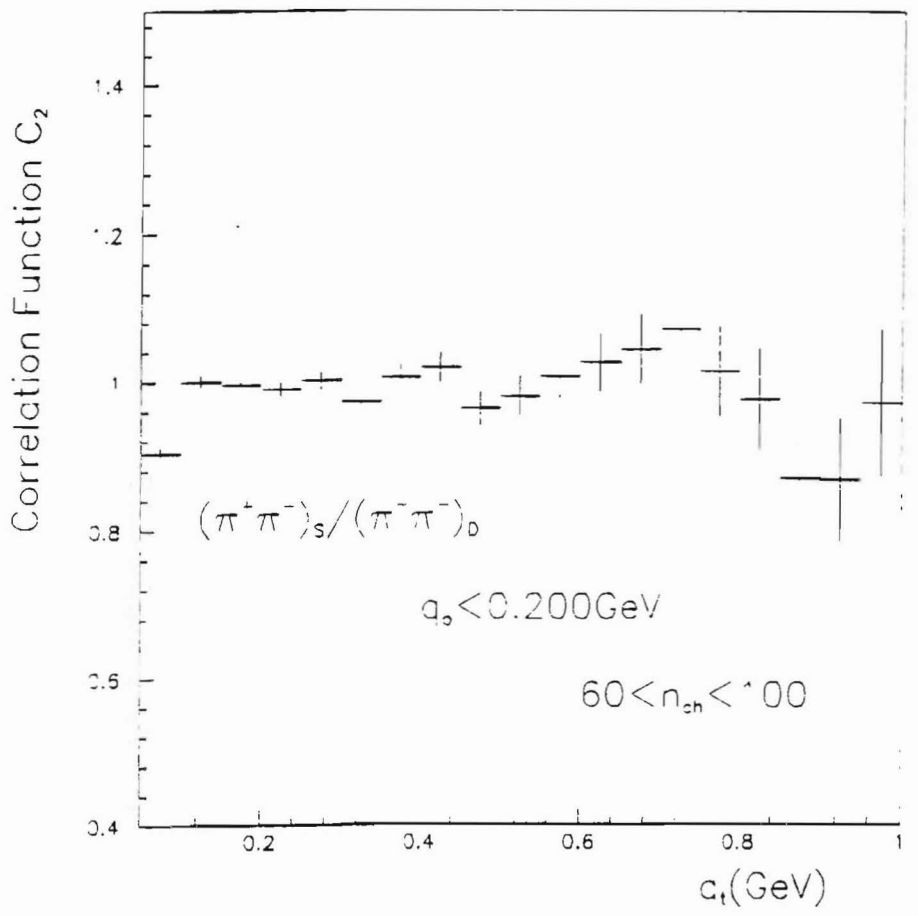

Figure 6.28: Correlation function, $C_2 = (\pi^+\pi^-)_S/(\pi^+\pi^-)_D$, as a function of q_t for charged multiplicity $60 < n_{ch} < 100$ and $q_0 < 0.200$ GeV.

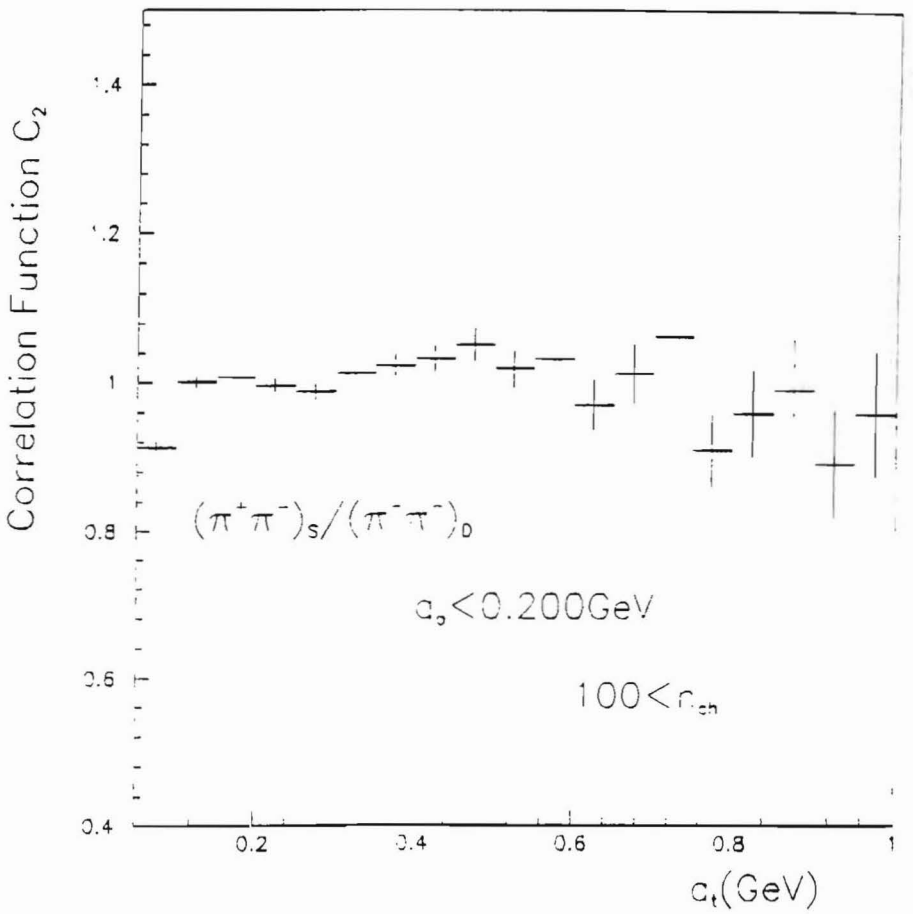

Figure 6.29: Correlation function, $C_2 = (\pi^+\pi^-)_S/(\pi^+\pi^-)_D$, as a function of q_t for charged multiplicity $100 < n_{ch}$ and $q_0 < 0.200$ GeV.

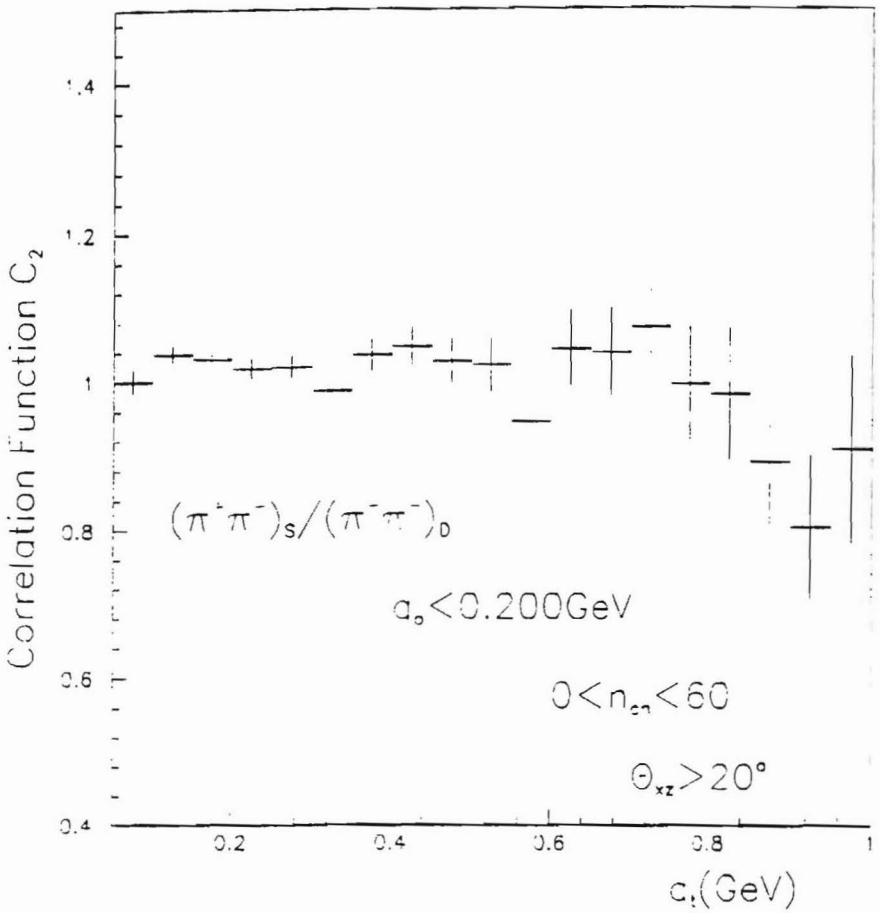

Figure 6.30: Correlation function, $C_2 = (\pi^+\pi^-)_S/(\pi^+\pi^-)_D$, as a function of q_t for charged multiplicity $0 < n_{ch} < 60$, $\theta_{xz} > 20^0$ and $q_0 < 0.200$ GeV.

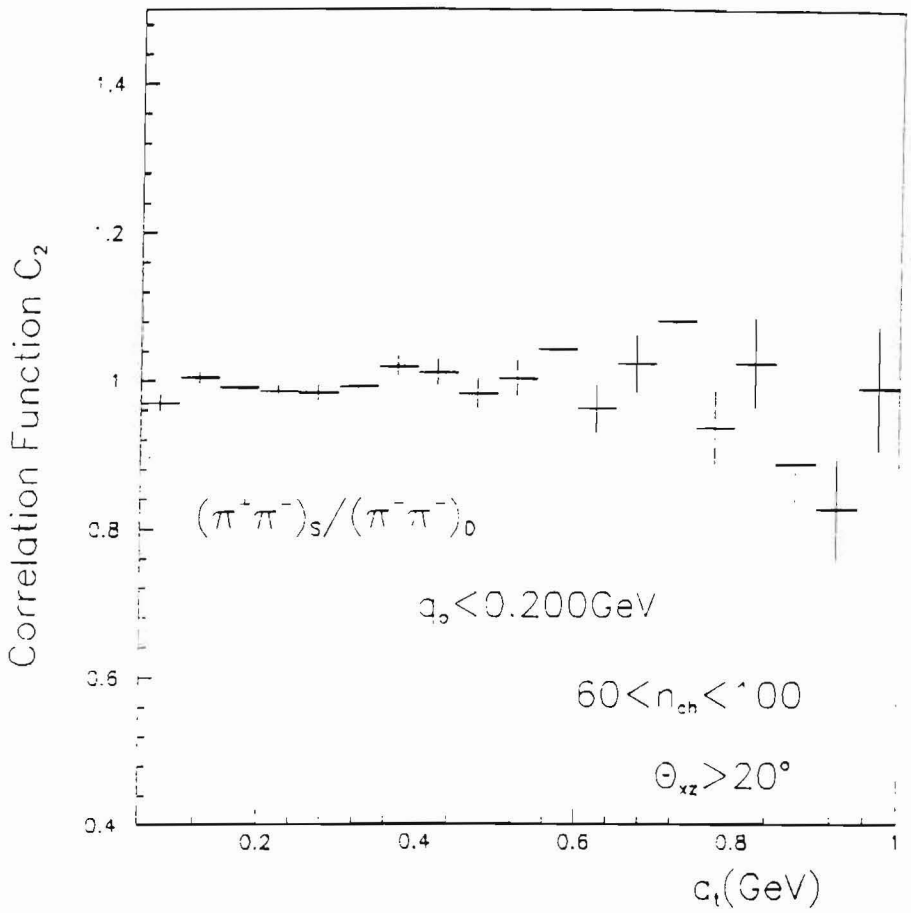

Figure 6.31: Correlation function, $C_2 = (\pi^+\pi^-)_S/(\pi^+\pi^-)_D$, as a function of q_t for charged multiplicity $60 < n_{ch} < 100$, $\theta_{xz} > 20^0$ and $q_0 < 0.200$ GeV.

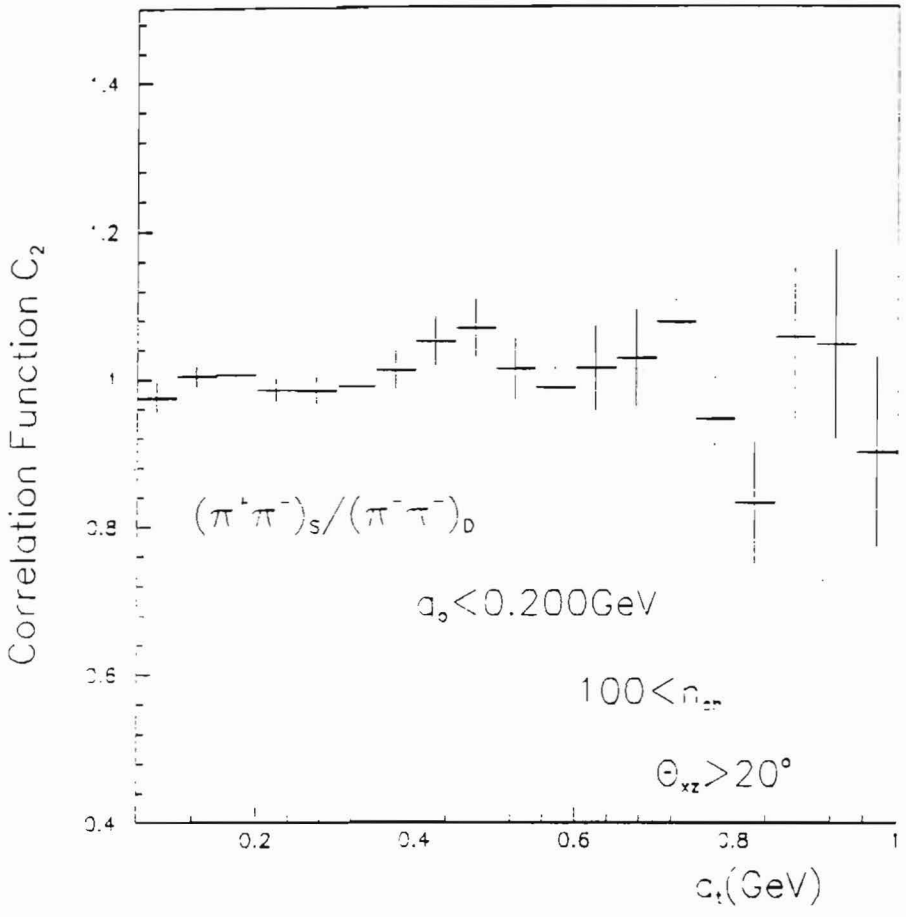

Figure 6.32: Correlation function, $C_2 = (\pi^+\pi^-)_S/(\pi^+\pi^-)_D$, as a function of q_t for charged multiplicity $100 < n_{ch}$, $\theta_{xz} > 20^0$ and $q_0 < 0.200$ GeV.

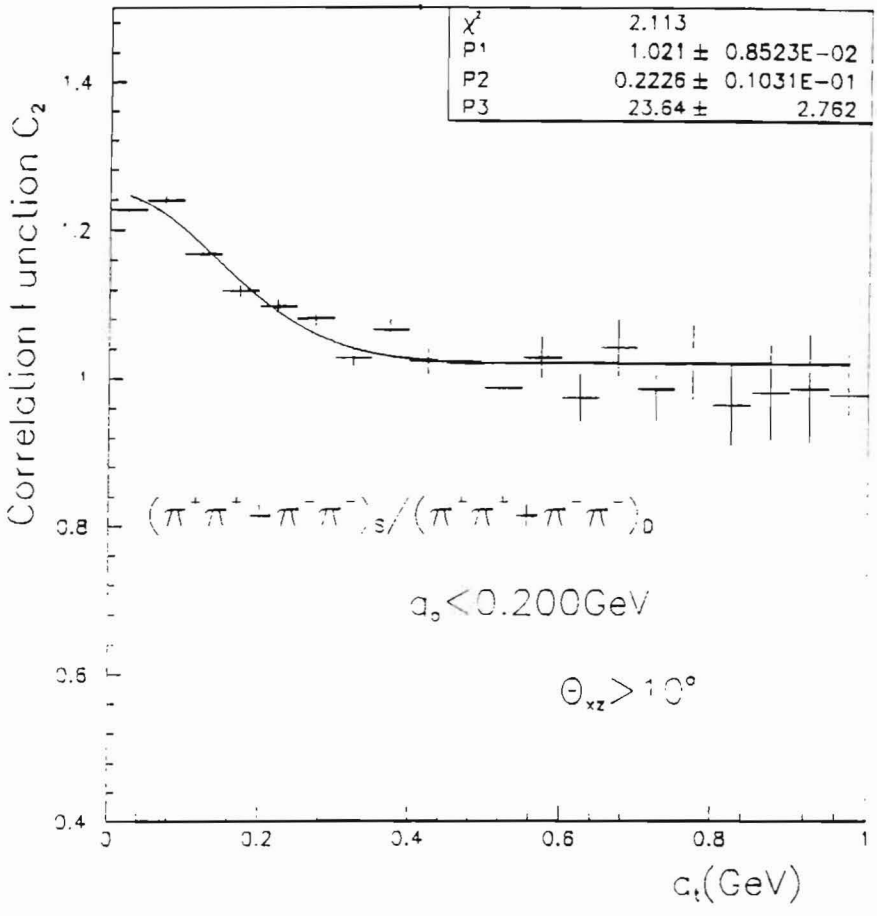

Figure 6.33: Correlation function, $C_2 = (\pi^+\pi^+ + \pi^-\pi^-)_S/(\pi^+\pi^+ + \pi^-\pi^-)_D$, as a function of q_t for $\theta_{xz} > 10^0$ and $q_0 < 0.200$ GeV.

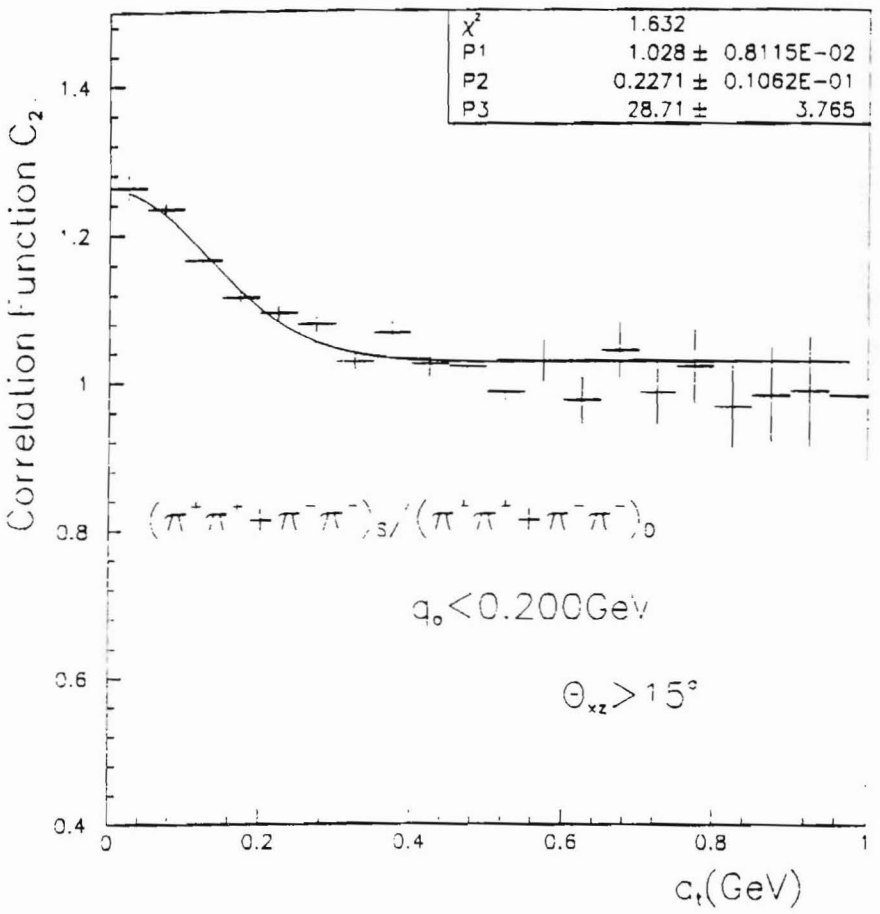

Figure 6.34: Correlation function, $C_2 = (\pi^+\pi^+ + \pi^-\pi^-)_S/(\pi^+\pi^+ + \pi^-\pi^-)_D$, as a function of q_t for $\theta_{xz} > 15^0$ and $q_0 < 0.200$ GeV.

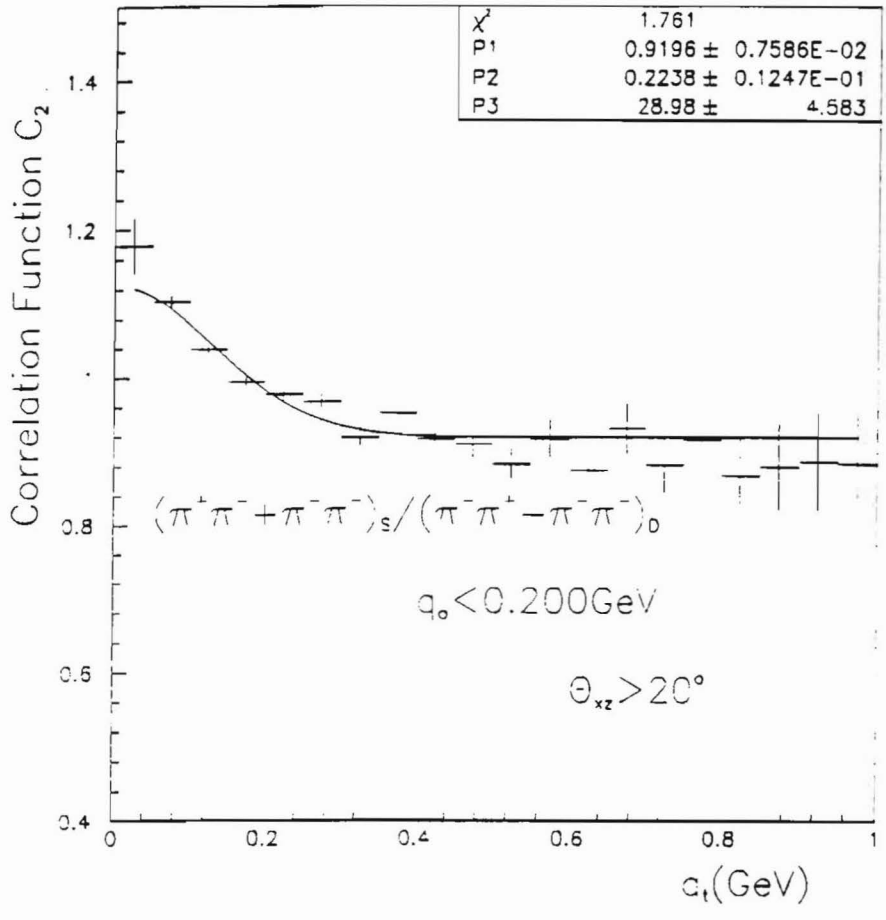

Figure 6.35: Correlation function, $C_2 = (\pi^+\pi^+ + \pi^-\pi^-)_S/(\pi^+\pi^+ + \pi^-\pi^-)_D$, as a function of q_t for $\theta_{xz} > 20^0$ and $q_0 < 0.200$ GeV.

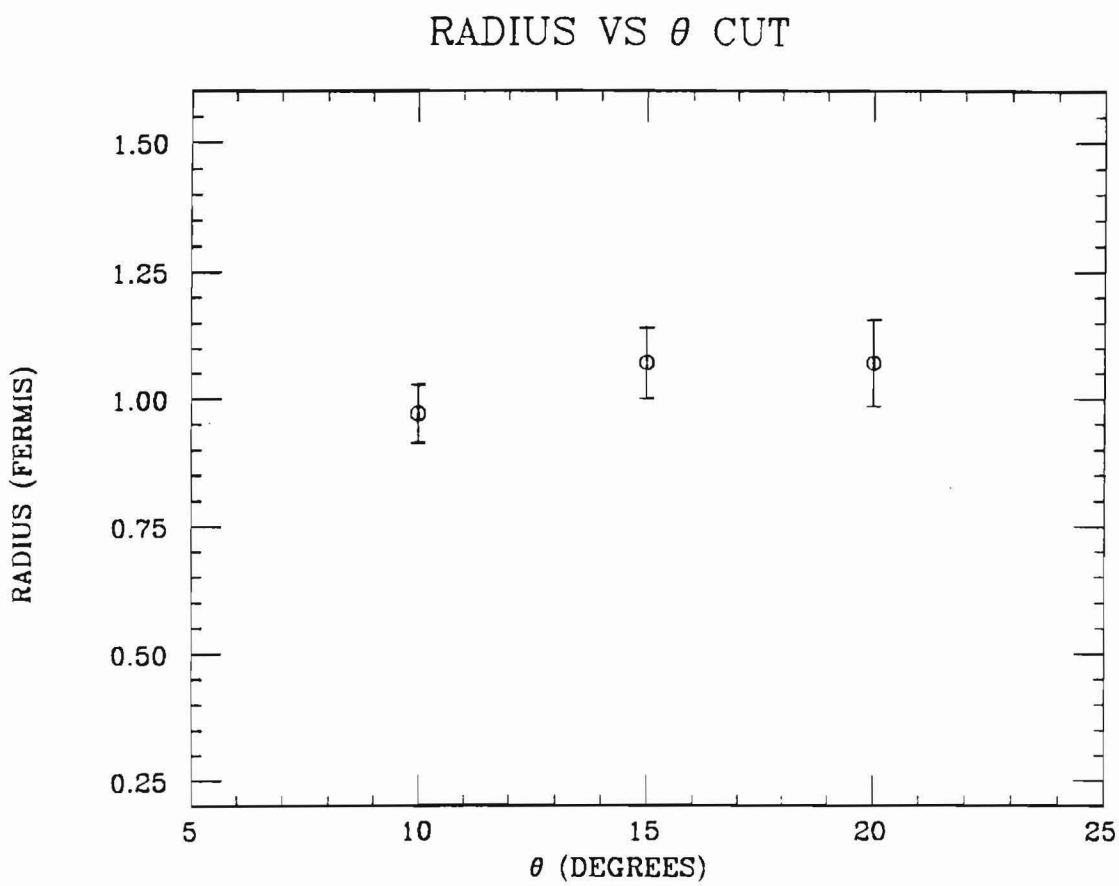

Figure 6.36: Radius of the source as a function of opening angle θ_{xz} cut.

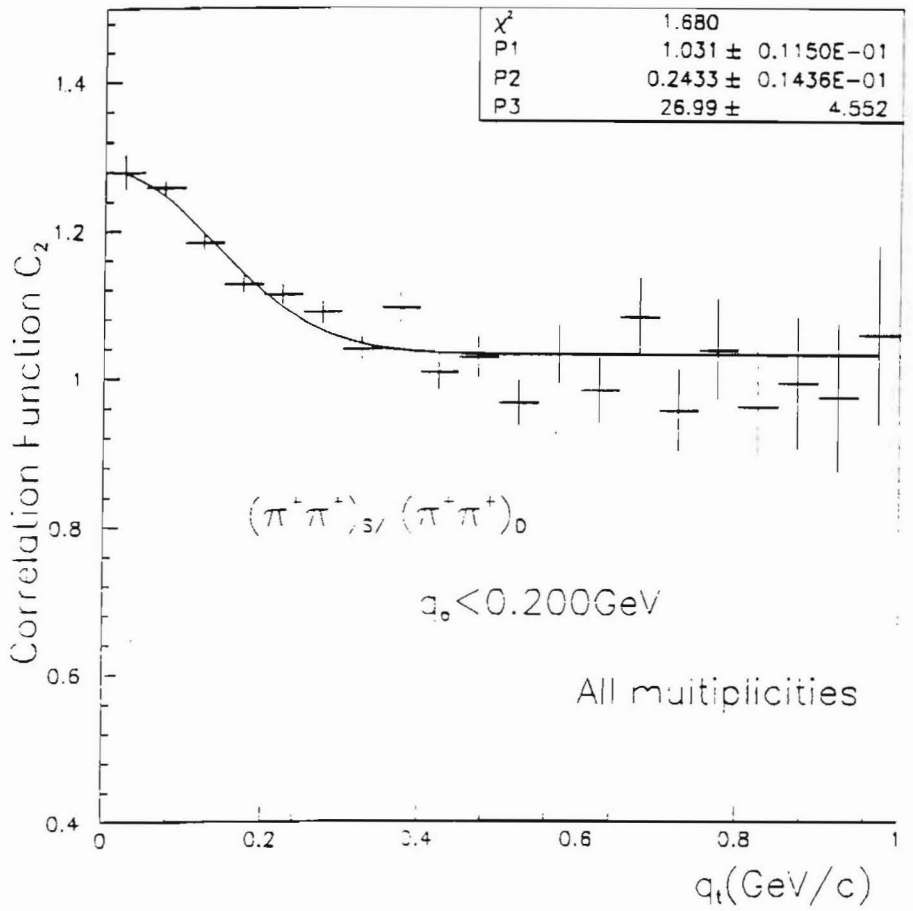

Figure 6.37: Correlation function, $C_2 = (\pi^+\pi^+)_S/(\pi^+\pi^+)_D$, as a function of q_t, $q_0 < 0.200$ GeV, and for all multiplicities. The fitted curve is of the form $C_2 = P_1(1 + P_2 \exp(-P_3 q_t^2))$.

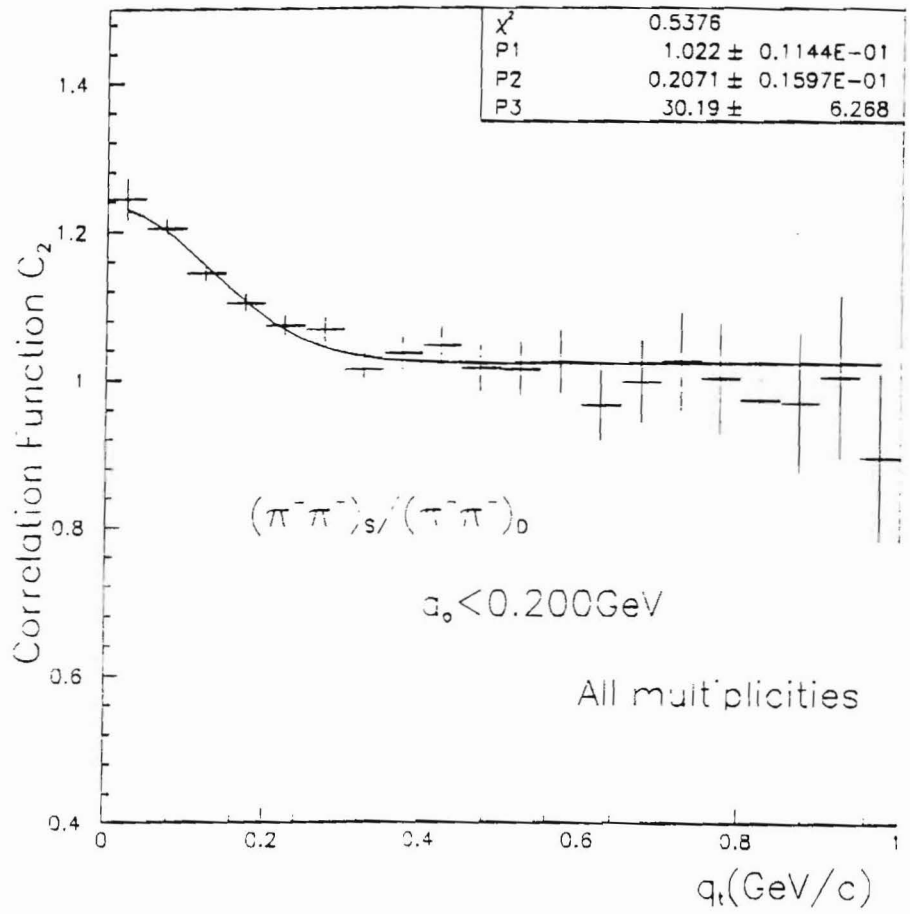

Figure 6.38: Correlation function, $C_2 = (\pi^-\pi^-)_S/(\pi^-\pi^-)_D$, as a function of q_t, $q_0 < 0.200$ GeV, and for all multiplicities. The fitted curve is of the form $C_2 = P_1(1 + P_2 \exp(-P_3 q_t^2))$.

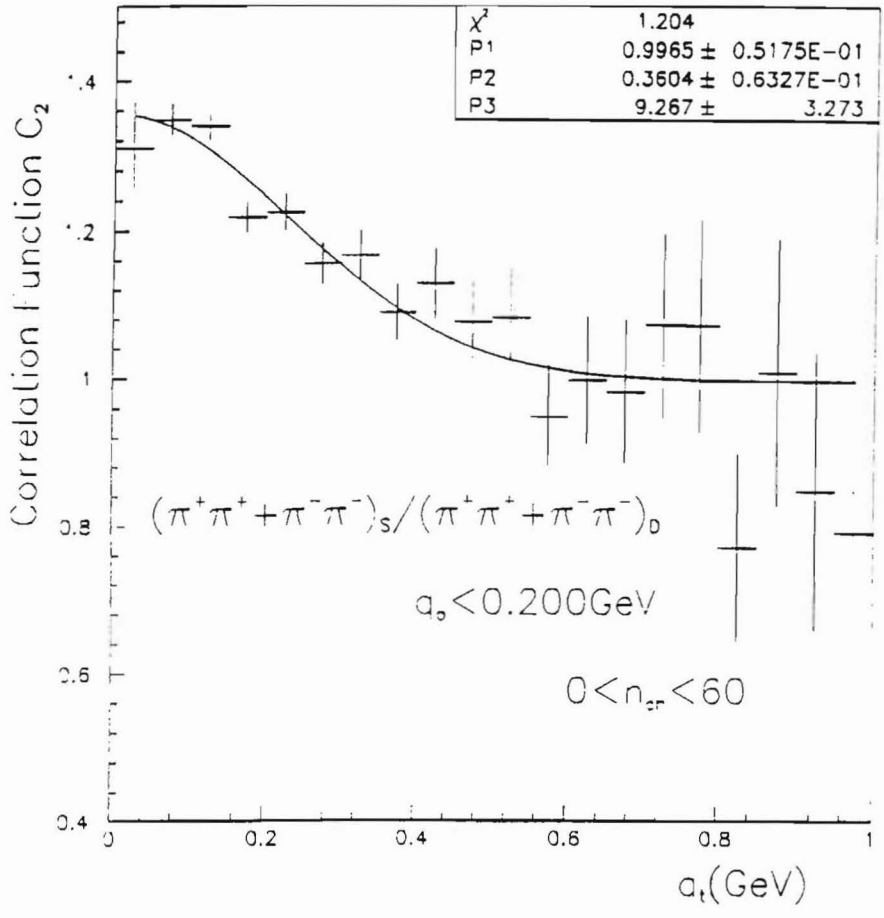

Figure 6.39: Correlation function, $C_2 = (\pi^+\pi^+ + \pi^-\pi^-)_S/(\pi^+\pi^+ + \pi^-\pi^-)_D$, as a function of q_t for $0 < n_{ch} < 60$ and $q_0 < 0.200$ GeV. The fitted curve is of the form $C_2 = P_1(1 + P_2 \exp(-P_3 q_t^2))$.

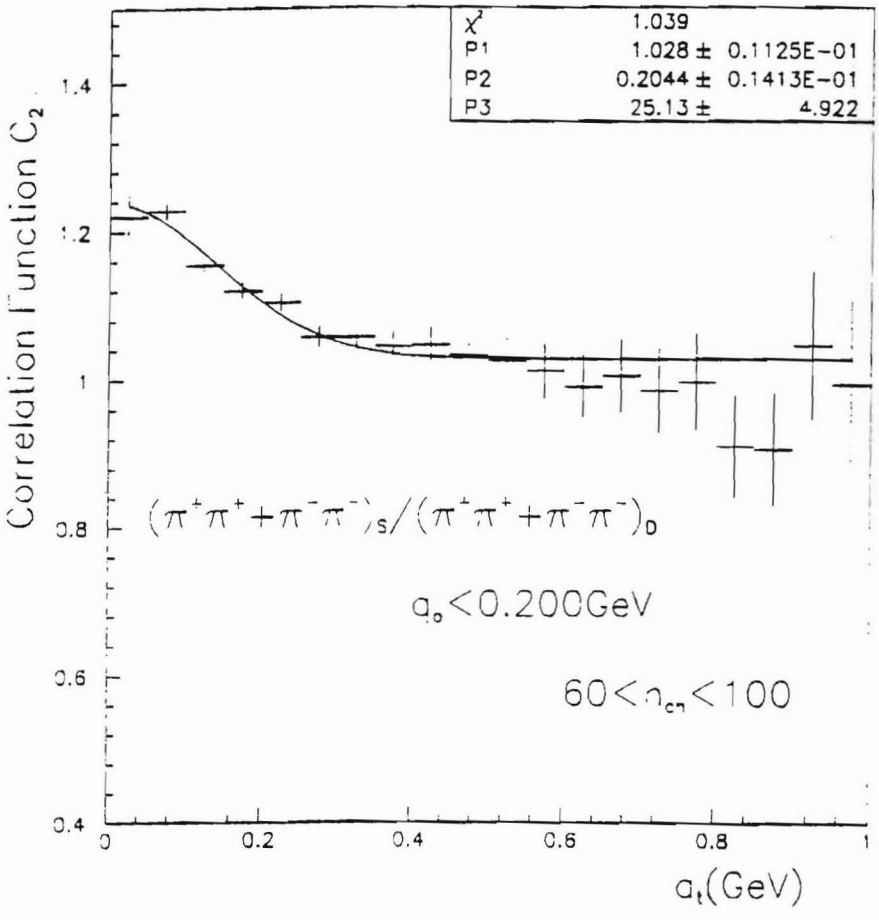

Figure 6.40: Correlation function, $C_2 = (\pi^+\pi^+ + \pi^-\pi^-)_S/(\pi^+\pi^+ + \pi^-\pi^-)_D$, as a function of q_t for $60 < n_{ch} < 100$ and $q_0 < 0.200$ GeV. The fitted curve is of the form $C_2 = P_1(1 + P_2 \exp(-P_3 q_t^2))$.

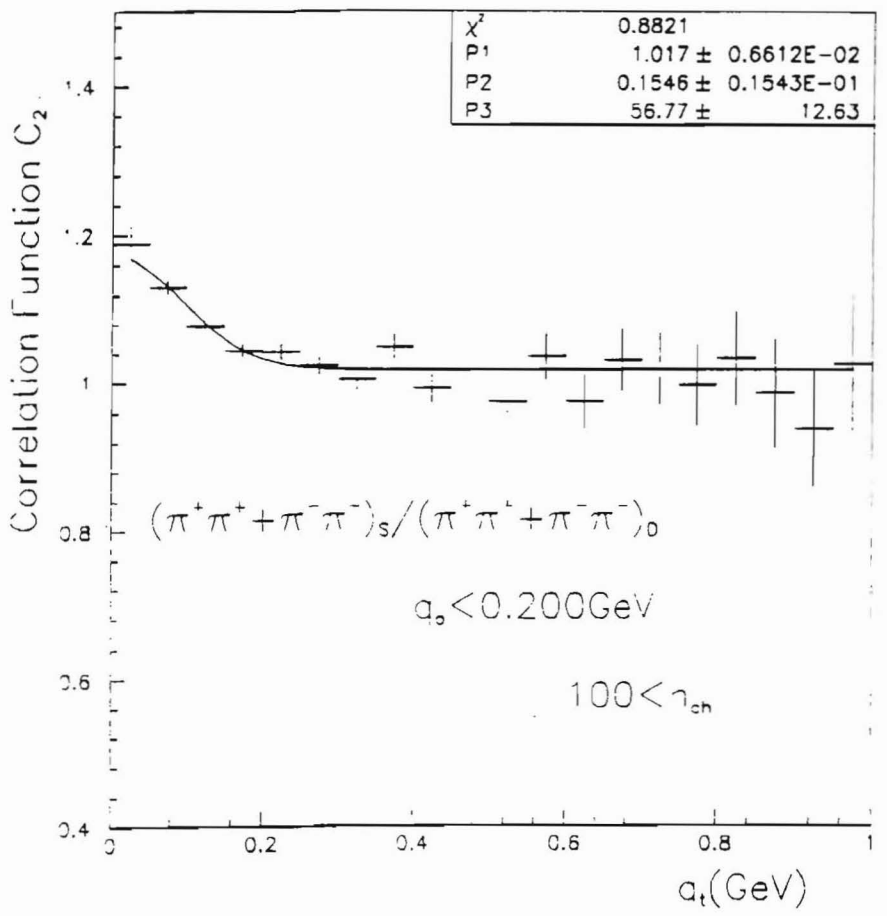

Figure 6.41: Correlation function, $C_2 = (\pi^+\pi^+ + \pi^-\pi^-)_S/(\pi^+\pi^+ + \pi^-\pi^-)_D$, as a function of q_t for $100 < n_{ch}$ and $q_0 < 0.200$ GeV. The fitted curve is of the form $C_2 = P_1(1 + P_2 \exp(-P_3 q_t^2))$.

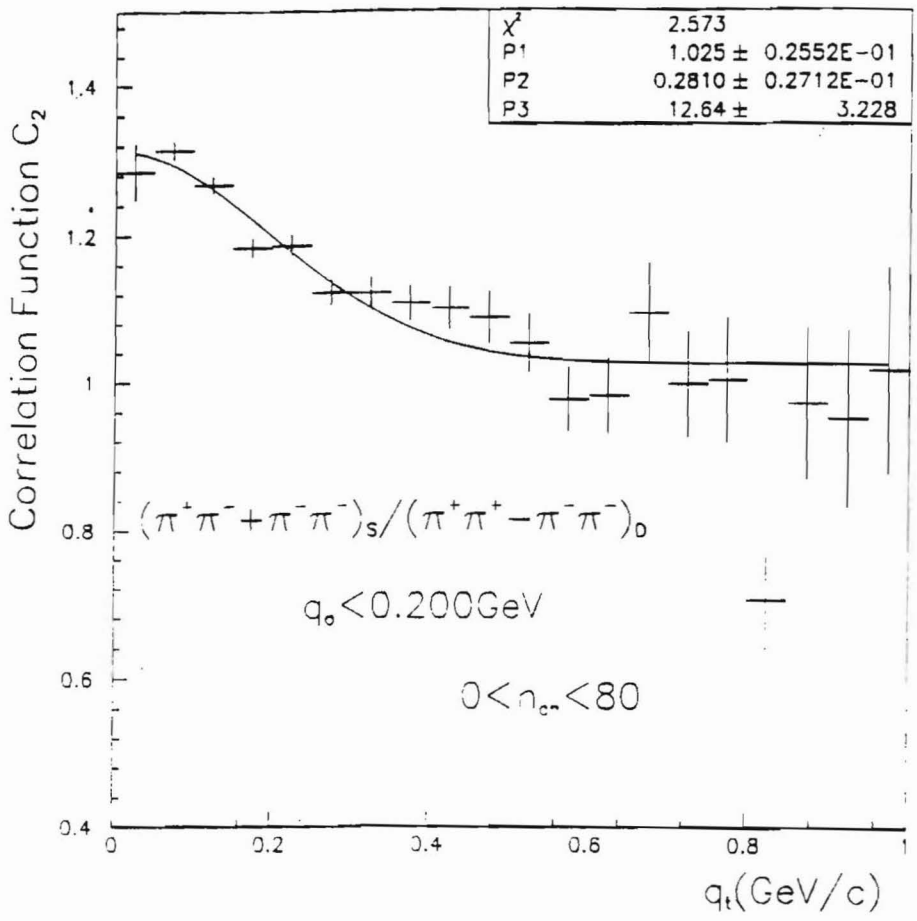

Figure 6.42: Correlation function, $C_2 = (\pi^+\pi^+ + \pi^-\pi^-)_S/(\pi^+\pi^+ + \pi^-\pi^-)_D$, as a function of q_t for $0 < n_{ch} < 80$ and $q_0 < 0.200$ GeV. The fitted curve is of the form $C_2 = P_1(1 + P_2 \exp(-P_3 q_t^2))$.

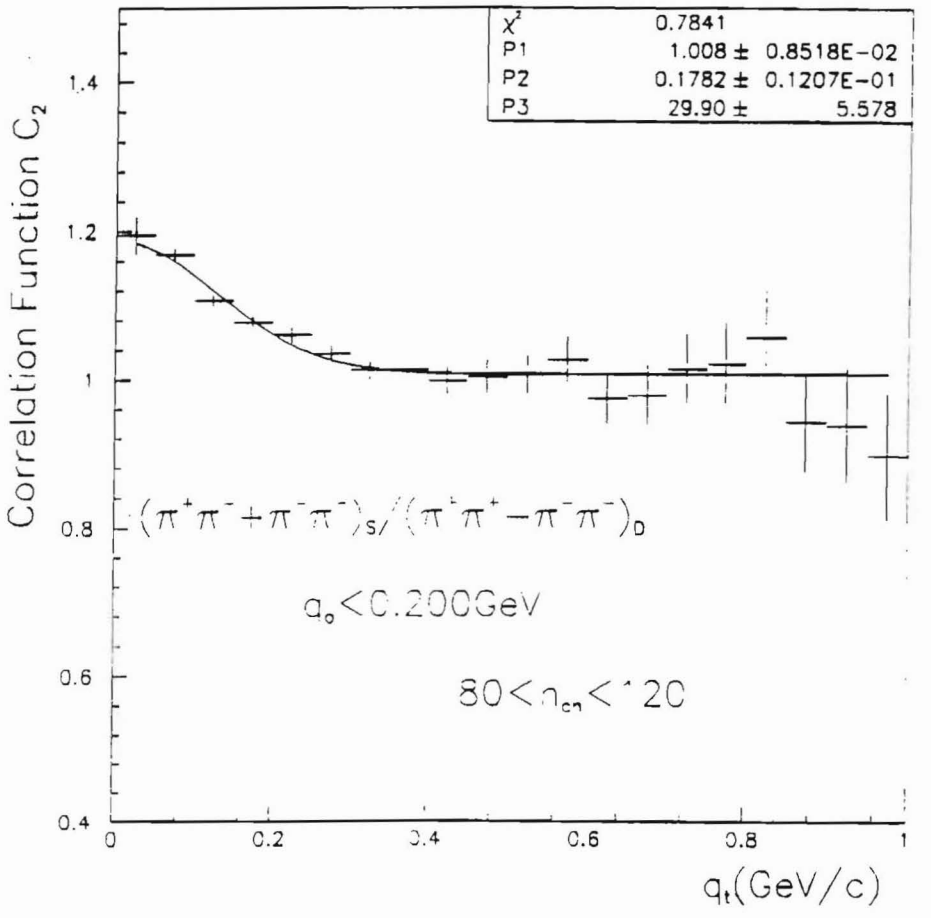

Figure 6.43: Correlation function, $C_2 = (\pi^+\pi^+ + \pi^-\pi^-)_S/(\pi^+\pi^+ + \pi^-\pi^-)_D$, as a function of q_t for $80 < n_{ch} < 120$ and $q_0 < 0.200$ GeV. The fitted curve is of the form $C_2 = P_1(1 + P_2 \exp(-P_3 q_t^2))$.

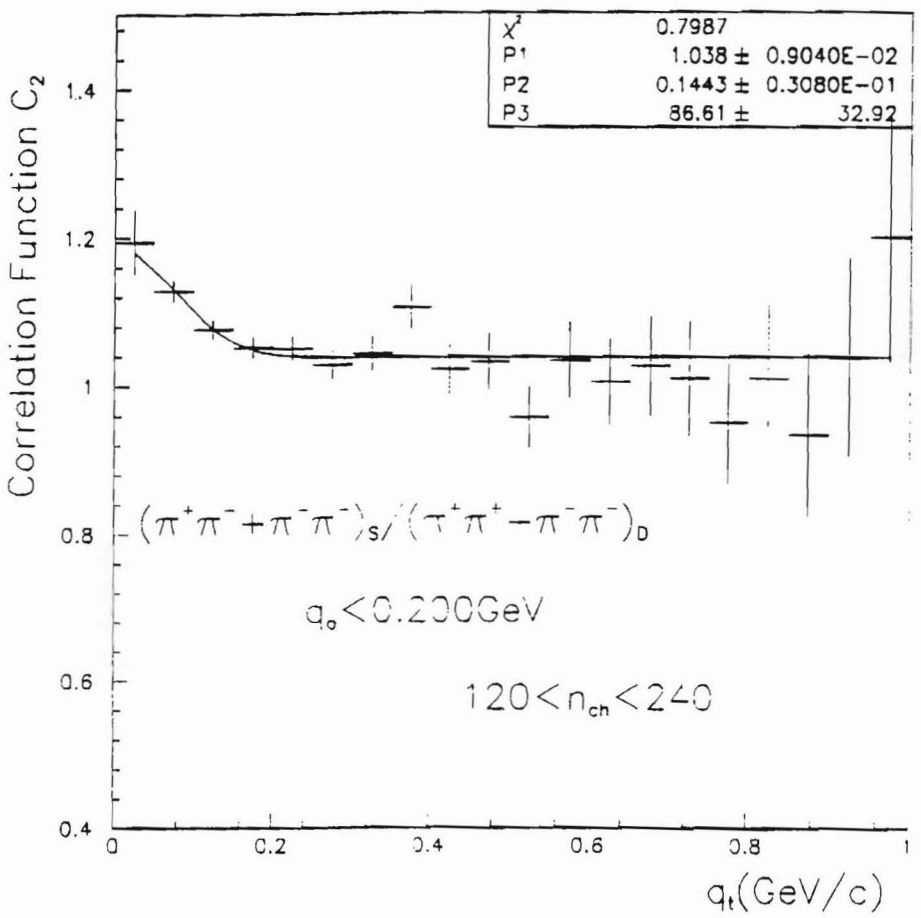

Figure 6.44: Correlation function, $C_2 = (\pi^+\pi^+ + \pi^-\pi^-)_S/(\pi^+\pi^+ + \pi^-\pi^-)_D$, as a function of q_t for $120 < n_{ch}$ and $q_0 < 0.200$ GeV. The fitted curve is of the form $C_2 = P_1(1 + P_2 \exp(-P_3 q_t^2))$.

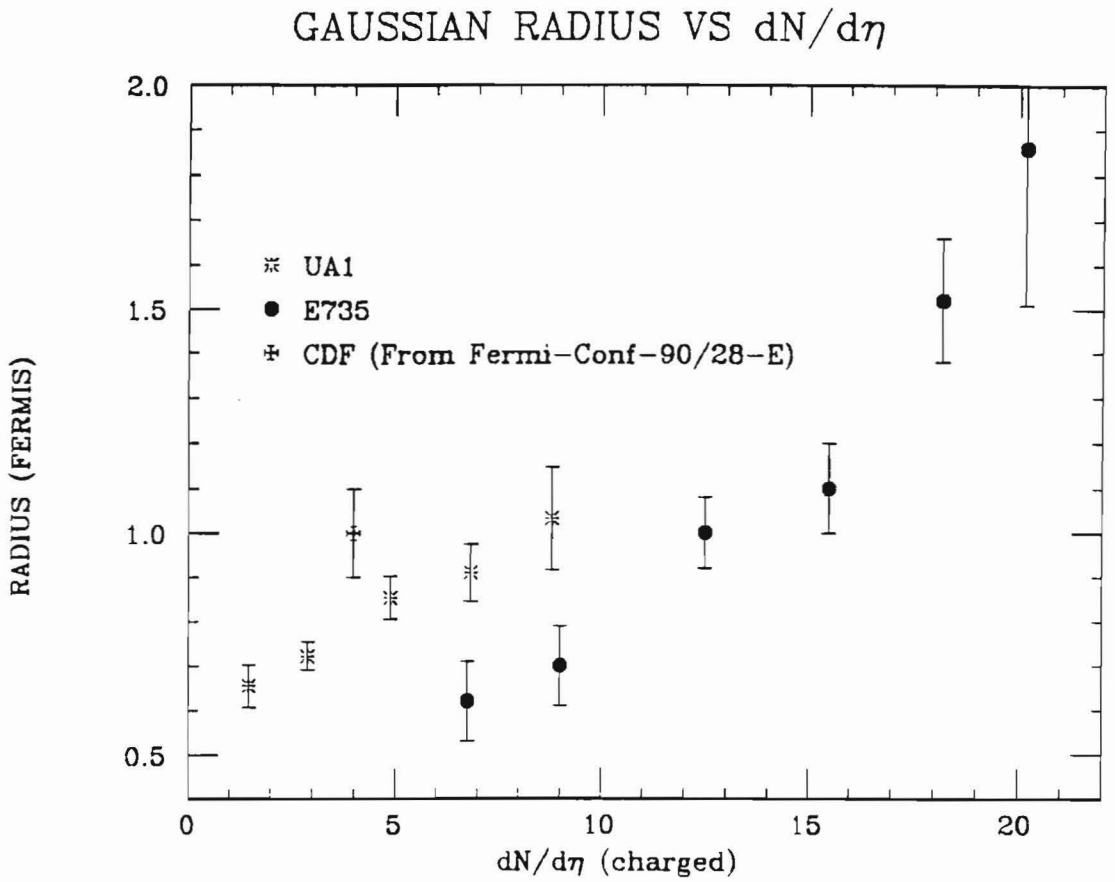

Figure 6.45: Radius of the source as a function of multiplicity in the Gaussian representation compared with the UA1 data points.

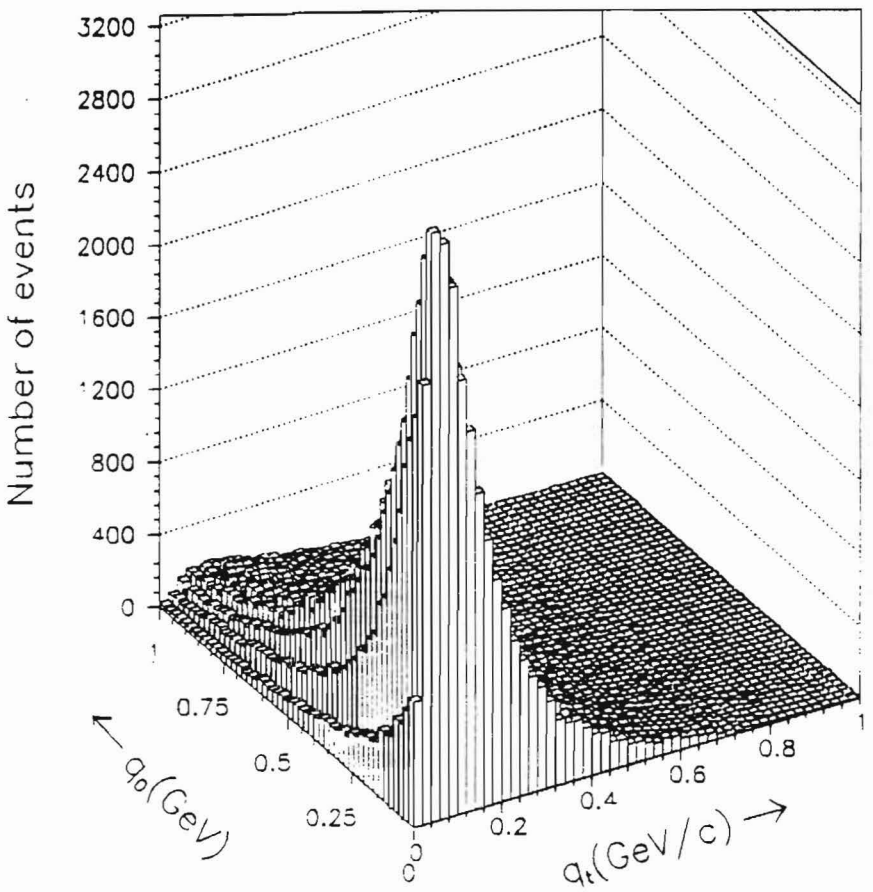

Figure 6.46: Momentum distribution. dn/dq_μ, as a function of $(|\vec{q_0}|, q_t)$ over the spectrometer acceptance used in this experiment.

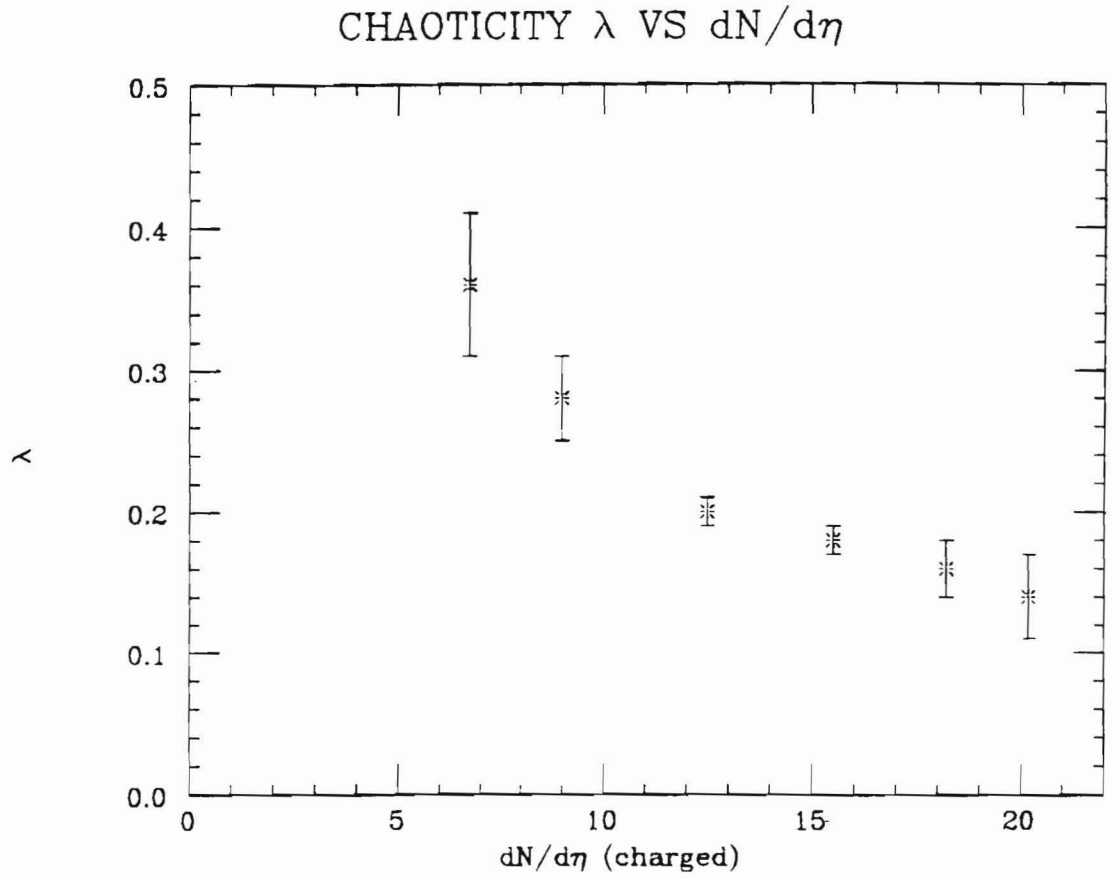

Figure 6.47: Chaoticity parameter, λ, versus mean charged multiplicity $< n_{ch} >$.

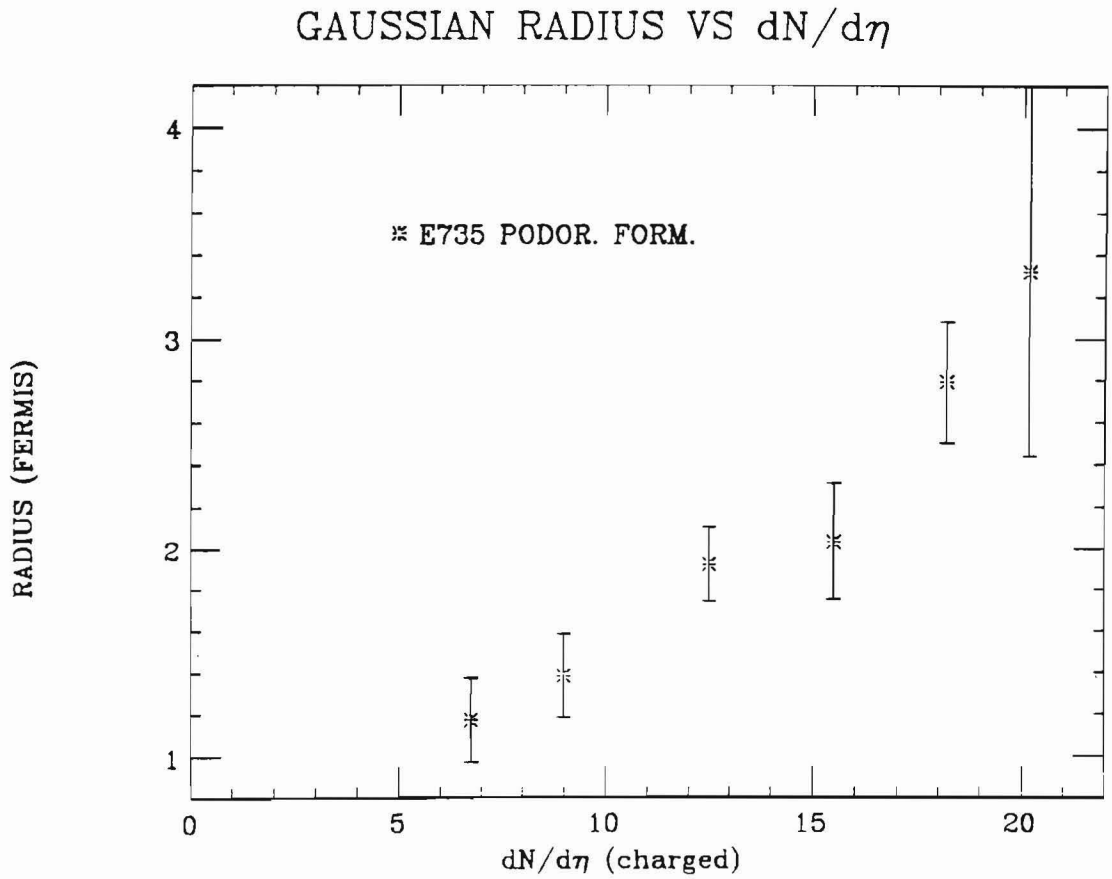

Figure 6.48: Radius of the source as a function of multiplicity in the Podgoretsky representation.

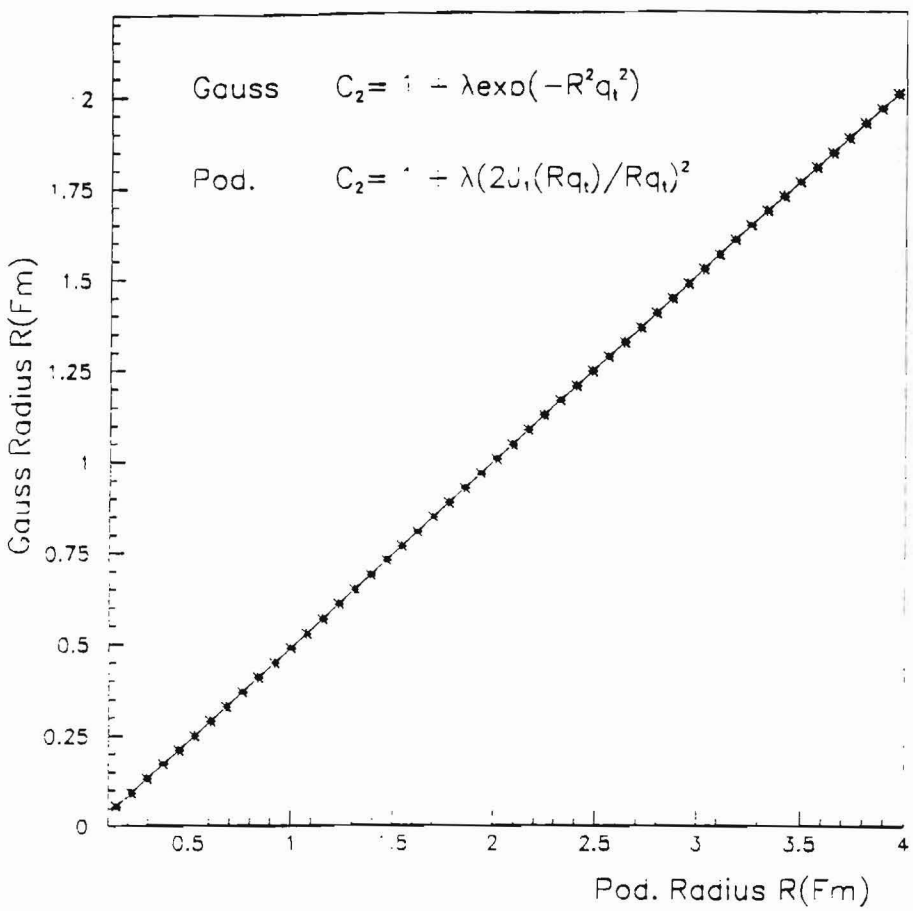

Figure 6.49: Radius of the source (R_g) extrapolated from a Gaussian parameterization of the correlation function ($C_2 = 1 + \lambda \exp(-R^2 q_t^2)$) vs radius of the source (R_p) extrapolated from a Podgoretsky parameterization of the correlation function ($C_2 = 1 + \lambda(2J_1(Rq_t)/Rq_t)^2$).

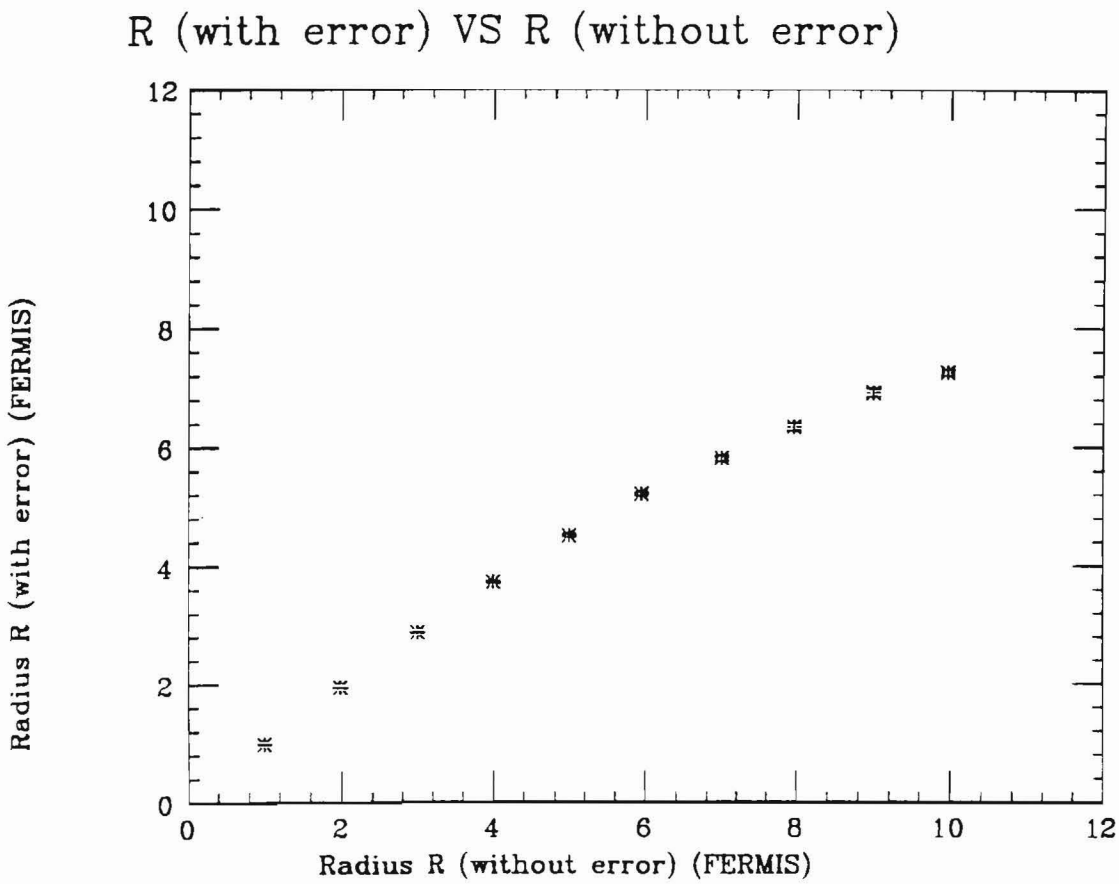

Figure 6.50: Radius of the source as a function of multiplicity in the Weiner representation.

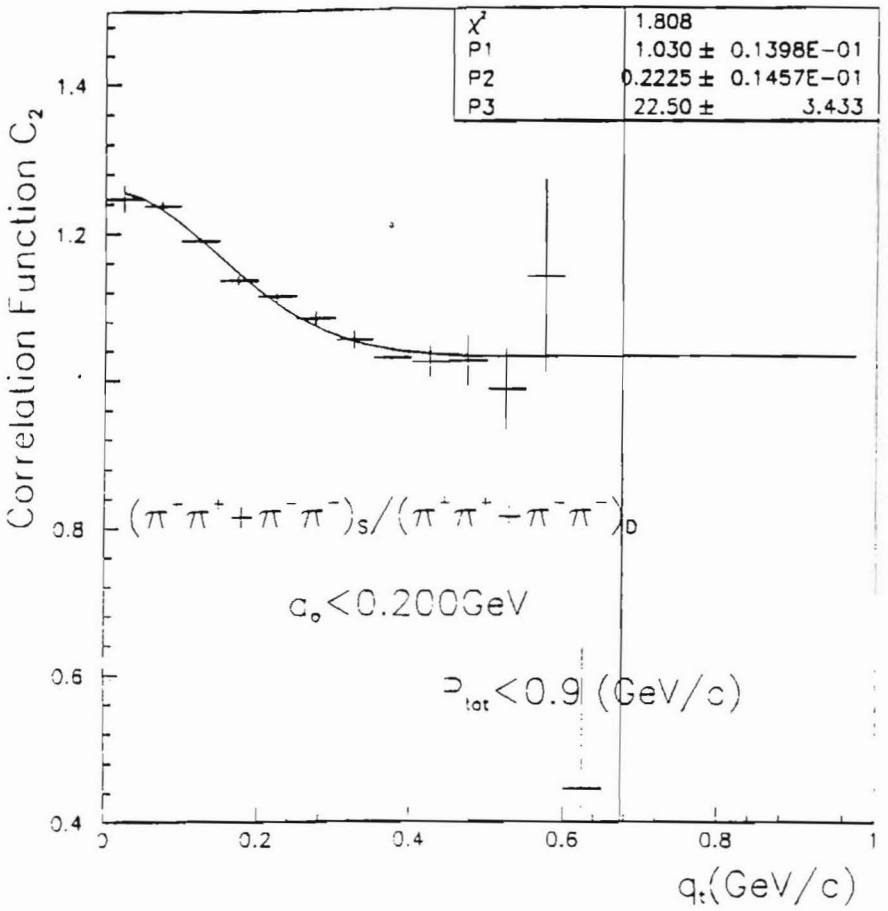

Figure 6.51: Correlation function, $C_2 = (\pi^+\pi^+ + \pi^-\pi^-)_S/(\pi^+\pi^+ + \pi^-\pi^-)_D$, as a function of q_t for $q_0 < 0.200$ GeV and total momentum of the pair $P_{tot} < 0.9$ GeV/c. The fitted curve is of the form $C_2 = P_1(1 + P_2 \exp(-P_3 q_t^2))$.

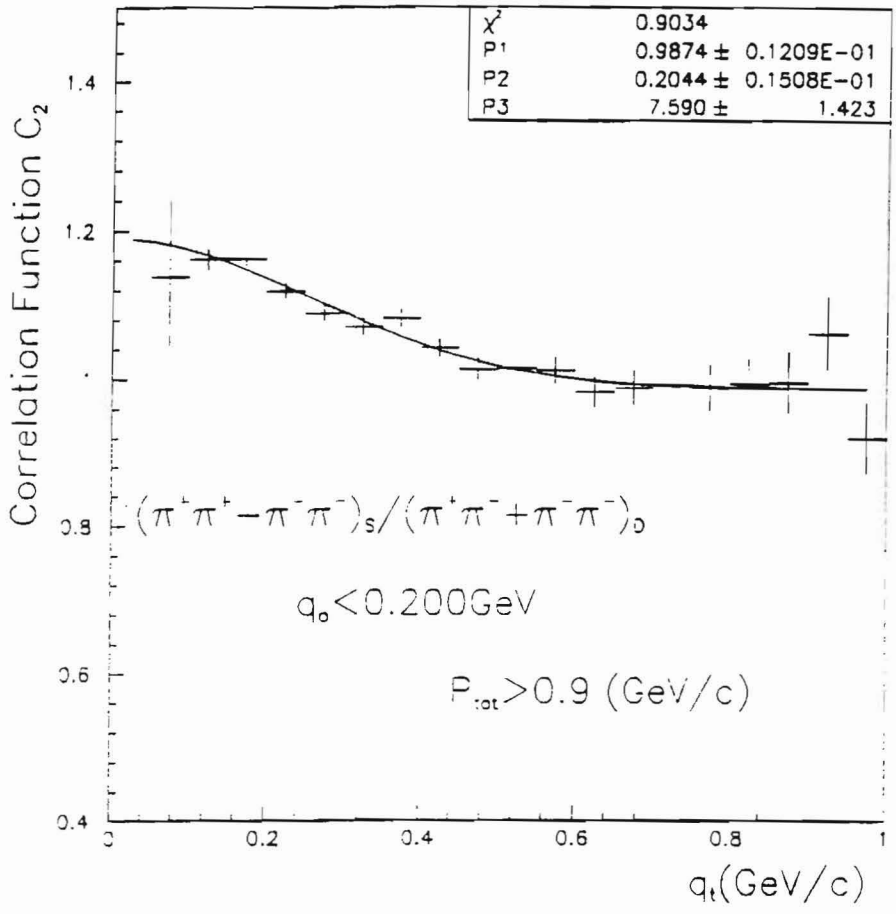

Figure 6.52: Correlation function, $C_2 = (\pi^+\pi^+ + \pi^-\pi^-)_S/(\pi^+\pi^+ + \pi^-\pi^-)_D$, as a function of q_t for $q_0 < 0.200$ GeV and total momentum of the pair $P_{tot} > 0.9$ GeV/c. The fitted curve is of the form $C_2 = P_1(1 + P_2 \exp(-P_3 q_t^2))$.

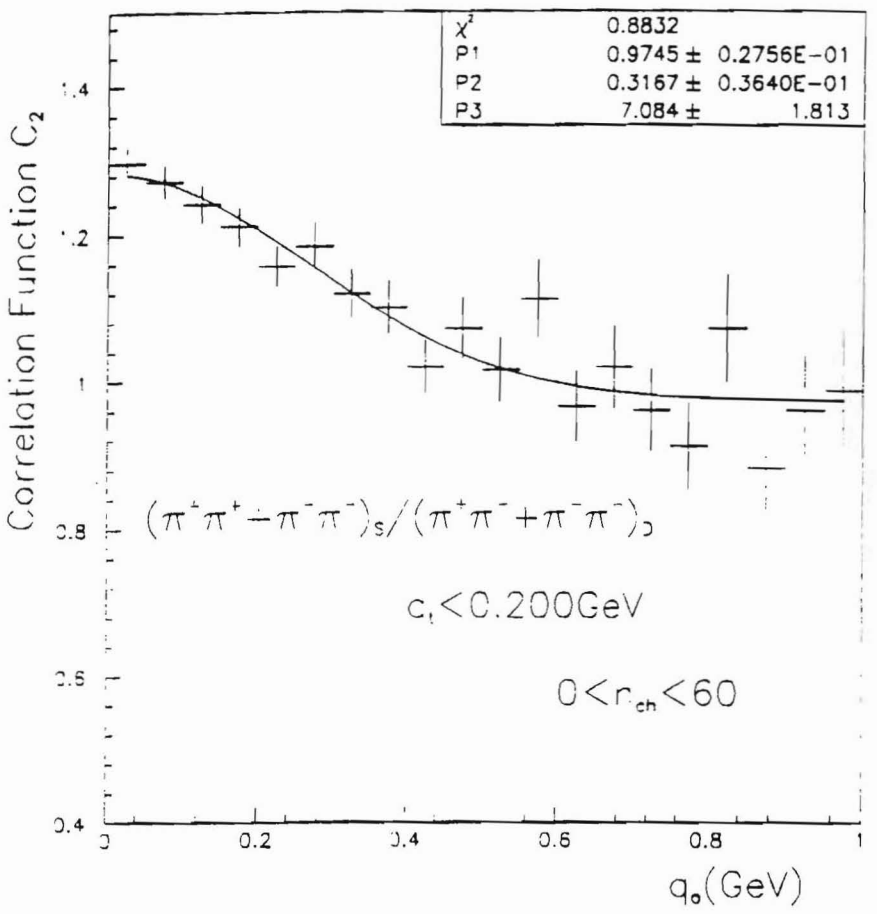

Figure 6.53: Correlation function, $C_2 = (\pi^+\pi^+ + \pi^-\pi^-)_S/(\pi^+\pi^+ + \pi^-\pi^-)_D$, as a function of q_0 for $0 < n_{ch} < 60$ and $q_t < 0.200$ GeV/c. The fitted curve is of the form $C_2 = P_1(1 + P_2 \exp(-P_3 q_0^2))$.

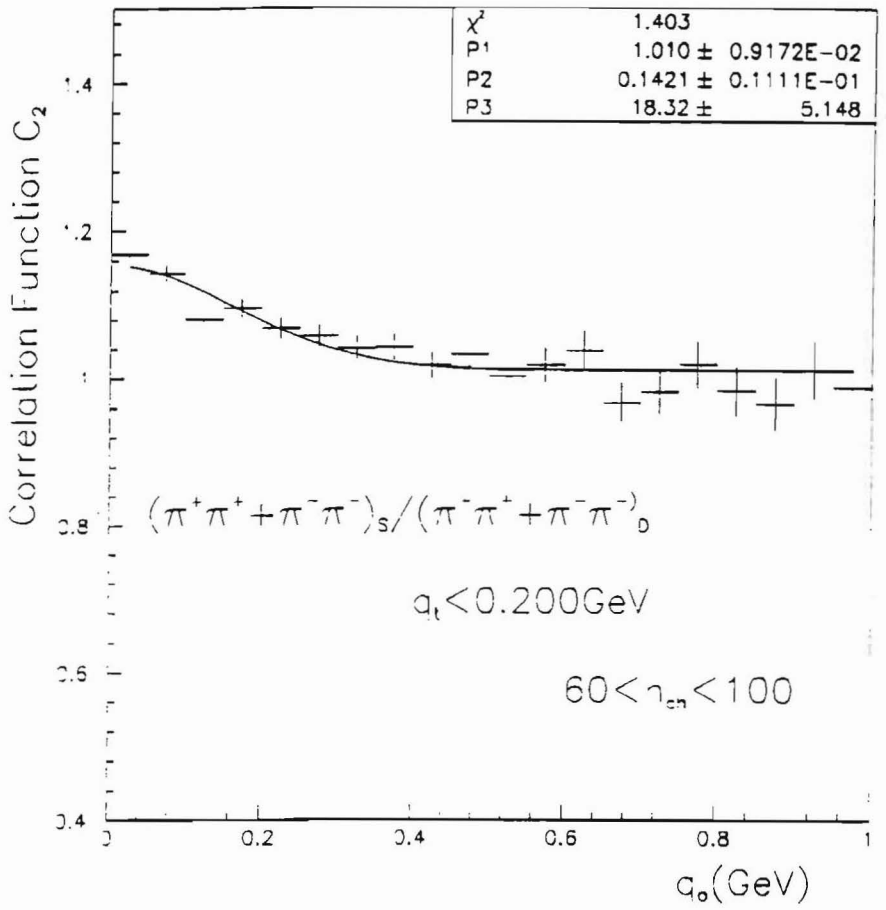

Figure 6.54: Correlation function, $C_2 = (\pi^+\pi^+ + \pi^-\pi^-)_S/(\pi^+\pi^+ + \pi^-\pi^-)_D$, as a function of q_0 for $60 < n_{ch} < 100$ and $q_t < 0.200$ GeV/c. The fitted curve is of the form $C_2 = P_1(1 + P_2 \exp(-P_3 q_0^2))$.

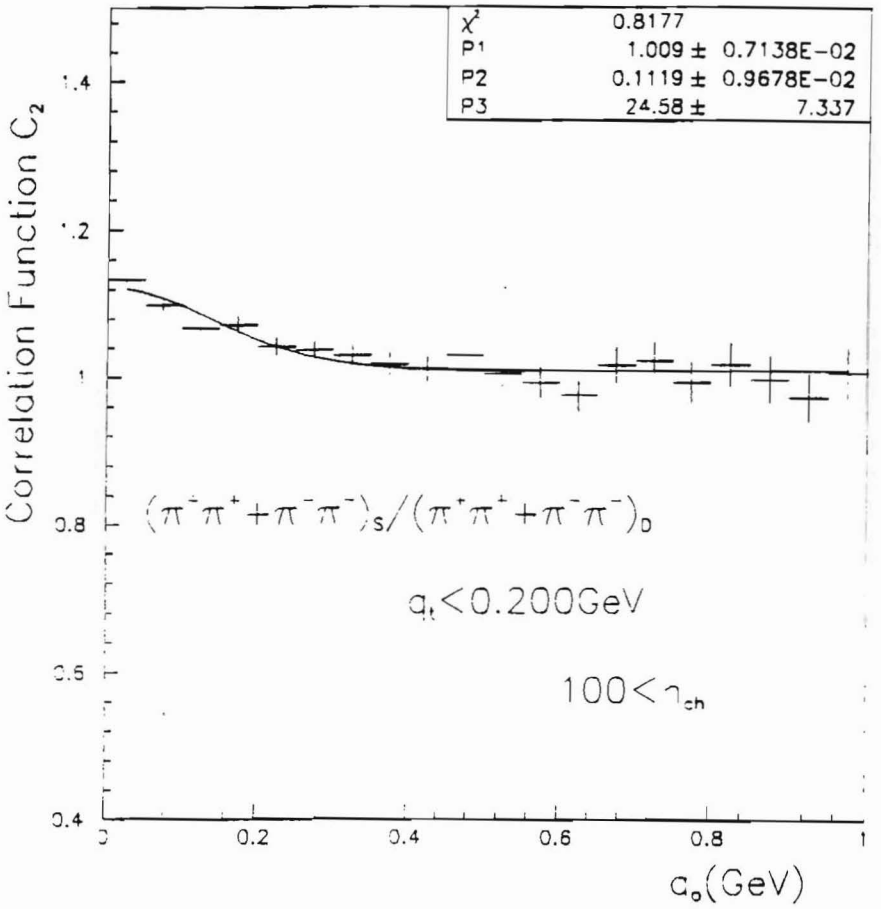

Figure 6.55: Correlation function, $C_2 = (\pi^+\pi^+ + \pi^-\pi^-)_S/(\pi^+\pi^+ + \pi^-\pi^-)_D$, as a function of q_0 for $100 < n_{ch}$ and $q_t < 0.200$ GeV/c. The fitted curve is of the form $C_2 = P_1(1 + P_2 \exp(-P_3 q_0^2))$.

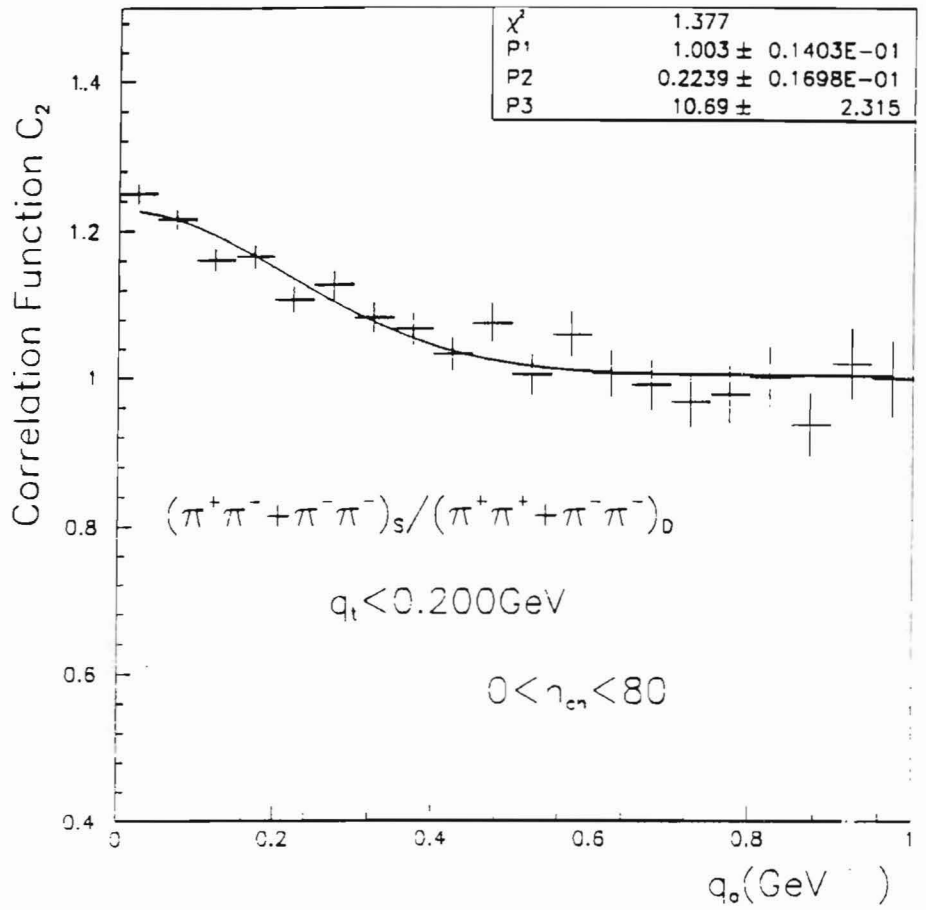

Figure 6.56: Correlation function, $C_2 = (\pi^+\pi^+ + \pi^-\pi^-)_S/(\pi^+\pi^+ + \pi^-\pi^-)_D$, as a function of q_0 for $0 < n_{ch} < 80$ and $q_t < 0.200$ GeV/c. The fitted curve is of the form $C_2 = P_1(1 + P_2 \exp(-P_3 q_0^2))$.

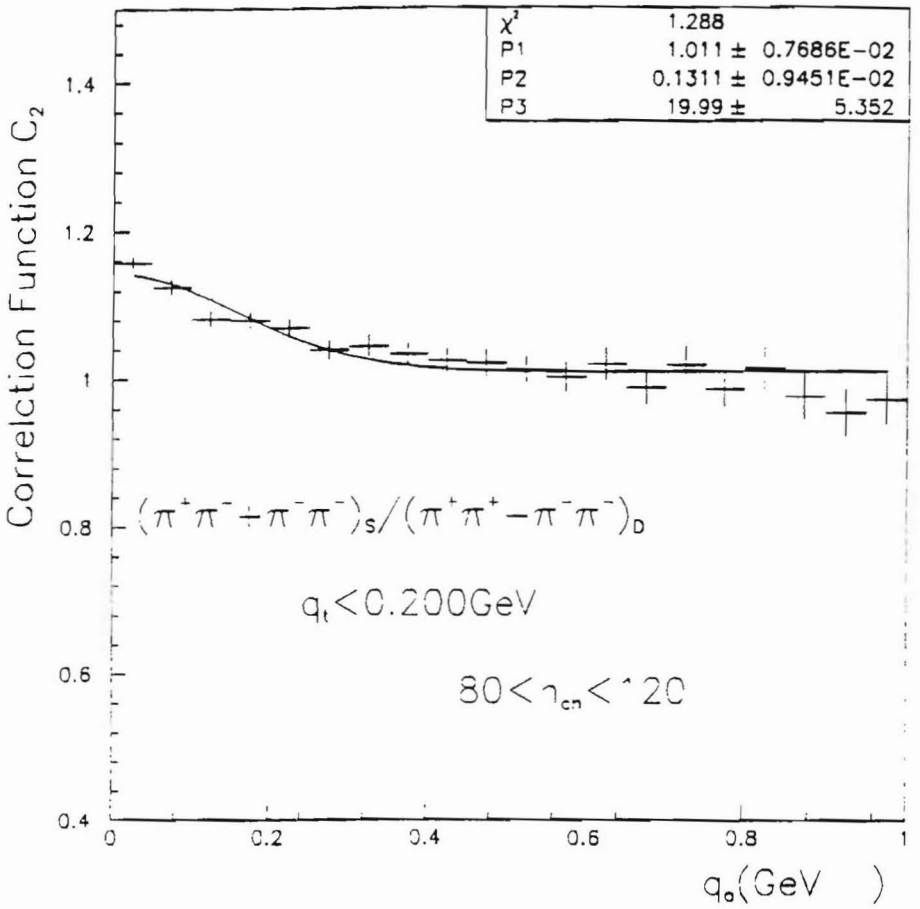

Figure 6.57: Correlation function, $C_2 = (\pi^+\pi^+ + \pi^-\pi^-)_S/(\pi^+\pi^+ + \pi^-\pi^-)_D$, as a function of q_0 for $80 < n_{ch} < 120$ and $q_t < 0.200$ GeV/c. The fitted curve is of the form $C_2 = P_1(1 + P_2 \exp(-P_3 q_0^2))$.

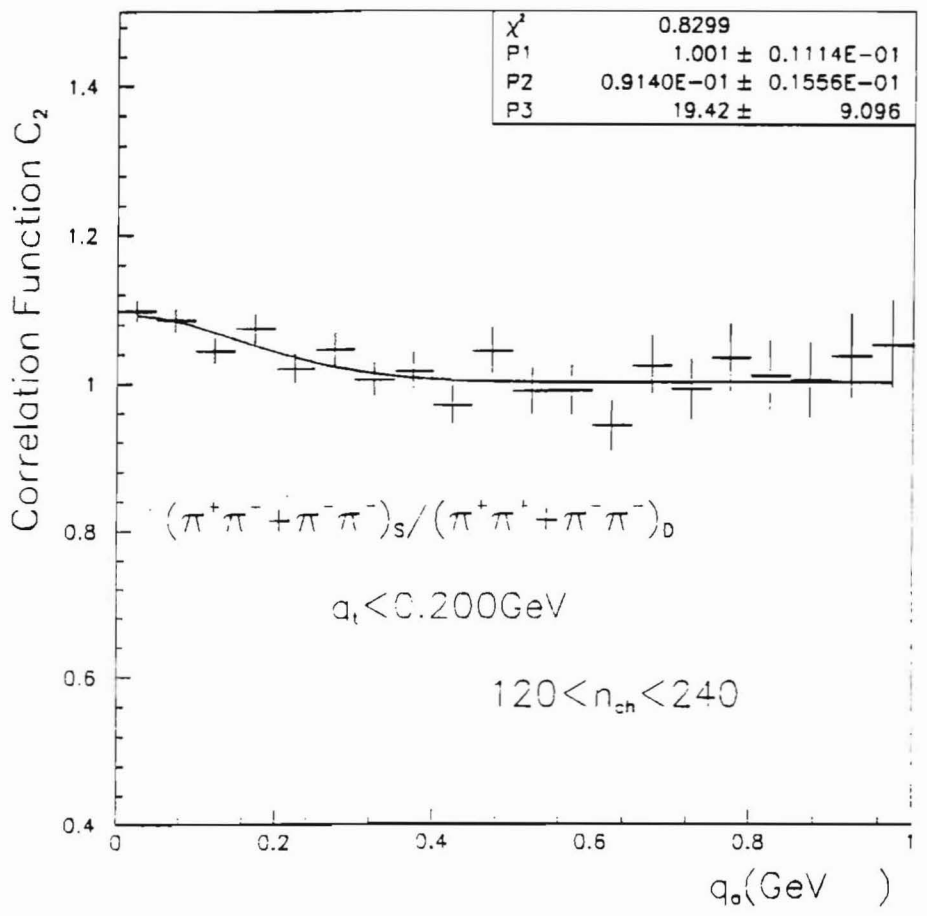

Figure 6.58: Correlation function, $C_2 = (\pi^+\pi^+ + \pi^-\pi^-)_S/(\pi^+\pi^+ + \pi^-\pi^-)_D$, as a function of q_0 for $120 < n_{ch}$ and $q_t < 0.200$ GeV/c. The fitted curve is of the form $C_2 = P_1(1 + P_2 \exp(-P_3 q_0^2))$.

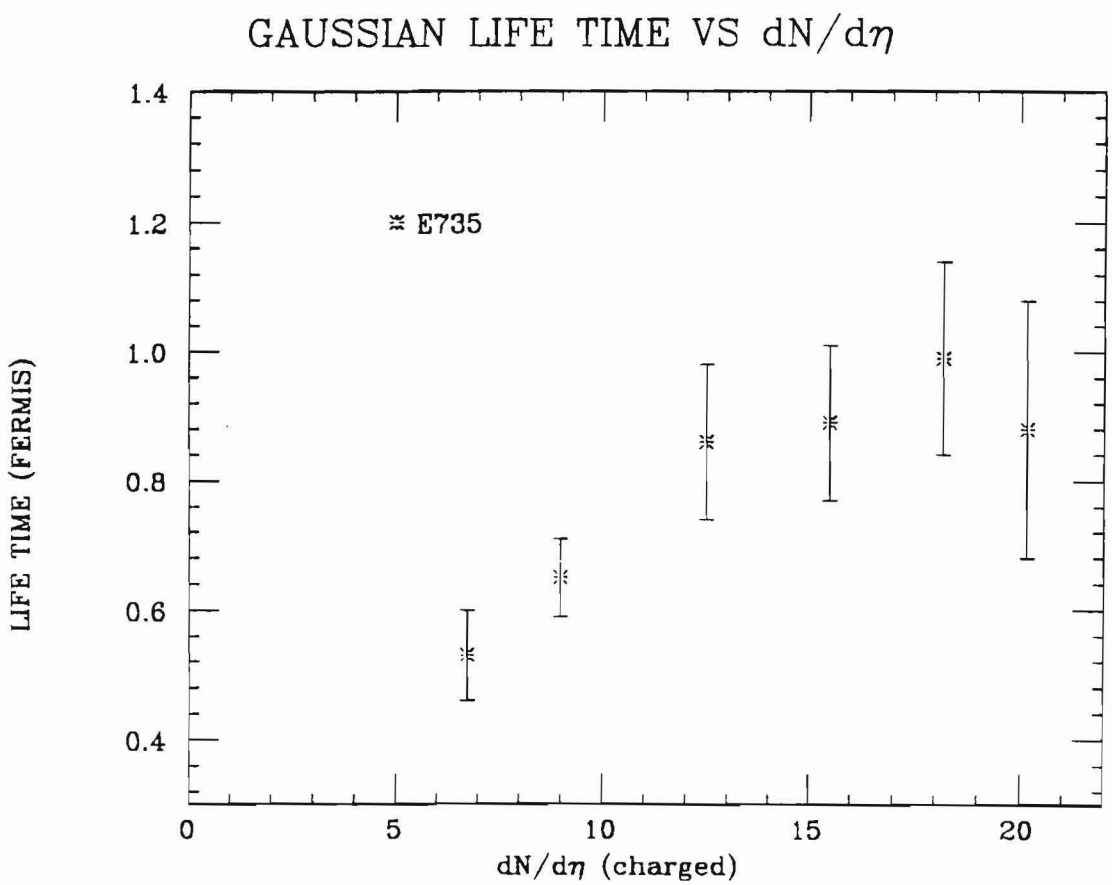

Figure 6.59: Lifetime of the source as a function of multiplicity.

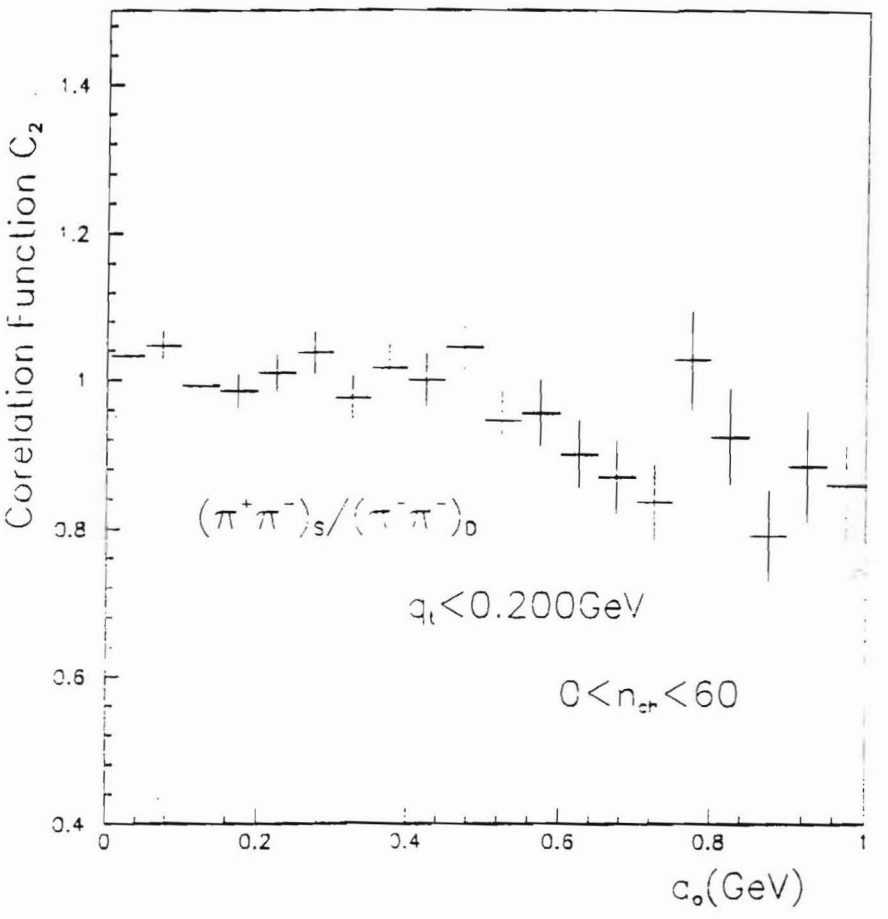

Figure 6.60: Correlation function, $C_2 = (\pi^+\pi^-)_S/(\pi^+\pi^-)_D$, as a function of q_0 for $0 < n_{ch} < 60$ and $q_t < 0.200$ GeV/c.

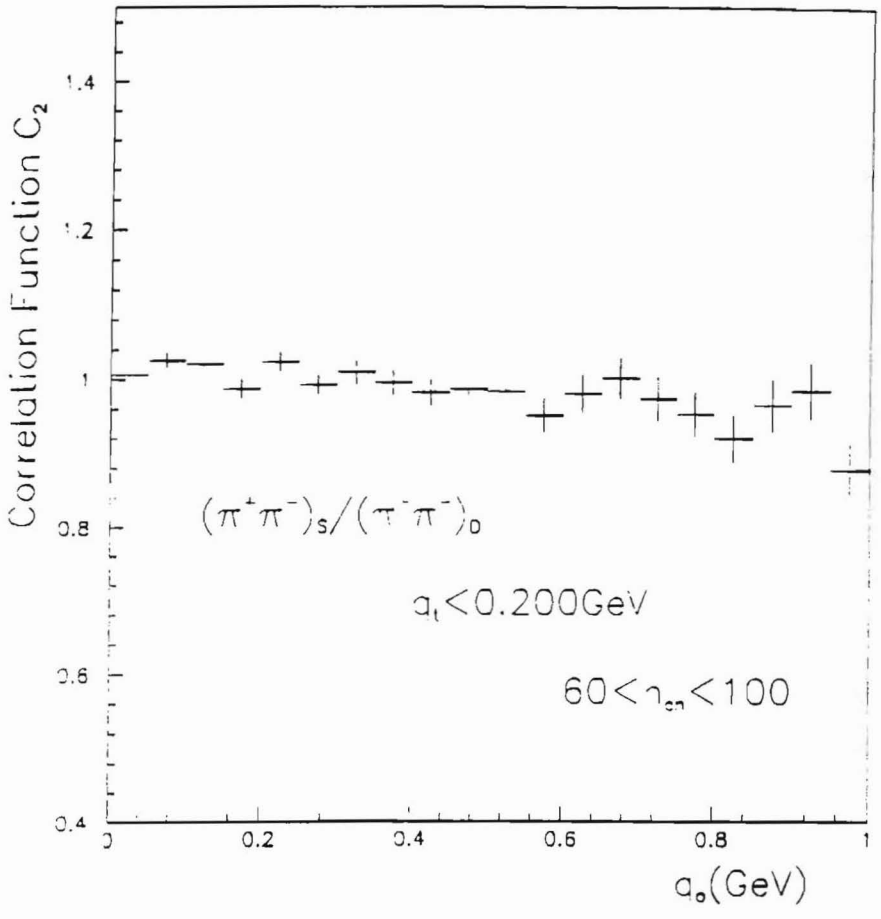

Figure 6.61: Correlation function. $C_2 = (\pi^+\pi^-)_S/(\pi^+\pi^-)_D$, as a function of q_0 for $60 < n_{ch} < 100$ and $q_t < 0.200$ GeV/c.

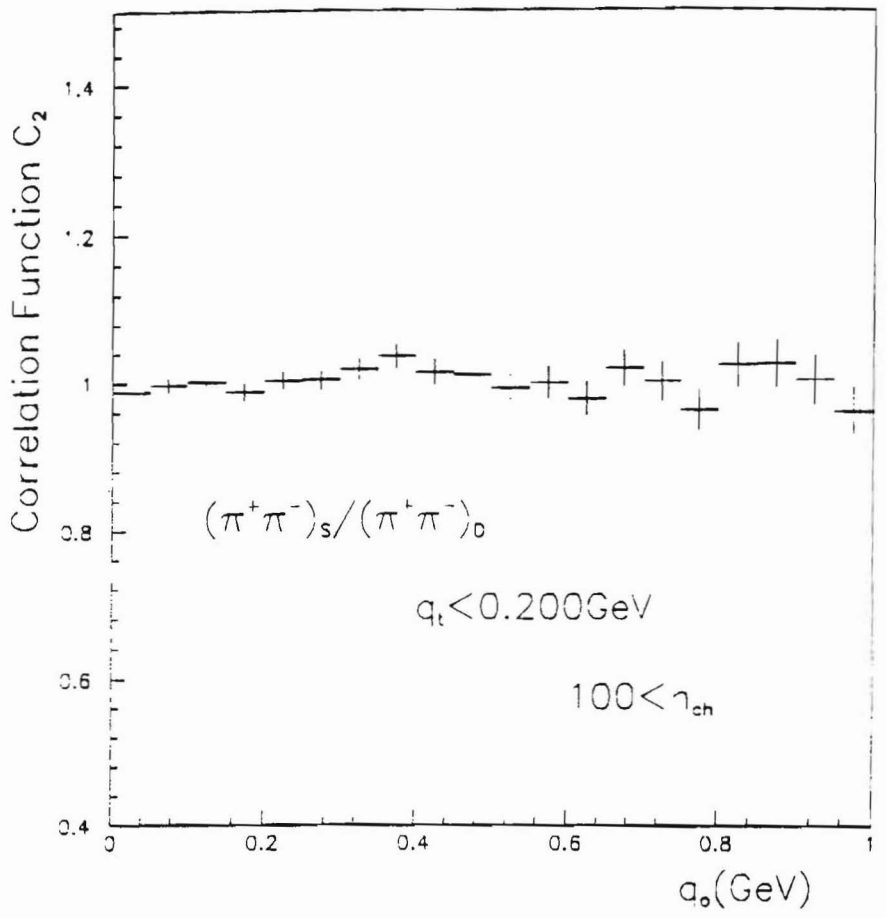

Figure 6.62: Correlation function, $C_2 = (\pi^+\pi^-)_S/(\pi^+\pi^-)_D$, as a function of q_0 for $100 < n_{ch}$ and $q_t < 0.200$ GeV/c.

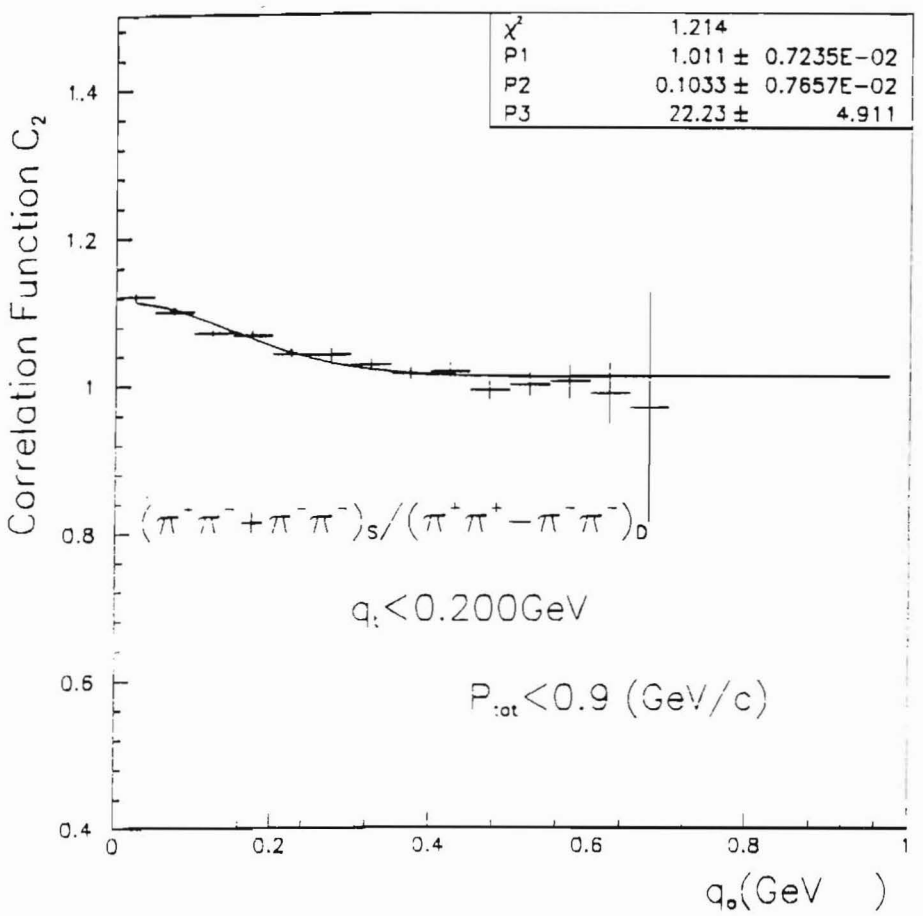

Figure 6.63: Correlation function, $C_2 = (\pi^+\pi^+ + \pi^-\pi^-)_S/(\pi^+\pi^+ + \pi^-\pi^-)_D$, as a function of q_0 for $q_t < 0.200$ GeV/c and total momentum of the pair $P_{tot} < 0.9$ GeV/c. The fitted curve is of the form $C_2 = P_1(1 + P_2 \exp(-P_3 q_0^2))$.

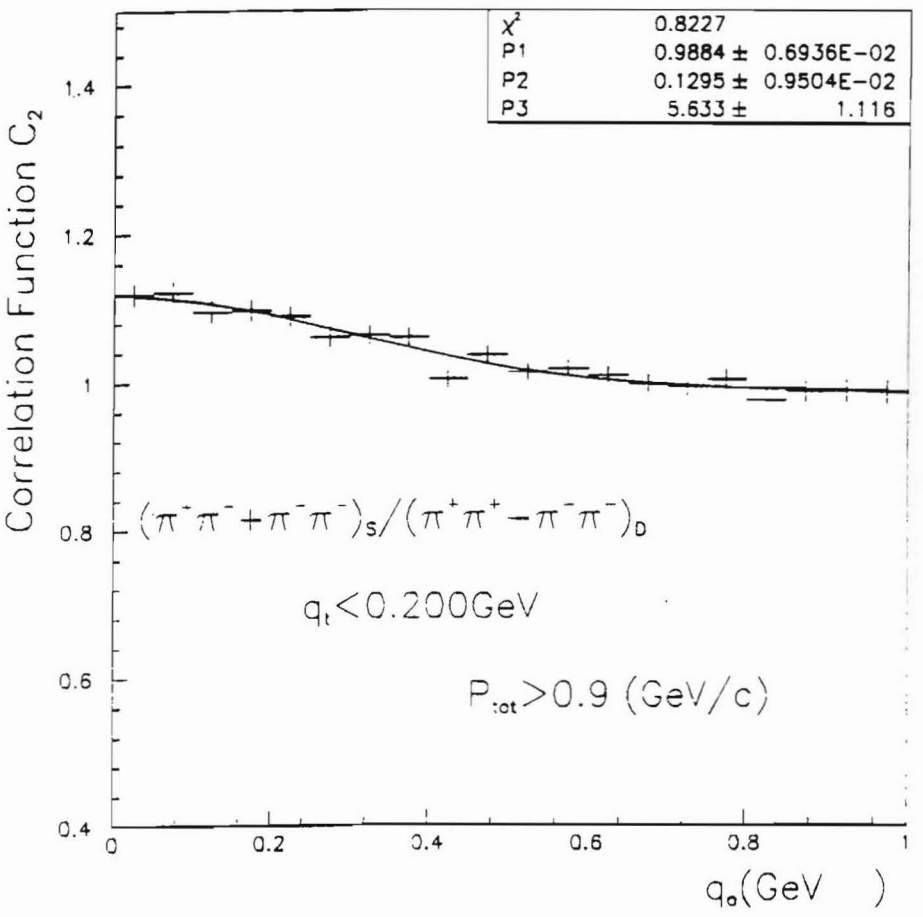

Figure 6.64: Correlation function, $C_2 = (\pi^+\pi^+ + \pi^-\pi^-)_S/(\pi^+\pi^+ + \pi^-\pi^-)_D$, as a function of q_0 for $q_t < 0.200$ GeV/c and total momentum of the pair $P_{tot} > 0.9$ GeV/c. The fitted curve is of the form $C_2 = P_1(1 + P_2 \exp(-P_3 q_0^2))$.

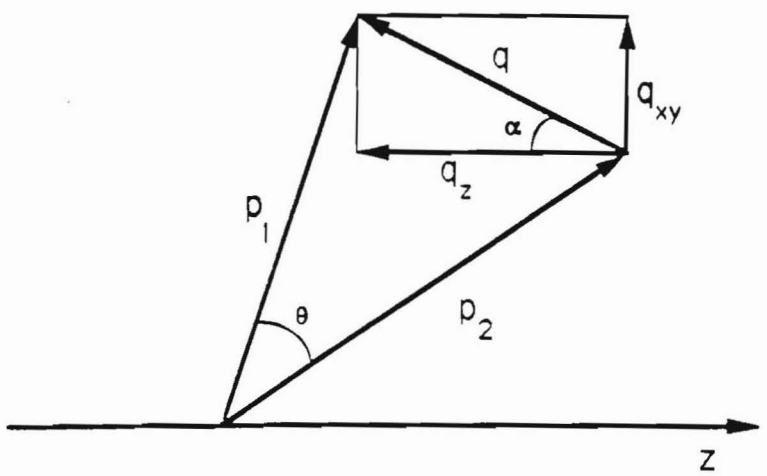

Figure 6.65: Angle, α, between the beam z-axis and the momentum difference of the pion pair.

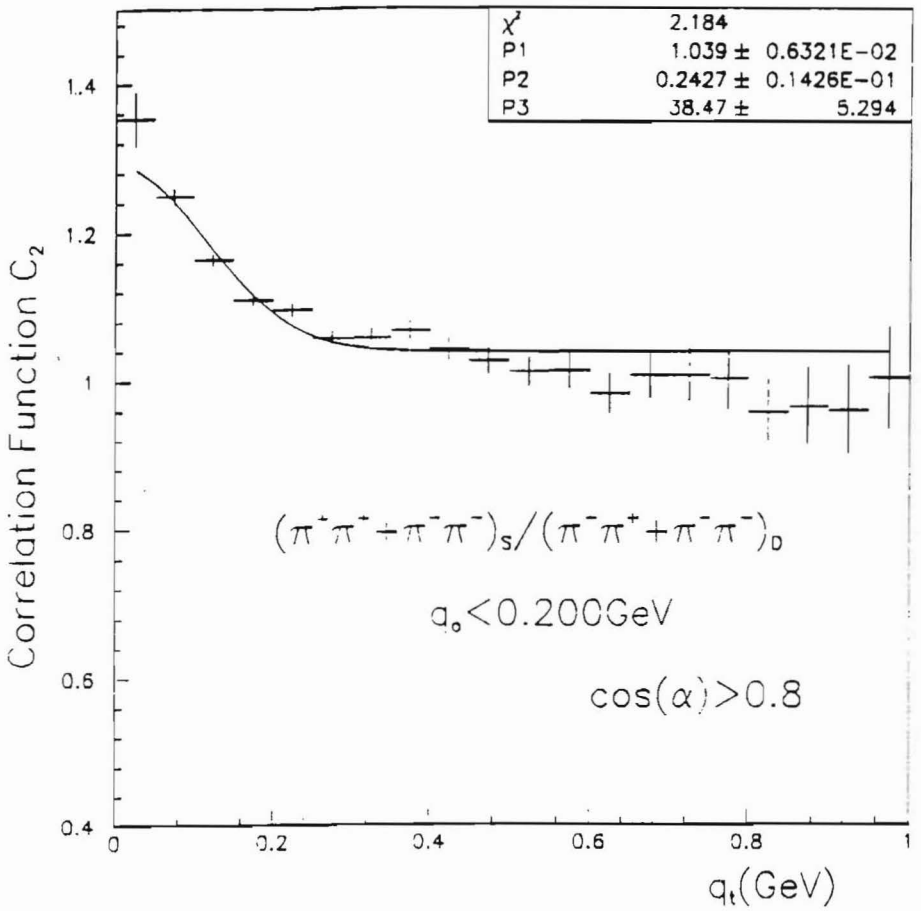

Figure 6.66: Correlation function, $C_2 = (\pi^+\pi^+ + \pi^-\pi^-)_S/(\pi^+\pi^+ + \pi^-\pi^-)_D$, as a function of q_t, $q_0 < 0.200$ GeV and $\cos\alpha > 0.8$. The fitted curve is of the form $C_2 = P_1(1 + P_2 \exp(-P_3 q_t^2))$.

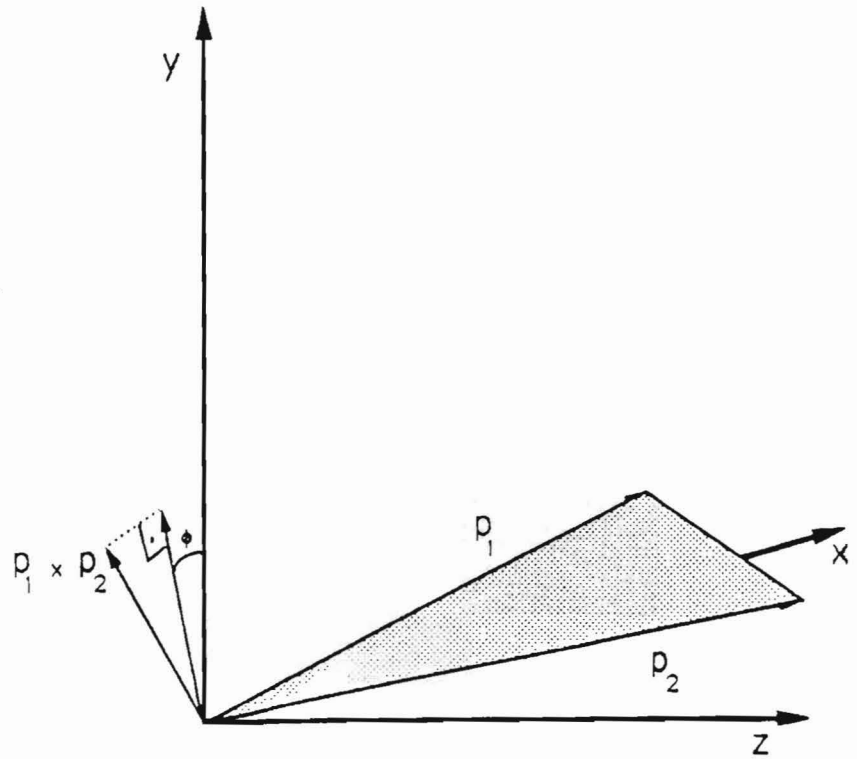

Figure 6.67: Angle ϕ illustrates the orientation of the pion pair plane.

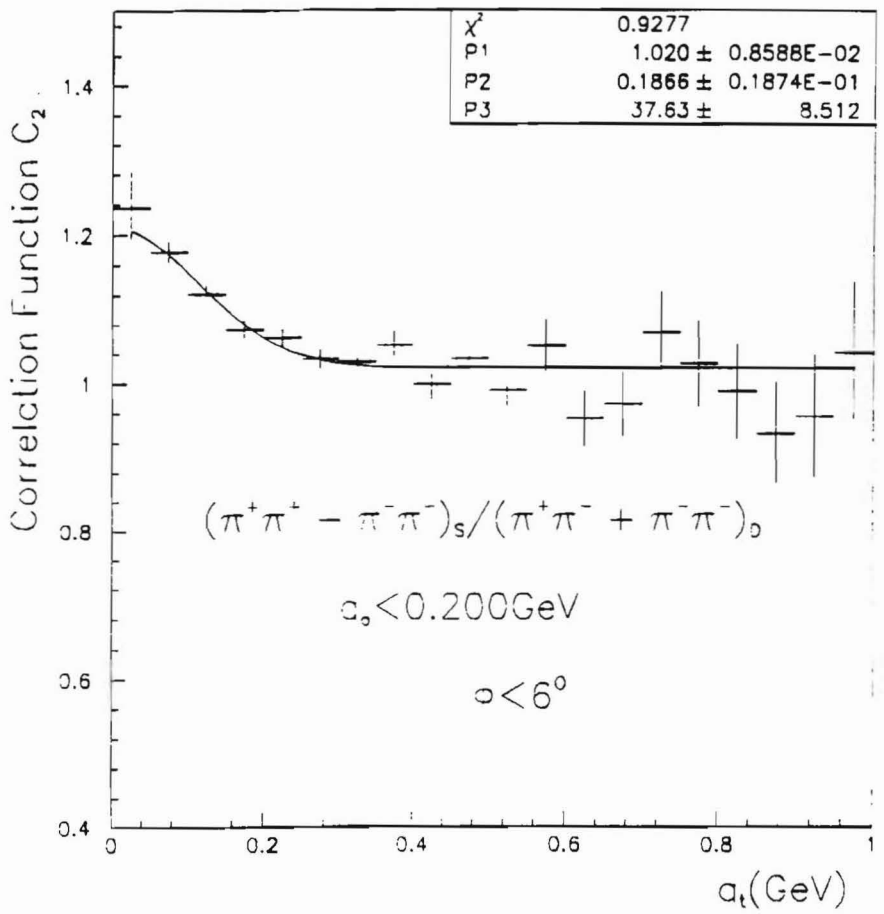

Figure 6.68: Correlation function, $C_2 = (\pi^+\pi^+ + \pi^-\pi^-)_S/(\pi^+\pi^+ + \pi^-\pi^-)_D$, as a function of q_t, $q_0 < 0.200$ GeV, and $\phi < 6^0$. The fitted curve is of the form $C_2 = P_1(1 + P_2 \exp(-P_3 q_t^2))$.

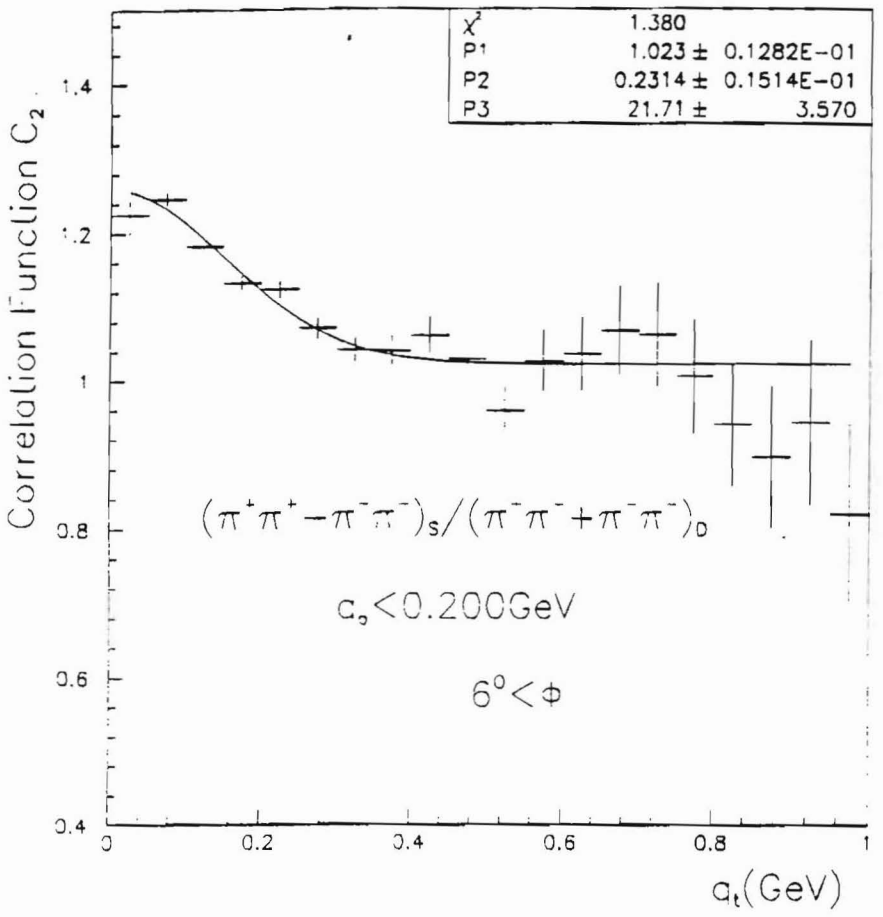

Figure 6.69: Correlation function $C_2 = (\pi^+\pi^+ + \pi^-\pi^-)_S/(\pi^+\pi^+ + \pi^-\pi^-)_D$ as a function of q_t, $q_0 < 0.200$ GeV, and $\phi > 6^0$. The fitted curve is of the form $C_2 = P_1(1 + P_2 \exp(-P_3 q_t^2))$.

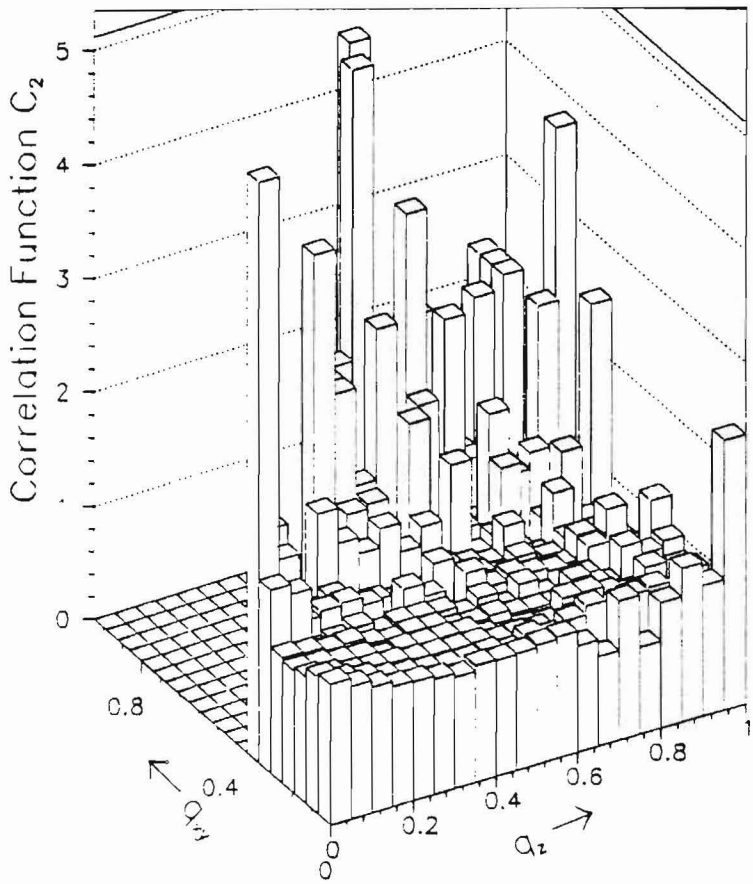

Figure 6.70: Correlation function, $C_2 = (\pi^+\pi^+ + \pi^-\pi^-)_S/(\pi^+\pi^+ + \pi^-\pi^-)_D$, as a function of (q_{xy}, q_z) for $q_0 < 0.200$ GeV.

Chapter 7

Conclusion: Summary of Observations

The Bose-Einstein interference effect for pions has been studied in the q_t and q_0 distributions for pairs of like-sign pions in the E735 spectrometer using 1988-1989 data. Only one way (out of several considered) to create the reference sample of particle pairs was worked; combinations of particles randomly chosen from different events of similar charged multiplicity. The results of this thesis are summarized as follows:

- Bose-Einstein correlations were observed for pions produced in $p - \bar{p}$ collisions at $\sqrt{s} = 1.8$ TeV were observed.
- For pairs of non-identical bosons of different charge $\pi^+\pi^-$, no correlations were found, nor were correlations found for $\pi K + \pi p + Kp$ pairs.
- No statistically significant differences were observed between $\pi^+\pi^+$ and $\pi^-\pi^-$ combinations.
- The radius of the source, R, increases with the mean charged multiplicity of the event, $< n_{ch} >$, up to 1.8 fm for the Gaussian parameterization. The rate of increase is larger than that of UA1 at $\sqrt{s} = 640$ GeV/c^2.

- The lifetime, τ, or the depth of the source, increases as a function of the mean charged multiplicity of the event, $< n_{ch} >$, as well, but only up to a value 1 fm for the Gaussian parameterization.

- The dependence of radius, R, and lifetime, τ, on mean charged multiplicity of the event $< n_{ch} >$, which is observed here, indicates a pion emitting source increasing in size with the number of pions emitted.

- The incoherence or chaoticity factor is not large $(0.1 < \lambda < 0.4)$ and seems to decrease with increasing mean charged multiplicity.

- The radius of the source, R, decreases as a function of the total momentum P_{tot} by almost a factor of two. This indicates a difference in behavior between slow and fast moving pairs.

- An attempt has been made to study the shape of the emitted source by selecting pion pairs emitted in specific directions. The result seems to indicate that the source shape is an ellipsoid, longer along the z-axis for an average charged multiplicity $< n_{ch} >= 97$.

- The magnitude and multiplicity dependence of the chaoticity factor λ is approximately the same for radius R and for lifetime τ.

A new method for identifying particle resonances using Neural Network methods was presented by using a feed-forward Neural Network. Furthermore, a new technique that constructs decay functions $G(z)$ for the determination of the event vertex was analyzed without the previous reconstruction of all tracks.

Future work for the E735 collaboration includes 3-pion Bose-Einstein Correlation $\pi^+\pi^+\pi^+$ and $\pi^-\pi^-\pi^-$. Three-pion Bose-Einstein Correlation, C_3, in principle can be studied as described in Section 1.3. Preliminary studies have shown that the 3-pion Bose-Einstein correlation as a function of Q_3 (see Section B.3) will be difficult due to lack of low invariant momentum Q_3 data, where the correlation function, C_3, is important. In addition using identified like-sign kaon pairs, Bose-Einstein correlation K^+K^+ and K^-K^- will be studied.

Appendix A

Computer Simulations

A Monte Carlo program [84] was developed for the study of the acceptance of the E735 spectrometer for stable pions, kaons, and protons, as well as the examination of particle resonances (e.g. Λ^0's, K°'s.)

A.1 Monte Carlo Program

The emphasis has been to create a simple model with short computing time per event so that large statistics (10^6 events) can be obtained in a relatively short running time. The simulation evaluates the effects of the limited solid angle of the aperture, the magnetic field bending, and the limited solid angles of the TOF detectors. The calculation and subsequent comparisons to the data for pion tracks will be described.

A.1.1 Monte Carlo Description

Particles generated at the beam line are given a momentum and z-vertex from random distributions. The particles are then propagated through a simplified model of the E735 spectrometer and the acceptance is calculated by counting

the number of tracks that intersect the planes of the time of flight detectors TOF_1 and TOF_2.

Our spectrometer model consists simply of:

- a rectangular aperture located at the position of the pre-magnet chamber,
- a magnetic field region to approximate the bending of the flight path, and
- apertures to approximate the acceptance of the TOF 1 and TOF 2 detectors.

The spectrometer model that was used for the simulation is shown in Figure A.1. Figure A.2 shows the individual steps of the calculations used for stable particles.

Spectrometer Acceptance

Given the initial momentum and position of the particle (p_x, p_y, p_z, and z), the flight path is extrapolated as a straight line from the beam line to the pre-magnet chamber. The acceptance of the magnet gap has been approximated as an aperture located from $-30.5 \leq z \leq +90.5$ cm to $0.0 \leq y \leq 20.0$ cm. Note that 2 cm has been removed from the z limits to compensate for the small dead space at the end of the pre-magnet chamber. Particle paths not intersecting this region are considered to have not entered the spectrometer and these events are rejected. The limits in the y and z directions were chosen by comparing various distributions from the Monte Carlo with actual events from the data [84].

Magnetic Field Bending

A number of simple algorithms were attempted in trying to approximate the bending of the particle as it traversed the magnetic field. The best agreement with the actual tracks from the data was found by using the technique described below. The magnetic field at the center of the magnet ($x-z$ plane) could be quite well fit using a χ^2 minimization to a function that was a linear superposition of two Gaussians:

$$B_y(x) = B_1 e^{-(x-\hat{x}_1)/2\sigma_1^2} + B_2 e^{-(x-\hat{x}_2)/2\sigma_2^2}. \tag{A.1}$$

The fit to the field measurements is shown is Figure A.3. The coefficients obtained are given in Table A.1.

i	B_i (kG)	$\hat{x}_i$ (cm)	σ_i (cm)
1	2.67	75.01	14.03
2	1.21	74.85	26.02

Table A.1: Coefficients used for modeling magnetic field $B_y(x)$ with functional form given by Equation A.1.

The bending in the $x-z$ plane can be determined by integrating the equation of motion using the parameters of the B-field

$$\frac{dp_z}{dt} = qB_y(x)v_x, \tag{A.2}$$

so that after substitution of Equation A.1 and integration, $p_z(x_f)$ was obtained:

$$\begin{aligned} p_z(x_f) &= p_z(x_i) + q\int_{x_i}^{x_f} B_y(x)dx \qquad (A.3) \\ &= p_z(x_i) + \\ &\frac{\sqrt{2\pi}qB_1\sigma_1}{2}\, erf(\frac{\hat{x}_1 - x_i}{\sqrt{2}\sigma_1}) + \frac{\sqrt{2\pi}qB_2\sigma_2}{2}\, erf(\frac{\hat{x}_2 - x_i}{\sqrt{2}\sigma_2}) + \\ &\frac{\sqrt{2\pi}qB_1\sigma_1}{2}\, erf(\frac{x_f - \hat{x}_1}{\sqrt{2}\sigma_1}) + \frac{\sqrt{2\pi}qB_2\sigma_2}{2}\, erf(\frac{x_f - \hat{x}_2}{\sqrt{2}\sigma_2}), \qquad (A.4) \end{aligned}$$

where

$$erf(x) = \frac{2}{\sqrt{\pi}}\int_0^x e^{-t^2}dt \tag{A.5}$$

is the error function. The final momentum component p_{xf} is obtained using momentum conservation, (and the assumption that the bend in the y-direction is negligible).

$$p_{xf}^2 = p_{xi}^2 + p_{zi}^2 - p_{zf}^2. \tag{A.6}$$

Magnetic Focusing

The smaller effect of the bending of the trajectory in the $x - y$ plane due to fringe fields at the entrance and exit of the magnet gap (magnetic focusing) has been approximated using a simple ray trace model analogous to the one used in tracing light paths through a thin lens. A diagram of the focusing model is shown in Figure A.4. The particle travels unaffected from the point x_1 to x_2, where x_2 is the position of the magnet entrance aperture. At x_2 the focusing effect occurs and the particle trace is bent. The bend is calculated using a focal length

$$f_i = \frac{|\vec{p}|}{qB_0} \cot \theta_i = \frac{|\vec{p}|}{qB_0} \frac{p_{xi}}{p_{zi}}, \tag{A.7}$$

where B_0 is the magnitude of the momentum component in the $x - z$ plane.

The particle then travels in a straight line path from x_2 to the magnet exit aperture x_3. The path is again bent with a focal length given by

$$f_f = \frac{|\vec{p}|}{qB_0} \cot \theta_f = \frac{|\vec{p}|}{qB_0} \frac{p_{xf}}{p_{zf}}. \tag{A.8}$$

The effect of the whole focusing system can be calculated using the transfer matrix formulation used in optics. The transfer matrix, T, from point x_1 to point x_4 is given by

$$T(x_1, x_4) = D(x_3, x_4) \cdot F_1(\theta_f) \cdot D(x_2, x_3) \cdot F_2(\theta_i) \cdot D(x_1, x_2), \tag{A.9}$$

where $D(x_i, x_f)$ is the matrix for calculating the trajectory through the "drift" spaces

$$D(x_i, x_f) = \begin{pmatrix} 1 & (x_f - x_i) \\ 0 & 1 \end{pmatrix}, \tag{A.10}$$

and $F(\theta)$ is the matrix for calculating the focusing

$$F(\theta) = \begin{pmatrix} 1 & 0 \\ -1/f(\theta) & 1 \end{pmatrix}. \tag{A.11}$$

TOF System

After the particle path exits the magnetic field region, the flight path is extrapolated from the final momentum, $|\vec{p_f}|$, to the $x - z$ plane of the TOF-1 and TOF-2 detectors. The TOF-1 and TOF-2 apertures are divided into seven and 32 regions, respectively. The positions of the individual regions were taken from the survey measurements of the scintillator block positions. The intersection at the TOF plane is determined and a scintillator block is assigned for that position. The distribution of hits in TOF-1 and TOF-2 can then be determined for calculation of their geometric acceptance.

A.1.2 Comparisons with the Data

For comparisons with the data, the following track selection criteria have been chosen:

- Tracks from the Wisconsin tracking algorithms RCT1, RCT2, and RCT3 are used.
- Events are rejected that have been identified as beam gas with the *LBG* flag.
- All tracks must have $\chi^2_{pdf} \leq 8$.

- Tracks must have z-vertex such that $|z_v| \leq 50$ cm.
- The difference in the z-chamber vertex and the z-intercept of the track $|z_v - z_{interc}| \leq 3$ cm.
- The track must have total momentum such that $|\vec{p}| \geq .08$ GeV/c.

A.1.3 Bending Algorithm

The accuracy of the bending algorithm can be seen by comparing the actual position of the track at the TOF-1 plane (extrapolated from the final momentum $\vec{p_f}$) with the prediction of the bending/focusing algorithms using only the intial position of the track at the beam line z_0 and the initial momentum $\vec{p_i}$.

Figures A.5 and A.6 show the difference in the z intercept $\Delta z = z_{data} - z_{M.C.}$ versus total momentum $|\vec{p}|$ for positive and negative tracks, respectively. The FWHM estimated from the figure is less than 2 cm. The shape of the distribution can be understood from examination of the scatter plots of Δz versus the momentum. The best agreement occurs at large momentum. The large non-Gaussian tail occurs for low momentum tracks and are the result of multiple scattering events (which we have not accounted for in the bending algorithm) and the fact that the lower momentum tracks have a greater probability of passing near the edges of the magnet where our approximation is not as accurate.

Figures for Appendices

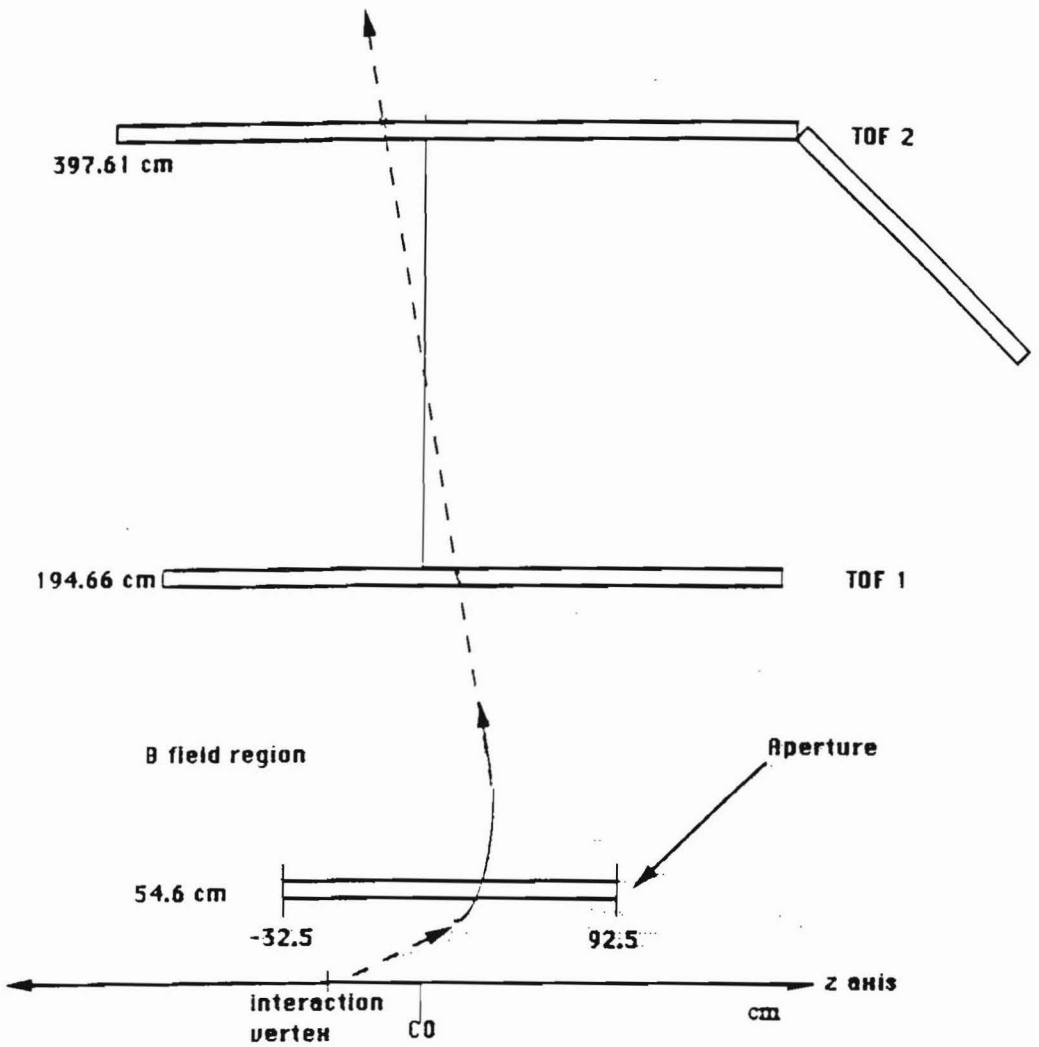

Figure A.1: Diagram of spectrometer model with dimensions used in the Monte Carlo simulation.

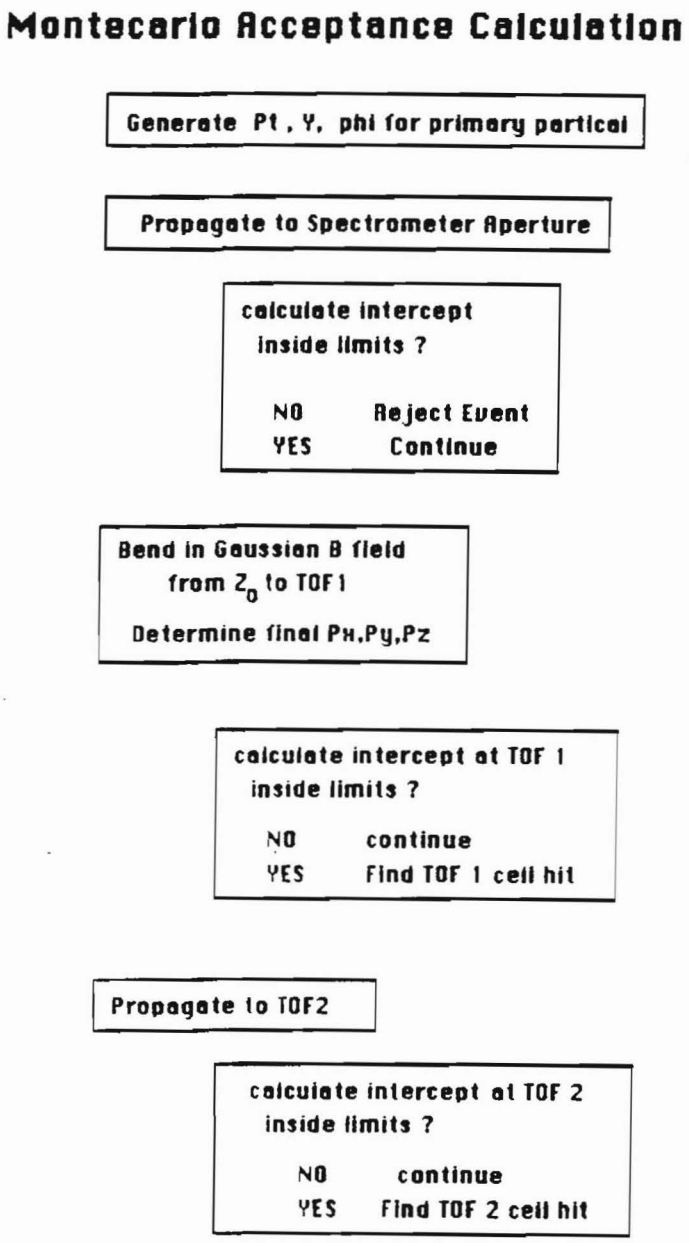

Figure A.2: Diagram of steps used in the calculation of spectrometer acceptance of stable pions.

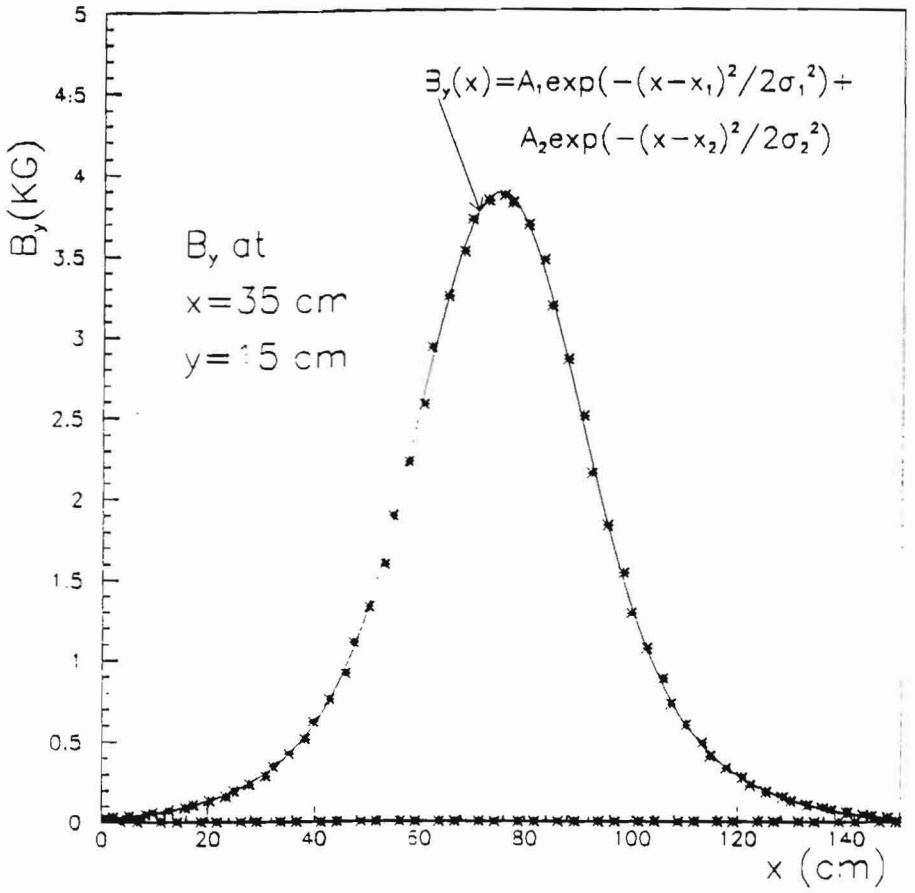

Figure A.3: Graph showing B-field ($B_y(x)$) measurements and fit to the superposition of two Gaussian functions.

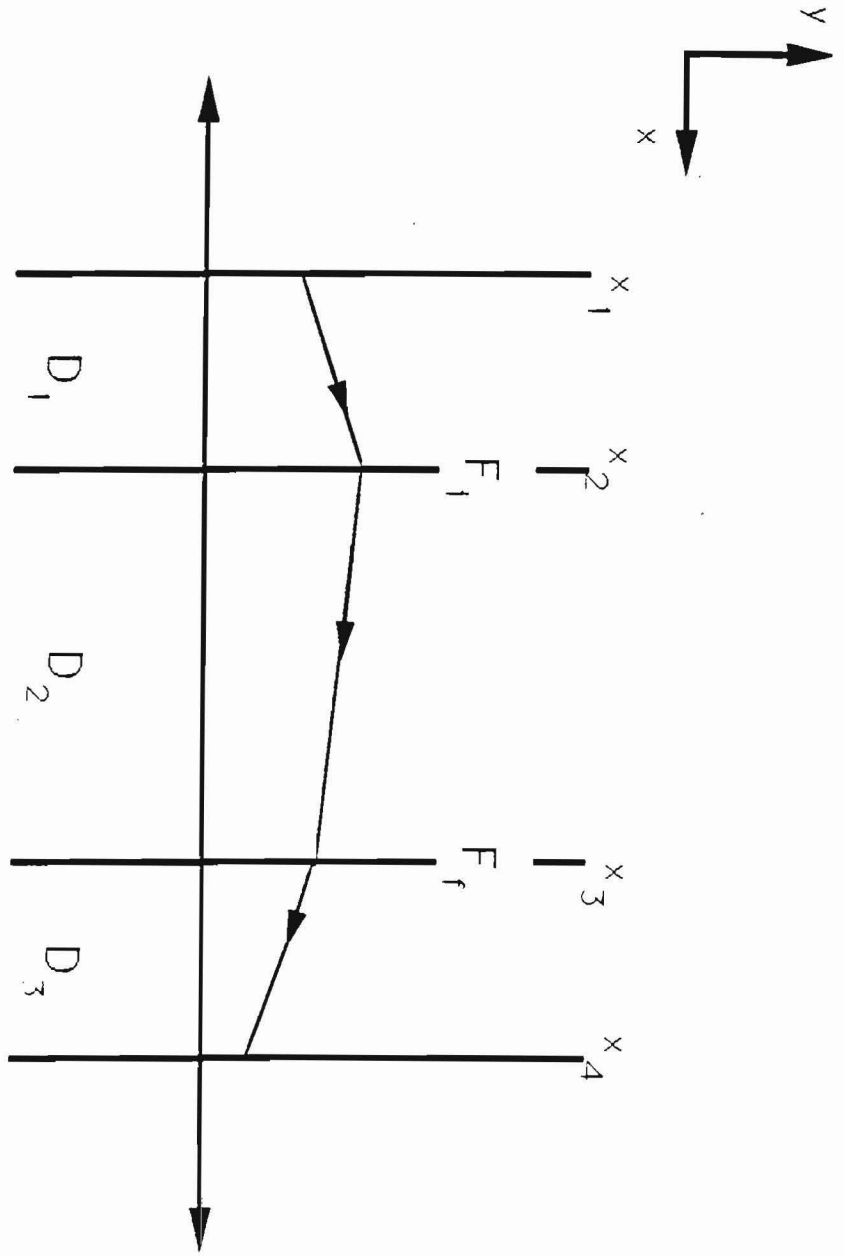

Figure A.4: Diagram used for calculating effects of magnetic focusing.

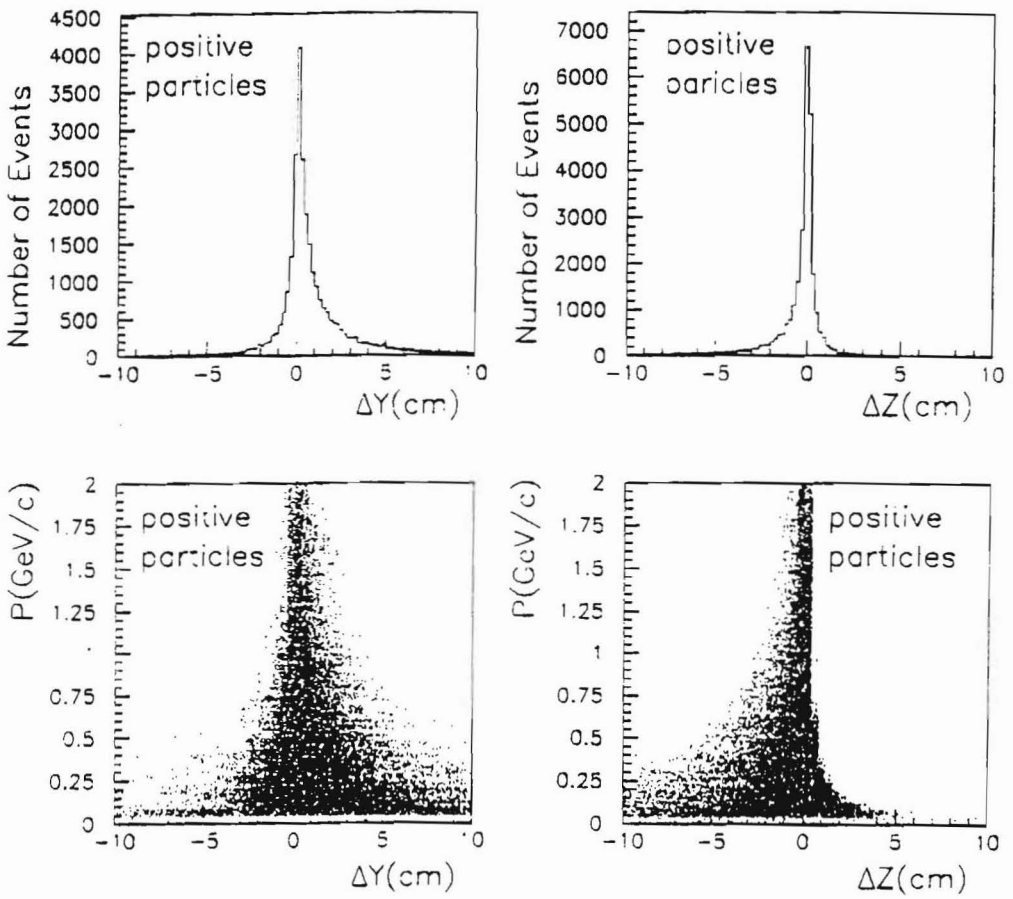

Figure A.5: Difference in calculated position of *positive* particle track at TOF_1 plane and position obtained from the RCT data tracking algorithms. The lower diagram shows the correlation with the momentum.

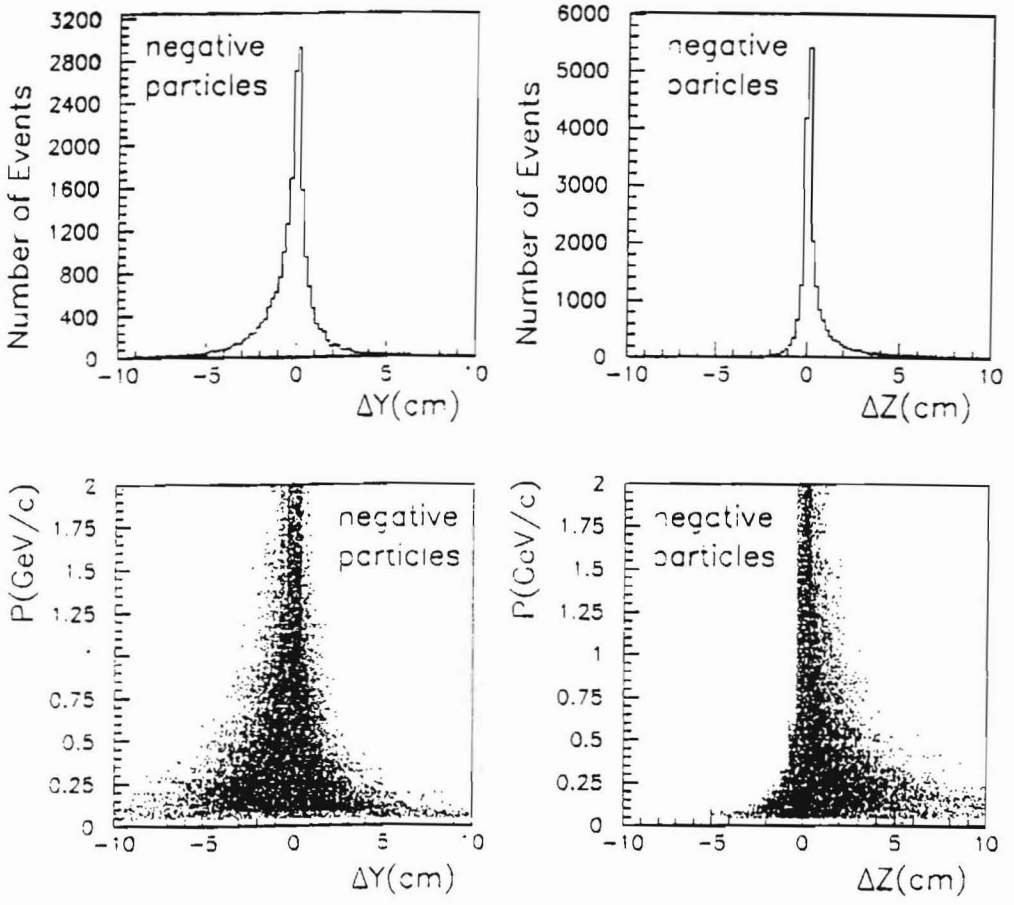

Figure A.6: Difference in calculated position of *negative* particle track at TOF-1 plane and position obtained from the RCT data tracking algorithms. The lower diagram shows the correlation with the momentum.

Appendix B

Useful Relations

In this appendix some of the most commonly used variables in B.E. correlations will be reviewed.

Let us consider two $\pi's$ that can be described in the lab system with 4-momenta, p_1^μ and p_2^μ, respectively, as shown in Figure 6.1. In the 4-vector representation, the 4-momenta can be written as:

$$p_1^\mu = (E_1, \vec{p_1}), \tag{B.1}$$

$$p_2^\mu = (E_2, \vec{p_2}), \tag{B.2}$$

where E_1, E_2 are the energies of the two pions and $\vec{p_1}$, $\vec{p_2}$ are their vector momenta.

B.1 $\vec{q_t}$, $\vec{q_l}$

From Figure 6.1, $\vec{q}$ can be written:

$$\vec{q} = \vec{q_t} + \vec{q_l}, \tag{B.3}$$

where $\vec{q_t}$ is the component of $\vec{q}$=$\vec{p_1}$-$\vec{p_2}$ normal to the total momentum of the pair, $\vec{p}$=$\vec{p_1}$+$\vec{p_2}$, and $\vec{q_l}$ is the component of $\vec{q}$=$\vec{p_1}$-$\vec{p_2}$ parallel to the total momentum of

the pair.

It can be shown that q_t and q_l are expressed as:

$$\vec{q_l} = \frac{\vec{p}(\vec{q}\cdot\vec{p})}{|\vec{p}|^2} = \sqrt{\frac{|p_1^2 - p_2^2|^2}{p_1^2 + p_2^2 + 2p_1p_2\cos\theta}}\hat{u}_l, \tag{B.4}$$

$$\vec{q_t} = \vec{q} - \frac{\vec{p}(\vec{q}\cdot\vec{p})}{|\vec{p}|^2} = \sqrt{\frac{4p_1^2p_2^2\sin^2\theta}{p_1^2 + p_2^2 + 2p_1p_2\cos\theta}}\hat{u}_t, \tag{B.5}$$

where $\hat{u}_t$, $\hat{u}_l$ are two unit vectors along $\vec{q_t}$, $\vec{q_l}$, and θ is the opening angle of the pair (Figure 6.1). In addition, q_t is given by:

$$|\vec{q_t}| = |\frac{(\vec{q}\times\vec{p})}{\vec{p}}|. \tag{B.6}$$

B.2 Invariant Mass M_2 and M_3

The invariant mass of the pair is given by:

$$M_2^2 = (p_1^\mu + p_2^\mu)(p_{1\mu} + p_{2\mu}). \tag{B.7}$$

It can also be expressed as:

$$M_2^2 = 2m_\pi^2 + 2E_1E_2 - 2\vec{p_1}\cdot\vec{p_2}, \tag{B.8}$$

where m_π is the mass of the π.

In the case of three particles with 4-momenta p_1^μ, p_2^μ, and p_3^μ; the invariant mass is given by:

$$M_3^2 = (p_1^\mu + p_2^\mu + p_3^\mu)(p_{1\mu} + p_{2\mu} + p_{3\mu}), \tag{B.9}$$

or

$$M_3^2 = 3m_\pi^2 + 2p_1^\mu p_{2\mu} + 2p_2^\mu p_{3\mu} + 2p_1^\mu p_{3\mu}. \tag{B.10}$$

B.3 Invariant Momentum Difference Q_2 and Q_3

The invariant momentum difference for two particles with momenta p_1^μ and p_2^μ is given by:

$$Q_2^2 = -(p_1^\mu - p_2^\mu)(p_{1\mu} - p_{2\mu}), \tag{B.11}$$

or

$$Q_2^2 = -q_0^2 + \vec{q}^{\,2}, \tag{B.12}$$

where $q_0 = |E_1 - E_2|$. By evaluating Q_2 in the rest mass frame of the pair of the two $\pi's$, one can write:

$$Q_2^2 = (M_2^2 - 4m_\pi^2), \tag{B.13}$$

or

$$Q_2^2 = 4p_1^{'2}, \tag{B.14}$$

where $p_1^{'}$ is the momentum of each π in the rest mass frame of the pair. From Equations B.12 and B.14

$$q_0 \leq |\vec{q}|. \tag{B.15}$$

In the case of three particles with momenta p_1^μ, p_2^μ, and p_3^μ; Q_3 is given by:

$$Q_3^2 = -(Q_{1,2}^2 + Q_{2,3}^2 + Q_{1,3}^2), \tag{B.16}$$

where

$$Q_{1,2}^2 = (p_1^\mu - p_2^\mu)^2, \tag{B.17}$$

$$Q_{2,3}^2 = (p_2^\mu - p_3^\mu)^2, \tag{B.18}$$

$$Q_{1,3}^2 = (p_1^\mu - p_3^\mu)^2. \tag{B.19}$$

Q_3^2 from Equation B.11 is written as:

$$Q_3^2 = -(q_{0,1,2}^2 + q_{0,2,3}^2 + q_{0,1,3}^2) + (\vec{q}_{1,2}^{\,2} + \vec{q}_{2,3}^{\,2} + \vec{q}_{1,3}^{\,2}), \tag{B.20}$$

where

$$\vec{q}_{1,2} = (\vec{p}_1 - \vec{p}_2), \tag{B.21}$$

$$\vec{q}_{2,3} = (\vec{p}_2 - \vec{p}_3), \tag{B.22}$$

$$\vec{q}_{1,3} = (\vec{p}_1 - \vec{p}_3), \tag{B.23}$$

$$q_{0,1,2} = E_1 - E_2, \tag{B.24}$$

$$q_{0,2,3} = E_2 - E_3, \tag{B.25}$$

$$q_{0,1,3} = E_1 - E_3. \tag{B.26}$$

By using Equation B.13, Q_3^2 can be expressed as:

$$Q_3^2 = M_3^2 - (3m_\pi)^2. \tag{B.27}$$

These ideas can be generalized to an n-particle system by using:

$$Q_n^2 = M_n^2 - (nm_\pi)^2. \tag{B.28}$$

B.4 Mean Velocity of the Pair of the π's

The mean velocity of the pair of the two $\pi's$ in the lab system is:

$$\vec{u} = \frac{\vec{p_1} + \vec{p_2}}{E_1 + E_2}. \tag{B.29}$$

Using Equation B.4, q_0 can be written as:

$$q_0 = \vec{u} \cdot \vec{q_l}, \tag{B.30}$$

or since $\vec{u}$ is perpendicular to $\vec{q}_t$,

$$q_0 = \vec{u} \cdot \vec{q}. \tag{B.31}$$

One can define the Lorentz γ factor for the π pair in the lab system as:

$$\gamma = \frac{1}{\sqrt{1 - \vec{u}^2}}, \tag{B.32}$$

or

$$\gamma = \frac{E_1 + E_2}{M_2}. \tag{B.33}$$

From

$$Q_2^2 = q_t^2 + q_l^2, \tag{B.34}$$

and Equation B.30, Q_2^2 is expressed in the following useful way:

$$Q_2^2 = q_t^2 + \frac{q_0^2}{(\gamma^2 - 1)}, \tag{B.35}$$

which tells us that for fast moving π pairs $Q_2 \simeq |\vec{q}_t|$.

Appendix C

Bose-Einstein Correlation and Metropolis Monte Carlo

Two different methods were used to simulate Bose-Einstein correlations using Monte Carlo data. One method was based on weighting pion pairs according to the Bose-Einstein correlation, and the second method was based on creating pion pairs according to Bose-Einstein correlations with a unit probability.

In the first method, each pion was created according to a momentum distribution given by:

$$dn/dp_t = e^{-p_t/T}, \tag{C.1}$$

where $p_t = \sqrt{p_x^2 + p_y^2}$ is the transverse momentum of a particle. Pions were created flat in rapidity, y, and azimuthal angle, ϕ. After creating two like-charged pions according to the previous description, the weight factor was calculated using the Bose-Einstein function, C_2:

$$C_2 = 1 + \lambda e^{-R^2 q_t^2}. \tag{C.2}$$

Each like-charged pion pair was weighted by the above factor C_2, however, the unlike-charged pion pairs were not.

Another method of generating Bose-Einstein pairs was studied using the Metropolis' algorithm [85]. This application of the Metropolis algorithm to Bose-Einstein correlations is due to W. Zajc [25]. A brief description of Metropolis' algorithm [86] will be given as well as its application to Bose-Einstein correlations.

C.1 Metropolis's Algorithm

The first application of the Metropolis's algorithm was made to solve the problem of simulating a system of N particles, confined in a volume V, at a fixed temperature T. Since only a finite number, m, of the total number, M, configurations can be generated. An estimation for the mean value $< A >$ can be obtained from:

$$< A > = \sum_{s=1}^{M} A_s e^{-\beta E_s} / \sum_{s=1}^{M} e^{-\beta E_s} \tag{C.3}$$

$$\sim \sum_{s=1}^{m} A_s e^{-\beta E_s} / \sum_{s=1}^{m} e^{-\beta E_s}, \tag{C.4}$$

where E_s and A_s are the energy and value of the physical quantity A in configuration s, and $\beta = 1/T$ is the inverse temperature of the system. A weighted Monte Carlo procedure is used to generate a configuration at random, calculate E_s, A_s, and the product $A_s e^{-\beta E_s}$, and evaluate the corresponding contribution of the configuration to the sum in Equation C.3. However, such a configuration would likely be very improbable and hence contribute little to the sum. Instead, another procedure can be used where a set of configurations can be generated according to a probability distribution P_s. In this case the mean value $< A >$ is

averaged over the m configurations of the biased sample and each configuration is weighted by $1/P_s$ in order to eliminate the bias:

$$< A > \sim \sum_{s=1}^{M} A_s \frac{1}{P_s} e^{-\beta E_s} / \sum_{s=1}^{M} \frac{1}{P_s} e^{-\beta E_s}. \tag{C.5}$$

A convenient choice of P_s is given by:

$$P_s = e^{-\beta E_s} / \sum_{s=1}^{M} e^{-\beta E_s}. \tag{C.6}$$

This choice is due to Metropolis *et al.* [85]. The above Metropolis idea can be formed in the following flow chart steps:

1. Create an initial configuration.

2. Make a random trial change in the initial configuration.

3. Compute ΔE, the change in the energy of the system due to the trial change.

4. If $\Delta E \leq 0$, accept the new configuration and go to step 8.

5. If $\Delta E > 0$, compute the probability $P = e^{-\Delta E/T}$.

6. Generate a random number $r \in [0, 1]$.

7. If $r \leq P$, accept the new configuration. Otherwise, retain the previous configuration.

8. Determine the value of the desired physical quantities.

9. Repeat steps (1) through (7) to obtain a sufficient number of configurations.

10. Compute averages over the configurations.

C.2 Application of Metropolis Algorithm to B.E. Correlation

The Metropolis' algorithm was used to generate pion pair or multi-pion pair events with a unit probability containing Bose-Einstein correlations. This is a general method which allows one to generate an ensemble of n-body configurations according to probability function $C_n(p_1, ..., p_i, ..., p_n)$. The flow chart of the generation of the ensemble is due to W. Zajc [25]:

1. Create an initial configuration of an n-pion state characterized by momenta: $(p_1, ..., p_i, ..., p_n)$.

2. Calculate the "old" probability P_o using the correlation function C_n, $P_o = C_n(p_1, ..., p_i, ..., p_n)$.

3. Compute a random trial change in the momentum of the i-th particle: $p_1^{'}$.

4. Calculate the "new" probability P_n, $P_n = C_n(p_1, ..., p_i^{'}, ..., p_n)$.

5. If $P_n \geq P_o$, accept the new momentum $p_1^{'}$ and replace the p_1.

6. If $P_n < P_o$, compute the relative probability $P = P_n/P_o$.

7. Generate a random number $r \in [0, 1]$.

8. If $r \leq P$, accept the new momentum $p_1^{'}$. Otherwise, retain the previous $p_1^{'}$.

9. Repeat steps (3) through (8) for all i particles.

10. Repeat steps (3) through (9) to obtain a sufficient number of configurations.

Appendix D

Electric and Potential Field of the Z-Chamber

The electric, potential field, and drift field of the z-chamber were calculated analytically using the known 2-dimensional potential for a multiwire proportional chamber. The expression for the complex potential, $\Psi(\omega)$, of an infinite grid of wires midway between a pair of parallel cathode planes is given by Erskine[87]:

$$\Psi(\omega) = -const. \times 2\ln(\frac{2(\sin\zeta - q^2\sin 3\zeta + q^6\sin 5\zeta - \ldots)}{1 - 2(q\cos 2\zeta - q^4\cos 4\zeta + q^9\cos 6\zeta - \ldots)}),$$

where $\zeta = (\pi\omega/s)$, $q = e^{-(4\pi L/s)}$, $\omega = z + ix$, s=spacing between the wires along z and L =distance along x from a plane to the grid (Figure 2.5, without the field wires). The value of the *const.* depends on the geometry of the chamber and the potential of the wires and the planes.

The electrostatic potential, Φ, and the electric field, $\vec{E}$, are

$$\Phi(z,x) = Re\Psi(\omega), \quad \text{and}$$

$$\vec{E}(z,x) = -\vec{\nabla}\Phi(z,x), \vec{\nabla} = (\frac{\partial}{\partial z}, \frac{\partial}{\partial x}).$$

In the case of the vertex chamber there is an additional (field) wire grid (Figure 2.5). For $s = 2L$, $q = 0.00187 \ll 1$. The resulting complex potential, $\Psi(\omega)$,

is the superposition of the two contributing potentials:

$$\Psi(\omega) = -C_1 2\ln(\frac{2\sin\frac{\pi\omega}{s}}{1-2q\cos 2\frac{\pi\omega}{s}}) - C_2 2\ln(\frac{2\sin\pi(\omega+\frac{s}{2})/s}{1-2q\cos 2\pi(\omega+\frac{s}{2})/s}) + C_3,$$

where terms of higher order in q are neglected. The three constants C_1, C_2, and C_3 can be found by applying the potential boundary conditions on the sense wires, field wires, and cathode planes:

$$\Psi(\omega) \quad |_{(\text{on sense wires})} = V_s.$$

$$\Psi(\omega) \quad |_{(\text{on field wires})} = 0.$$

$$\Psi(\omega) \quad |_{(\text{on cathode window})} = 0.$$

Thus, a system of three equations with three unknowns was derived:

$$-C_1 2\ln(\frac{\frac{2\pi r_s}{s}}{(1-2q)}) - C_2\ln 4 + C_3 = V_s, \tag{D.1}$$

$$-C_1\ln 4 - C_2 2\ln(\frac{\frac{2\pi r_f}{s}}{1-2q}) + C_3 = 0, \tag{D.2}$$

$$-C_1 2\ln(\frac{2\sinh\frac{L\pi}{s}}{1-2q\cosh\frac{2L\pi}{s}}) - C_2 2\ln(\frac{2\sinh\frac{L\pi}{s}}{1-2q\cosh\frac{2L\pi}{s}}) + C_3 = 0, \tag{D.3}$$

where r_s and r_f are the radii of the sense and field wires, respectively.

Isochronous lines are found by using

$$t = \int_0^{(z,x)} \frac{d\sigma}{v(|\vec{E}(z,x)|)},$$

where $v(z,x)$ is the drift velocity as a function of $|\vec{E}(z,x)|$, given by Sauli [40]. The path of integration σ is along the electric field lines which can be derived from the field line equations:

$$\frac{dz}{d\sigma} = -Re(\frac{\overline{\Psi'(\omega)}}{|\Psi'(\omega)|}) \tag{D.4}$$

and

$$\frac{dx}{d\sigma} = -Im(\frac{\overline{\Psi'(\omega)}}{|\Psi'(\omega)|}), \tag{D.5}$$

using the Runge-Kutta integration method. $\overline{\Psi'(\omega)}$ is the complex conjugate of the potential $\Psi(\omega)$ and $\Psi'(\omega)$ is obtained by analytical differentiation of $\Psi(\omega)$.

Appendix E

E735 Collaboration

The E735 Collaboration consists of the following members:

T. Alexopoulos[f], C. Allen[e], E. W. Anderson[c], H. Areti[b], S. Banerjee[d], P. D. Beery[d], P. Bhat[a], J. Bishop[d], N. N. Biswas[d], A. Bujak[e], D. D. Carmony[e], T. Carter[a], P. Cole[e], Y. Choi[e], R. Debonte[e], V. DeCarlo[g], A. R. Erwin[f], C. Findeisen[f], A. T. Goshow[a], L. J. Gutay[e], A. S. Hirsch[e], C. Hojvat[b], J. R. Jennings[f], V. P. Kenney[d], D. Koltick[e], C. S. Lindsey[c], C. Loomis[a], J. M. LoSecco[d], T. McMahon[e], A. P. McManus[d], N. K. Morgan[e], K. Nelson[f], S. H. Oh[a], J. Piekarz[d], N. T. Porile[e], D. Reeves[b] , W. R. Robertson[a], R. P. Scharenberg[e], S. R. Stampke[d], B. C. Stringfellow[e], M. A. Thompson[f], F. Turkot[b], W. D. Walker[a], C. H. Wang[c], D. K. Wesson[a], H. Zuong[d]

[a] Duke University- [b] Fermi National Accelerator Laboratory- [c] Iowa State University, Ames- [d] University of Notre Dame- [e] Purdue University- [f] University of Wisconsin-Madison, Madison- [g] DePauw University

List of E735 Publications

[1] T. Alexopoulos, *et al.*, Phys. Rev. Lett. *60* (1988) 1622.

[2] S. Benerjee, *et al.*, Phys. Rev. Lett. *62* (1989) 12.

[3] T. Alexopoulos, *et al.*, Phys. Rev. Lett. *64* (1990) 991.

[4] T. Alexopoulos, *et. al.*, Phys. Scripta *32T* (1990) 122.

[5] Mass Identified Particle Yields in $\bar{p}p$ Collisions at $\sqrt{s} = 1.8$ TeV, T. Alexopoulos, *et al.*, Proceedings of the XXIV International Conference on High Energy Physics, Munich, West Germany, p. 632, August 1988.

List of E735 Thesis

[1] T. Alexopoulos, Ph.D. Thesis, University of Wisconsin-Madison, Madison, 1991, "A Measurement of the Bose-Einstein Correlation for Two Pions in Proton-Antiproton Collisions at Center of Mass Energy 1.8 TeV"

[2] S. Banerjee, Ph.D. Thesis, University of Notre Dame, Notre Dame, 1989, "Multiplicity Correlations in $p\bar{p}$ Collisions at $\sqrt{s} = 1.8$ TeV"

[3] P. Beery, Ph.D. Thesis, University of Notre Dame, Notre Dame, 1990, "Two Particle Bose-Einstein Correlations at $\sqrt{s} = 1.8$ TeV"

[4] T.G. Carter, Ph.D. Thesis, Duke University, 1990, "Photon Production from $p\bar{p}$ Collisions at $\sqrt{s} = 1.8$ TeV"

[5] T. McMahon, Ph.D. Thesis, Purdue University, West Lafayette, 1989, "Phase Transition, Thermodynamics and Transverse Momentum Spectra of Mass Identified Hadrons in 1.8 TeV Center of Mass in $p\bar{p}$ Collisions"

[6] A.P. McManus, Ph.D. Thesis, University of Notre Dame, Notre Dame, 1989, "Inclusive Charged Particle Production in proton-antiproton Collisions at $\sqrt{s} = 1.8$ TeV"

[7] D. Wesson, Ph.D. Thesis, Duke University, 1990, "Λ and $\bar{\Lambda}$ Production in $p\bar{p}$ Collisions at $\sqrt{s} = 1.8$ TeV"

The E735 detector was built by the collaborative effort of the institutions listed above. Below the hardware construction and support responsibilities are listed by institution:

- Duke University: Straw Chamber.
- Fermi National Accelerator Laboratory: Hodoscope counter, Trigger Processor, Magnet.
- Iowa State University: Hodoscope Counter.
- University of Notre Dame: TOF system.
- Purdue University: Central Tracking Chamber, Magnet.
- University of Wisconsin-Madison: Z-, Pre-, Post-, Endcap Chambers, Spectrometer and dE/dx trigger.

I was personally involved in all the Wisconsin hardware and software projects.

Bibliography

[1] R. Hanbury-Brown and R.Q. Twiss, Phil. Mag. *45* (1954) 663.

[2] E735 proposal.
T. Alexopoulos, *et al.*, Phys. Rev. Lett. *64* (1990) 991.
T. Alexopoulos, *et al.*, Phys. Scripta *32T* (1990) 122.

[3] F. Abe, *et al.*, CDF Collabor., Nucl. Instr. and Meth. *A271* (1988) 387.

[4] T. Mutsi, Nucl. Phys. *461A* (1987) 27c.

[5] K. Kajantie and L. McLerran, Ann. Rev. Part. Sci. *37* (1987) 293.

[6] J.D. Bjorken, Phys. Rev. *27D* (1983) 140.

[7] Rapidity is defined for a particle with the 4-momentum $(E, \vec{p})$ as $y = 0.5\ln((E + p_z)/(E - p_z))$, p_z is the component of the momentum $\vec{p}$ along the beam direction.

[8] C. Findeisen, (E735 Collaboration), Proceedings from LES RENCONTRES DE PHYSIQUE DE LA VALEE D'AOSTE,"RESULTS AND PERPECTIVE IN PARTICLE PHYSICS".

[9] A. Shor, Phys. Rev. Lett. *54* (1985) 1122.

[10] R. Hanbury-Brown and R.Q. Twiss, Nature *177* (1956) 27.
R. Hanbury-Brown and R.Q. Twiss, Nature *178* (1956) 1046.

[11] G. Goldhaber, *et al.*,Phys. Rev. *120* (1960) 300.

[12] E. Fermi, Prog. Theor. Phys. *5* (1950) 570.

[13] N. Xuong, *et al.*, Phys. Rev. *128* (1962) 1849.
K. Bosebeck, *et al.*, Nucl. Phys. *52B* (1973) 189.

[14] M. Deutschmann, *et al.*, Nucl. Phys. *B204* (1982) 333.

[15] T. Akesson, *et al.*, Phys. Lett. *B187* (1987) 420.

[16] T. Akesson, *et al.*, Z. Phys. *C36* (1987) 517.

[17] W.J. Zajc, *et al.*, Phys. Rev. *C29* (1984) 2173.

[18] H. Aihara, *et al.*, Phys. Rev. *D31* (1985) 996.

[19] P. Avery, *et al.*, Phys. Rev. *D32* (1985) 2294.

[20] J. Juricic, *et al.*, Phys. Rev. *D39* (1989) 39.

[21] M. Arneodo, *et al.*, Z. Phys. *C32* (1986) 1.

[22] G.I. Kopylov and M.I. Podgoretsky, Sov. J. Nucl. Phys. *15* (1972) 219.

[23] G.I. Kopylov, Phys. Lett. *50B* (1974) 472.
G.I. Kopylov and M.I. Podgoretsky, Sov. J. Nucl. Phys. *19* (1974) 434.
G.I. Kopylov and M.I. Podgoretsky, Sov. J. Nucl. Phys. *18* (1973) 656.
G.I. Kopylov and M.I. Podgoretsky, Sov. J. Nucl. Phys. *15* (1972) 392.

[24] G. Cocconi, Phys. Letters *49B* (1974) 459.

[25] W.A. Zajc, Phys. Rev., *35D* (1987) 3396.

[26] S.Y. Fung, *et al.*, Phys. Rev. Lett. *41* (1978) 1592.

[27] M.I. Podgoretsky, Sov. J. Part. Nucl. *20* (1989) 266.

[28] W.A. Zajc, "Bose Einstein Correlations: From Statistics to Dynamics", HADRONIC MULTIPARTICLE PRODUCTION, edited by Carruthers, World Scientific Press, 1988.

[29] R.M. Weiner, Phys. Lett. *B232* (1989) 278.
I.V. Andreev and R.M. Weiner, Phys. Lett. *B253* (1991) 416.

[30] G. Baym, Lectures on Quantum Mechanics, The Benjamin/Cummings Publishing Company, INC. 1981.

[31] A. Nejenhuis and H.S. Wilf, Combinatorial Algorithms, Academic press, New York 1978.

[32] J. Peoples, Proceedings of the Workshop on the Design of a Low Energy Antimatter Facility held at the U.W.-Madison, Edited by D.B. Cline, World Scientific 1986.

[33] R.C. Fernow, Introduction to Experimental Particle Physics, Cambridge University Press, 1986.

[34] "A One Meter Long Low-Mass Mini Drift Vertex Chamber Used at the Tevatron Collider", T. Alexopoulos, *et al.*, 1st draft under review for submission to Nucl. Instr. and Methods.

[35] C.S. Lindsey, *et al.*, Nucl. Instr. and Methods *A294* (1987) 212.

[36] High voltage breakdown in chambers with hydrocarbon gas mixtures accelerates the deposit of various substances on chamber wires. Carbon whiskers render a chamber inoperative more quickly than some other deposits. See reference [51] for further discussion.

[37] The Kevlar reinforced Rohacell panels (125 × 30 × 0.5 cm) were fabricated by Fostergill Composites, Inc., Bennington, VT 05201, USA.

[38] J. Fischer, *et al.*, Nucl. Instr. and Methods *A238* (1985) 249.

[39] I.E. Chirikov-Zorin, *et al.*, Nucl. Instr. and Methods *A260* (1987) 142-145.

[40] A. Peisert and F. Sauli, Drift and Diffusion of Electrons in Gases: A Compilation, CERN 84-08, 1984.

[41] Gray Epoxy Adhesive 2216 B/A, flexible two component epoxy, manufactured by 3M, St. Paul, MN 55144, USA.

[42] Epolite 5313, Hardener B (two component epoxy) manufactured by Hexcel, Chatsworth, CA 91311.

[43] Sense and field wires manufactured by California Fine Wire, Grover City, CA 93433, USA.

[44] Silicone rubber compound RTV41, manufactured by General Electric Company, Silicone Products Division, Waterford, New York 12188, USA.

[45] The manufacturer of aluminum clad window panels was Advanced Dielectric Inc., Freemont, CA 94539, USA.

[46] Silicone rubber sheet manufactured by Alasco, Rubber and Plastics Corporation, Belmont, CA 94002, USA.

[47] Manufactured by Omnifit, United Kingdom.

[48] Balston Filter Products, Lexington, MA 02173, USA.

[49] P. Jarron and M. Goyot, Nucl. Instr. and Methods *226* (1984) 156.

[50] Other possible causes for a cluster are optical and electronic cross talk between neighbor cells in the same plane.

[51] Proceedings of the Workshop on Radiation Damage to Wire Chambers, Lawrence Berkeley Laboratory, (1986).

[52] S. Allen, *et al.*, Nucl. Instr. and Methods *A264* (1990) 108.

[53] E.W. Anderson, *et al.*, Nucl. Instr. and Methods *A295* (1990) 86.

[54] T. Alexopoulos, *et al.*, Phys. Rev. Lett. *60* (1988) 1622.

[55] R. Veenhof, CERN Computer Library, POOL-W5050 (1989)

[56] M.A. Thompson, *et al.*, IEEE Trans. on Nucl. Sc. *35* (1988) 184

[57] T. McMahon, Ph.D. Thesis, Purdue University, West Lafayette, 1989.

[58] D.K. Wesson, Ph.D. Thesis, Duke University, 1990.

[59] S. Banerjee, *et al.*, Nucl. Instr. and Methods *A269* (1990) 121.
A. McManus, Ph.D. Thesis, University of Notre Dame, Notre Dame, 1989.

[60] A.R. Erwin, *et al.*, Nucl. Instr. and Methods *A237* (1985) 493.

[61] S. Tufte and C. Findeisen, 'Some Preliminary End Cap Chamber Results', E735-WIS.12-10-89 internal report (unpublished).

[62] F. Turkot, from E735 Collab., Fermilab-Conf-90/205-E.

[63] A.R. Erwin, *et al.*, "An Ionization Density Trigger for E735', E735-WIS.05-05-89 internal report (unpublished).

[64] Yu. A. Yatsunenko, Vertex Reconstruction Without Track Reconstruction, Nucl. Instr. and Methods *A287* (1990) 422.

[65] "Application of a Generalized Method of Least Square for Kinematical Analysis of Track in Bubble Chambers", R. Bock, CERN 60-30.

[66] A. Ralston, H.S. Wilf, Mathematical Methods for Digital Computers, John Wiley, New York 1960.

[67] C.S. Lindsey, E735-ISU.11-03-89 internal report (unpublished).

[68] J. Bevic and A. Erwin, "Mass Resolution vs. Momentum", E735-WIS.10-29-90 internal report (unpublished).

[69] M. Aguilar-Benitez, *et al.*, Phys. Lett. *B239* (1990) 1.

[70] A. Erwin and T. Alexopoulos, "Momentum errors for 1988 Data From Magnet-Off Runs", E735-WIS.09-11-90 internal report (unpublished).

[71] C.S. Lindsey and B. Denby, Fermilab report, FERMILAB-Pub-90/192.
B. Denby, Comp. Phys. Commun. *49* (1988) 429.
C. Peterson, Nucl. Instr. and Methods *A279* (1989) 537.
T.C. Awes, Nucl. Instr. and Methods *A276* (1989) 468.
D. Cutts, *et al.*, Comp. Phys. Commun. *57* (1989) 478.
B. Denby, *et al.*, Comp. Phys. Commun. *57* (1989) 297.

B. Humpert, Comp. Phys. Commun. *56* (1989) 299.
P. Treleaven, *et al.*, Comp. Phys. Commun. *57* (1989) 543.
B. Denby, *et al.*, FSU report, FSU-SCRI-89-79.
B. Denby *et al.*, Fermilab report, FERMILAB-Conf-90/20.
C. Peterson, *et al.*, Lund Univ. report, LU TP 89-1.
C. Peterson, *et al.*, Lund Univ. report, LU TP 90-6.
T.D. Gottschalk and R. Nolty, Caltech Univ. report, CALT-68-1680.
C. Peterson, *et al.*, Lund Univ. report, LU TP 90-8 .

[72] R. Hecht-Nielsen, Neurocomputing, Addison-Wesley, New-York 1990.

[73] B. Muller, J. Reinhardt, Neural Networks: An Introduction, Springer-Verlag, Berlin Heidelberg 1990.

[74] W.H. Press, B.P. Flannery, S.A. Teukolsky, W.T. Vetterling, Numerical Recipes: The Art of Scientific Computring, Cambridge, New-York 1989.

[75] JETNET-1.1,"A Neural Network Program for Jet Discrimination and Other High Energy Physics Triggering Situations", L. Lonnblad, *et al.*, University of Lund, Lund Sweden.

[76] C. Peterson, *et al.*, Lund Univ. report, LU TP 90-8 .

[77] P. Beery, Ph.D. Thesis, University of Notre Dame, Notre Dame, 1990.

[78] A.S. Davydov, Quantum Mechanics, translated, edited, and with additions by D. ter Haar (Pergamon, London, 1965).

[79] M. Adamus, *et al.*, Z. Phys. *37C* (1988) 347.

[80] G. Arnison, *et al.*, Phys. Lett. *118B* (1982) 167.
G. Salvini from UA1 Collab., Proceedings of the XXIV International Conference on High Energy Physics, Editor R. Kotthaus and J. Kuhn, Springer-Verlag Berlin, Heidelberg 1989.
J.D. Dowell from UA1 Collab., Proceedings of the VII Topical Workshop on Proton-Antiproton Collider Physics, p.115, World Scientific 1989.

[81] M. Binkley from CDF Collab., FERMILAB-Conf-90/28-E.

[82] S. Barshay, Phys. Letters *130B* (1983) 220.

[83] M. Deutschmann, *et al.*, Nucl. Phys. *103B* (1076) 198.
J.L. Bailly, *et al.*, NA23 Collab., CERN/EP 88-17.
T. Akesson, *et al.*, AFS Collab., CERN/EP 86-215.
J.S. Pearson and P.M. Yager, University of California-Davis preprint, UCD-PPL-77-02-10.

[84] T. Alexopoulos, A. Erwin, and J. Jennings, 'Monte Carlo Analysis of Pion Tracks', E735-WIS.02-20-91 internal report (unpublished).

[85] N. Metropolis, *et al.*, J. Chem. Phys., *21* (1953) 1087.

[86] H. Gould, J. Tobochnik: Computer Simulation Methods, Part 2, Addison-Wesley New-York 1988.

[87] G.A. Erskine, Nucl. Instr. and Methods, *198* (1982) 325-336.

VITA

Theodoros Alexopoulos was born on May 1st, 1960, in Aegaleo Athens, Greece. He graduated from B' Aegaleo Athens High school in Greece and received a Bachelor of Science degree in Physics from the University of Athens in 1983. He received a scholarship from 1982-1985 from the Nuclear Research Center "Democritos" located in Greece. He was a Research Assistant in high-energy physics at the University of Wisconsin - Madison from Jan. 1985 working under the supervision of Professor Albert Erwin. He completed the requirement and received a MS degree in physics from the University of Wisconsin-Madison in May 1987. He completed the requirement and received a Ph.D. degree in physics from the University of Wisconsin-Madison in May 1991.

List of Publications

[1] T. Alexopoulos *et al.*, Phys. Rev. Lett. *60* (1988) 1622.

[2] T. Alexopoulos *et al.*, Phys. Rev. Lett. *64* (1990) 991.

[3] T. Alexopoulos *et al.*, Phys. Scripta *32T* (1990) 122.

[4] "A One Meter Long Low-mass Mini Drift Vertex Chamber Used at the Tevatron Collider", T. Alexopoulos, *et al.*, 1st draft under review for submission to Nucl. Instr. and Methods.

[5] "Estimation of the Magnetic field in a region from measurements of the field at discrete points", T. Alexopoulos *et al.*, DEMO (Greece) 84/14.

[6] Mass Identified Particle Yields in $\bar{p}p$ Collisions at $\sqrt{s} = 1.8$ TeV, T. Alexopoulos, *et al.*, Proceedings of the XXIV International Conference on High Energy Physics, Munich, West Germany, p. 632, August 1988.